THE UNIVERSITY OF READING

High Resolution Atmospheric Modelling of a Tropical Island for Space Geodesy

Thomas Lloyd Webb

A thesis submitted for the degree of
Doctor of Philosophy

Department of Meteorology

September 2015

Declaration

I confirm that this is my own work and the use of all material from other sources has been properly and fully acknowledged.

Thomas Webb

for my father ...

Acknowledgements

This thesis was funded by a Natural Environmental Research Council studentship and by the Department of Meteorology, University of Reading.

I would like to direct my sincere gratitude to Geoff Wadge for his patience, understanding and guidance throughout my PhD and for his meticulous attention to detail especially whilst writing up this thesis. Praise also goes to Chris Holloway for his advice especially in the closing months of this project.

Recognition goes to my office colleagues, Rob Lee and Mark Richardson for keeping me entertained for so many years and to some of the most exceptionally fun housemates I have ever had the pleasure of living with, Simon Thomas, Trevor Mitchell, Julian Mann, Aidan Brocklehurst and Michael Glinton. Additional thanks to my colleagues both in the ESSC and department of Meteorology of which there are too many to name all individually. However I would like to take this opportunity to thank Dan Bretherton for going beyond the cally of duty to respond to many of my IT requests.

I would like to recognise here the staff of the Montserrat Volcano Observatory (MVO) for providing me with support whilst in the field. Additional thanks for support during my fieldwork goes to Antonio Costa (INGV) and Charles Werner (GAMMA). Special praise goes to Karen Pascal (MVO) who performed the GAMIT processing of GPS data for this project and who I stayed with on my 3rd field campaign to Montserrat. The MVO and government of Montserrat I thank for providing me with climatological data. Matthew Pitchard and the Italian Space Agency I thank for providing me with COSMO-SkyMed radar images.

Finally I would like to thank my parents, Edward and Catherine, sister, Zoe, and fiancée, Ruth for providing additional support to me during my PhD.

Abstract

Turbulent mixing processes over terrain cause local horizontal variations in water vapour from a variable vertically stratified profile. Temporal variations in water vapour distribution cause delays in phase used in the space geodetic InSAR technique. To correct for this, dynamic atmospheric models are used to simulate water vapour distribution and hence variable refractive phase delay over a small volcanic island in the humid tropics, Montserrat. Initialised by ECMWF analysis data at 16 km resolution, the Weather Research and Forecasting (WRF) model is nested to 300 m resolution. Synthetic simulations of trade wind flow with the WRF Montserrat Model (WMM) demonstrate its ability to replicate gravity waves. WMM simulates atmospheric delay fields during the InSAR imaging of Montserrat by X-band radar (COSMO SkyMed) from two viewing geometries during December 2014. Field measurements during imaging and the recording of zenith wet delay (ZWD) by a 14-receiver GPS network are used for comparison with the radar data and atmospheric models. WMM and ZWD delay difference images appear to show two main influences: (static) topographic modulation and dynamic modulation due to the trade winds flowing over and around the mountains. Mitigation of the unwanted delay field in COSMO-SkyMed interferograms using the WMM fields gives standard deviations of the residual delay field in the range 19-38 mm. Statistical calculations of pixel-wise delay estimates place model accuracy in the range 64-81%. The reasons for this level of mitigation may be truncation of initial conditions to WMM, the large amount of liquid water in the atmosphere and simulation of trade wind flow across Montserrat.

Contents

List of Figures

List of Tables

Chapter 1

Introduction

1.1 Background

Surface deformation measurements made from space by Interferometric Synthetic Aperture Radar (InSAR) are limited in accuracy by errors known to be caused by water in the atmosphere. This is a well documented problem at Soufrière Hills Volcano, Montserrat (SHV) [Wadge et al., 2006]. The research in this thesis presents a new way to use forward atmospheric modelling of water constituents in the atmosphere to determine the atmospheric water distribution over SHV, analyse the errors to satellite measurements resulting from this water and thereby improve surface deformation measurements [Jolivet et al., 2011].

Water is held by the atmosphere in three states, solid, liquid and as a vapour. In each of these states the water distribution varies to a great extent over different distances and timescales. This variation is large over mountainous terrain where complex flow patterns and orographic uplift can cause a highly localised, extremely variable water distribution [Smolarkiewicz et al., 1988].

An observation of water in the atmosphere is very useful as a tool for meteorologists to determine the current condition of the atmosphere or provide a prediction of future conditions. However, for geophysicists, who wish to use satellite-based radar to determine the Earth's surface deformation, the effect of water is to generate noise embedded within the radar signal and often making surface deformation hard to observe [Ding et al., 2008]. Thus observing and predicting the water distribution over mountainous terrain at high temporal and spatial scales, using meteorological methods, can potentially benefit geodetic geophysicists. This is specifically of interest to the scientists at the Montserrat Volcano Observatory (MVO) concerned with measuring the ground deformation of the volcano.

1.2 Water in the troposphere

The layer of the atmosphere closest to the Earth, the troposphere, is up to twenty kilometres deep in the tropics. Solar heating is enhanced in low-latitudes relative to high latitudes because the Sun's energy is spread out over less of the Earth's surface due to the curvature of the Earth. This gives rise to more ocean evaporation and higher sea surface temperatures in the tropics. As a result tropical air is usually warm, moist and buoyant, rising high into the atmosphere via convection and forming clouds. So the tropics are the most cloudy and most humid places on Earth. The tropics are where most of the atmospheric water is located.

The location of Montserrat (Lon. 62W, Lat. 16N) in the Lesser Antilles island arc is shown in Figure 1.1. Volcanic processes cause a plume of vapour and condensates to travel from SHV usually to the west, as the island is in the north-east trade wind region of the tropics. However, Montserrat's proximity to the inter-tropical convergence zone and the high tendency for Eastern African waves in the area sometimes makes the wind direction change as mesoscale systems pass through the region [Heleno et al., 2010].

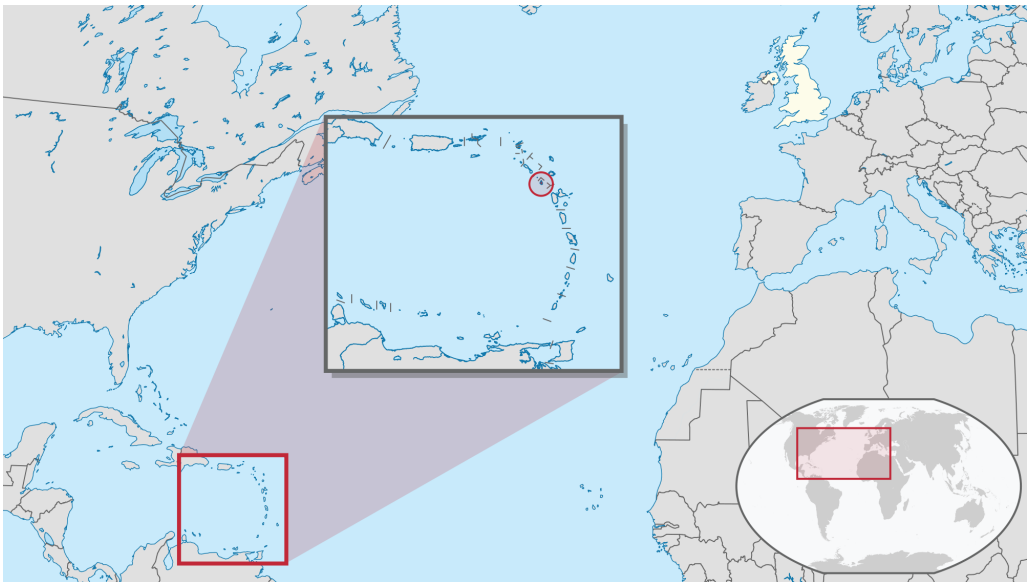

Figure 1.1: Montserrat, circled in the inset, is located in east Carribean in the tropical trade wind zone.

As far as InSAR is concerned, water vapour has two important distributional characteristics shown conceptually in Figure 1.2. First, there is a vertical gradient of water vapour content, decreasing upwards. Secondly, there is a turbulent, dynamic effect due to atmospheric flow caused by convection and orographic lifting around terrain [Smith et al., 2009]. The turbulent flow of water vapour varies greatly over

spatial and temporal scales but diminishes to negligible proportions at the top of the troposphere.

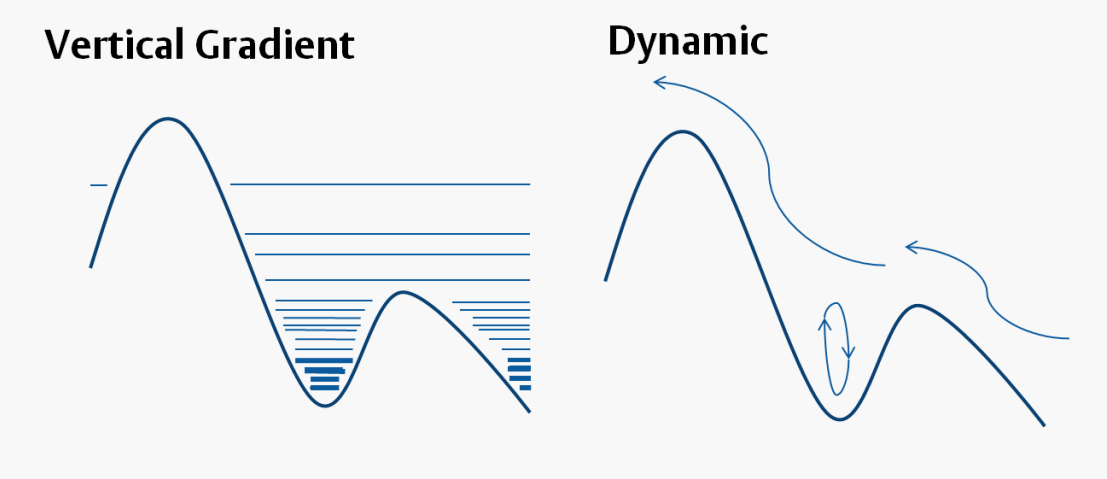

Figure 1.2: (Left) Water vapour content increases with decreasing altitude. Intersection with orography produces a terrain-following signal. (Right) Convection and orographic uplift produce a complex dynamic signal.

1.3 InSAR

To measure deformation at the Earth's surface with an InSAR technique an interferogram is constructed which measures the complex difference between the phases of each spatially resolved radar signal at two different points in time. If the atmosphere was completely identical on both occasions or different by a constant amount across the whole field of view, the interferogram would contribute no effective signal except for that from any ground motion. This is rarely the case because water in the atmosphere changes greatly across spatial and temporal scales so the refractive noise in the radar signal manifests itself as a signal delay and an apparent ground motion [Pinel et al., 2014].

An example interferogram produced with European Remote-Sensing Satellite (ERS) C-band radar for Montserrat with images taken on 13th and 14th May 1999 is shown in Figure 1.3. The outline of Montserrat is clearly visible within areas of incoherency over the sea. One phase cycle received from red to green to purple represents increasing two-way 56 *mm* path delay, in received radar phase, along the radar line of sight through the atmosphere. Incoherent areas over the centre of the island are due to unstable scattering surfaces (leaves) in forested areas. On the southern side of Montserrat there are phase 'stripes' which match up with gullies and are a result of orography.

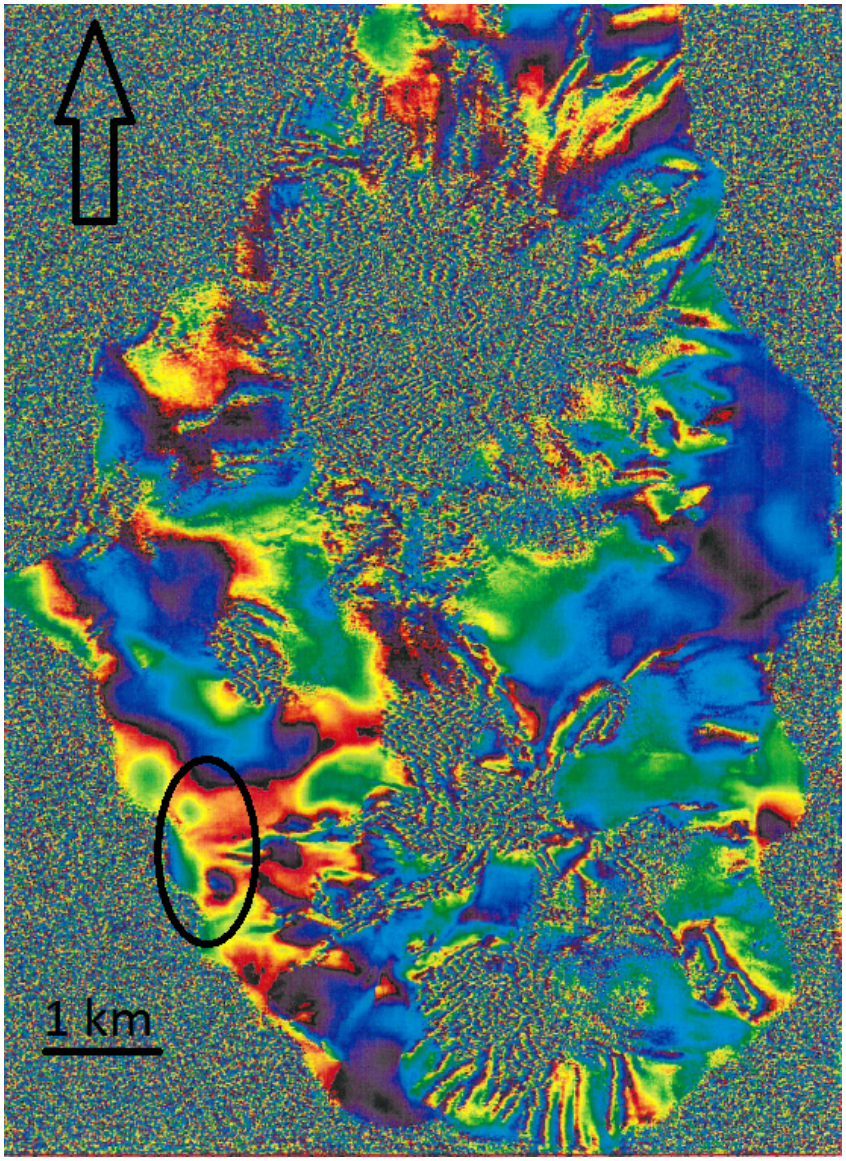

Figure 1.3: ERS-1 and -2 interferogram of Montserrat taken with images on 13th and 14th May 1999. Black arrow indicates North. Ellipse towards bottom left of island shows an area of one phase cycle from red to green to purple corresponding to 56 mm two-way atmospheric delay.

The ionosphere can also modify the radar refractivity, usually leading to a path advance, as solar heating causes plasma bubbles to rise just before sunset and a tropical jet to form [Mendillo, 2006]. This is especially prevalent in years of solar maxima, i.e. 2013. However, this only affects long wavelength radars (L-band 24cm) and operates over large spatial scales [Gray et al., 2000].

1.4 Atmospheric effects on radar signals

Increased water vapour along the radar path changes the refractivity, producing an apparent radar path length increase. This can be calculated from the refractivity Equation (1.1). Additionally, on encountering a liquid water droplet, the radar wave front induces a dipole moment in the droplet generating a secondary wave front. The radar wave front and secondary wave front interfere with each other to cause a radar path length variation [Hanssen, 2001]. The general change in refractivity is given by:

$$N_\delta = 10^{-8}\rho R_v \left(\frac{k_1}{T_m}\right) q_v + \left(\frac{2.2779 \pm 0.0024 P_s}{1 - 0.00266 cos 2\lambda - 0.00028 H}\right) + \delta_{cu} z_{cu} - \left(\frac{\partial \delta_{ion}}{\partial TEC}\right) \tag{1.1}$$

where N_δ is refractivity, ρ is the density of liquid water, q_v is culmulative water vapour along a chosen line of sight, R_v is the specific gas constant of water vapour, equal to 461.524 $J\ Kg^{-1}$, T_m is the mean atmospheric temperature, k_1 equals 3.75x10^5 $K^2\ hPa^{-1}$, P_s is the surface pressure in millibars, λ is the latitude, H is the surface height in km above the ellipsoid, δ_{cu} is the delay caused by cumulus cloud, usually in the range 0.7 to 3.1 $mm\ km^{-1}$ (Table 1.1). z_{cu} is the aggregate distance traced through cloud in km, δ_{ion}, in m, is the ionospheric advance and TEC is the total electron content in $TECU$ (10^{16} electrons m^{-2}).

The first term on the right hand side of Equation (1.1) quantifies water vapour delay at the zenith from the effects of induced and permanent dipole moments of the water vapour molecules. The second term quantifies the hydrostatic component from the effects of the induced dipole moment on the non-water vapour constituents of the air. The third term quantifies liquid water delay in clouds. The fourth term quantifies the ionospheric delay, changes in the refractivity of the ionosphere influenced largely by solar wind variation which changes the number of free electrons causing a dispersive delay of radio signals.

Uncertainties in the second term arise from uncertainties in the calculations of the refractivity of dry air, acceleration due to gravity, the universal gas constant and the dry mean molar mass, a discussion of which can be found in [Davis et al., 1985] and elsewhere.

Different cloud types have differing particle number densities so each type has a different liquid water content associated with it and hence a different typical radar delay, (Table 1.1). Owing to Montserrat's location and hence the high likelihood that clouds formed over it are caused by convection and orographic uplift, I assume that all cloud over Montserrat is cumulus. Ice has an even smaller impact on path delay and is ignored here.

Table 1.1: Liquid water content in clouds, [Hanssen, 2001].

Type of Cloud	Water Content ($g\ m^{-3}$)	Delay ($mm\ km^{-1}$)
Stratiform	0.05-0.25	0.1-0.4
Small cumulus	0.5	0.7
Cumulus congestus and cumulonimbus	0.5-0.2	0.7-3.1

1.5 Techniques for eliminating atmospheric delay from InSAR

Most techniques for eliminating atmospheric delay are broadly split into three categories. First, those that use independent observations to capture the details of the water distribution in the atmosphere at the times the radar images are acquired [Katsougiannopoulos, 2006], secondly those that employ a statistical approach to reduce the water vapour signal from the InSAR imagery iteself [Hetland et al., 2012], and thirdly, forward atmospheric models. We will give a brief overview of each type.

Each of the main methods of atmospheric delay elimination has faults associated with it that effectively render that technique less generally applicable. My study uses a forward atmospheric model approach [Jolivet et al., 2014]. This allows a high temporal-spatial resolution output of radar delay fields that cannot be obtained from observations alone [Gong et al., 2015]. In the past this sort of technique has been tried with several model types, but has not been able to produce high resolution output at low computational cost, from high resolution initial conditions. However, technological advances enable the model approach of this thesis to produce significant improvements in InSAR motion retrievals [Gonzalez et al., 2013].

1.5.1 Independent Measurements

Ground-, upper air- and satellite-based techniques have been used. Ground-based radiometers can measure column water vapour along different slant angles. Hand-held radiometers have been found to produce much more inaccurate measurements than their tripod mounted counterparts [Porter et al., 2001]. In the case of solar radiometers these also need the sun at the measurement slant angle for an accurate measurement. It is also known that generally, the resolution provided by radiometers in the lower troposphere is often much less accurate than that demanded for InSAR correction. Upper-air sounding techniques from radiosondes do not provide high enough horizontal spatial resolution and temporal resolution for InSAR correction. In the case of Montserrat, the nearest radiosonde is deployed daily, eighty kilometres from the island, but is useful for validation of other results.

Global Positioning System (GPS) receivers measure the range to multiple satellites [Onn and Zebker, 2006]. A least squares fitting approach to the satellite signals using their different geometries is routinely used to calculate a zenith delay from each GPS station, [Bevis et al., 1992]. The delay can be split into that due to the hydrostatic atmosphere (dry delay) and that due to the water vapour (wet delay), (Equation (1.1)). This method can provide estimated values every minute but is limited by the spatial and distribution area of the GPS network [Webley et al., 2002], [Cheng et al., 2012], [Zhenhong et al., 2006]. A coarse network ($\gtrsim$ 20 km station spacing) does not offer the resolution needed to correct InSAR accurately. Montserrat has a 14-station GPS network shown in Figure 1.4. Table 1.2 shows the altitude of each GPS station.

Table 1.2: Altitude of each GPS station.

GPS station	(m)
AIRS	84
FRGR	554
HARR	244
HERM	437
MVO1	244
NWBL	147
OLVN	41
RCHY	313
SGH1	317
SPRI	253
SSOU	408
TRNT	-23
WTYD	151
GERD	125

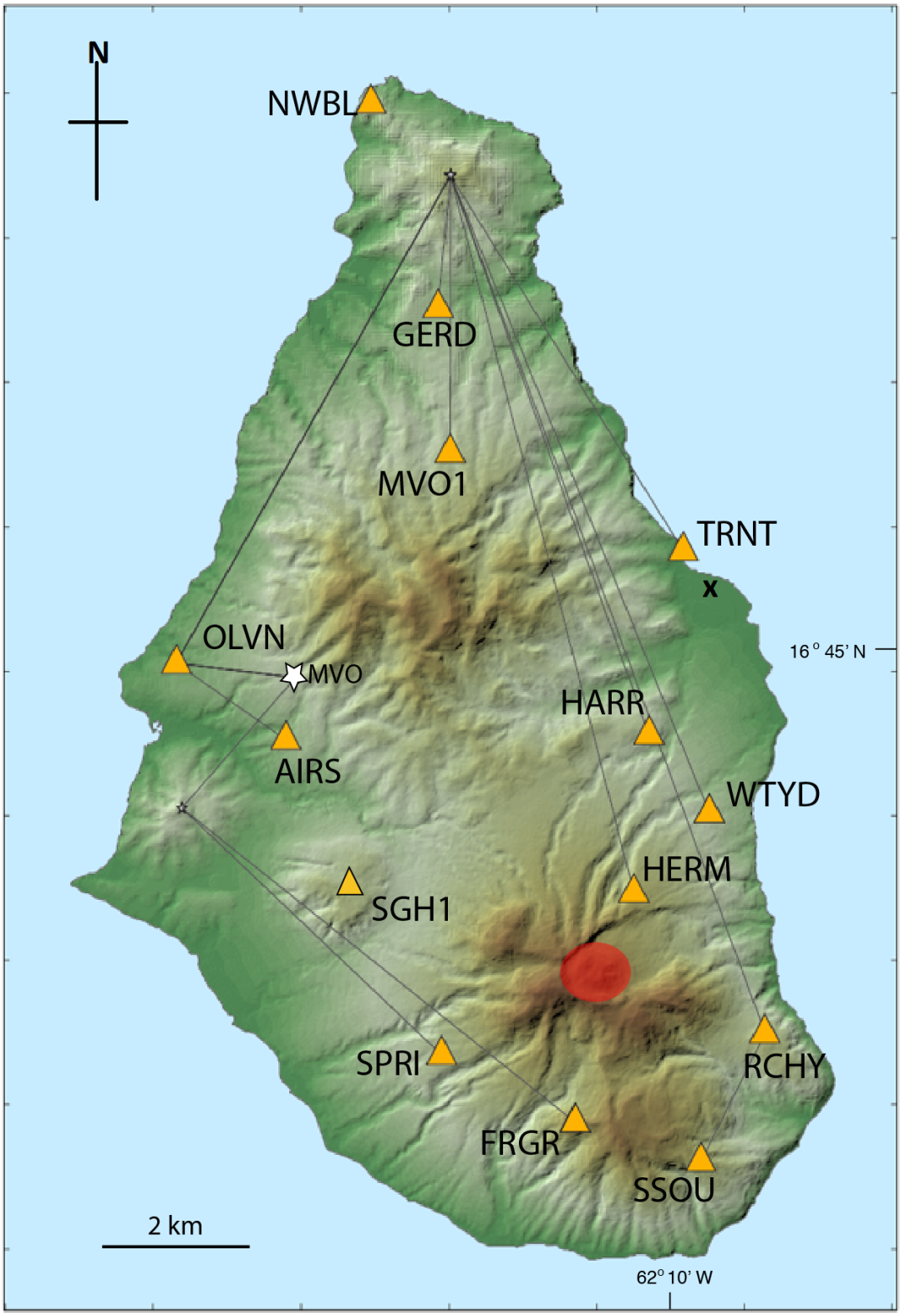

Figure 1.4: Map of Montserrat ~16 km long and 10 km across. Yellow triangles correspond to GPS measurement sites. GPS sites: AIRS - Air Studios, FRGR - Fergus Ridge, GERD - Geralds, HARR - Harris Lookout, HERM - Hermitage Estate, MVO1 - Mongo Hill, NWBL - North West Bluff, OLVN - Olveston, RCHY - Roache's Yard, SGH1 - St. Georges Hill, SSOU - South Soufriere Hills, SPRI - Spring Estate, TRNTS - Trants, WTYD - White's Yard. Low terrain is green, high terrain is brown. Montserrat Volcano Observatory - white star. Soufrière Hills Volcano lava dome - red circle. 'X' marks location of meteorological mast.

Satellite radiometers, e.g. the Moderate Resolution Imaging Spectroradiometer (MODIS) and Medium-spectral Resolution Imaging Spectrometer (MERIS) image water vapour by measuring the depth of water absorption features in the infra-red. They provide a fairly high nadir resolution (1000m - MODIS, 300m - MERIS), but the scene may be obscured by clouds and, for MODIS, is not at the same time as the radar aquisition. Additionally water can limit space-borne techniques by high attenuation in the upper troposphere, as a result of which the lower troposphere, where most of the atmospheric water lies, is under-represented. In general most ground- and air-based observations are limited by poor spatial resolution whilst satellites are mainly limited by sparse repeat times [Li et al., 2005].

1.5.2 Time Series Methods

A time series is a collection of observations of well-defined data items obtained through repeated measurements over time; three popular techniques are briefly explained here. Stacking is one such technique which relies on the basic assumption that the water vapour effect is randomly distributed in space through each series of independent interferograms in order for it to be reduced by averaging at a rate of $sqrt(n-1)$, where n is the number of interferograms [Sandwell and Price, 1998]. However we know from Section 1.2 that this assumption may not be true because terrain causes water vapour to mix in a way defined by atmospheric flow over that fixed terrain.

Persistent Scatterer Interferometry (PSI) estimates the atmospheric delay [Gong et al., 2015], sometimes referred to as the *atmospheric phase screen (APS)*, based on residuals after low-pass time-domain filtering [Ferretti et al., 2001]. Persistent scatterers (PS), coherent over long time intervals are identified from a few tens of SAR images and the interferometric phase is considered only for those scatterers, but is interpolated over the whole image. As the APS from non-subsequent SAR images is completely decorrelated in time, the interpolated APS for each PS can be estimated and removed from each interferogram. Thirdly, the Small Baseline Subset (SBAS) algorithm additionally uses pairs of SAR images selected to minimise the spatial and temporal separation between acquisition orbits in order to reduce delay due to atmospheric water to its minimum [Berardino et al., 2002]. However this does not elimate the delay, only reduce it to its lowest amount without addressing it formally. Each of these statistical techniques requires a large number of InSAR aquisitions (typically more than 10-20) to produce meaningful results.

1.5.3 Numerical Modelling of the Troposphere

Numerical modelling uses the basic prognostic equations of motion and conservation of energy of the atmosphere integrated with respect to time and space. These are expressed with set boundary and initial conditions such that the equations can be solved with high performance computers (HPC) to calcuate an approximation for atmospheric flow at each physical point in time. Weather Research and Forecasting (WRF) is a research model [Skamarock et al., 2008], having high enough horizontal and vertical resolutions to forecast mesoscale weather phenomena and needing accurate boundary conditions from a global model.

In the last ten years, high resolution mesoscale models have been used to study the water distribution in the atmosphere needed for InSAR correction. Noteable studies in the development of this technique thus far includes NH3D at 1.7km horizontal resolution [Wadge et al., 2002], MM5 at 3km horizontal resolution [Foster et al., 2006] and WRF at 1km horizontal resolution [Liu, 2012] and [Kinoshita et al., 2013].

In order to capture the highly varying temporal and spatial water distribution in the lower troposphere, dominated by local topographic and mesoscale features, a forward, nested set of numerical models is employed [Doin et al., 2009]. In this thesis I use the European Centre for Medium Range Weather Forecasting (ECMWF) analysis model as the initial conditions for a set of four increasingly higher resolution models nested within each other in order to capture the structure of the atmopshere over Montserrat using the WRF-Montserrat Model (WMM). The models are validated using measurements of zenith wet delay (ZWD) from a network of 14 GPS stations on Montserrat with high spatial coverage, atmospheric radiosonde ascents from nearby Guadeloupe and Kestrel portable weather station data.

1.6 Thesis Outline

Following this brief statement of the problem and its proposed solution, the thesis develops as follows:

Chapter 2 is a preliminary review of WRF Modelling and InSAR.

Chapter 3 presents the details of two field campaigns and climate data obtained by the project to provide meteorological context for Montserrat. This chapter includes an overview of the WMM and provides analysis of synoptic and mesoscale weather conditions in the region during the field campaigns. This starts with an introduction to idealised mountain atmosphere modelling, the development of the WMM through sensitivity testing and analysis to provide an accurate representation

of water vapour fields on Montserrat.

Chapter 4 comprises of InSAR processing for the dates of the third field campaign, limitations of the study and comparison to both observation and statistical InSAR correction.

Chapter 5 presents the GPS wet delay measurements for the 2012 and 2013 field campaigns and compares this data with WMM output.

Chapter 6 presents the mitigation of InSAR data with WMM water vapour fields. This introduces delay estimates made at InSAR slant angles validated with data from the 2014 field campaign.

Conclusions and recommendations for future research are given in chapter 7. This includes the modelling of volcanic plume SO_2 emissions and DOAS wind correction for sulphur flux measurements. There is also a description of how the WMM can be coupled with chemistry code (WRF-Chem) to produce an atmospheric dispersion inside the model to simulate degassed volcanic volatiles (dominated by water).

1.7 My Significant Findings/ Achievements

- Observing idealised flow of atmosphere over a mountain consistent with theory. Recording WMM observations such as mesoscale systems and gravity (lee) waves.
- Producing an operational weather forecast of Montserrat, a tropical island, at 300 m resolution using ECMWF initial conditions. Sensitivity testing of parameterisations up to 1 km resolution using Global Forecast System (GFS) initial conditions.
- Mounting three field campaigns in Montserrat to collect weather, satellite and GPS data - for WMM validation purposes. Obtaining and analysing a climatological dataset for Montserrat.
- Planning a COSMO-SkyMed observational campaign to produce interferograms.
- Performing slantwise ray-tracing through the WMM. Integrating the WMM with interferometric data using sampling and interpolation methods.
- Interpolating GPS data to produce ZWD fields for validation with WMM.
- Performing atmospheric mitigation to interferometric data using the WMM and measuring its forecast skill.

Chapter 2

Methods and Tools

2.1 The WRF model

The atmospheric simulations described in this thesis are conducted using the Weather Research and Forecasting (WRF) model version 3.1.1 in Advanced Research mode, which was released in September 2011. Chapter 3 will evaluate initial conditions, parameterisations, chemistry integration and preprocessor steps. For this section I will provide an overview of the spatial and temporal discretisation used in WRF. Following this I discuss the governing equations, taken largely from [Skamarock et al., 2008].

A schematic workflow of WRF for my uses (WMM) is shown in Figure 2.1 - where initial conditions are prepared for preprocessor steps and then interpolated with initial conditions to run the model. In this thesis idealised models refer to hydrostatic models and non-idealised (real) models refer to non-hydrostaitc models.

2.1.1 Model grid

In this section I briefly outline the spatial and temporal discretisation. The horizontal and vertical model co-ordinates follow the Arakawa-C grid as shown in Figure 2.2. On the model grid column-mass-coupled variables are defined relative to the uncoupled variables, Coriolis and curvature terms define the map projection (isotropic in the case of WMM) and variables are advected in the form of a flux divergence. WRF uses the third order Runge-Kutta (RK3) scheme to advect momentum and scalars (Section 2.1.1.2).

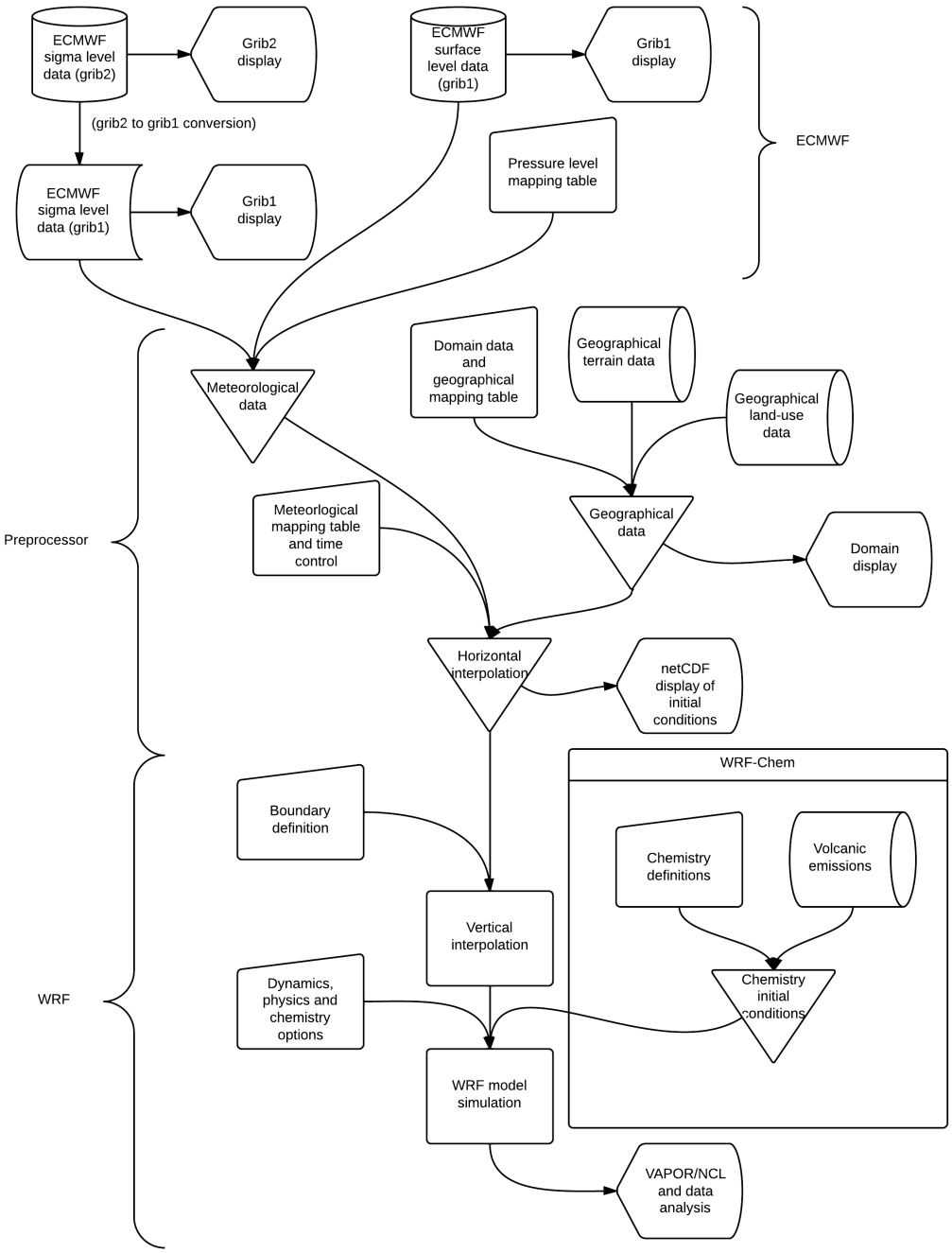

Figure 2.1: WMM workflow, initial conditions from the ECMWF are processed in preprocessor steps alongside surface boundary data.

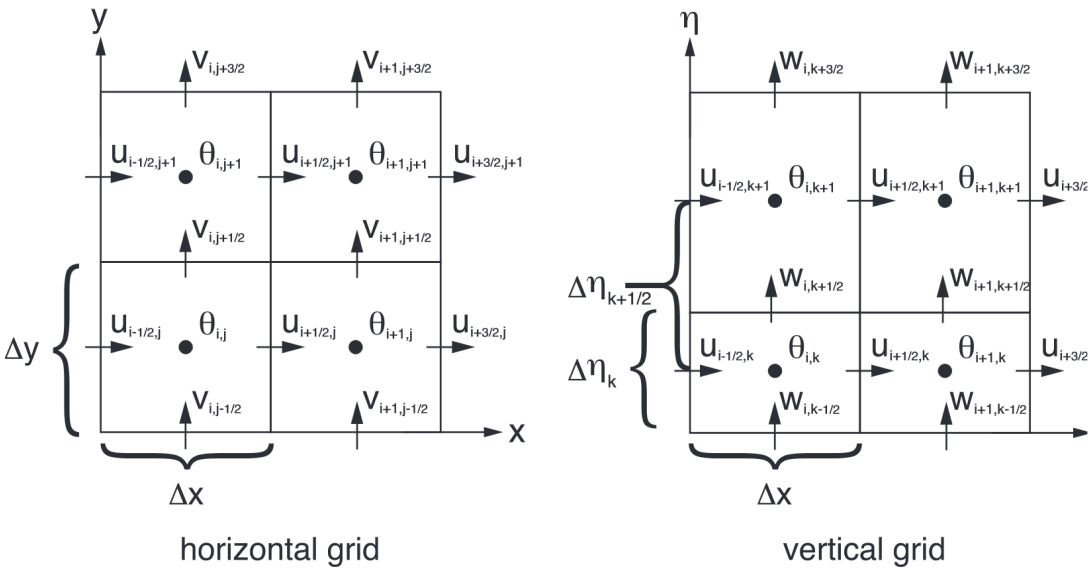

Figure 2.2: Arakawa-C horizontal and vertical grids used by WRF where velocities (u,v,w) are staggered one-half grid lengths from the thermodynamic variable (θ) locations (i,j,k), [Skamarock et al., 2008].

2.1.1.1 Vertical grid

The vertical levels (η) are determined using vertical co-ordinates (Equation (2.1)) [Laprise, 1992] as long as $\eta = 1$ at the surface, $\eta = 0$ at the model top and η decreases monotonically between the surface and the model top. These are terrain-following hydrostatic-pressure co-ordinates meaning that near the bottom of the model they follow terrain produced from WRF- preprocessed geographic data and the levels slowly adjust to a constant pressure at the top of the model, Figure 2.3.

$$\eta = \frac{(p - p_t)}{\mu}, \tag{2.1}$$

where η is the difference between the hydrostatic component of pressure along the surface and top model boundaries, p is the hydrostatic component of pressure and p_t is the dry hydrostatic component of pressure along the top of the model. This varies from 0 at the domain top to 1 at the domain bottom because μ represents the total weight per unit area of air in the column.

2.1.1.2 Temporal discretisation

WRF integrates the governing equations using a time-split approach in which low frequency modes are integrated using the third order Runge-Kutta (RK3) scheme. The time-splitting allows these modes to be integrated with the model time step, t, leaving the high frequency modes (corresponding to acoustic waves) to be inte-

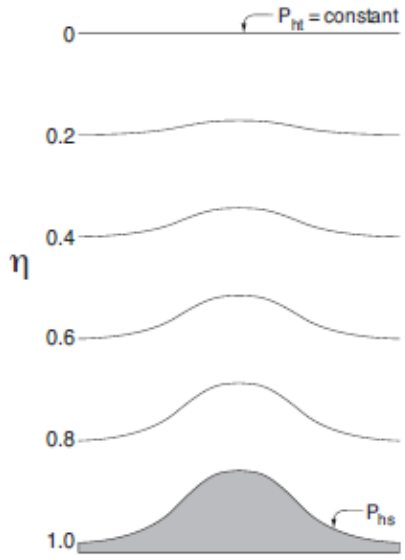

Figure 2.3: Terrain-following hydrostatic-pressure co-ordinate example from [Skamarock et al., 2008].

grated on the smaller time step necessary to maintain numerical stability (acoustic timestep). These high frequency modes are integrated using a forward-backward integration scheme in the horizontal and an implicit scheme in the vertical.

In idealised modelling, the WRF model is fully compressible, which requires that numerical stability is maintained with respect to high frequency acoustic waves. This is achieved with the RK3 approach. The hydrostatic pressure, potential temperature, inverse density and geopotential can be found using the hydrostatic assumption.

Due to WMM nesting, at small spatial length scales the maximum stable timestep is likely to be larger than any one fixed timestep chosen to produce a stable integration for the whole model run. So I now discuss adaptive timestepping and stability constraints.

Adaptive timestep

In an adaptive timestep model run, WRF chooses each progressive RK3 timestep based on temporally-evolving wind fields. This means that dynamics integrates faster, the physical updates are called less often and run-time can be reduced. Each new timestep (Δt_c) is calculated using Equation (2.2).

$$\Delta t_c = min\left(1 + f_i, \frac{Cr_t}{Cr_d}\right)\Delta t_p, \tag{2.2}$$

where f_i is the regulated increase, Cr_t is the target maximum Courant number, Cr_d is the maximum Courant number in the domain, and Δt_p is the previous time step. The time step is reduced when model stability has been compromised which is when the computed maximum domain-wide Courant number exceeds the targeted maximum allowable Courant number (Equation (2.3)).

$$\Delta t_c = max\left(1 - f_d, \frac{Cr_t - 0.5(Cr_d - Cr_t)}{Cr_d}\right)\Delta t_p, \tag{2.3}$$

where f_d is the factor to decrease the time step. Lower and upper bounds on the time step can be enforced by the WRF user. Inside a nest, the child domain must maintain an even number of integration time steps within the parent domain. The adaptive time step is based on the wind fields of the inner-most child domain (where there is the smallest physical horizontal spacing) for Mercator projections.

The timestep is initialised for all domains at the start of this model and with every time increment a new timestep is chosen based in the stability of the inner-most domain. That is to say if the inner-most domain requires a half its original timestep to perform the next iteration stably then each of the timesteps of the other domains are also halved. Timesteps can increase as well as decrease in value.

Stability

Both the model time step (used by RK3) and the acoustic time step (used by time-split integration procedure) are used in WRF and are limited by Courant numbers.

The RK3 time step is limited by the advective Courant number ($u\Delta t/\Delta x$) and choice of advection schemes. As previously discussed (Section 2.1.1.2) RK3 is more stable than other integration schemes. To obtain a stable time step WRF uses Equation (2.4) which finds the theoretical maximum timestep (Δt_m).

$$\Delta t_m < \frac{Cr_y}{\sqrt{3}}\frac{\Delta x}{u_m}, \tag{2.4}$$

where Cr_y is the theoretical max Courant number [Wicker and Skamarock, 2002], Δx is the grid spacing and u_m is the maximum expected wind velocity. In practise this number is set to 25 % less than this, so there is a stability safety buffer for time-splitting constraints.

The acoustic time step ($\Delta\tau$) has a maximum Courant number associated with ($< 1/\sqrt{2}$) that is subjected to a stability safety buffer so that the acoustic time step

used in WRF is:

$$\Delta\tau < 2\frac{\Delta x}{c_s}, \tag{2.5}$$

where c_s is the speed of sound.

2.1.2 Governing Equations

The equations solved by WRF are the equation of state (2.8), momentum equations (2.9)-(2.11), mass conservation equation (2.12), geopotenital equation (2.13), conservation equations for potential temperature (2.14), (2.15) and hydrostatic relation (2.16).

2.1.2.1 Equation of state

The conservation equation for dry air (2.6) which is one of the flux-form Euler equations allows us to define coordinates with respect to dry-air mass and not to couple variables to the moist air mass. This allows (2.1) to be rewritten as (2.7). With the dry air mass (μ_d) coupled to potential temperature, contravariant vertical velocity and the covariant velocities ($\mathbf{v} = (u, v, w)$) so moisture can be included in the model; using the moist Euler equations.

$$0 = \vartheta_t \mu + (\nabla \cdot \mathbf{V}), \tag{2.6}$$

where $\mathbf{V}$ the flux-form variable of the covariant velocities ($\mu\mathbf{v}$) as $\mu(x, y)$ represents the mass per unit area within each column in the model.

$$\eta = \frac{(p_d - p_{dt})}{\mu_d}, \tag{2.7}$$

where p_d is the hydrostatic pressure of the dry atmosphere and p_{dt} is the hydrosatic pressure at the top of the dry atmosphere. Hence the equation of state for 'moist' pressure becomes:

$$p = p_0 \left(\frac{R_d \theta_m}{p_0 \alpha_d}\right)^{\gamma}, \tag{2.8}$$

where γ is the ratio of specific heat capacity to heat capacity at constant volume for dry air (1.4), R_d is the gas constant for dry air, p_0 is a reference pressure (10^5 Pa), α_d is the inverse density of dry air ($1/\rho_d$) and θ_m takes into account the potential

temperature from different states of water.

2.1.2.2 Pertubation equations

For the WMM it is useful to think of pertubations from a hydrostatically-balanced reference state, that are a function of height only and that satisy the governing equations at rest. This allows the reduction of truncation errors in the horizontal pressure gradient calculations in the discrete solution and machine rounding errors in the vertical pressure gradient and buoyancy calculations. In hydrostatic balance, the reference state is a function of $\bar{z}$ only. Thus the pressure, geopotential, inverse density and air mass can be written in the form $n = \bar{n}(\bar{z}) + n'$ where n is the quantity perturbed and $\bar{n}$ is the quantity's reference profile. In this form the momentum equations become:

$$\begin{aligned} F_U = \vartheta_t U + m_x[\vartheta_x(Uu) + \vartheta(Vu)] + \vartheta_\eta(\Omega u) \\ + \frac{m_x}{m_y}\frac{\alpha}{\alpha_d}[\mu_d(\vartheta_x\phi' + \alpha'_d\vartheta_x\bar{p}) + \vartheta_x\phi(\vartheta_n p' - \mu'_d)], \end{aligned} \tag{2.9}$$

where F is force, ϕ is the geopotential, m_x and m_y are map scale factors - the ratio of the distance in computational space to the corresponding distance on the Earth's surface, U, V and Ω are redefined momentum variables (for map scale); $U = \mu_d u/m_y$, $V = \mu_d v/m_x$, $\Omega = \mu_d \check{\eta}/m_y$ where $\check{\eta}$ is the contravariant vertical velocity.

$$\begin{aligned} F_V = \vartheta_t V + m_x[\vartheta_x(Uv) + \vartheta(Vv)] + \vartheta_\eta(\Omega v) \\ + \frac{m_x}{m_y}\frac{\alpha}{\alpha_d}[\mu_d(\vartheta_x\phi' + \alpha'_d\vartheta_x\bar{p}) + \vartheta_x\phi(\vartheta_n p' - \mu'_d)] \end{aligned} \tag{2.10}$$

$$\begin{aligned} F_W = \vartheta_t W + \frac{m_x m_y}{m_y}[\vartheta_x(Uw) + \vartheta_y(Vw)] + \vartheta_\eta(\Omega w) \\ -m^{-1}{}_y g\frac{\alpha}{\alpha_d}[\vartheta_\eta p' - \bar{\mu}_d(q_v + q_c + q_r)] + m^{-1}{}_y\mu'_d g, \end{aligned} \tag{2.11}$$

where W is a redefined momentum variable (for map scale); $W = \mu_d w/m_y$. Map scales are required by WRF to support anistropic projections (latitude-longitude grid). As the WMM uses an isotropic Mercator projection, $m_x = m_y = m$. The mass conservation equation becomes:

$$0 = \vartheta_t\mu'_d + m_x M_y[\vartheta_x U + \vartheta_y V] + m_y\vartheta_\eta\Omega \tag{2.12}$$

The geopotential equation becomes:

$$0 = \vartheta_t \phi' + \mu^{-1}_d [m_x m_y (U \vartheta_x \phi + V \vartheta_y \phi) + m_y \Omega \vartheta_\eta \phi - m_y g W] \tag{2.13}$$

Conservation equations:

$$F_\Theta = \vartheta_t \Theta + m_x m_y [\vartheta_x (U\theta) + \vartheta_y (V\theta)] + m_y \vartheta_\eta (\Omega \theta) \tag{2.14}$$

$$F_{Q_m} = \vartheta_t Q_m + m_x m_y [\vartheta_x (U q_m) + \vartheta_y (V q_m)] + m_y \vartheta_\eta (\Omega q_m) \tag{2.15}$$

The hydrostatic relation becomes:

$$\vartheta_\eta \phi' = -\bar{\mu}_d \alpha'_d - \alpha_d \mu'_d \tag{2.16}$$

Note that the equation of state cannot be written in a perturbed form due to the γ exponent in Equation (2.8). The governing equations in pertubation form (2.9) - (2.15) contain Coriolis terms, mixing terms and parameterisations. Whilst parameterisations are described in Chapter 3, Coriolis and mixing terms will be explained here.

Coriolis terms

For isotropic projections (WMM uses a Mercator projection); the Coriolis terms become (2.17) - (2.19). Note that $f = 2\Omega_e sin\psi$ and $e = 2\Omega_e cos\psi$ where Ω_e is the angular rotation of the Earth and ψ is the latitude.

$$F_{U_corr} = \left(f + u\frac{\vartheta m}{\vartheta y} - v\frac{\vartheta m}{\vartheta x} \right) V - eW cos\alpha_r - \frac{uW}{r_e}, \tag{2.17}$$

where α_r is the local rotation angle between the y-axis and the meridians and r_e is the radius of the earth.

$$F_{V_corr} = \left(f + u\frac{\vartheta m}{\vartheta y} - v\frac{\vartheta m}{\vartheta x} \right) U - eW cos\alpha_r - \frac{vW}{r_e} \tag{2.18}$$

$$F_{W_{corr}} = e(Ucos\alpha_r - Vsin\alpha_r) + \left(\frac{uU + vV}{r_e}\right) \tag{2.19}$$

For idealised cases all the curvature terms are removed by setting $m_x = m_y = 1$ and e and $1/r_e$ to be 0.

Mixing terms

Turbulent mixing and filtering terms are needed in WRF either for numerical reasons or to represent sub-grid turbulence processes that cannot be resolved on the grid. Most of the mixing terms are intended for the latter which remove energy from the model solution or represent energy sink terms. Mixing processes are too numerous to go into detail here, however a full description is provided in [Skamarock et al., 2008].

2.2 Interferometric Synthetic Aperture Radar (InSAR)

In this section I review the fundamental aspects of InSAR and discuss some limitations. Chapter 4 will discuss InSAR processing in more detail.

2.2.1 SAR

SAR is a technique which uses signal processing to improve the resolution of a radar image beyond the limitation of a physical antennae aperture. The antenna's forward motion is used to synthesize an extension of the antenae. This means that a small antena may be used, having a larger virtual representation. The larger the antena is, the higher the resolution of image that can be obtained in the azimuth (along track) direction. In a SAR image each element in a volume posesses a probability (initialy zero) of a reflective surface being at that location in space. For each received pulse, the entire volume is iterated using time delay of the pulse to represent distance through the volume. The sample value at that position in the pulse is then added to the element's probability value. This represents a possible echo from a target at the position of the element. Next a judgement is made to decide what element probability values represent solid objects. A threshold is employed, elements whose probability is below that threshold are ignored. The threshold level chosen must at least be higher than the peak energy of any single pulse otherwise that pulse

peak appears as a sphere of false probability across the entire volume. Thus to detect a point on a target, there must be at least two different antenna echoes from that point. Consequently, there is a need for large numbers of antenna positions to properly characterise a target. The elements that pass threshold criteria are visualised in 2D or 3D.

2.2.2 SAR Satellites

Owing to the small size of SAR antennas, this technology lent itself to spaceborne instruments which were first used to investigate planetary surfaces in 1978 aboard the NASA SEASAT satellite. SAR systems operate with a side-looking geometry and illuminate the Earth with a series of microwave pulses. As the spacecraft moves, the SAR sweeps out a swath in the direction of movement, Figure 2.4.

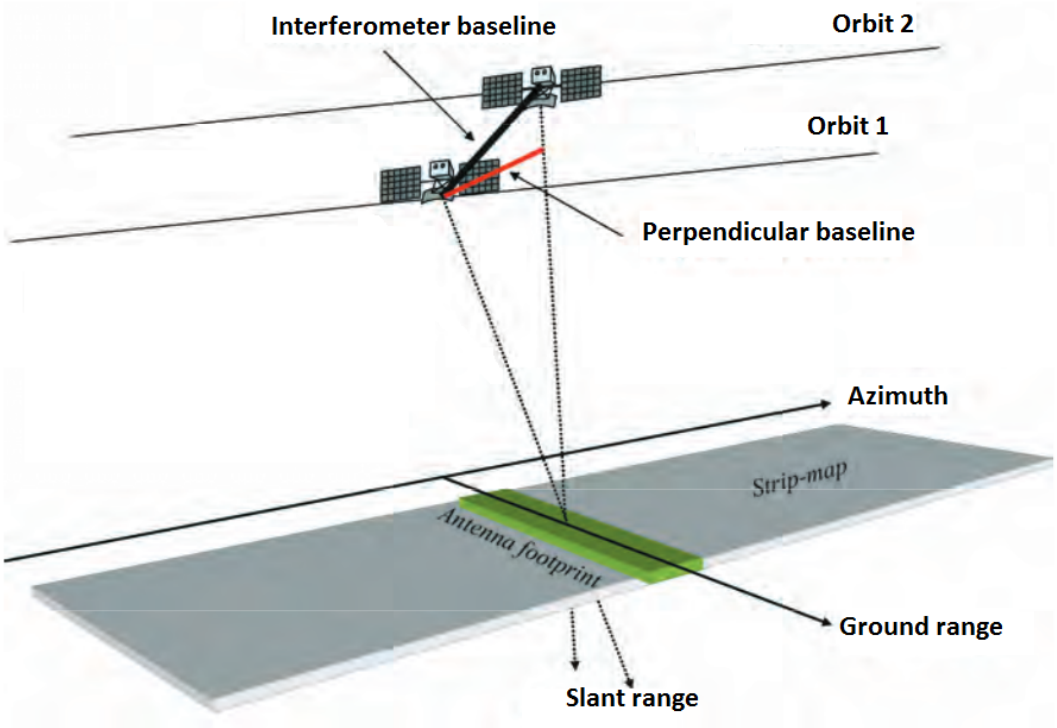

Figure 2.4: Geometry of a satellite interferometric SAR system. The orbit seperation is named the interferometer baseline, and its projection perpendicur to the slant range direction is an important measure of this technique [Hanssen, 2001].

SAR detects echoes of previous microwave pulses it sent out, scattered from the Earth. The raw data collected by the SAR is then focused to form an image in the direction perpendicular to the flight direction (range). In range direction, bandwidth is provided by the pulse. In azimuth (flight direction), bandwidth is provided by the variation in frequency due to the Doppler effect associated with the movement of the

sensor relative to the Earth. Algorithms and implementations to carry out image processing are described in greater detail in later chapters. At full resolution, the value for each pixel in the image is related to the scattering properties of a resolvable patch of the Earth. Specifically it is the coherent sum of the echoes from all the individual scatterers within the patch convolved with a low-pass impulse response function. Each pixel value has both amplitude and phase. Because echoes can add both constructively and destructively, the amplitude values over the image fluctuate around the nominal values for each pixel based on its radar brightness, which is known as the speckle effect.

2.2.3 InSAR

If a second image is acquired over the same area, either by a different sensor or (usually) by the same sensor at a different time,the phase of the second image can interfere with the first image. Practically this effect is the same as multiplying the complex conjugates of each image. Generally, the second image is acquired from a slightly different position in space so it is first resampled to the same geometrical framework as the first image. The phase of the resulting interferogram is the difference in phase between the two images. The difference in phase depends on many factors such as change in path length, ionospheric effects and difference in pulse propagation speed through the atmosphere caused by refractivity changes (Section 1.4). Thus InSAR provides a means to estimate topography (from path length) given that these other factors can be accounted for [Zebker and Goldstein, 1986].

The phase detected by SAR sensors is modulo 2π so it is not possible to calculate absolute height, only relative height between two points in an interferogram. In order to calculate the relative height between all points, the differential phase between all neighbouring pixels is integrated over the interferogram, a process named phase unwrapping which is discussed more in later chapters. The phase due to topography can also be estimated, either from InSAR or, usually, a digital elevation model (DEM), and subtracted from the interferogram phase. If decorrelation and atmospheric effects are ignored, the remaining phase will be due to any deformation of the Earths' surface between the two radar acquisitions.

Over the past two decades InSAR has proven to be a very effective technique for measuring deformation associated with active volcanism [Massonnet et al., 1995], [Rosen et al., 1996].

2.2.3.1 Limitations

Most interferograms include large areas where the signals decorrelate and no measurement is possible. If the surface is vegetated or water, the scattering properties change with time leading to a loss of interferometric coherence and the resulting image is temporally decorrelated. Consequently many InSAR studies focus on areas that are dry and sparsely vegetated, for example, the pyroclastic flow deposits around SHV.

Decorrelation also results from variations in imaging geometry. If the perpendicular baseline between the spacecraft position at the two times at which the images are acquired is non-zero, the difference in incidence angle alters the coherent sum of pulses from the many small scattering elements within a resolution element, so that measurements do not repeat exactly. This is known as spatial decorrelation. Spatial decorrelation increases as the baseline increases. Poor orbit control produces InSAR image pairs with excessive baselines that cannot be used to produce interferograms. A corresponding decorrelation results from changes in squint angle (the angle between the radar beam and the radar trajectory). A change in squint angle alters the SAR Doppler frequency range leading to decorrelation. Although these decorrelation effects can be reduced by filtering, there are critical values of baseline and squint angle difference beyond which there is complete loss of interferogram coherence. In summary, even if SAR data are regularly acquired, temporal and spatial decorrelation limit the number of possible interferograms and hence temporal resolution.

After decorrelation, the next most significant limitation of conventional InSAR is the variation in the delay of the signal as it propagates through the atmosphere, which leads to an additional phase term that varies over the image. Most of the variation in this term over the typical dimensions of an interferogram is due to variation in the distribution of water phases in the atmosphere leading to refractivity changes between InSAR aquisitions. The turbulence-induced change in phase loses spatial correlation over minutes to days. A common method for reducing atmospheric signal is, therefore, to stack multiple interferograms acquired over time. However, any variation in the spatial or temporal nature of deformation over the period of the stack is then lost.

Chapter 4 describes InSAR processing and analyses InSAR data collected from Montserrat for this study.

Chapter 3

Developing the WRF Montserrat Model (WMM)

3.1 Introduction

Section 2.1 presented the governing equations of the WRF Montserrat Model (WMM). In this chapter we build on that knowledge by considering the development of the WMM to represent most accurately the tropospheric water distribution over Montserrat. In doing so, a comprehensive study into idealised trade wind flow over SHV is made, sensitivity of physics parameters to changes in tropospheric water are tested and non-idealised simulations are run for several case studies. Field trips used to collect WMM validation data were undertaken in 2012 and 2013.

3.2 Initialisation

Data are needed to provide an initial reference state for the WMM. Boundary conditions allow meteorological data to be represented at different heights around the model boundaries whilst terrain conditions allow topographic and land-use properties to impact the WMM. Metadata for the model run are also contained within initial conditions, e.g. map projection, dates of model run, model grid dimensions.

In the case of idealised models, the initial data take the form of a user-created sounding profile of meteorological values and user-created terrain for surface values and the model is assumed to be in hydrostatic balance. This assumption only holds true if the processes simulated are on a scale of 10 km or more, beneath which small scale processes are filtered, e.g. orographic waves. To obtain higher resolutions the model cannot be assumed to be in hydrostatic balance and processes need to be parameterised - these are non-idealised models. For non-idealised models the initial

data use simulations of the real atmosphere at a high level of complexity, e.g. a global numerical weather model. Meteorological variables are computed assuming a dry atmosphere to find their reference state, and water added to find the atmospheric moist state. In my idealised runs I assumed a dry atmosphere and did not add water into the initial sounding.

3.2.1 Idealised simulations

For idealised models we need to know values of pressure, potential temperature, water vapour mixing ratio and horizontal wind components at each vertical level above the surface. With pressure and potential temperature as surface boundary conditions the water vapour pressure is found at each height in the atmosphere by integrating the hydrostatic equation between each vertical level. Once the water vapour pressure is known, the dry hydrostatic pressure is calculated by integrating the hydrostatic equation from the model top downwards, subtracting the water vapour pressure at each height. The full hydrostatic pressure at each height is the addition of dry hydrostatic pressure and water vapour pressure. The potential temperature is interpolated from each initial data sounding level to each pressure level [Skamarock et al., 2008].

The pressure at the model top is found using a linear interpolation of sounding pressures given the model top height. The column mass is found by calculating the dry hydrostatic pressure at the surface by interpolation and subtracting this value from the pressure at the model top. This uses the assumptions that the model is in hydrostatic balance and the acceleration due to gravity is constant. Equation (2.1) is modified to find the dry air pressure at each eta (η) level, Equation (3.1) [Laprise, 1992].

$$\eta = \frac{(p_d - p_{dt})}{\mu_d}, \tag{3.1}$$

where μ_d is the difference between dry hydrostatic component of pressure along the surface and top model boundaries. η is a value between 0 and 1, p_d is the dry hydrostatic component of pressure and p_{dt} is the dry hydrostatic component of pressure along the top of the model. The geopotential is found from the hydrostatic relation (3.2).

$$\delta_n \phi = -\alpha_d \mu_d, \tag{3.2}$$

where $\delta_n \phi$ is the change in geopotential and α_d the inverse density. SHV is approx-

imately 1000 m tall. The 2D model terrain is represented as an infinite Gaussian-shaped ridge perpendicular to the atmospheric flow. Such a setup is useful to observe the idealised flow with climatological wind speeds which in this region are dependant on the strength of the trade winds - weak trade winds, $3m\ s^{-1}$, moderate trade winds, $6m\ s^{-1}$, and strong trade winds, $12m\ s^{-1}$, for the neighbouring island of Guadeloupe [Cece et al., 2014]. The idealised flow is perturbed by the idealised topography and we can investigate the disturbance using the Froude number (F_r the ratio of intertial to gravitational forces) described in Equation (3.3).

$$F_r = \frac{U}{Nh}, \tag{3.3}$$

where U is the undisturbed wind velocity, N is the Brunt-Vaisala frequency, h is the vertical length scale. There are four cases of airflow behaviour defined by F_r and each is explained here. When $F_r << 1$ the air will flow around the SHV or be blocked by it, the airflow is slow and stable with higher wind speeds around the obstacle, if possible. When $F_r < 1$ the air thins when it approaches SHV. When $F_r > 1$ the air thickens when crossing SHV [Miranda and James, 1992]. When $F_r >> 1$ the air flows over SHV and is not displaced around it, this type of windflow is likely to form precipitation and clouds as in Figure 3.1. Using the climatological wind speeds from [Cece et al., 2014], Montserrat's weak trade wind events would have a F_r value of about 0.4, a moderate F_r value of about 0.8 and a strong F_r value of 1.5. Thus from the idealised model we expect to see flow both over SHV and split around it.

In the case of an infinite ridge the surface terrain height (ht) is purely a function of one horizontal direction (Equation (3.4)).

$$ht(i) = \frac{h_m}{(1 + (\frac{(i-icm)}{x_a})^2)}, \tag{3.4}$$

where ht is the terrain as a function of each horizontal direction, i and j, h_m is the maximum amplitude of the terrain, icm is the midpoint of the grid in the i direction and x_a is the halfwidth of the ridge. However, for the case of a bell-shaped mountain the surface terrain becomes a function of both horizontal directions and so I chose to use a 2-dimensional Gaussian function (Equation 3.5).

$$ht(i,j) = h_m exp\left[- \left[\frac{(i-icm)^2}{2\sigma_i^2} + \frac{(j-jcm)^2}{2\sigma_j^2} \right] \right], \tag{3.5}$$

where σ_i is the spread of the mountain in the i direction, σ_j is the spread of the mountain in the j direction and jcm is the midpoint of the grid in the j direction.

Figure 3.1: A lenticular cloud begins to form over SHV to the east (upwind) and the volcanic plume is advected to the west. Photo taken by the author from the northwest.

3.2.2 Non-Idealised simulations

To represent physical processes as realistically as possible on a user-defined grid requires non-hydrostatic representation. Lateral meteorological boundary conditions are given to the entire grid at the start of the WMM simulation. The WMM grid consists of four domains nested within each other and is shown in Figure 3.2. The outermost domain at 8.1 km resolution (27 km resolution in test cases) uses lateral boundary conditions supplied by a global weather simulation, e.g. ECMWF, GFS, NCEP, at regular time intervals after the start of the simulation run. A zone of five grid cells is used in the outermost domain to relax the interpolated initial conditions from the global forecast to the WMM. We use the two-way nesting technique where the fine domain solution replaces the coarse domain solution for all the coarse domain points lying inside the fine domain. There is a scale change of 3 between each domain, recommended [Wang et al., 2014] for this type of simulation to minimise errors, so the finer domains have cell sizes of 2.7 km, 0.9 km and 0.3 km respectively (9 km, 3 km and 1 km in test cases). Domain 3 and domain 4 are offset to allow more resolving power focussed upwind of the trade winds incident on Montserrat from the east and also so that the terrain of Guadeloupe does not intersect the boundary of domain 3.

At initialisation, static fields and meteorological conditions are interpolated onto the WMM grid. The reference state is defined in the same way as for the idealised case (Section 3.2.1) and all the 3-D initial data are vertically interpolated in dry pressure space so that pressure, density and height can be found at any point in the WMM. Additional perturbation fields for pressure, density and geopotential are found by subtracting the reference dry field from the column total dry field.

3.2.2.1 GFS and ECMWF initial conditions

There are several different types of global weather data that could have been used as initial conditions for this model. Global Forecast System (GFS) data is a free data source at 111.12 km horizontal resolution and 27 vertical levels and was originally designed to be used with a system like the WMM. I used it extensively for testing of WMM physics parameterisations. The European Centre for Medium Range Weather Forecasts (ECMWF) produces an operational analysis dataset with 16 km horizontal resolution which provides the highest resolution dataset available globally. This model can be obtained in pressure coordinates (22 vertical levels) and η coordinates (137 vertical levels from 2013). The newly established World Meteorological Organisation Deterministic Forecast Verification [*Comparison of weather*

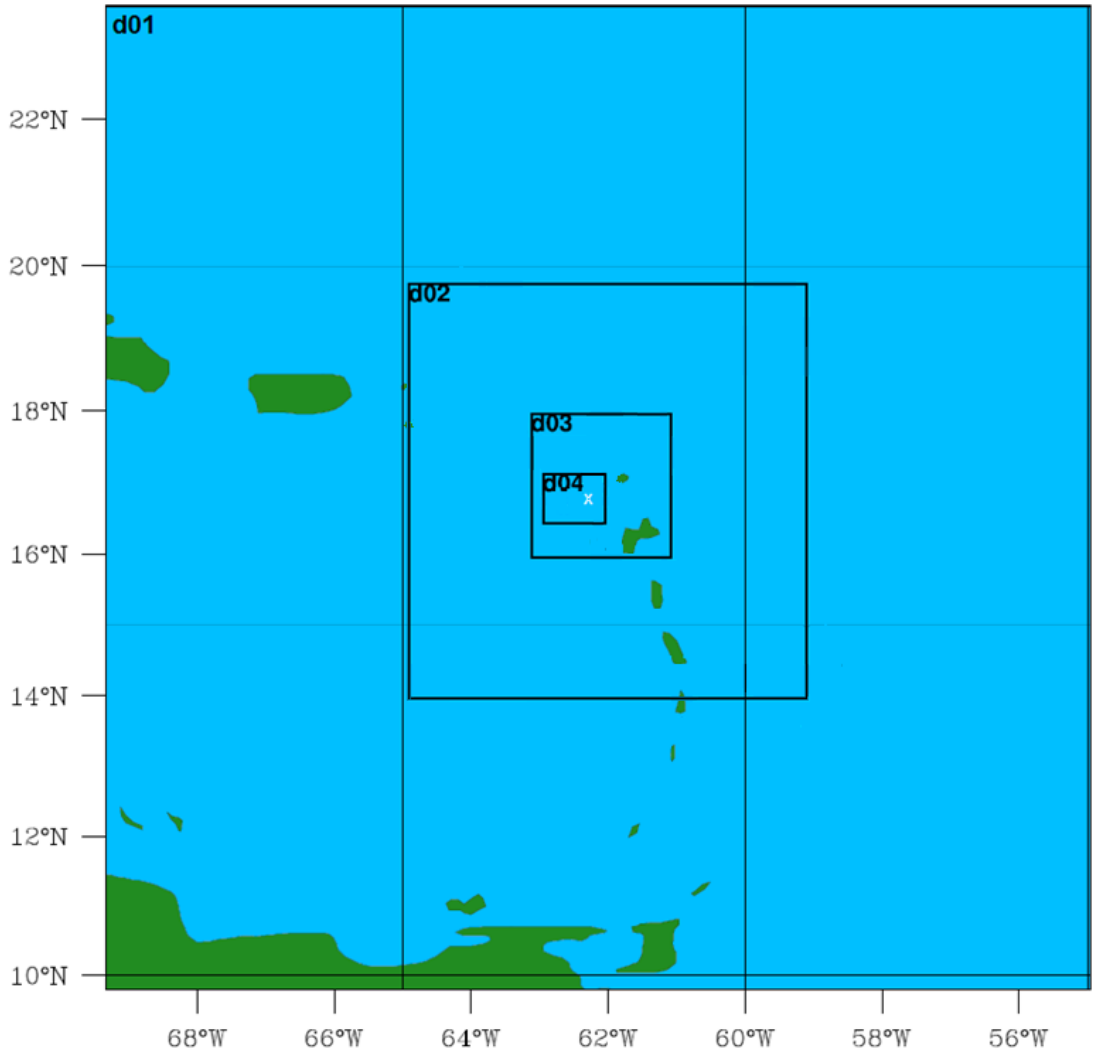

Figure 3.2: WMM nested domains in the Eastern Carribean, white X indicates location the of Montserrat. Full model domain resolution: d01 - 8.1 km, d02 - 2.7 km, d03 - 0.9 km, d04 - 0.3 km. Test model domain resolution: d01 - 27 km, d02 - 9 km, d03 - 3 km, d04 - 1 km (Section 3.2.2.6).

models, 2014] can be used to show that the ECMWF analysis model consistantly outperforms the GFS model. However the GFS model is a far less computationally intensive initialisation method to use and the η coordinates ECMWF-WRF integration is novel. So, whilst the GFS is useful for parameterisation tests to find out what schemes the WMM is most sensitive to, ECMWF initial conditions are used for the main WMM.

3.2.2.2 ECMWF initial conditions

The ECMWF produce operational forecasts at a maximum resolution of 15.67 km, this resolution was found to be incompatible with the WRF-preprocessor and so was truncated onto a lower resolution grid - 19 km was chosen. The ECMWF forecast is a spectral formulation but for representation purposes a grid point system is used. A latitude-longitude grid is unsuitable for this because of the convergence of the meridians toward the poles leading to numerical instabilities and data redundancy. For these reasons a reduced Gaussian grid is incorporated whereby east-west separation between points at different latitudes is constant and kept that way by decreasing the number of grid points towards the poles at every latitude. In the region I am concerned with, between 24N and 24S a regular Gaussian grid is applied and so resolution does not decrease with latitude in this thesis. Three regular Gaussian grid resolution truncations to the maximum forecast resolution have been explored, shown in Table 3.1.

Table 3.1: Comparison of selected ECMWF-model level truncation schemes.

Spectral resolution	Gaussian resolution	Lat/lon resolution	Resolution (km)	WRF model compatibility
TL255	N128	0.7	77.78	5 uppermost levels vertical damping[1]
TL1023	N512	0.176	19.56	10 uppermost levels vertical damping[1]
TL1279	N640	0.141	15.67	WRFV3.3.1 preprocessor incompatible

[1]Diffusive damping, 0.01 damping coefficient. Other stability measures include 0.3 s off-centering of vertical sound waves and adaptive timesteps.

There are several points of consideration when truncating the ECMWF forecast to a coarser resolution in order to provide initial- and lateral boundary-conditions to the WMM (for the purpose of forecasting phases of water). These are terrain

resolution in the initial conditions, representation of lateral atmospheric gradients, and errors proporgating from the lateral boundary conditions.

Firstly, terrain plays an important factor in the distribution of water vapour. The ECMWF uses 1 km resolution terrain upscaled to model resolution ($\sim$ 16 km). The outermost WMM domains at 8.1 km and 2.7 km resolution have a terrain resolution of 2 arcmin (3.7 km) and the terrain aspects of the water vapour field are introduced by finer domains which have a sub-grid scale terrain resolution $\sim$ 25 m. Both the ECMWF and two outermost WRF domains have terrain resolution that is insufficient to capture the sub-grid orographic varibility needed for local flow. However the outermost WMM domains can block the airflow, in a mountain ridge effect giving rise to local winds and gravity waves. Whilst the ECMWF does have additional sub-grid scale representations of flow blocking and gravity wave generation to compensate for coarse terrain resolution, Montserrat and the surrounding area will only take up one terrain grid square and so be poorly represented. So we can say that the initial conditions do not contribute as much as the WMM to terrain effects on water vapour distribution.

Secondly, by upscaling the ECMWF forecast we lose information about meteorological features at finer resolutions for example, $\sim$ 20-40 km features in moving from the 19 km resolution model to the 77 km resolution model. For a small island, like Montserrat metre and kilometre scale gradients on water vapour dominate, produced by finer scale domains. For example the surface water vapour fields (integrated over the lowest model level only) in the inner-most WMM domain (0.3 km) on the first timestep of a chosen model run, have little change in magnitude of water vapour between 19 km and 77 km initial conditions, Figure 3.3. Note that the background gradient field is different in each case, for 19 km it is east-west orientation whereas for 77 km it is south-east to north-west. The same field across the whole region at the outer-most WMM domain (9 km) is shown in Figure 3.4 at 19 km and 77 km initial conditions. Whilst the data interpolated from the 19 km field onto the 8.1 km WMM domain is more detailed, that relating to the 77 km field contains the main mesoscale features required for the forecast. Note that water vapour is a derived field in the WMM at the first timestep.

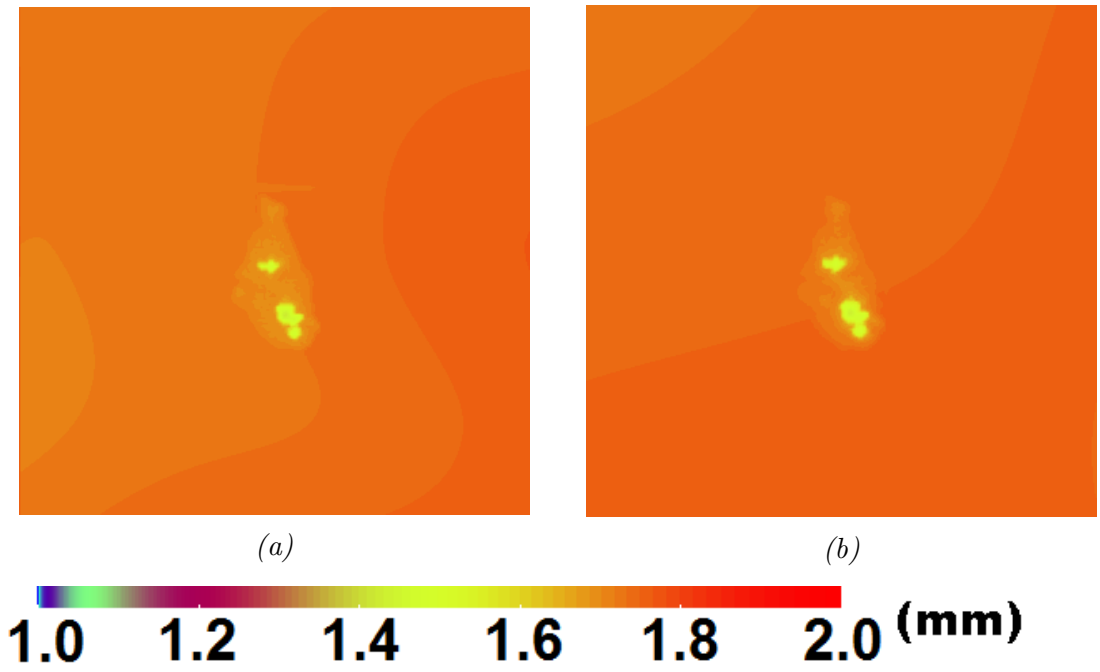

Figure 3.3: Water vapour field (mm) at surface on first timestep of innermost WMM domain (0.3 km-DO4). Both sets of truncated initial conditions are dervived from a 16 km operational analysis ECMWF forecast on 2nd December 2014. (a). Using 19 km initial conditions. (b) Using 77 km initial conditions.

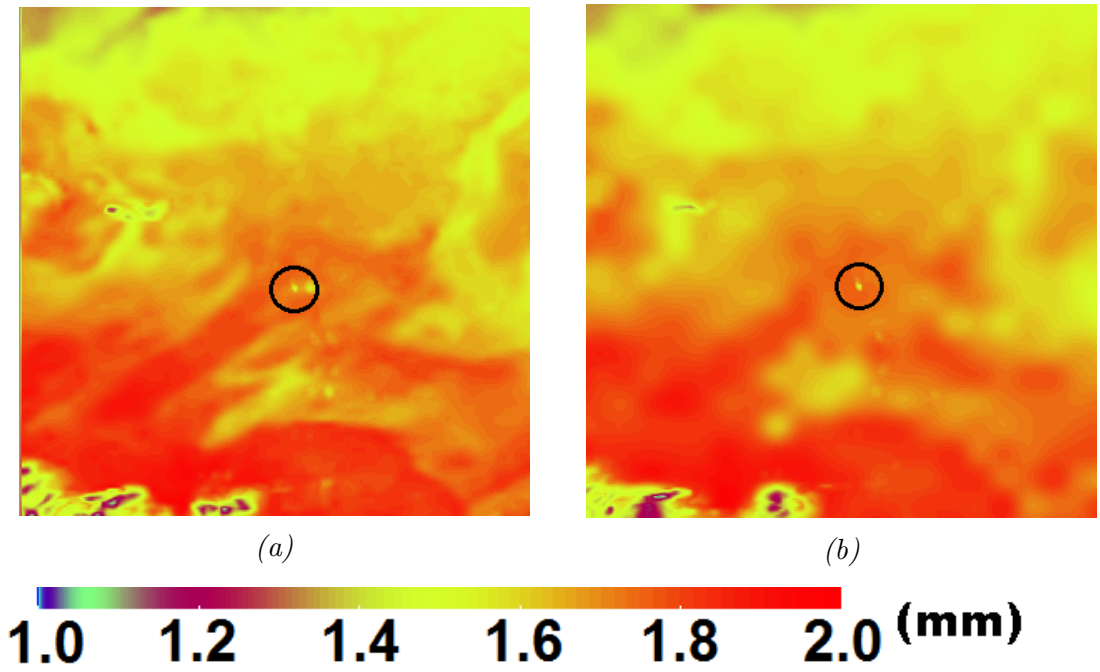

Figure 3.4: Water vapour field (mm) at surface on first timestep of outtermost WMM domain (8.1 km-D01). Both sets of truncated initial conditions are dervived from a 16 km operational analysis ECMWF forecast on 2nd December 2014. Black circle shows location of Montserrat. (a). Using 19 km initial conditions. (b) Using 77 km initial conditions.

Thirdly, using a truncated forecast would incur domain boundary errors due to

a jump in resolution at the lateral domain boundaries, reinitialised every six hours. This jump also occurs for the 16 km forecast but the errors are less for the finer resolution forecasts than for the coarser resolution forecasts. Experiments with both the 19 km and 77 km showed that both grids were numerically stable with a jump in resolution to 8.1 km for the outermost domain of the WMM.

During spin-up most of the initial conditions will be swept away. If we consider a theoretical propagation speed of 10 ms^{-1} from the east (high trade winds) and a distance from Montserrat to the eastern boundary ∼700 km away, in most cases the WMM forecast is over before the lateral eastern boundary conditions reach Montserrat. Note that this assumes we reset the model every 12 simulation hours. Lateral boundary smoothing is also used in WMM to improve the consistency of nested domains.

For these reasons I have decided to also explore a 77 km initial condition truncation as it can be argued that it will not have an adverse effect on the WMM compared with 19 km initial conditions - WRF forecasts have been initialised by coarse resolution models for InSAR mitigation studies in the recent past [Bekaert et al., 2015] and there is a computational gain by using truncated models.

3.2.2.3 Vertical interpolation

There are many possible vertical level interpolation schemes for models, e.g. Gal-Chem and Somerville, hybrid, SLEVE, isentropic, cut-cell [Good et al., 2014]. We now briefly discuss the pressure level systems used by GFS and ECMWF-pressure and then the hybrid terrain-following hydrostatic pressure vertical coordinates (eta levels) used by WMM and ECMWF-sigma. Pressure levels are calculated by integrating the hydrostatic equation to calculate the pressure at each height. This results in a smoothing towards the model top. Levels are parallel to the Earth's surface near the ground. As there is no vertical velocity at the ground, the lower boundary conditions become easier to solve using this method. Additionally, this allows the representation of very high vertical resolution near the surface which proves valuable to the capture of water vapour at high resolution in the lowermost troposphere. However, over complex terrain, steep orography can cause vertical grids to become less orthogonal and cause errors. It was therefore necessary to investigate terrain smoothing to prevent this. The transition to pressure levels in the upper troposphere follows the same format as previously discussed up to the model top (WMM default 50 hPa, an altitude of 17.5 km). This reduces the need for terrain smoothing, as errors are not propagated into the pressure smoothed upper levels of the model [Skamarock et al., 2008].

In the WMM during runs, 51 vertical levels are used, skewed to the lower troposphere, whose sigma levels (2.1.1.1) are 1.00, 0.9969, 0.9935, 0.9899, 0.9861, 0.9821, 0.9777, 0.9731, 0.9682, 0.9629, 0.9573, 0.9513, 0.9450, 0.9382, 0.9312, 0.9240, 0.9165, 0.9088, 0.9008, 0.8925, 0.8840, 0.8752, 0.8661, 0.8567, 0.8471, 0.8371, 0.8261, 0.8141, 0.8008, 0.7863, 0.7704, 0.7531, 0.7341, 0.7135, 0.6911, 0.6668, 0.6406, 0.6123, 0.5806, 0.5452, 0.5060, 0.4630, 0.4161, 0.3656, 0.3119, 0.2558, 0.1982, 0.1339, 0.0804, 0.0362 and 0.0000.

For the WMM it is most important to represent water in the lower troposphere and so the model level spacing has a 300 m vertical resolution in the upper troposphere and logarithmically increasing resolutions as the surface is approached, to take full advantage of boundary layer effects. Although most of the atmospheric water exists within 10 km of the surface, but we do need to represent the top of the troposphere (17.5 km), especially in the case of deep convection. A few ($\sim$5) levels at the top of the model are closely spaced to prevent numerical instabilities.

It is widely thought that vertical level spacing should be an order of magnitude less than horizontal level spacing to fully capture vertical velocities, e.g. [Zhang and Wang, 2003].

3.2.2.4 Terrain boundary layer conditions

WMM uses a bespoke mapping of a 4-category land-use scheme at 25 m horizontal resolution developed using a United States Geological Survey (USGS) 24-category classification [Wang et al., 2014] and a $\sim$ 25 m resolution terrain from a digital elevation model (DEM) of Montserrat (Table 3.2).

Table 3.2: Terrain Type USGS options used with WMM.

Option	Description
19	Barren or sparsely vegetated
16	Water bodies
15	Mixed forest
3	Irrigated cropland and pasture

The default surface physics parameterisation (NOAH land surface mode [Tewari et al., 2004]) and MM5 similarity soil [Beljaars, 1994] is used with the bespoke surface. Each domain is appropriately nested, Figure 3.2, to avoid boundaries intersecting any areas of high topography which could result in spurious steps in elevation when moving from one domain to the next. Terrain and landuse for the WMM are shown in Figure 3.5.

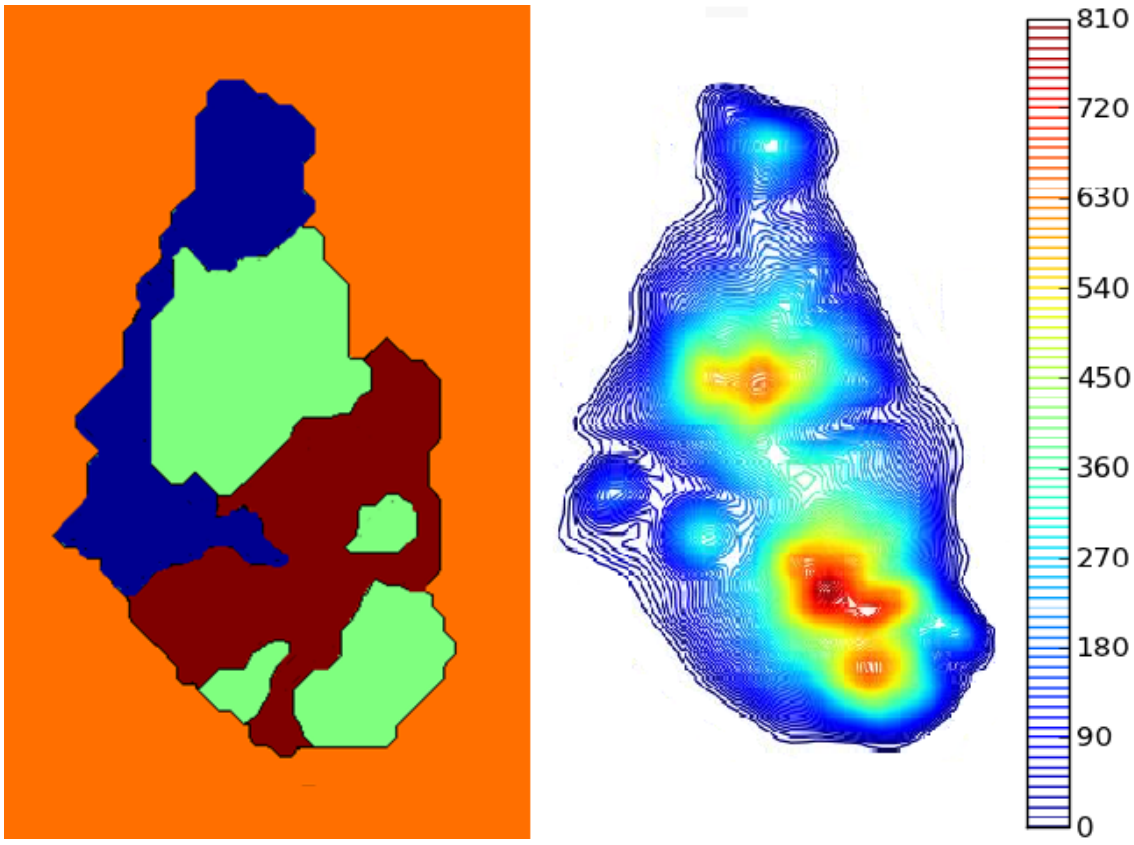

Figure 3.5: (Left) WMM land-use, orange - ocean (16), blue - farming (3), red - bare rock (19), green - forest (15). (Right) Topography with elevation contours at 10 m intervals. Island outline can be seen in detail in Figure 1.4.

3.2.2.5 Physics parameterisations

There are five categories of physical parameterisation available to the WMM, each of which aligns with an atmospheric process. The physics parameterisation options consist of an array of schemes for each of the categories. Each scheme handles that physics parameterisation in a different way and all of these will be examined. Figure 3.6 shows schematically how the categories interact.

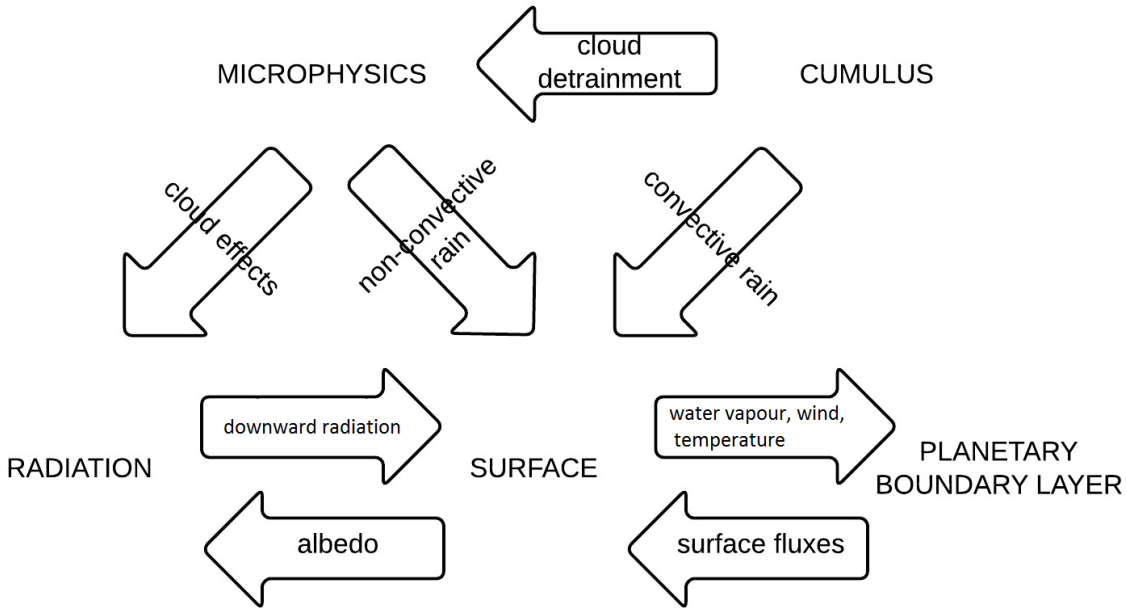

Figure 3.6: WRF physics interactions. Cumulus schemes interact with surface physics by convective rain and cloud microphysics by detrainment. Microphysics interacts with surface physics via non-convective rain and radiation schemes via cloud effects. Downward shortwave and longwave radiation are exchanged with surface physics and reflected upwards. The planetary boundary layer exchanges water vapour, wind and temperature with surface physics options and returns surface fluxes [Skamarock et al., 2008].

3.2.2.6 Testbed

To select physics options a testbed was created using GFS initial conditions. The four test domains to represent the different grid sizes of the full WMM simulation were 27 km, 9 km, 3 km and 1 km, and the same domain regions as shown in Figure 3.2. Deep convection in the GFS model is simulated based on Grell convection schemes which indicates that Grell schemes may be most compatible. More information on convection and other parameterisations in GFS can be found at [**?**]. Two-way nesting was used from GFS initial conditions at 1° resolution. All runs start on the 28th July 2001 at 00:00 UTC and are allowed a twelve hour spin up

time. I consider this generous as myself and others (e.g. [Weiss et al., 2008]) have found 6-8 hours to be adequate but accept that twelve hours of spinup fully allow for non-parameterised values to become defined on the most inner domain. The 29th July 2001 corresponds to a precipitation event that produced a lava dome collapse on Montserrat, and which should be evident in the Caribbean on the previous day [Matthews et al., 2002]. Note that we expect some domain boundary effects when all the domains are being used in the simulation because variables will not be smooth across all domain boundaries especially when we have feedback in both directions. In particular the eastern boundary of the 27 km initial domain has spurious values. For the purposes of testing the WMM used a default number of vertical levels (27), the first seven of which are evenly spaced in the bottom 1000 m and the rest between 1000 m and the model top, evenly spaced.

Microphysics

Microphysics schemes provide atmospheric heat and moisture tendencies mainly to simulate the phase changes of water and include most water vapour, cloud and precipitation processes [Skamarock et al., 2001] and so they are vital to this study. Table 3.3 shows a summary of all the microphysics options available to WMM, the principal differences being how each scheme treats the advection of water phases. The microphysics option is applied at the end of the timestep and the heating effects are transferred to the subsequent timestep. Sedimentation and saturation processes are also contained within the microphysical schemes. The Kessler scheme includes warm rain, no ice, idealised microphysics and time-split rainfall terms. The 5-class Purdue Lin scheme includes graupel, ice sedimentation and time-split fall terms. Ferrier has an advection of total condensate and vapour, assumed water and ice fractions fixed during advection, a rime factor, supercooled liquid and ice melt. The 6-class Thompson scheme includes graupel, double moment ice and time split fall terms. Out of 8 microphysics schemes provided in the WMM framework, 4 could run to completion for the WMM. Kessler, Purdue Lin, Ferrier NAM and Thompson (Table 3.3). As the microphysics scheme selected has a major influence on precipitation, a comparison was made of total precipitation over 12 hour runs, allowing for model spin-up, before the rainfall-triggered 29th July 2001 dome collapse at SHV [Matthews et al., 2002] on the inner-most domain at 1 km resolution. Note that the Kain-Fritsch cumulus scheme was used for all microphysics test simulations, switched on at the 27 km and 9 km domains.

In all four cases there was a strong similarity for the 2001 storm case example (not shown here). Missing precipitation values in the domains 2, 3 and 4 show that

Table 3.3: Microphysics options.

Scheme	Number of Variables	Ice-PP[1]	Mixed-PP[1]
Kessler	3	N	N
Purdue Lin	6	Y	Y
WSM3	5	Y	N
Ferrier NAM	5	Y	N
WSM6	6	Y	Y
Eta GCP	2	Y	Y
Thompson	7	Y	Y
Goddard	6	Y	Y
Morrison 2-Moment	10	Y	Y

[1]PP - phase processes.

cumulus schemes are needed to parameterise the coarser scale domains as grid-scale processes are not capable of doing so. As these schemes all show similar performance, I chose the Ferrier NAM scheme as I found it to be the most efficient to run. In the Ferrier NAM scheme water vapour, rain, snow, cloud ice and cloud water are held in five different arrays, allowing for enhanced water state properties not relevant in the troposphere in the tropics. It also treats the water and ice saturation processes separately making it a good choice of microphysics scheme for models between mesoscale and cloud-resolving.

Cumulus

Cumulus parameterisation is responsible for sub-grid scale effects of convective or shallow clouds, representing vertical fluxes due to unresolved up/down-drafts and compensating motions outside the cloud [Wang and Seaman, 1997]. This simulates the growth and decay of cloud fields and coupled dynamic and hydrological processes in the atmosphere and on the ground through heat, moisture, momentum exchange and by influencing the hydrological and radiative processes. The scheme acts on individual columns to provide vertical heating and moistening profiles. Additionally, some schemes provide cloud and precipitation fields in the column and so the choice of cumulus scheme is particulary relevant here. Table 3.4 summarises the cumulus schemes available and all are compatible with the WMM. Also cumulus schemes may be switched off and on in the WMM at a domain resolution where grid-scale processes resolve processes explicitly. Cumulus schemes are linked to precipitation in microphysics schemes, Figure 3.6, and so we test the schemes using the precipitation event that occured at Montserrat on 29th July 2001. Unwanted domain boundary effects are indicative of the model incorrectly interpolating from a lower to a higher resolution. Precipitation starting at the second domain (9 km)

Table 3.4: Cumulus options.

Scheme	CD[2]	Closure	MT[1,2]	MomT[2]	SC[2]
Kain-Fritsch	Y	CAPE removal	C, R, V, S	N	Y
Betts-Miller-Janjic	N	sounding	-	N	Y
Grell-Devenyi	Y	Various	C, R, V	N	N
Grell-3D	Y	Various	C, V	Y	Y

[1] C - cloud, R- rain, V - vapour, S - snow.
[2] CD - cloud detrainment, MT - moisture tendencies, momT - momentum tendencies, SC - shallow convection.

can be compared with Tropical Rainfall Measuring Mission (TRMM) data of approximately the same resolution, Figure 3.7. All three outer domains have cumulus parameterisation switched on and the innermost one does not.

TRMM data, Figure 3.7, shows a low level of precipitation throughout the region and increased precipitation around Montserrat, Dominica and to the east of the Lesser Antilles. This mesoscale feature is approaching from the south-east and was responsible for Montserrat precipitation on 29th July 2001. Only the Grell schemes represent this feature in the correct location. The location of precipitation over Puerta Rico is in the same place amongst schemes tested, in the same location as TRMM shows. Its magnitude is not correctly calculated by the Kain-Fritsch scheme, Figure 3.8, over 40.5 mm compared with TRMM values of 9-18 mm. The other schemes make good approximations to TRMM magnitude of accumulated precipitation. TRMM shows no sign of accumulated precipitation to the south-west of the image. The Grell-Devenyi scheme, Figure 3.10, is the only scheme to mirror this lack of precipitation. Both the Grell-3D in Figure 3.11 and Betts-Miller-Janjic in Figure 3.9 schemes have areas of extreme accumulated precipitation, greater than 40.5 mm, in the south-west of their domains. I now detail accumulated precipitation characteristics of each scheme.

The Kain Fritsch scheme, Figure 3.8, 1 km and 3 km domains are poorly represented. On the 27 km domain precipitation is over-estimated.

The Betts-Miller-Janjic scheme, Figure 3.9, 1 km domain is poorly represented. Increased precipitation exists on the 3 km and 9 km domains. High local precipitation values are not representative of the TRMM data.

The Grell-Devenyi scheme, Figure 3.10, 1 km domain is poorly represented, but all other parameterised domains look reasonable, though some of the local precipitation values are a little extreme.

The Grell 3D scheme, Figure 3.11, 1 km domain is poorly represented. East-west streak artefacts are present on the 9 km domain. Increased precipitation caused by

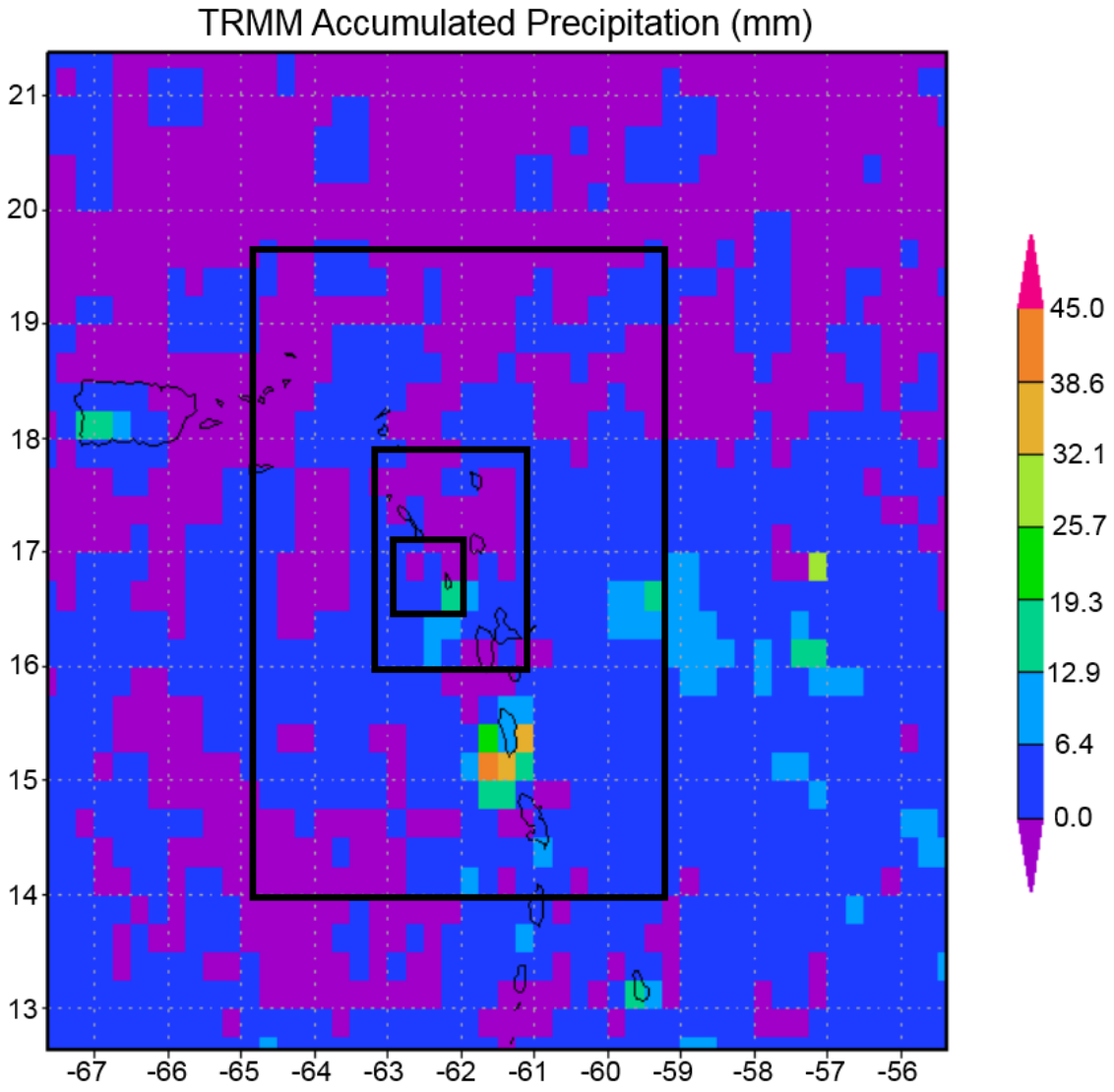

Figure 3.7: TRMM accumulated rainfall (mm) from 12:00 UTC 28th July 2001 until 00:00 UTC 29th July 2001 for the Carribean region. The three innermost domains from Figure 3.2 outlined by black boxes with different horizontal scalings than previously shown. TRMM landmask shown in black.

topography over the Lesser Antilles is visible. Sharp boundary effects exist on the 3 km - 9 km domain and some precipitation is extreme in comparison to TRMM, Figure 3.7.

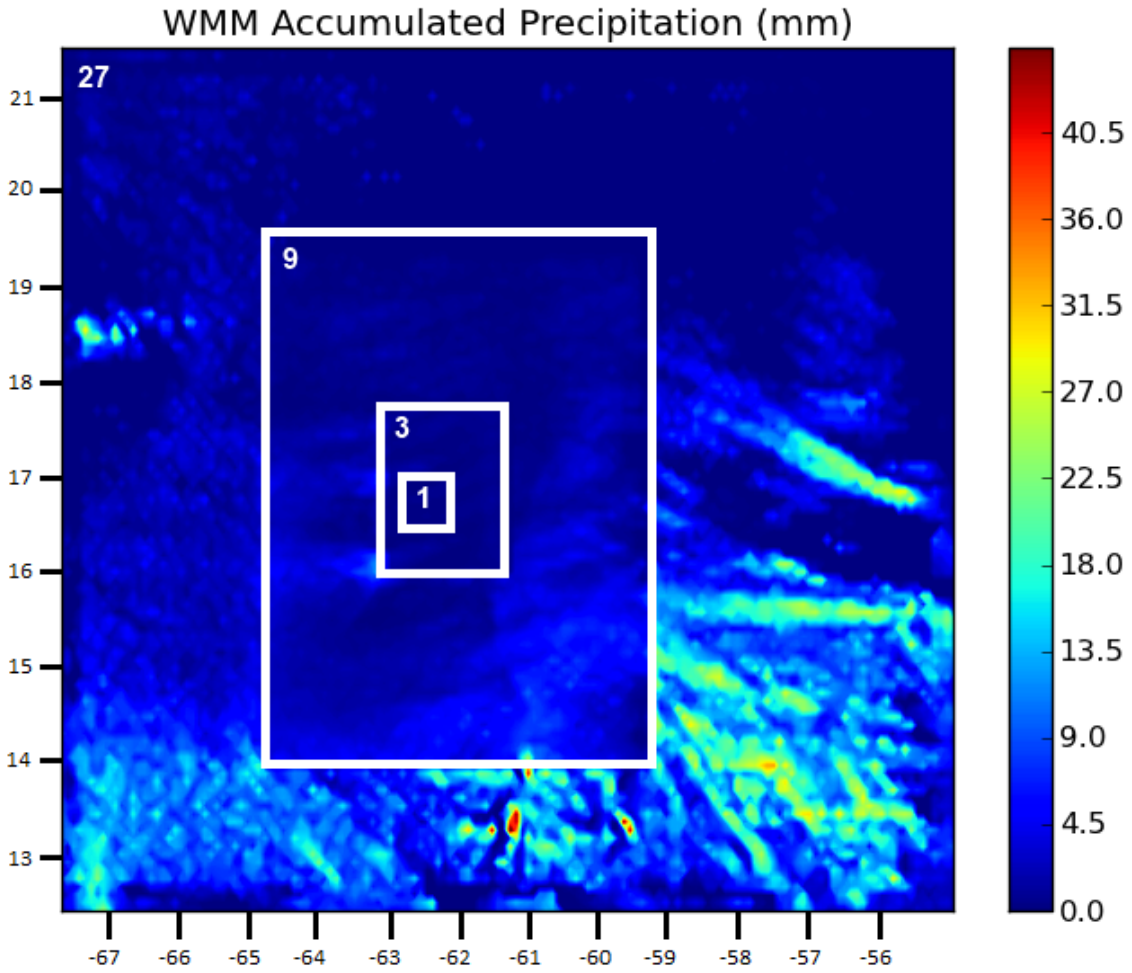

Figure 3.8: Kain Fritsch scheme - accumulated precipitation (mm) 12:00 UTC 28th July 2001 to 00:00 UTC 29th July 2001. Domains from Figure 3.2 shown in white. Numbers in top left corners of domains are domain resolution (km).

The scheme best suited to the Montserrat WRF model is the Grell Devenyi because it well represents the precipitation on both the inner and outer domains. The multiple-closure Grell-Devenyi scheme allows explicit updrafts, downdrafts and cloud and ice detrainment. It also carries slightly less computational cost than the competing Grell 3D case. Comparisons in the literature find the Grell Devenyi to be the most practical [Gilliland and Rowe, 2007] but do not take into account the Grell 3D cases.

Cumulus schemes are switched on at domains where the parameterisations can be representative of the sub-grid characteristics. The absence of precipitation at the 1 km grid level leads us to believe that cumulus should be parameterised (switched

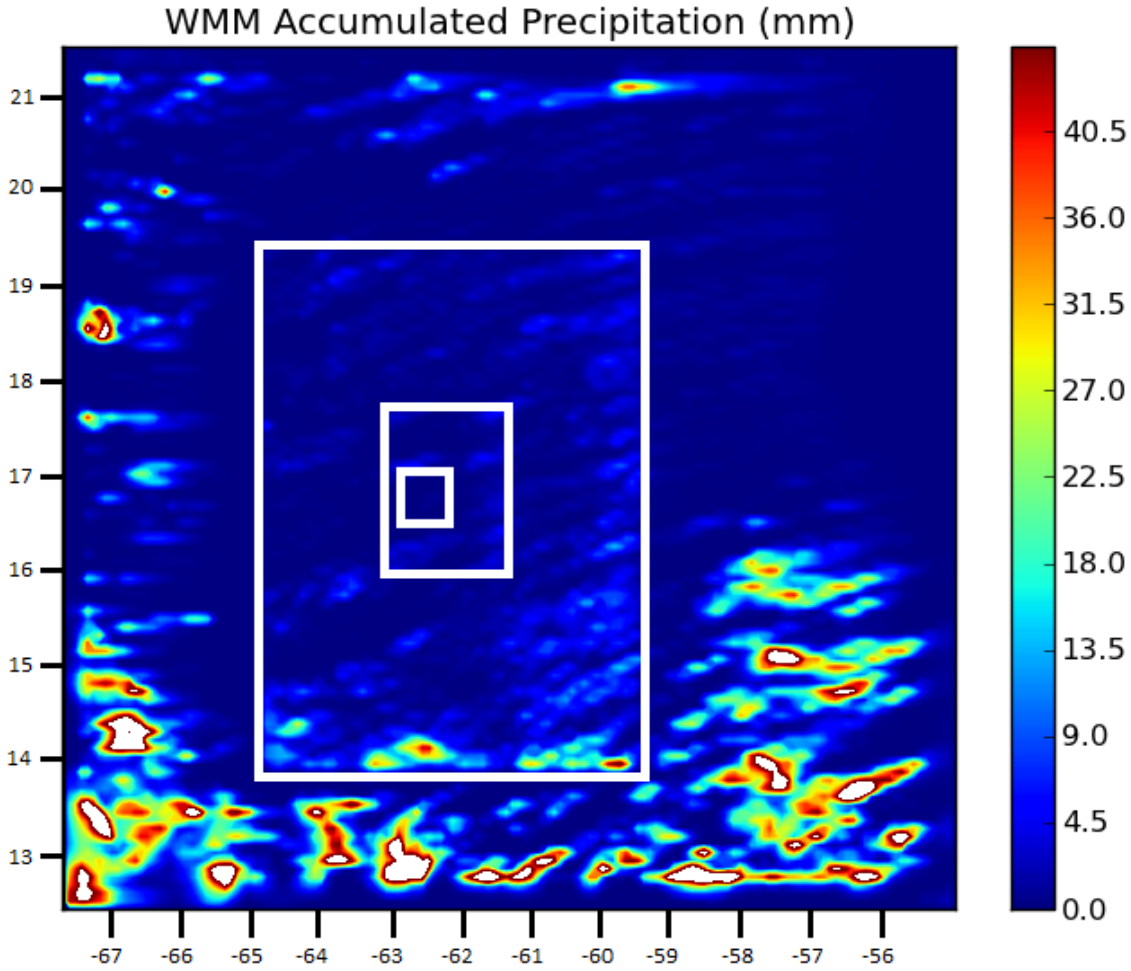

Figure 3.9: Betts-Miller-Janjic scheme - accumulated precipitation (mm) 12:00 UTC 28th July 2001 to 00:00 UTC 29th July 2001. Domains from Figure 3.2 shown in white.

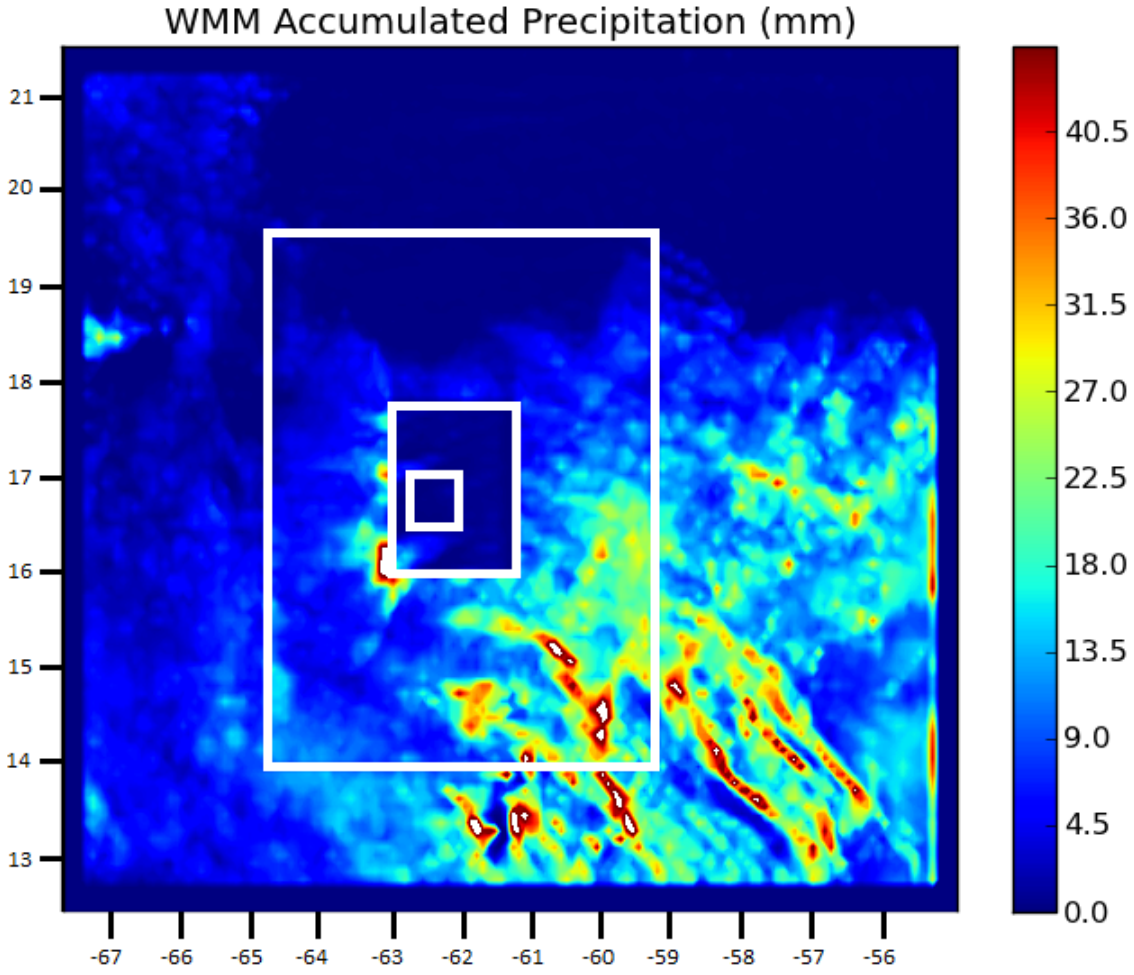

Figure 3.10: Grell-Devenyi scheme - accumulated precipitation (mm) 12:00 UTC 28th July 2001 to 00:00 UTC 29th July 2001. Domains from Figure 3.2 shown in white.

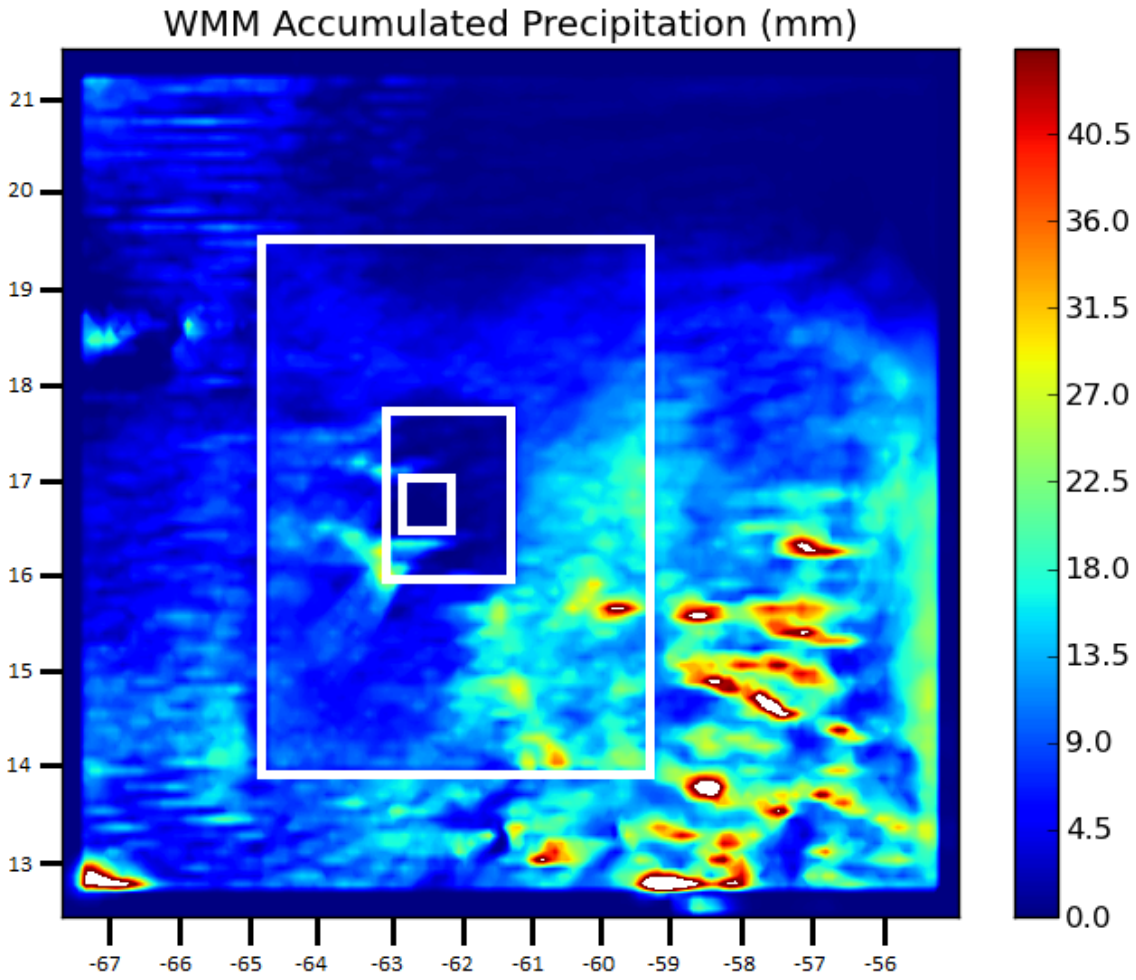

Figure 3.11: Grell 3D scheme - accumulated precipitation (mm) 12:00 UTC 28th July 2001 to 00:00 UTC 29th July 2001. Domains from Figure 3.2 shown in white.

on) at the 1 km grid level. At higher resolution domains parameterise cumulus effects where they cannot be explicitly represented. This can lead to errors as these parameterisation effects can simply be interpolated from the lower resolution grids. Therefore I have decided to switch cumulus parameterisation off below a 1 km grid level. It has been shown that the Grell Devenyi scheme is the best at representing cumulus processes whilst maintaining computational efficiency. Day-long runs show that East Carribean storm precipitation moved east to west from 28th to 29th July 2001 consistent with the literature [Matthews et al., 2002] and TRMM data.

Planetary boundary layer

Planetary boundary layer (PBL) schemes determine the near surface (up to 2 km altitude) moisture and winds by parameterising turbulent vertical fluxes of heat and momentum [Hu et al., 2010]. The PBL schemes examined were the Mellor, Yonsei and Troen-Mahrt. Local closure estimates the turbulent fluxes for each grid cell from the average corresponding meteorological variable for that cell e.g. the Mellor scheme. The Mellor scheme uses 1.5-order turbulence closure to represent turbulence above the surface layer and determines eddy diffusion coefficients from turbulence kinetic energy. Non-local closure does not assume fluxes dependent purely on local meteorological conditions, as in the Yonsei and Troen Mahrt schemes. The Yonsei 1st order scheme has an inverse gradient term in the eddy diffusion equation and includes a Richardson number of 0.25 over land to increase the amount of mixing of the stable boundary layer. The Troen-Mahrt 1st order scheme includes a non-local vertical mixing in the boundary layer and free atmosphere.

Both the Mellor scheme and the Yonsei scheme have been widely used to provide weather forecasts, though the Mellor is a local scheme and so works best with stable flows. The Troen-Mahrt scheme is more closely related to medium-range weather forecasts. The ACM2(PX) scheme, referred to in much of the literature, e.g. [Shin and Hong, 2011], is not available with the version of WRF being used, but in the past has been used in air quality modelling successfully for predicting ozone concentrations. To undertake sensitivity testing of these schemes, they would each need to be tested with several microphysics, land surface and surface layer schemes to monitor temperature, water vapour mixing ratio, wind, cloud cover and precipitation over several months. This is not viable with the current setup. However existing studies indicate that both the Yonsei and the ACM2 give the most unbiased performance [Shin and Hong, 2011] and [Pagowski, 2014]. We proceed with the Yonsei scheme. The same boundary layer scheme is used at all domain resolutions.

Radiative transfer

Rapid radiative transfer models (RRTMs) use a correlated-k distribution to calculate radiation fluxes and heating rates over 14 bands in the shortwave and 16 in the longwave part of the spectrum. Modelled molecular absorbers are water vapour, carbon dioxide, ozone, nitrous oxide, methane, oxygen and halocarbons. A similar scheme has also been optimised for global climate models (RRTMG).

The radiation schemes examined are the Dudhia rapid radiate transfer model (Dudhia RRTM) and the rapid radiative transfer model for Global Circulation Models (RRTMG). As radiation schemes have an impact on temperature, water vapour mixing ratios and wind speed, we would need to monitor these values over several months simulation to capture seasonal biases to the diurnal cycle. This is not viable at present and so existing studies are used to highlight the best scheme to use. Both the Dudhia RRTM and the RRTMG longwave-shortwave radiation schemes are available for this version of WRF. In the past the Dudhia RRTM scheme has been preferred to other schemes when being used with the Yonsei PBL scheme [Otkin et al., 2006] and RRTMG has a long run time. In addition RRTM is meant for stand-alone models where as RRTMG is provided for Global Circulation Model applications. Hence the Dudhia RRTM scheme is used.

3.2.3 Other quantitative observations of water distribution

Several field studies were undertaken which aimed to capture regional, synoptic and local weather conditions on the island and these will be compared with the WMM later in this chapter in order to validate its accuracy.

3.2.3.1 Climatological Dataset

In 2014 a climatological dataset was obtained for Montserrat. Wind speed, pressure, temperature and relative humidity values were obtained by a meteorological mast at the northern, Geralds, airport between 1996 and 2013. Additionally rainfall data was collected from a rain guage at the same site, twice daily from 2010 to 2014.

3.2.3.2 Sun Photometer

A hand-held sun photometer was used in the field in 2012 to measure path integrated water vapour content. The most accessible handheld sun photometer is the Microtops II which is very portable and user friendly. It determines the water vapour column by absorption measurements at the water absoption peak - 936nm and at a wavelength only affected by aerosol scattering - 1020nm [Reagan et al., 1987].

The main source of noise with this technique is unsteady off-target pointing at the sun. To reduce the error in Microtops II measurements due to sun targeting accuracy, a series of 32 measurements are taken over a period of ten seconds. A signal strength factor is calculated based on the signal from all UV channels. Only the records with highest ranking signal strength were averaged and passed on for further processing. In practice in the field, despite performing five minute averages, a 600% error was found between measurements due to the variable position of the sun in the Microtops II viewfinder. As a result only 8% of collected data (880 measurements) was deemed physically realistic and these sun photometer measurements will not be used further in this thesis.

3.2.3.3 Weather station

Hand-held weather stations can provide estimates of relative humidity, wind speed, temperature and pressure at high temporal resolution. The portable Kestrel 4000 weather station was used in this way in field work in 2013 and 2014. This can store up to 2000 data points, recording variable measurements every minute which are downloaded at the end of each day via bluetooth. The Kestrel could be mounted to a tripod using its carrycase to take all recordings over several days before recharge.

A meteorological mast was placed on a pyroclastic flow deposit on the eastern side of Montserrat for the duration of the 2014 field campaign. An anemometer and wind vane provided wind speed and direction measurements every 5 minutes, Figure 1.4.

3.2.3.4 Satellite data

The Moderate Resolution Imaging Spectroradiometer (MODIS) has been operating for over ten years providing data in 36 spectral bands at varying spatial resolutions from 250m to 1km. Although this instrument provides data about many different earth-system processes we are particulary interested in cloud cover and water vapour (Section 3.4.2) over Montserrat.

It is also advantageous to look at liquid water for reasons explained in Section 1.4. The Tropical Rainfall Measuring Mission (TRMM) provides a distribution of rainfall and latent heating over the whole of the outer domain in the WMM, Figure 3.2. This is a three-hourly combined microwave-infra-red estimate of precipitation.

The Geostationary Operational Environment Satellites (GOES) have been operating for eight years and provide visible, infra-red and water vapour products processed in three hourly intervals from 00 UTC each day. We are interested in GOES-13 (East) which maintains geosynchronous orbit at 75° West, providing re-

gional water vapour coverage of the Eastern Caribbean. This is useful as an indication of water vapour flow patterns but not as absolute values of precipitable water vapour because the GOES Sounder is only effective in a cloud-free atmosphere. The derived Special Sensor Microwave Imager Sounder (SSMIS) water vapour product can be used in a cloudy atmosphere and so this is used for point-source values of water vapour.

The Constellation of Small Satellites for the Mediterranean Basin Observation (COSMO-SkyMed) has been in orbit since 2007, providing satellite radar data from 4 satellites in sun synchronous polar orbits with a 97.9° inclination at a nominal altitude of 619 km and an orbital period of 97.2 min. Each satellite repeats the same ground track on the Earth every 16 days and all of the satellites follow the same ground track. The satellites are phased in the same orbital plane, with COSMO-SkyMed's 1, 2 and 4 at 90° to each other and COSMO-SkyMed 3 at 67.5° from COSMO-SkyMed 2. COSMO-SkyMed images of Montserrat were aquired as part of a (Committee on Earth Observation Satellites) CEOS pilot scheme run by Professor Matthew Pritchard during the 2014 field campaign to produce InSAR images.

3.2.3.5 Ground-based rain radar, Guadeloupe

The rainfall radar at Guadeloupe provides quarter-hourly reflectivity measurements over a footprint that includes Montserrat [*Meteo-france Rainfall Radar*, 2015]. The rainfall radar measures reflectivity which is proportional to drop size distribution and rainfall rate. In this thesis it is presented as a means to locate areas of precipitation rather than a guide to the absolute values of precipitation at those locations. Thus it in not important when using rainfall radar in this context to take into account the natural variability of drop-size and the effect of orography on rain rate.

3.2.3.6 Radiosonde, Guadeloupe

Radisonde ascents are recorded at Le Raizet in Guadeloupe (about 100 km south-east of Montserrat) at 16:00 UTC and 0100 UTC every day [*Wyoming Radiosonde Database*, 2015]. These measurements give an indication of profile temperature and water vapour mixing ratio which are useful for our purposes. These measurements are only an approximation for profile readings due to drift of the radiosonde with winds aloft.

3.2.3.7 Local observational data

Local observations of weather made in diary form during field trips noting cloud cover, general weather conditions and extreme events throughout each day are useful when used with other data to show how regional weather conditions affected ground conditions on Montserrat. In the WMM cloud depth is calculated between cloud base and top and converted into a liquid phase delay using Table 1.1 and assumptions explained in Section 1.4. A hand-held infra-red thermometer can be used, with a lapse rate found from neaby radiosonde ascents at Guadeloupe, to measure the ground and cloud temperatures and so find the difference between them. Hand-held infra-red thermometer measurements during the 2013 case study were very sensitive to local changes in cloud base height. So these infra-red thermometer results will not be used in this thesis.

3.3 Summary of WMM

The main impact of atmospheric water vapour on radio wave delay (for InSAR) comes from the lower to middle troposphere (<10 km), is greatest at sea level and decreases logarithmically with altitude. The water vapour field also has high temporal and spatial variability. To simulate the field we use high resolution numerical atmospheric models, which include water vapour, at the spatial scale of 300 m. The Weather Research and Forecasting (WRF) mesoscale model version 3.3.1 is used for this on Montserrat: the WRF Montserrat Model (WMM). ECMWF analysis initial conditions are truncated from a resolution of 16 km onto 19 km and 77 km resolution grids. Table 3.5 shows the parameterisations used for each of the four nested domains of the WMM. Parameterisation options have been judged optimum via sensitivity tests and using other studies. Each domain within the model uses an adaptive timestep (T_s) which decreases if the Courant Friedrichs Lewy (CFL) condition is greater than 1.2 on the innermost domain, the N-dimensional case of which is shown in Equation 3.6.

$$CFL = \delta t \sum_{i=1}^{n} \frac{u_{xi}}{\delta x_i} \leq 1.2, \tag{3.6}$$

where u_x is the velocity of each variable, δt is the time step, n is each dimension and δx is the grid spacing. This is useful to maintain the stability of the WMM, due to its high vertical and horizontal resolutions, and is checked at every timestep.

A digital elevation model (DEM) of Montserrat, at $\sim$ 25 m resolution, was used, with a 3.7 km terrain model for the rest of the region. To avoid steep terrain

gradients each WMM gridpoint, on the innermost domain, takes the terrain to be averaged over an area one grid cell (300 m) in all directions. USGS landuse data was used for the region with four categories overlaid onto Montserrat consisting of bare rock, water, dense vegetation and agriculture mapped onto the region using nearest neighbour interpolation. The WMM outputs the following chosen variables every ten simulated minutes over a model space for the innermost domain of 190 x 190 x 50: temperature, pressure, water vapour mixing ratio, liquid water mixing ratio, cloud fraction.

Table 3.5: Parameterisation options of each domain in WMM.

	Domain 1	Domain 2	Domain 3	Domain 4
Resolution(km)	8.1	2.7	0.9	0.3
Starting Ts[1]	4	3	2	1
Model grid points (x,y)	190x190	190x190	190x190	190x190
Vertical Levels[2]	50	50	50	50
i start offset[3]	1	65	65	52
j start offset[3]	1	65	62	62
PBL	Yonsei	Yonsei	Yonsei	Yonsei
Radiation	Dudhia RRTM	Dudhia RRTM	Dudhia RRTM	Dudhia RRTM
Cumulus	Grell Devenyi	Grell Devenyi	None[4]	None[4]
Microphysics	Ferrier	Ferrier	Ferrier	Ferrier
Cumulus physics calls (min)	8	8	N/A[4]	N/A[4]
PBL physics calls[5]	0	0	0	0

[1] Timestep used at the start of a model run before adaption by CFL condition.
[2] Vertical level spacing is discussed in section 3.2.2.3.
[3] Grid offset from previous domain, units determined by outer domain.
[4] No cumulus parameterisation needed at this domain resolution.
[5] A call time of 0 means at every timestep.

The WMM typically uses 16 CPU's running with shared memory and requires 2.5 Gb hard drive space for the outputs. It can be run so as to forecast the weather as the WMM is highly scalable. However due to the nature of the problem and resource restrictions I have chosen to run at a ratio of 1 wall-clock day producing one day of simulation output.

3.4 Results

This section presents idealised wind flow over Montserrat using the WMM and compares with analytical and other numerical results. Ambient field and climatological data relevant to the model validation are discussed.

3.4.1 Validation of Idealised models

Simulations of atmospheric flow over an idealised 2D ridge and a 3D isolated mountain have been made. The 2D ridge shows idealised flow over a mountain of the same height of SHV in normal trade wind conditions (see section 3.2.1). The 3D isolated mountain shows how WMM replicates the equivalent analytical and earlier numerical tests for this, e.g. [Miranda and James, 1992].

Firstly, in the case of low Froude number (0.22) shown in Figure 3.12, surface flow is characterised by an windward side stagnation point at $x = -2a$, $y = 0$, strong splitting around the mountain and a very well defined vortex pair in the mountain wake. In the beginning of the windward slope the surface flow is opposed until $x = -0.7a$, where it changes to upslope flow. Downstream of the mountain the mountain the vortices are centred at the two points $x = 2a$, $y = \pm a$ and are associated with other surface stagnation points at $x = 0.7a$, $y = 0$ and $x = 3.5a$, $y = 0$. In the region between the vortex pair the flow is reversed and goes upslope. The wind on the central plane shows a very well defined layer of reversed flow, and a possible hydraulic jump after the topographic maximum. The circulation is essentially in horizontal planes. The only region with significant vertical velocity is associated with the weak jump, very close to the mountain peak.

The $Fr = 0.66$ case shown in Figure 3.13 shows flow splitting around the mountain and vertical winds immediately after the mountain peak. [Miranda and James, 1992] found an apparent long-period fluctuation in surface drag (~ 3.5 hours). WRF idealised models do not parameterise drag and I chose to look at the t=3 h case, which is at the beginning of breakdown transition from high to low surface drag.

There is a small vortex pair forming in the mountain wake, with a stagnation point at $x = 2a$, and the flow opposes the background wind until about $x = 4a$, where there is another stagnation point. Figure 3.13 has similar features to Figure 3.12 - the reversed flow on the windward slope (weaker) and the leeside vortex pair (weaker and farther from mountain). Unlike Figure 3.12 there is very little horizontal circulation in the wake. On the vertical plane there is an intense and broad hydraulic jump with vertical winds above most of the lee slope and several rotors forming in the breakdown transition.

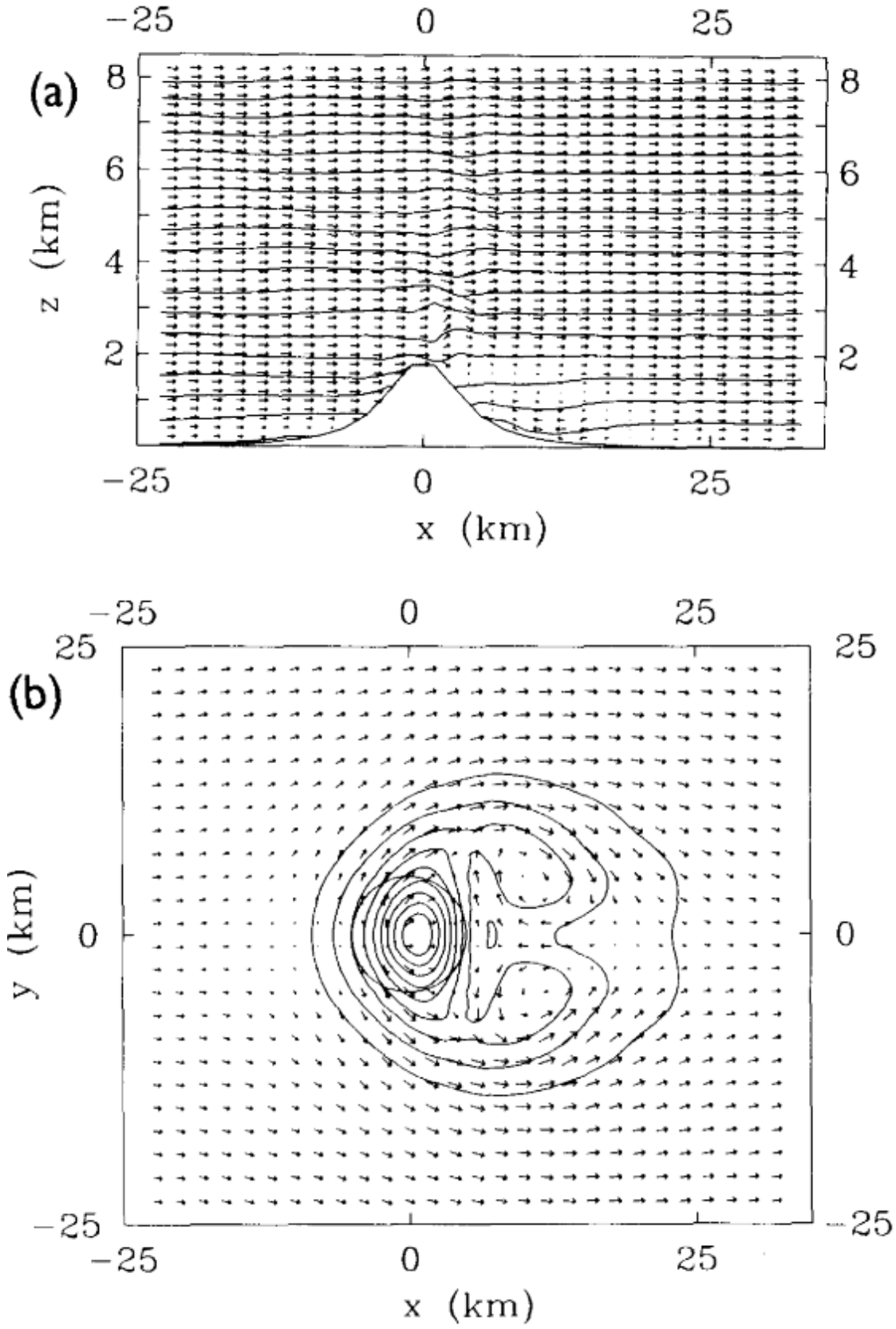

Figure 3.12: Model results for idealised mountain in section. Initial sounding equivalent to $Fr = 0.22$ from the left. (a) Potential temperature (θ) (black lines) and wind field (u,w) arrows on the y plane. Contours of θ every 5 K. (w and height, z have been multiplied by 4.) (b) Potential temperature and wind field (u,v) on the lowest model level in map view. Contours of θ every 2 K. Spherical mountain shown ($r = a$) at (0,0) (from [Miranda and James, 1992]).

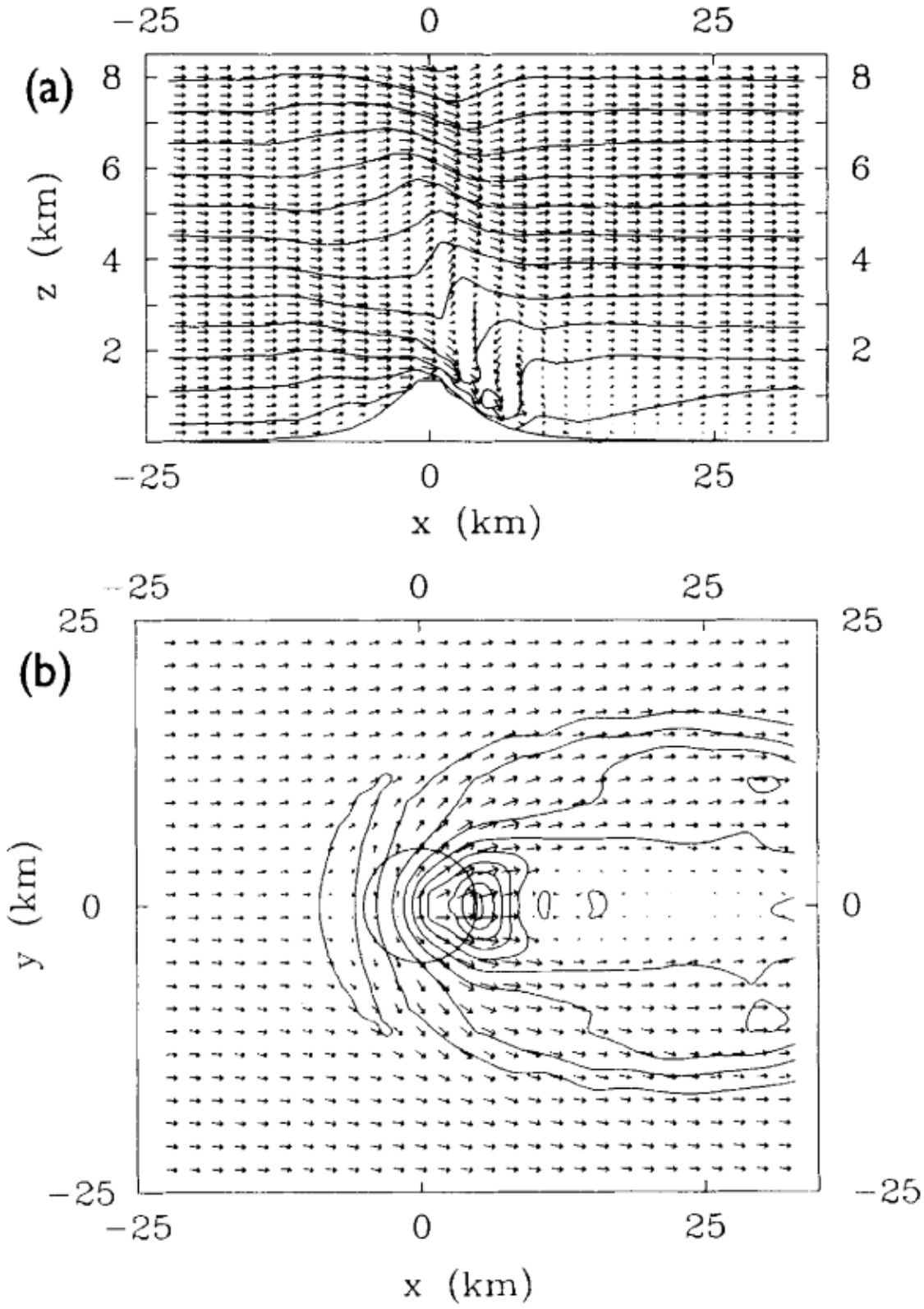

Figure 3.13: Model results for idealised mountain in section. Initial sounding equivalent to $Fr = 0.66$ from the left. (a) Potential temperature (θ) (black lines) and wind field (u,w) arrows on the central y plane. Contours of θ every 2 K. (w and height, z, have been multipled by 4.) (b) Potential temperature (θ) and wind field (u,v) on the lowest model level in map view. Contours of θ every 0.2 K. Also shown is the circular mountain $r = a$ at (0,0) (from [Miranda and James, 1992]).

3.4.1.1 Infinite ridge

An infinite Gaussian ridge with a height of 1000 m and half width of 5 km is used to simulate the scale of SHV. Vertical sounding values are applied to the right-hand side of the model with trade-wind-like (eastern boundary) flows with equivalent Froude numbers of 0.375 shown in Figure 3.14, 0.75 shown in Figure 3.15 and 1.5 shown in Figure 3.16. Due to the nature of the simulation there is no 'sideways' component of horizontal wind and air cannot move horizontally around the ridge. Only the central part of the model is shown in Figures 3.14 - 3.16. The $Fr = 0.375$

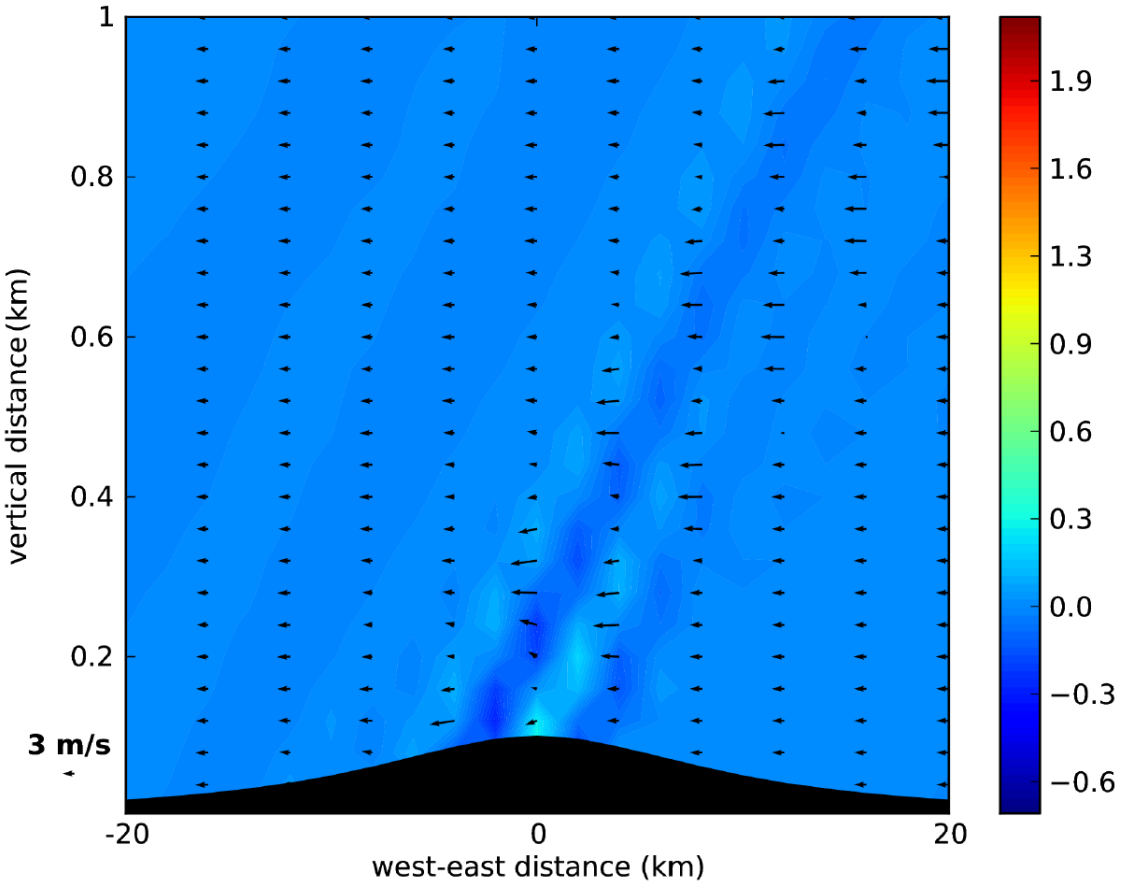

Figure 3.14: 2D WRF flow across an infinite ridge shown in black, horizontal velocity is shown by wind barbs (ms^{-1}) and vertical velocity is colour-coded (ms^{-1}). Initial sounding equivalent to $Fr = 0.375$ from the right.

initial wind forcing case shown in Figure 3.14 has an area of uplift at the top of the ridge at the surface. Strengthening windspeeds correspond to an area of uplift that runs from the top of the ridge to the windward side with increasing height. This is consistent with the idea of a jet forming over the ridge.

The $Fr = 0.75$ initial wind forcing case shown in Figure 3.15 has deviation from a uniform wind field strengthening from the surface at about 10 km and 0 km to the windward side with increasing height. Between these two bands of increased wind

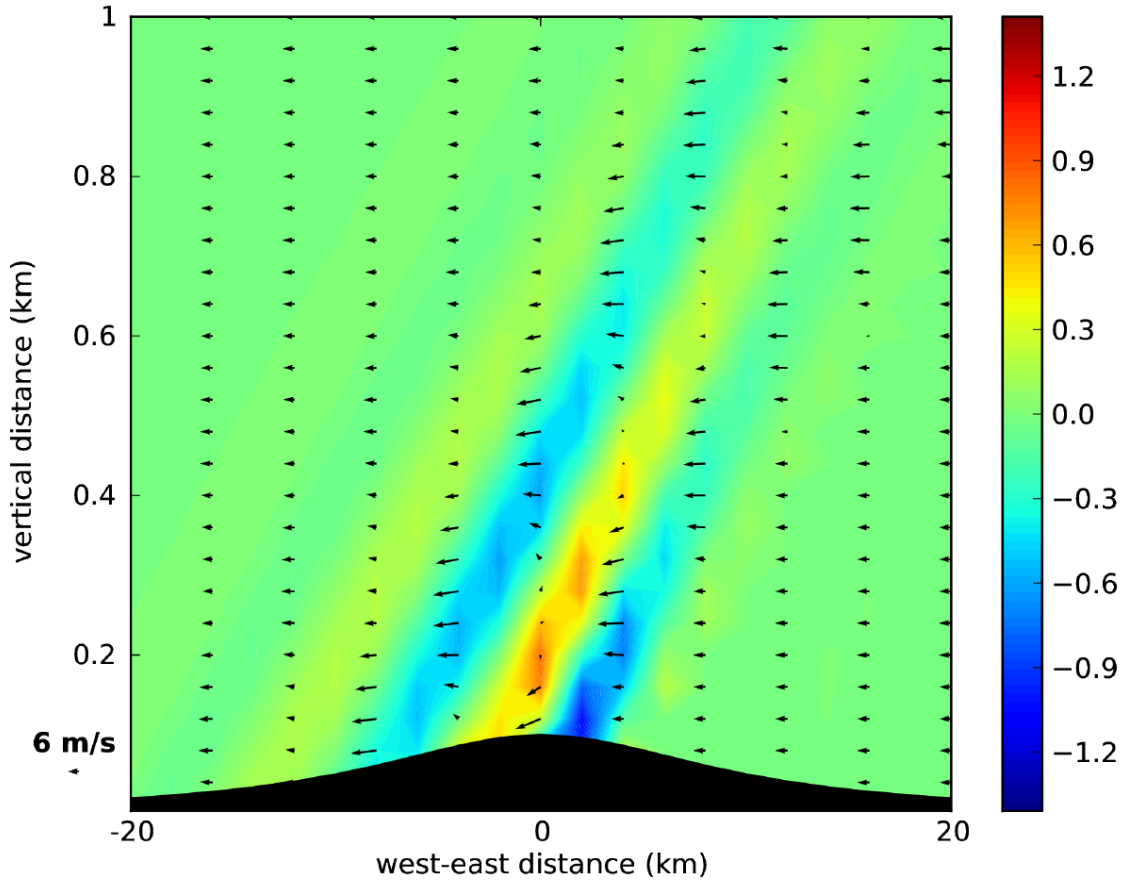

Figure 3.15: 2D WRF flow across an infinite ridge shown in black, horizontal velocity is shown by wind barbs (ms^{-1}) and vertical velocity is colour-coded (ms^{-1}). Initial sounding equivalent to $Fr = 0.75$ from the right.

speeds there is a region of low wind speeds. The development of low windspeed linear mountain waves is evident in the vertical velocity field as a series of uplift and downdraft zones running from the leeside to the windward side, stronger on the leeside and strengthening in the lower levels across the top of the ridge.

The $Fr = 1.5$ initial wind forcing case shown in Figure 3.16 shows increased horizontal winds at 0 km and an inclined zone of increasing uplift dipping to the leeside and decreasing in strength in that direction. A inclined down draft zone across the top of the ridge has increased winds in the lower levels. An inclined zone of uplift of smaller magnitude is tilted to the windward side.

In all cases linear mountain waves are present between the surface and 1 km [Hammouya, 1994].

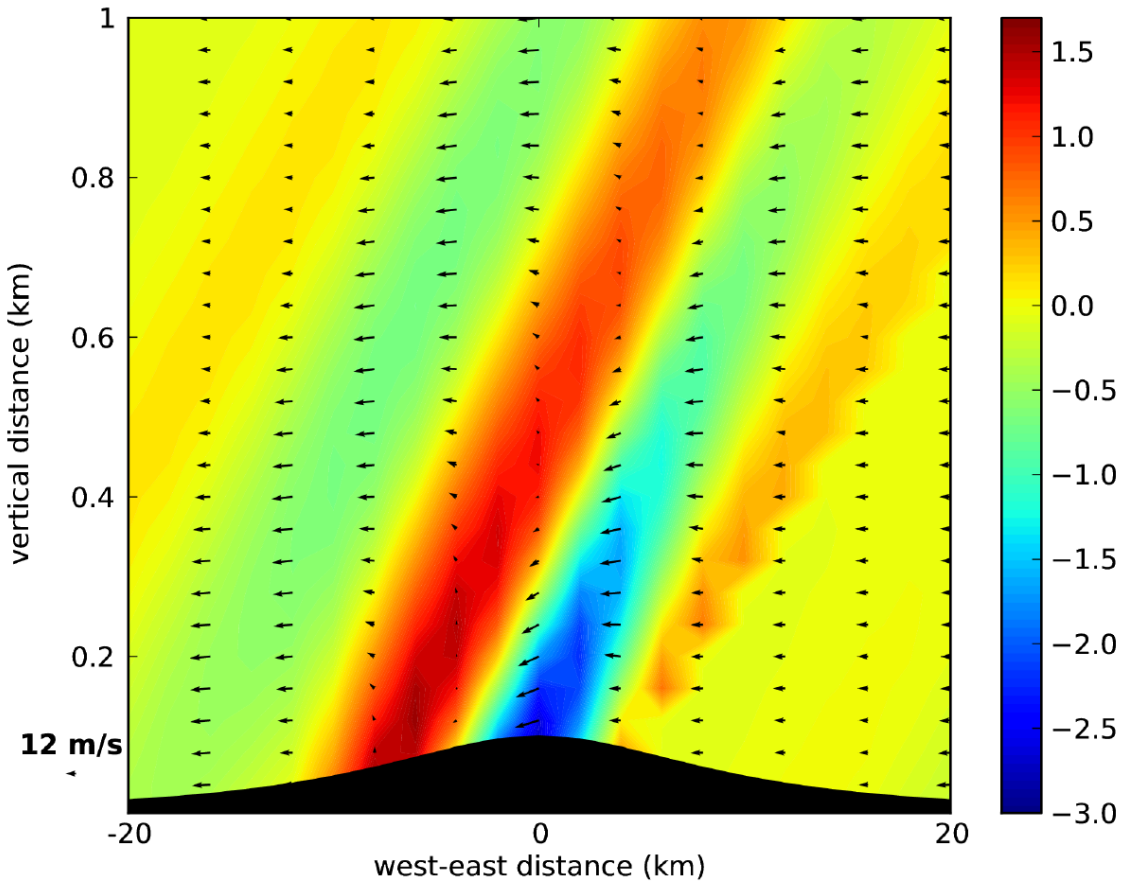

Figure 3.16: 2D WRF flow across an infinite ridge shown in black, horizontal velocity is shown by wind barbs (ms^{-1}) and vertical velocity is colour-coded (ms^{-1}). Initial sounding equivalent to $Fr = 1.5$ from the right.

3.4.1.2 3D mountain

A three dimensional approximation to a bell-shaped, symmetrical mountain of height 1000 m and spread of 4 km is used to simulate flow around an obstacle of the scale of SHV for 10 hours of simulation.

For the $Fr = 0.375$, Figure 3.17, initial forcing case, surface flow is characterised by the formation of a well defined vortex pair in the mountain wake. On the windward slope flow is opposed at the foot of the mountain but then changes to upslope flow over the mountain. Downstream of the mountain the vortices are centred on two areas $\pm 2.5 - 5km$ of the centre of the y-axis. In the region between the vortex pair the flow is reversed and goes upslope. The wind on the central plane shows a very well defined layer of reversed flow, and a possible hydraulic jump after the mountain peak. Regions with significant vertical velocities are associated with the weak jump close to the mountain peak and the upwind formation of lee waves.

These features compare well with leeside reversed flow and mountain linear wave

formation seen in Figure 3.12, even though the mountain in [Miranda and James, 1992] is larger and flattened at the summit (which may alter flow characteristics) and the Froude number in Figure 3.12 is slightly less. These results are also similar to [Hunt and Snyder, 1980] and [Smolarkiewicz and Rotunno, 1989].

For the $Fr = 0.75$, Figure 3.18, initial forcing case, there is a small vortex pair formed in the mountain wake and reversed flow on the windward slopes between the vortex pair. These are weaker and do not have as great extent as in Figure 3.17. On the vertical plane mountain linear waves are forming above the lee and windward slopes and a hydraulic jump at the summit of the mountain.

These features compare well with the extent of the reduced reversed leeside flow and stronger mountain linear wave formation exhibited in Figure 3.13. The reduction is size of the vortex pair is also consistant with [Hunt and Snyder, 1980].

For the $Fr = 1.5$ case, Figure 3.19, initial forcing shows no streamline splitting, the flow accelerating straight over the crest of the mountain. After the summit of the mountain there is an increase in the vertical component of the wind. Stronger linear mountain waves are forming and lower, at a height of about 50 m.

From these simulations we can expect in normal trade-wind conditions ($Fr =$ 0.375-$Fr = 1.5$) that a mountain of similar size on Montserrat, e.g. Soufri'ere Hills Volcano (SHV), will have reduced wind speeds on its windward side at the surface. If these trade winds are weak we can expect flow-splitting and increased wind speeds around the sides of the mountainl. If the trade winds are strong ($Fr = 1.5$) we can expect flow over the mountain causing orographic convection on the leeward side accompanied by an increased wind strength. As the strength of trade winds increases we can also expect the formation of mountain linear waves of increasing strength.

The work of [Miranda and James, 1992] to explore wind velocity around a 3D mountain is consistant in its conclusions with my study. Therefore in normal trade-wind conditions ($Fr = 0.375$-$Fr = 1.5$) idealised mountain WRF models accurately represent true wind flow.

Turbulent water vapour fields are formed by wind-flow patterns. Regions of velocity stagnation are where water vapour pools and regions of increased velocity are where water vapour disperses. Therefore low and moderate trade-wind values ($Fr = 0.375$ -$Fr = 0.75$) will create a tendency for water vapour to split around a mountain like SHV whereas stronger trade-wind velocities ($Fr = 1.5$ will create a tendency for water vapour to go over the summit of the mountain and pool on its leeside. This pattern should be more evident with the introduction of non-idealised modelling.

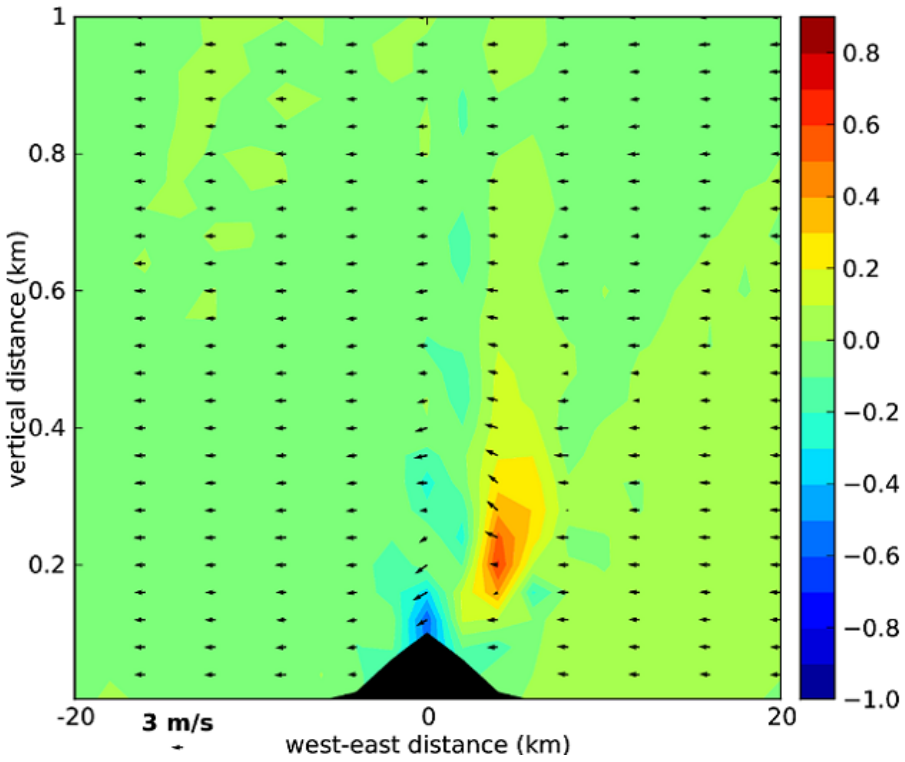

(a) y-plane.

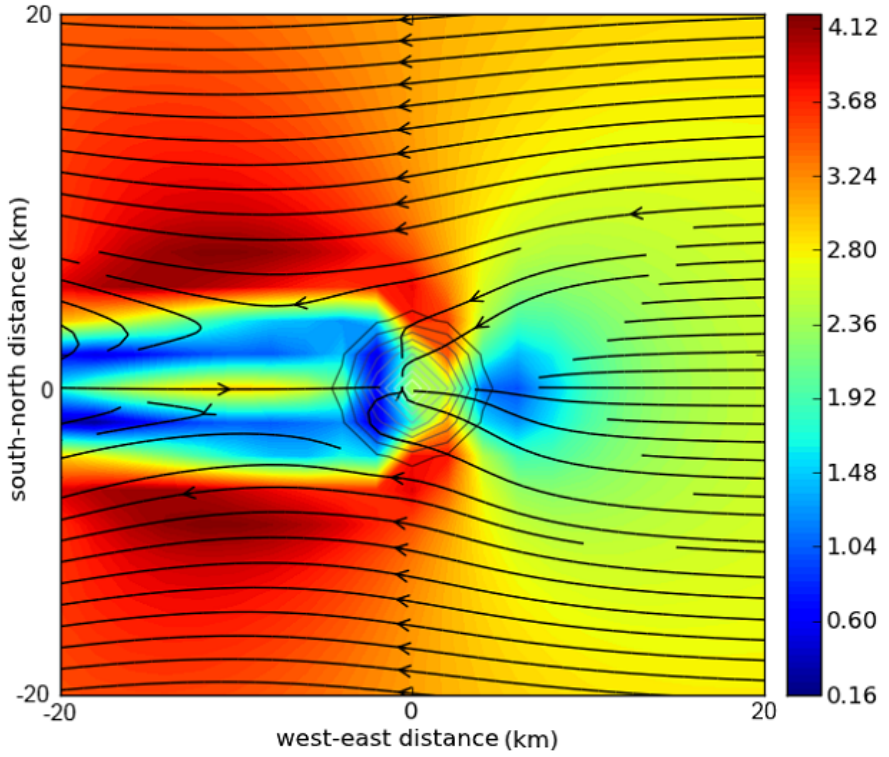

(b) Surface level.

Figure 3.17: WRF simulated 3D flow over an approximation to a bell-shaped, isolated mountain. Initial sounding equivalent to $Fr = 0.375$ from the right (east). (a) mountain shown in black, wind barbs (u,w) and vertical velocity is colour-coded (ms^{-1}). Wind barbs vertical velocity multiplied by 4. (b) mountain contours lines every 100m in centre of diagram (grey), streamlines show direction of horizontal flow (black) and corresponding wind speeds are colour-coded (ms^{-1}).

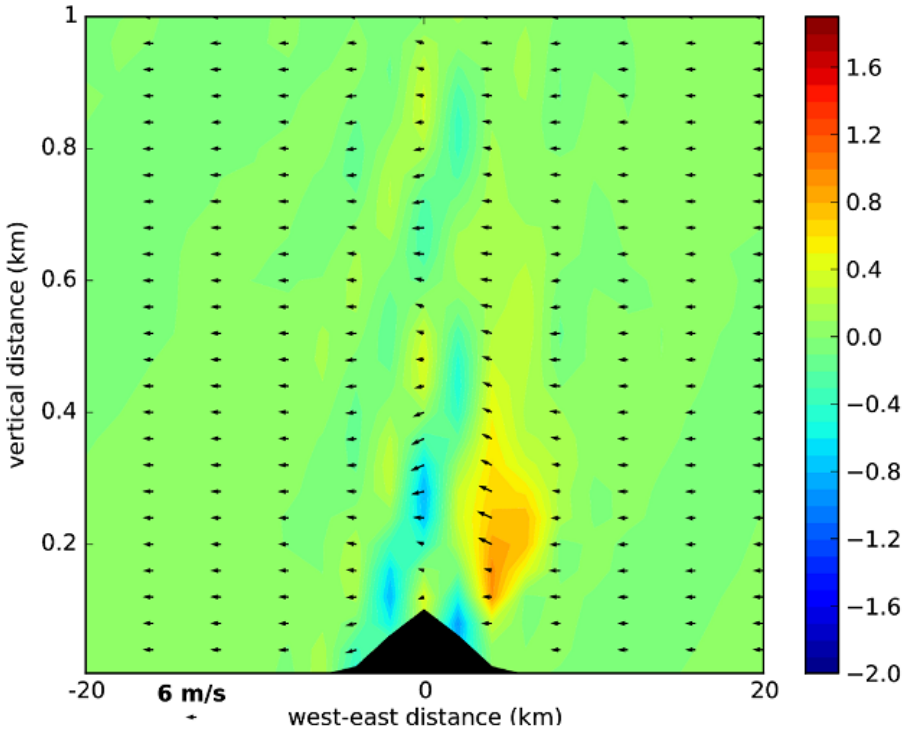

(a) y-plane.

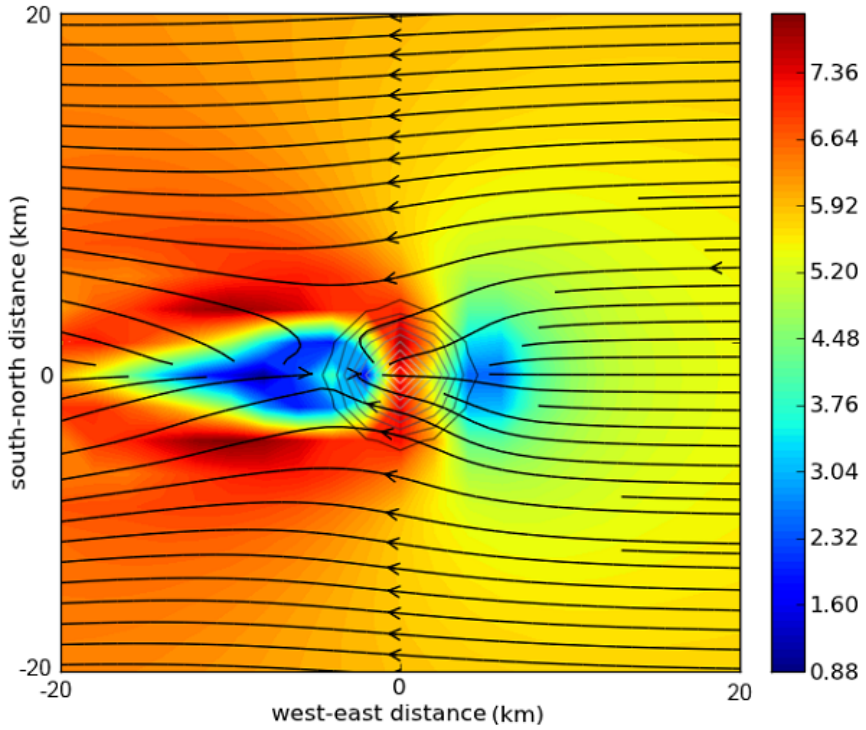

(b) Surface level.

Figure 3.18: WRF simulated 3D flow over an approximation to a bell-shaped, isolated mountain. Initial sounding equivalent to $Fr = 0.75$ from the right (east). (a) mountain shown in black, wind barbs (u,w) and vertical velocity is colour-coded (ms^{-1}). Wind barbs vertical velocity multiplied by 4. (b) mountain contours lines every 100m in centre of diagram (grey), streamlines show direction of horizontal flow (black) and corresponding wind speeds are colour-coded (ms^{-1}).

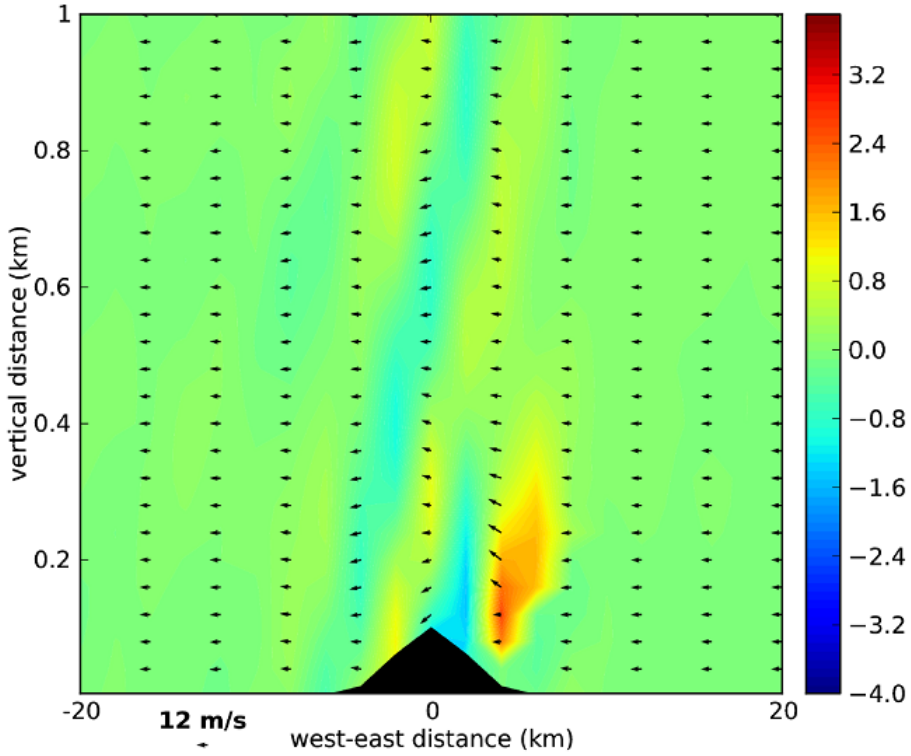

(a) y-plane.

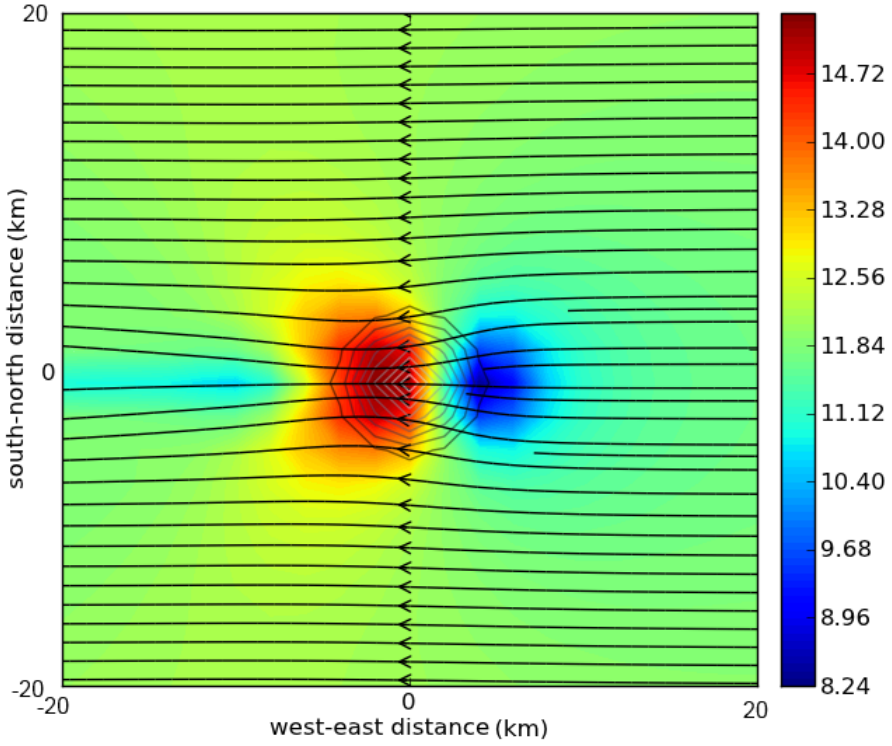

(b) Surfacel level.

Figure 3.19: WRF simulated 3D flow over an approximation to a bell-shaped, isolated mountain. Initial sounding equivalent to $Fr = 1.5$ from the right (east). (a) mountain shown in black, wind barbs (u,w) and vertical velocity is colour-coded (ms^{-1}). Wind barbs vertical velocity multiplied by 4. (b) mountain contours lines every 100m in centre of diagram (grey), streamlines show direction of horizontal flow (black) and corresponding wind speeds are colour-coded (ms^{-1}).

3.4.2 Field observations, measurements and comparisons

Field studies in Montserrat took place between 30th September - 6th October 2012, 2nd - 14th August 2013 and 22nd November - 19th December 2014 and we will now examine satellite-dervived cloud products, surface specific humidity values, nearby radiosonde data and observational data obtained during these campaigns. The weather diaries (Tables 3.6, 3.7, 3.8), MODIS visible imagery (1 km resolution), GOES-East water vapour imagery (9 km resolution), and radiosonde data, have been used to give context to and to validate the local WMM data during the 2012 and 2013 field trips. The 2013 field trip also includes a comparison of meteorological data collected by the Kestrel weather station. The 2014 field trip coincides with data obtained by COSMO-SkyMed overpasses.

3.4.2.1 Montserrat climatological data

An 18-year climatological dataset (covering the recent eruption phases of SHV) was obtained from the Government of Montserrat (courtesy of the MMVO). These measurements are made by instruments on a meteorological mast based at Geralds airport shown in Figure 1.4 and recorded as daily averages of wind parameters, relative humidity, pressure and temperature. This data is used, at this point, to provide climatological context for measurements obtained during the field campaigns.

[Cece et al., 2014] used three reference windspeeds which have been previously used to run idealised hydrostatic simulations (Section 3.4.1) - 3 ms^{-1}, 6 ms^{-1} and 12 ms^{-1}. The trade-winds are initially east-west to east-southeast - west-northwest in direction and between 3 ms^{-1} and 12 ms^{-1} in strength, mainly in the 6 ms^{-1} - 9 ms^{-1} range, Figure 3.20. Sea-level pressure on Montserrat is predominantly between 1013 hPa and 1019 hPa. In the summer months (June, July, August) there is a tendency for higher pressure values and in December and January there is a tendency for lower pressure values, Figure 3.21. Relative humidity is usually between 70 % and 85 %, it tends to be lower at the start of the year, Figure 3.22. A typical year on Montserrat is characterised by a dry season between January and June corresponding to high pressure and low relative humidity values, and a wet season running from July to December corresponding to low pressure and high relative humidity values. Rainfall values for the years 2010 - 2014 support this assertion, Figure 3.23. The 2012 and 2013 field campaigns took place in the wet season and the 2014 field campaign took place at the start of the dry season. Note that August 2013 had less than a third of the rainfall of October 2012. The climatological data shows that the 2012 and 2013 field trips occured during normal atmospheric behaviour.

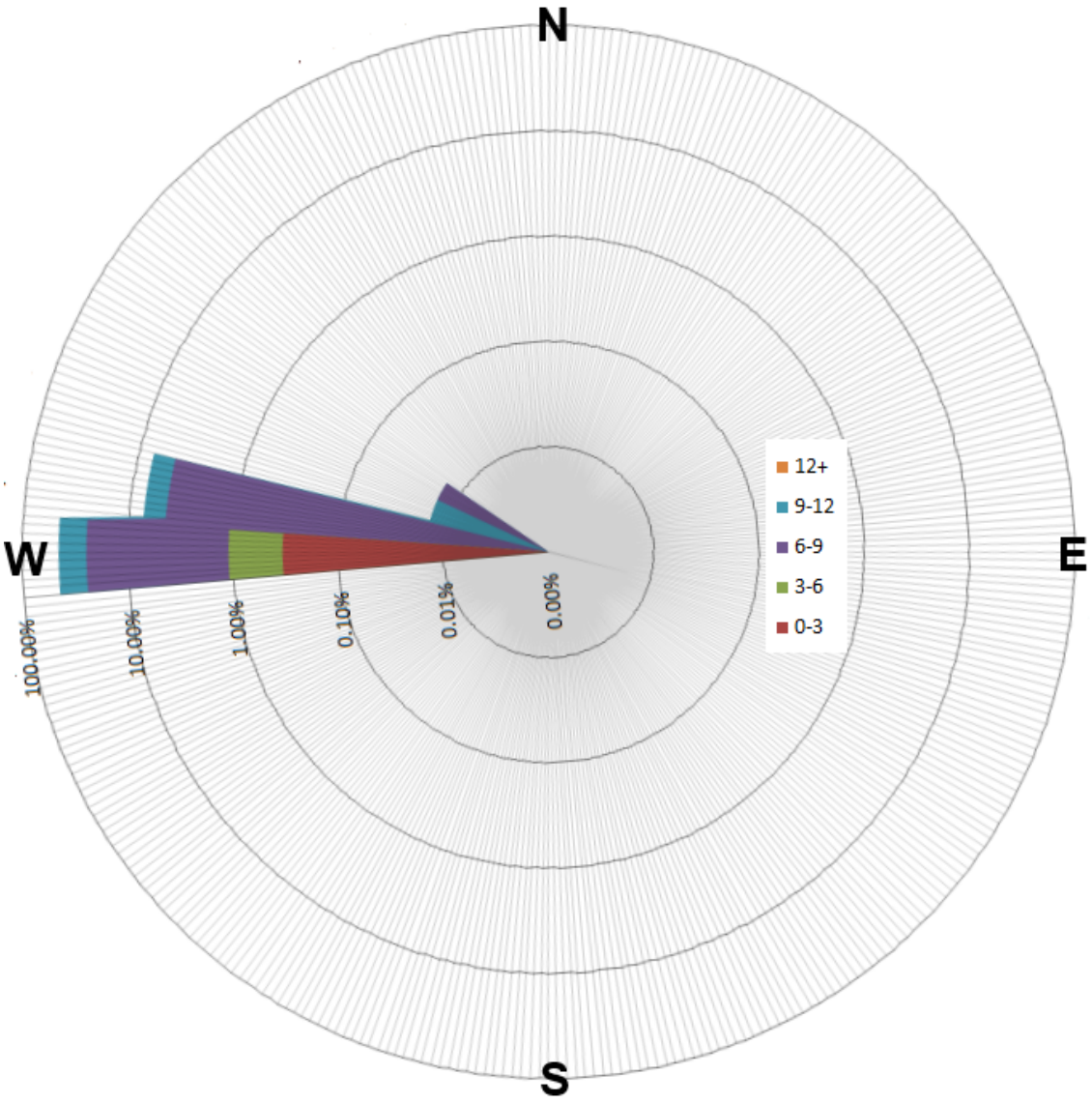

Figure 3.20: Wind rose of climatological data from 1996 - 2014. Number density of each windspeed group is shown as a colour coded percentage (logarithmic scale).

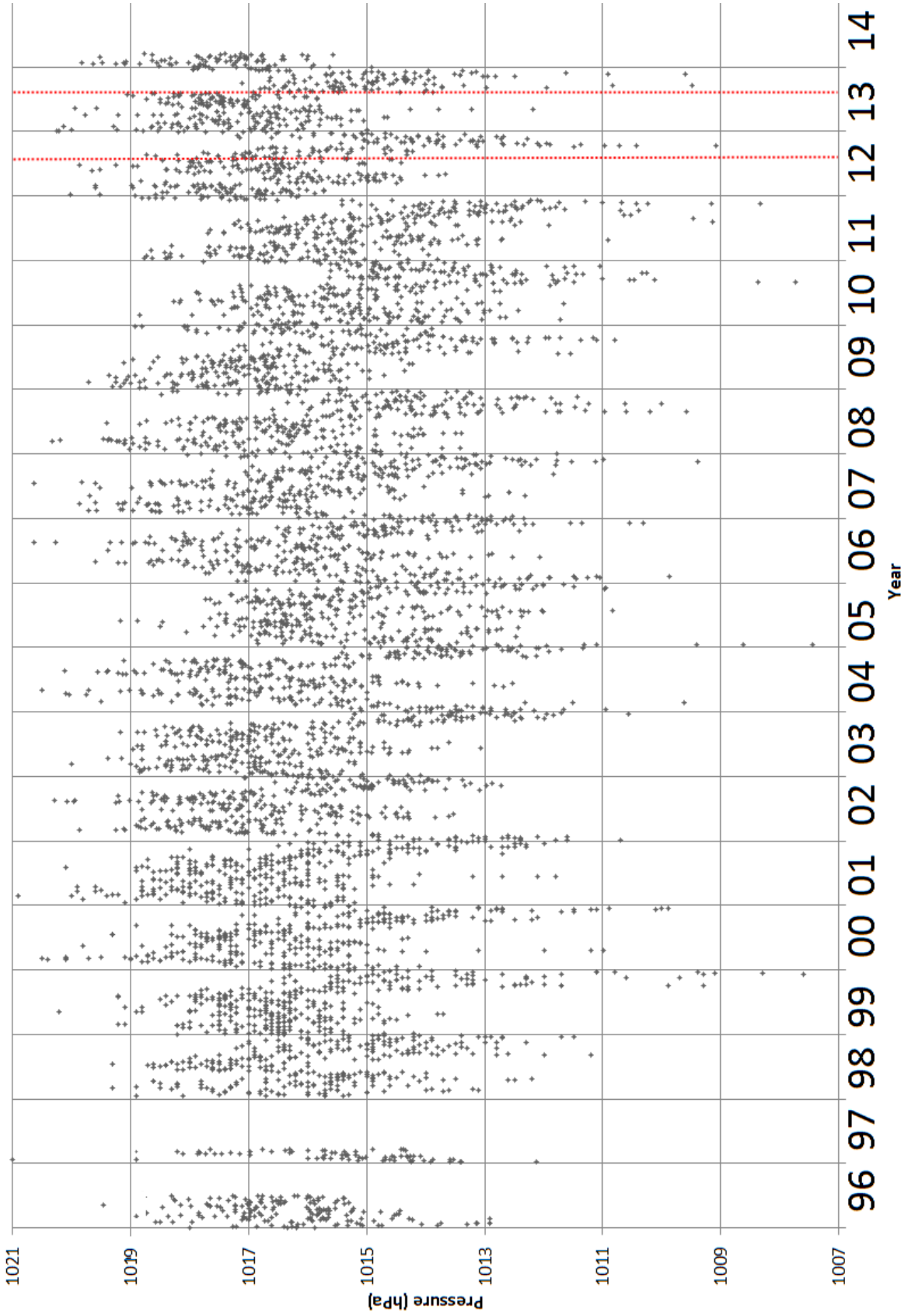

Figure 3.21: Surface pressure (hPa) between 1996 - 2014.Field trips shown by red lines.

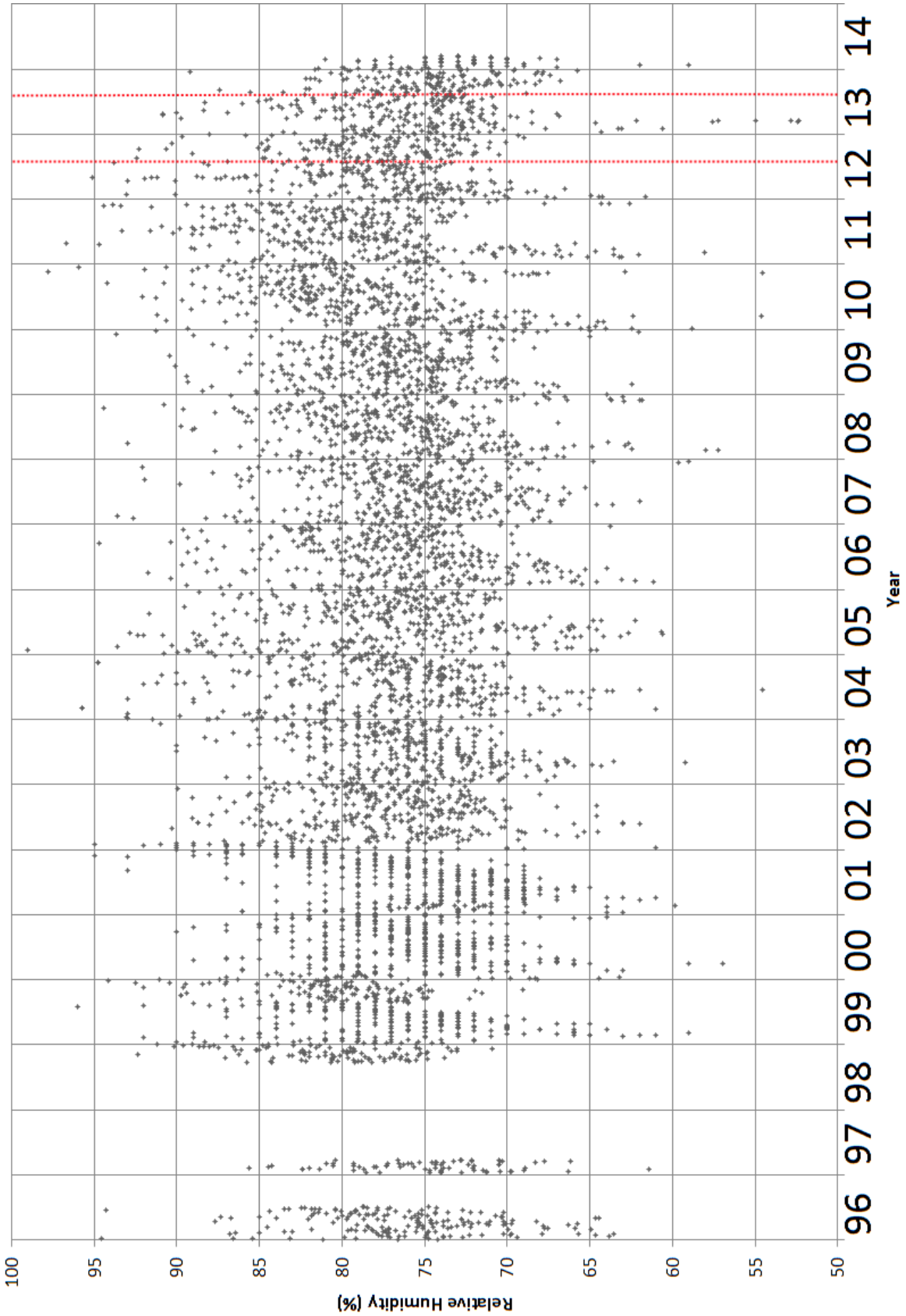

Figure 3.22: Relative humidity (%) between 1996 - 2014. Field trips shown by red lines.Missing data due to eruptive episodes.

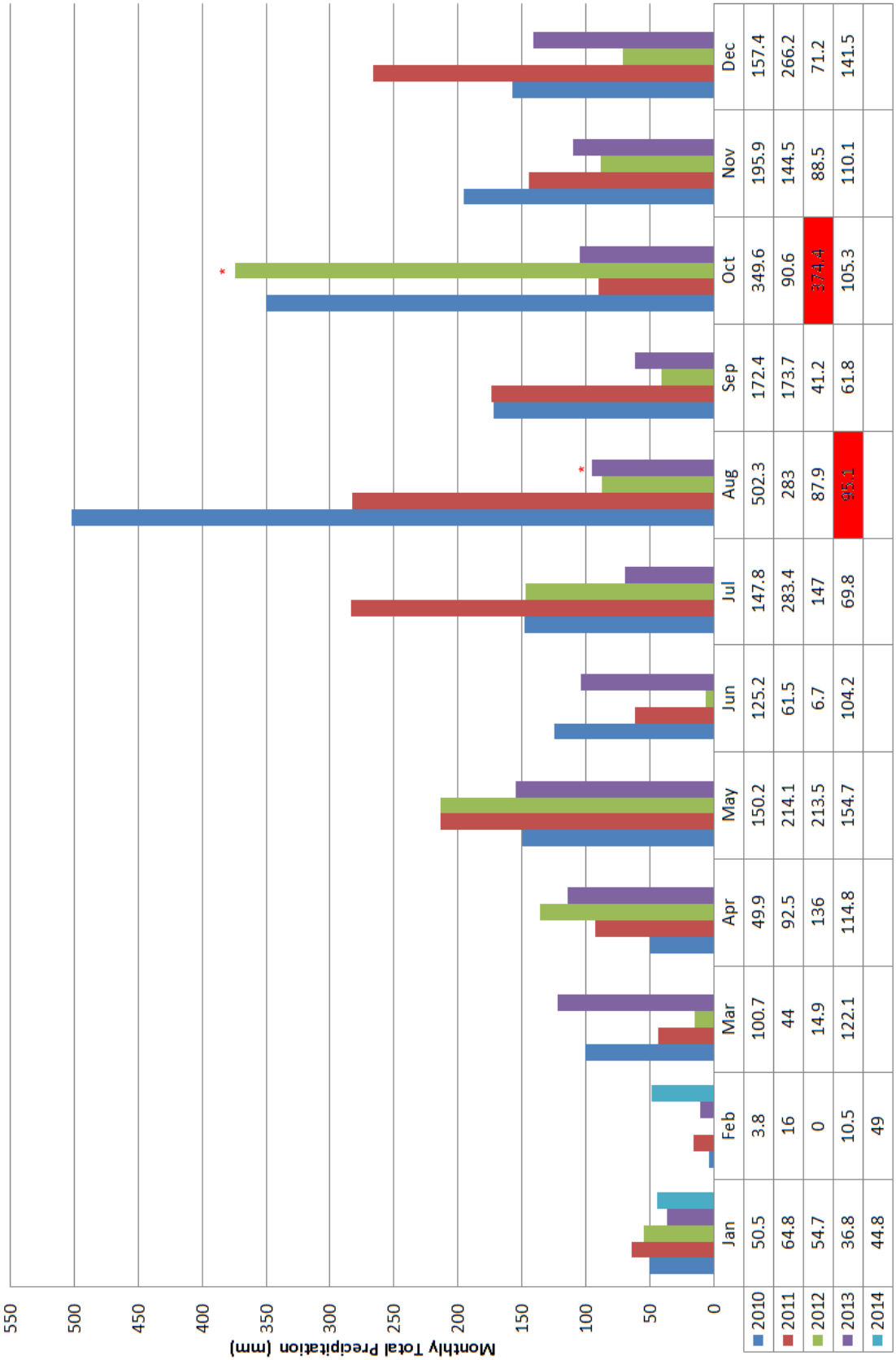

	Jan	Feb	Mar	Apr	May	Jun	Jul	Aug	Sep	Oct	Nov	Dec
2010	50.5	3.8	100.7	49.9	150.2	125.2	147.8	502.3	172.4	349.6	195.9	157.4
2011	64.8	16	44	92.5	214.1	61.5	283.4	283	173.7	90.6	144.5	266.2
2012	54.7	0	14.9	136	213.5	6.7	147	87.9	41.2	374.4	88.5	71.2
2013	36.8	10.5	122.1	114.8	154.7	104.2	69.8	95.1	61.8	105.3	110.1	141.5
2014	44.8	49										

Figure 3.23: Monthly total precipitation (mm) colour-coded by year from 2010 until 2014. Note that only two months of data were available in 2014. Red stars and shaded boxes indicate months of field trips. Missing data due to eruptive episodes.

3.4.2.2 Weather diaries

Although the first two field trips took place in the Montserrat hurricane season (July-November) there were only a few local thunderstorms and mesoscale systems (Tables 3.6, 3.7). The 2014 field trip was in normal weather conditions for the dry season (Table 3.8).

Table 3.6: Weather conditions on Montserrat during 2012 field trip.

Date	Summary
30th September	Plume blown to NW in morning swung to west in afternoon. Cloudy, a few showers.
1st October	Plume to west. Cloudy with showers. Increasing 100-km scale cloud in afternoon.
2nd October	Plume to west. Thunderstorm early morning, showers in afternoon. 100 km-scale cloud masses.
3rd October	Plume to west southwest. Calmer conditions, little cumulus cloud. Dome partially visible from north.
4th October	Plume to west. Showers and much cloud to east. Clearer in afternoon in the west. MODIS shows 100 km scale cloud mass to east.
5th October	Plume to southwest. Early morning thunderstorm, much clearer later in morning with much of dome visible. Cumulus forms to west.

Table 3.7: Weather conditions on Montserrat during 2013 field trip.

Date	Summary
2nd August	Easterly wind, gravity wave rolls to west.
3rd August	Easterly wind, gravity wave rolls to west.
4th August	Light topographically generated cloud.
5th August	Light topographically generated cloud.
6th August	Morning cloud, afternoon topograhically generated cloud to east.
7th August	Patchy cloud at 50-100km scale.
8th August	Plume to west. Scattered rain showers all day. Patchy cloud at 50-100km scale.
9th August	Plume to south, northerly winds. Scattered rain showers all day. Mesoscale system over island at 16:00. Patchy cloud at 50-100km scale.
10th August	Dome clear especially in the morning. Early in the day topographic leeward cloud leading to later regional high cloud cover.
11th August	Plume to west.
12th August	Plume to west. Scattered showers. Topographically generated cloud on leeward side.
13th August	Plume to west. 70% regional cloud cover.
14th August	Plume to west. Storm at night.

Table 3.8: Weather conditions on Montserrat during 2014 field trip.

Date	Summary
23rd November	Easterly wind, gravity wave rolls to west.
24th November	Easterly-North-Easterly wind, scattered convective showers throughout day.
25th November	Easterly wind, gravity wave rolls to west.
26th November	Easterly wind, gravity wave rolls to west.
27th November	Easterly wind, gravity wave rolls to west.
28th November	Southerly wind.
29th November	Easterly wind, gravity wave rolls to west.
30th November	Easterly wind, gravity wave rolls to west.
1st December	Easterly wind, gravity wave rolls to west.
2nd December	Easterly wind, gravity wave rolls to west..
3rd December	Easterly wind, gravity wave rolls to west.
4th December	Easterly wind, gravity wave rolls to west, plume over Olveston at midnight.
5th December	Easterly wind, gravity wave rolls to west in morning. Rain after 13:00, plume blowing in all directions.
6th December	Westerly wind. In afternoon Southerly wind and gravity waves travelling northwards. Radar shows mesoscale system to south-east in morning.
7th December	Easterly wind, gravity wave rolls to west.
8th December	Easterly wind, gravity wave rolls to west.
9th December	Easterly wind, gravity wave rolls to west.
10th December	Easterly wind, gravity wave rolls to west.
11th December	Northerly wind, rain during night.
12th December	Easterly wind, gravity wave rolls to west. Swell offshore, rain intermittent all day.
13th December	Easterly wind, gravity wave rolls to west. Light rain in morning.
14th December	Easterly wind, gravity wave rolls to west. Plume over Olveston in morning.
15th December	Winds light southerly. Dome on view. Mesoscale feature to North.
16th December	Dome on view. No winds. Mesoscale feature to North.
17th December	Easterly wind, gravity wave rolls to west.
18th December	Easterly wind, gravity wave rolls to west.Radar shows small stationary mesoscale system to north-east.
19th December	Easterly wind, gravity wave rolls to west.

3.4.2.3 Water vapour comparison - 2012 and 2013

Data comparison from the 2012 and 2013 field study shows radiosonde temperature and mixing ratios, MODIS visible imagery showing clouds, Goes-East water vapour images (uncalibrated) and WMM water vapour column totals. Note that the WMM data are synchronous with the MODIS data. Although there is sometimes a delay between available MODIS data and available GOES-East data, the MODIS dataset is often closely matched to the GOES-East as high water vapour is correlated with the positions of visible cloud. GOES-East by itself cannot be directly compared with WMM column water values because GOES-East can only observe upper-troposphere water vapour and is affected by high clouds.

The 2nd October 2012 shown in Figure 3.24 is an example of a day with moderate water vapour values. The radiosonde ascent shows that the air is close to saturation. Figure 3.25 shows these data for the 4th October 2012 when mesoscale features dominated the water vapour field. This feature is shown to the north-east of Montserrat in the MODIS imagery. The GOES-East shows high, localised areas of water vapour in the vicinity of Montserrat.

GOES-East shows a variety of water vapour conditions including a dry intrusion on 4th August 2013 shown in Figure 3.26 causing low water vapour amounts to a large mesoscale system on 8th August 2013, causing high water vapour amounts (not shown). Radiosonde ascents often indicate the presence of low level cloud within the boundary layer at Le Raizet with the exception of 4th August 2013, Figure 3.26. Figure 3.27 shows the conditions on the 5th August, where GOES-East shows moderate water vapour between the two extremes.

WMM simulations show a general east-west asymmetry in water vapour values across the island. For 2nd-4th August 2013 downwind linear mountain waves are observed in the WMM water vapour field. On the 2nd and 3rd August 2013 these can also be seen in the MODIS imagery and correspond to lower water vapour to the west, leeside, of SHV and immediately offshore and these waves were recorded by the weather diary (Table 3.7). On 4th August 2013, Figure 3.26a, these mountain waves are still evident in the WMM results. On all three of these days GOES-East shows low background water vapour and I propose this is the typical condition for Montserrat when there are no mesoscale weather features. On 4th August 2013 the radiosonde shows a boundary layer inversion shown in Figure 3.26b.

Comparing the two non-extreme field trip cases (Figures 3.24 and 3.27) the water vapour values nearby to Montserrat range from 40 mm to 53 mm. The lower water vapour values are over the hills and in the case of the 2012 field study, to the West. In both cases there are small high areas of water vapour offshore.

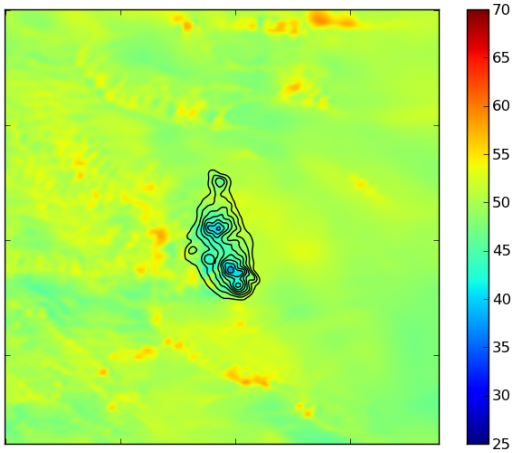

(a) WMM 15:30 - Water Vapour (mm)

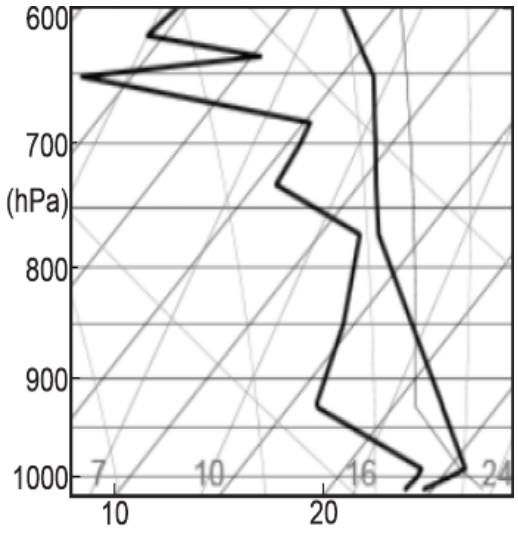

(b) Le Raziet 16:00

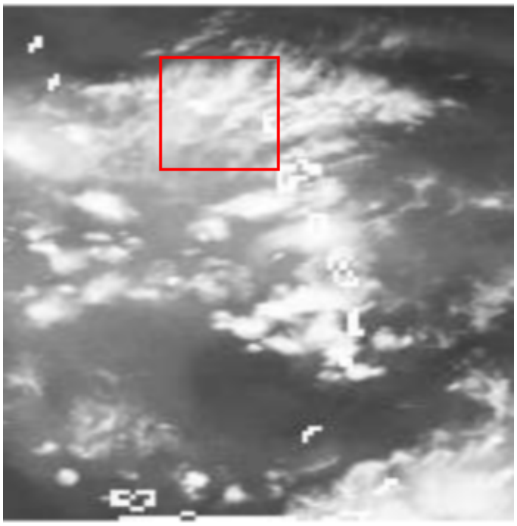

(c) GOES-East 15:00

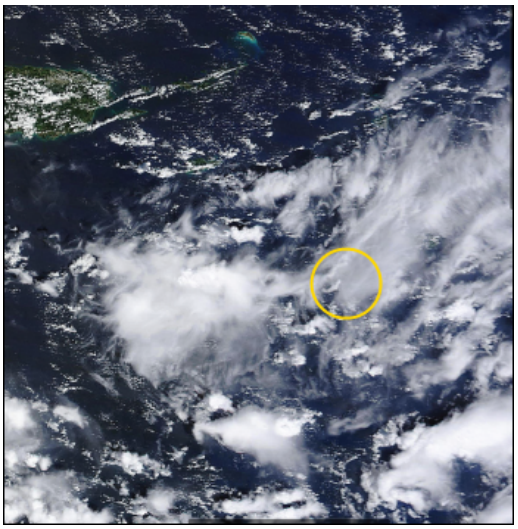

(d) MODIS 15:30

Figure 3.24: WMM water vapour cumulative column (mm) model output (a) at 15:30 UTC on 2nd October 2012, Montserrat terrain shown by black contour lines every 100 m. Le Raizet radiosonde ascent 16:00 UTC on 2nd October 2012 (b), skewT-logP plot y: pressure (hPa) x: temperature (°C) right curve, values below axis and mixing ratio (g kg^{-1}) left curve, values above axis. GOES-East water vapour channel (c) at 15:00 UTC on 2nd October 2012 (MODIS domain shown by red box) and MODIS Aqua visible image (d) at 15:30 UTC on 2nd October 2012 (Montserrat circled).

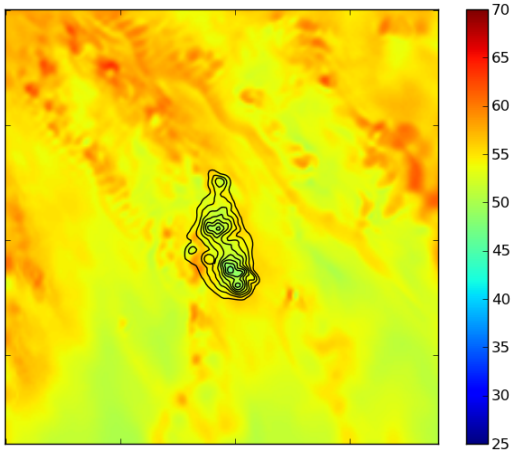

(a) WMM 15:10 - Water Vapour (mm)

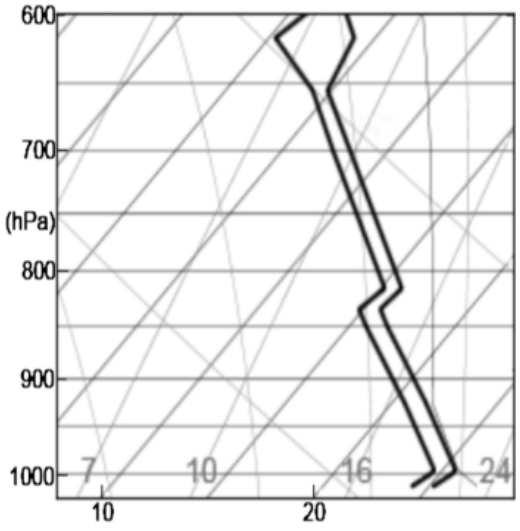

(b) Le Raziet 16:00

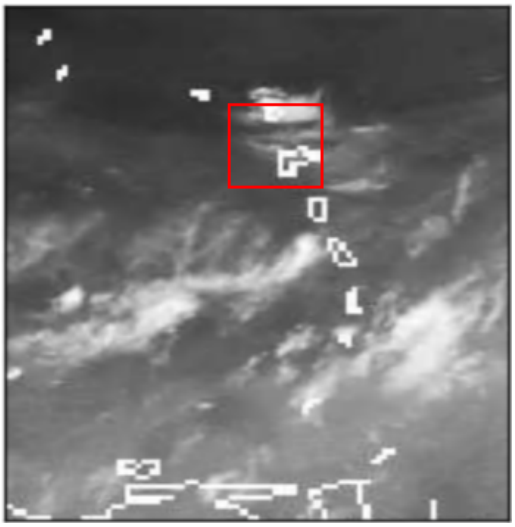

(c) GOES-East 15:00

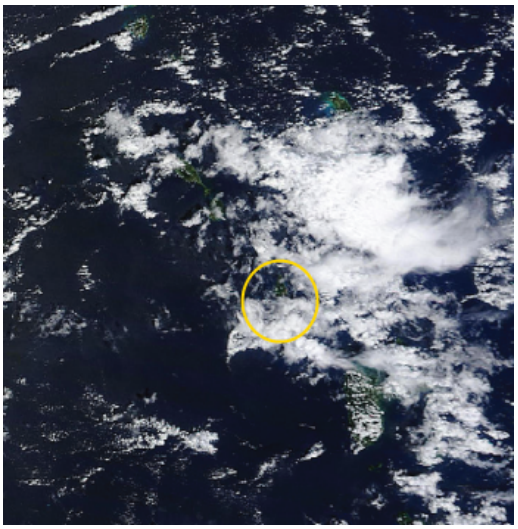

(d) MODIS 15:10

Figure 3.25: WMM water vapour cumulative column (mm) model output (a) at 15:10 UTC on 4th October 2012, Montserrat terrain shown by black contour lines every 100 m. Le Raizet radiosonde ascent 16:00 UTC on 4th October 2012 (b), skewT-logP plot y: pressure (hPa) x: temperature (°C) right curve, values below axis and mixing ratio (g kg^{-1}) left curve, values above axis. GOES-East water vapour channel (c) at 15:00 UTC on 4th October 2012 (MODIS domain shown by red box) and MODIS Aqua visible image (d) at 15:10 UTC on 4th October 2012 (Montserrat circled).

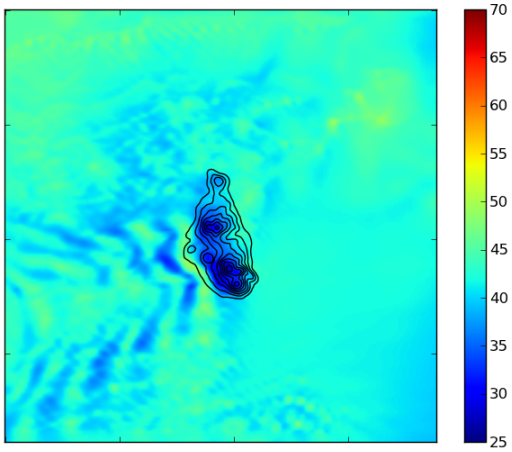

(a) WMM 15:10 - Water Vapour (mm)

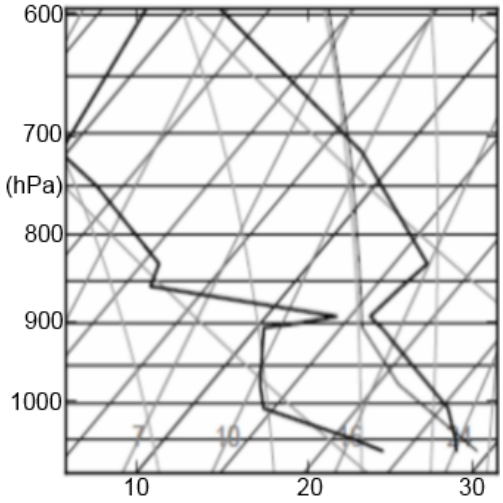

(b) Le Raziet 16:00

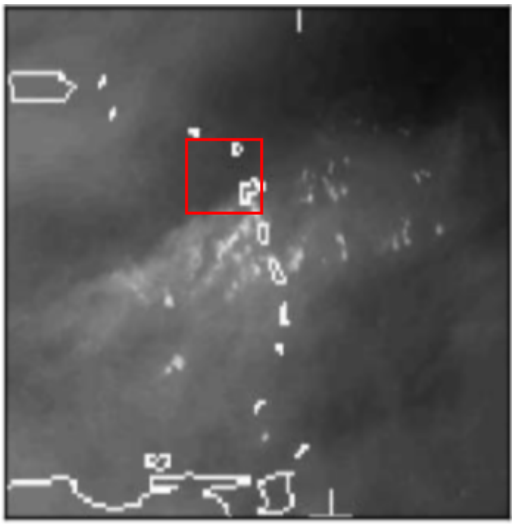

(c) GOES-East 15:00

(d) MODIS 15:10

Figure 3.26: WMM water vapour cumulative column (mm) model output (a) at 15:10 UTC on 4th August 2013, Montserrat terrain shown by black contour lines every 100 m. Le Raizet radiosonde ascent 16:00 UTC on 4th August 2013 (b), skewT-logP plot y: pressure (hPa) x: temperature (°C) right curve, values below axis and mixing ratio (g kg^{-1}) left curve, values above axis. GOES-East water vapour channel (c) at 15:00 UTC on 4th August 2013 (MODIS domain shown by red box) and MODIS Terra visible image (d) at 15:10 UTC on 4th August 2013 (Montserrat circled).

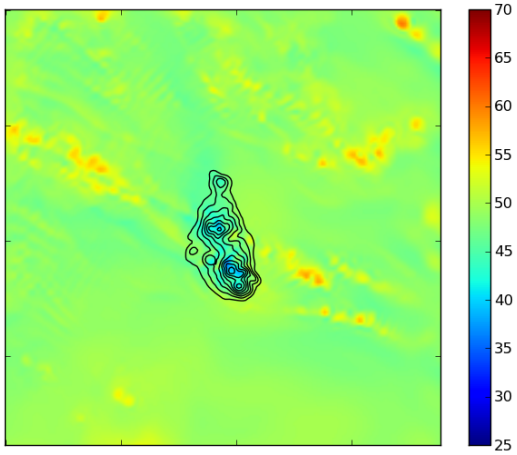

(a) WMM 14:20 - Water Vapour (mm)

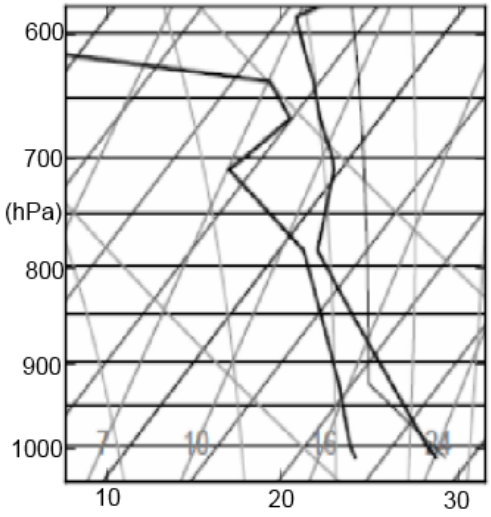

(b) Le Raziet 16:00

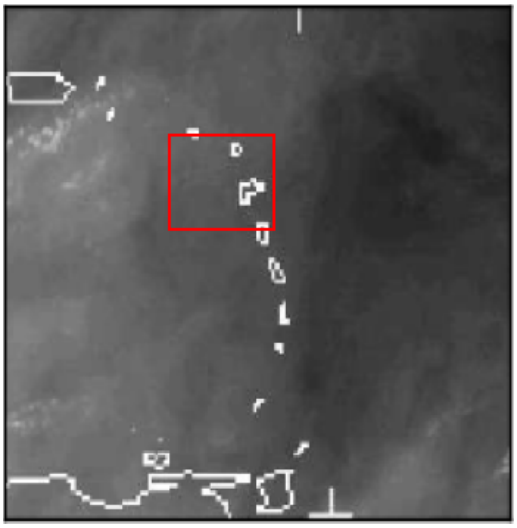

(c) GOES-East 15:00

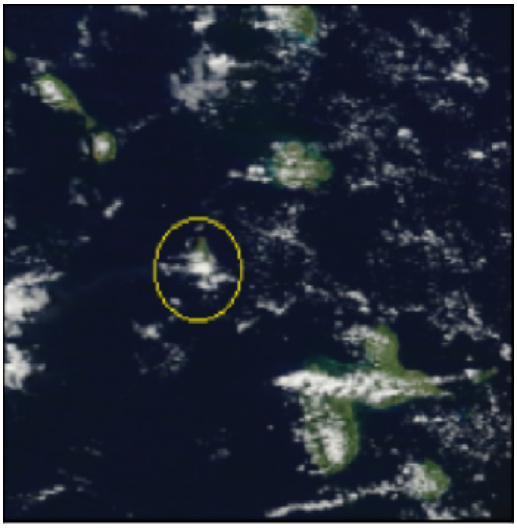

(d) MODIS 14:20

Figure 3.27: WMM water vapour cumulative column (mm) model output (a) at 14:20 UTC on 5th August 2013, Montserrat terrain shown by black contour lines every 100 m. Le Raizet radiosonde ascent 16:00 UTC on 5th August 2013 (b), skewT-logP plot y: pressure (hPa) x: temperature (°C) right curve, values below axis and mixing ratio (g kg^{-1}) left curve, values above axis. GOES-East water vapour channel (c) at 15:00 UTC on 5th August 2013 (MODIS domain shown by red box) and MODIS Terra visible image (d) at 14:20 UTC on 5th August 2013 (Montserrat circled).

3.4.2.4 Kestrel diurnal data

The Kestrel weather station recorded three surface level products during the 2013 field trip applicable to the validation of the WMM: surface temperature, pressure and relative humidity. Surface temperature and pressure are used in the WMM water vapour to ZWD conversions in Chapter 4.

Although surface temperature was recorded with highs of 40°C (direct sunlight affected) and lows of 21°C the average temperature was found to be 29°C, Figure 3.28. Typically, the temperature increased from 28°C at 8 am to a peak of 33°C at about 13:00 local time.

Pressure readings have been removed because they have been corrupted.

The hours of daylight showed the biggest variation in relative humidity, Figure 3.29. It generally fell by 25% between 6 am and 12 am rising again after sunset. This range and times can also be seen in the WMM data. Relative humidity varies between 40% and 100%, but mostly between 60% and 90%.

A number of local storms on the 10th and 11th August 2013 caused a rise relative humidity to 100% because of saturation by precipitation and as expected coincides with a temperature drop, Figure 3.28. In general falls in relative humidity align with rises in temperature and vice versa.

3.5 Summary of the WMM model

This chapter has described the setup of the WMM model needed to simulate water vapour fields over Montserrat using high quality initial meteorological conditions and static geographic data, combined with a parameterisation sensitivity testing. It has been shown how idealised hydrostatic flow generated by WMM around obstacles of the same scale as Montserrat agrees qualitatively with previous results. The idealised simulations do not include a parameterisation for drag because there is not one available using WRF. As was found in [Miranda and James, 1992] and others drag alters the surface characteristics. This could be included by initialising the drag field, hardcoding the land surface paramters.

Additionally precipitation output from WMM has been analysed at a regional length-scale and compared with TRMM data. The main conclusions of the TRMM comparison are that the Grell-Devenyi cumulus scheme should be switched on for the 8.1 km and 2.7 km domains. The setup of the WMM has been described in Table 3.5.

It has also been shown how non-idealised, non-hydrostatic models can be used to find water vapour fields at the time of satellite overpasses. The output of these

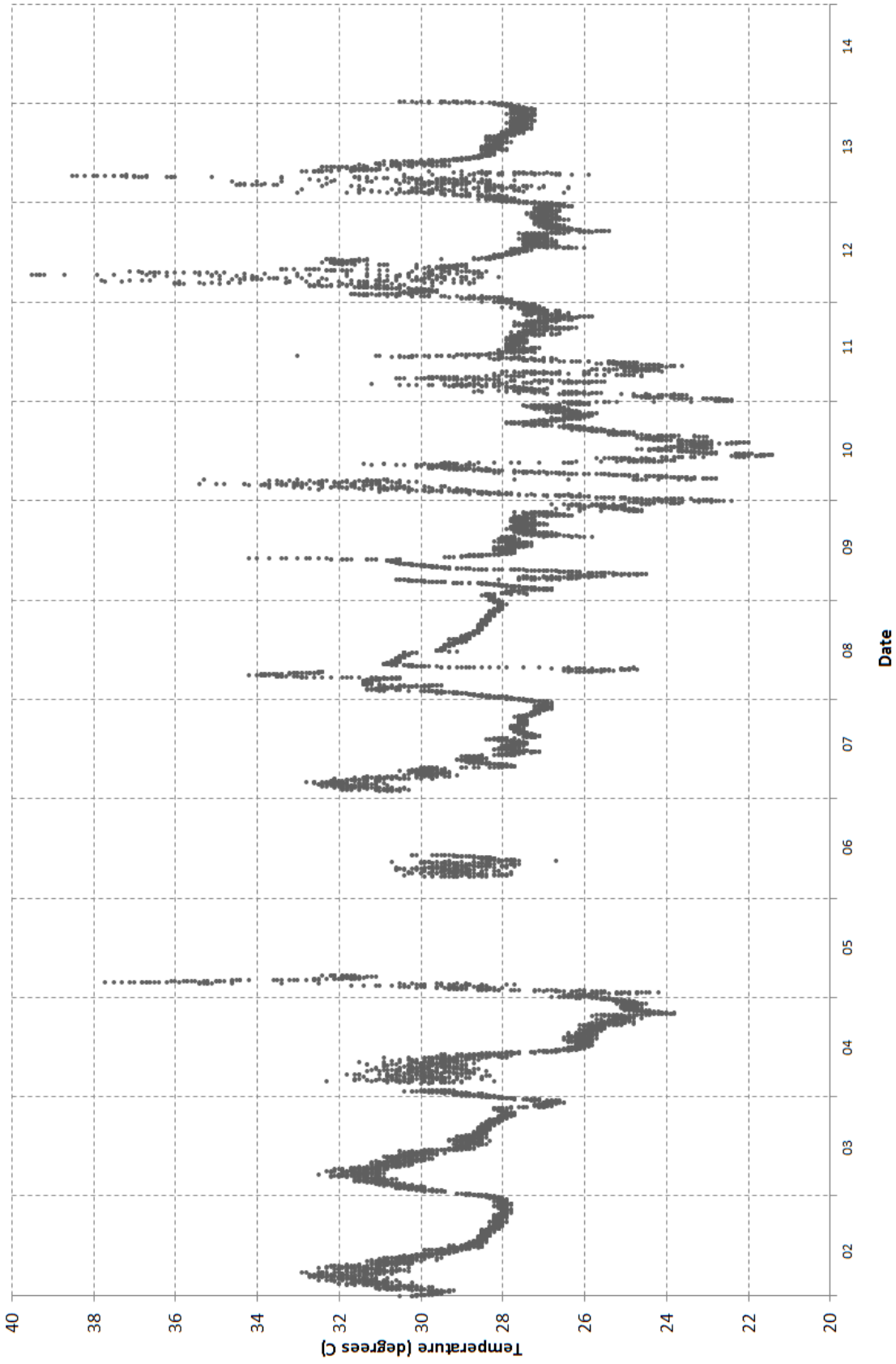

Figure 3.28: Kestrel surface temperature (°C) recorded every minute for all days of the 2013 field trip. The date in August is shown on the bottom axis starting at 00 UTC. Note the extreme peaks to 40 °C are due to heating of the thermometer by sunlight.Missing data due to loss of power to instrument.

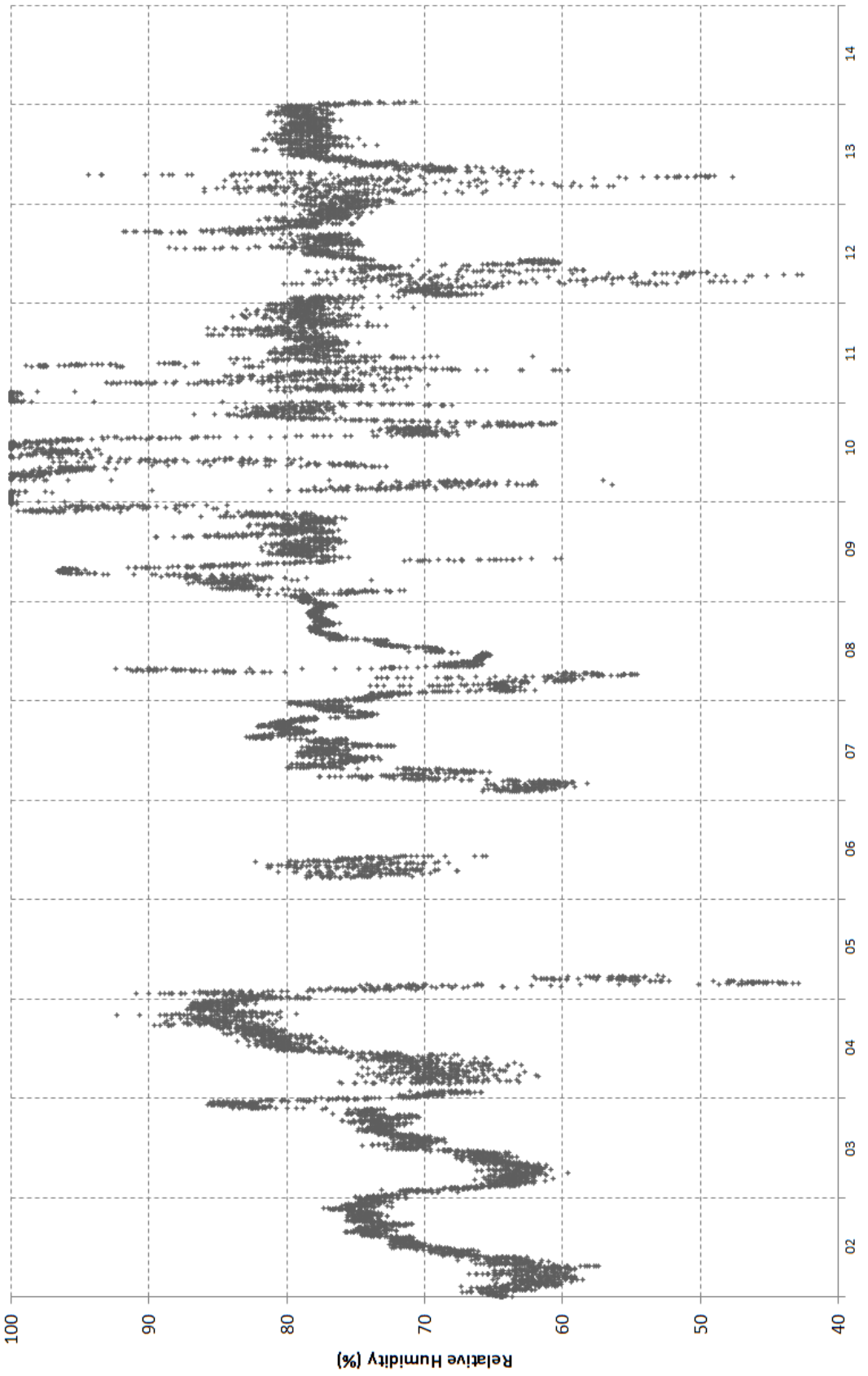

Figure 3.29: Kestrel relative humidity (%) recorded every minute for all dates of the 2013 field trip. The date in August is shown on the bottom axis starting at 00 UTC.Missing data due to loss of power to instrument.

fields have been compared qualitatively with MODIS, radiosonde, weather diary and GOES-East data at a resolution of 300 m to build up an idea of how WMM performs at a local lengthscale during field trips to Montserrat in 2012 and 2013. A more detailed validation of the WMM water vapour field against GPS data will be discussed in Chapter 5.

Kestrel weather station data has been recorded from the 2013 field trip to show typical temperature and relative humidity values which will be used in subsequent chapters. The 2012 and 2013 field trips took place in conditions normal for the wet season from a climatological perspective (Section 3.4.2.1).

Weather diary data for the 2014 field trip will be used in the next chapter.

Chapter 4

InSAR Processing

4.1 Introduction to InSAR Processing

SAR processing refers to the generation of a focussed SAR image starting from raw range and Doppler data. Matched filtering of the raw data in range and azimuth with corresponding reference functions are used to turn the data into Single Look Complex (SLC) format. Processing of SAR imagery results in separate manipulation of range and azimuth spectra and in SLC images each image pixel corresponds to a single look and is a complex number, representing intensity and phase. I now begin with an overview of the processing of two SLC images into an interferogram (InSAR) and use the term SLC to refer to an SLC image. This treatment follows the typical processing chain used in the GAMMA software ([*GAMMA Software*, 2015]). SLC format images of Montserrat (COSMO-SkyMed) were supplied by the Italian Space Agency.

4.1.1 Co-registration

The SLCs forming an image pair are not registered spatially and the computation of the interferogram requires first a co-registration step so that corresponding pixels in the two images match to sub pixel accuracy. Since all the information contained in the SLC to be resampled should be preserved, the accuracy in the co-registering operations must be exceptional. A registration accuracy of better than 0.2 pixels is required in order not to reduce interferometric correlation by more than 5%. Precision co-registration requries using the image data to obtain residual errors less than 0.05 pixel.

Co-registration consists of computation of offsets between the two SLCs and resampling one SLC in order to match with the reference image. The offsets are used to determine the coefficients of the interpolation function needed for resampling. The

offsets between the SLC images can be computed using orbit data, correlation of image intensities or fringe visibility.

With the intensity cross-correlation optimisation procedure, also known as intensity tracking, a number of windows distributed over the image are set and offset fields are generated with a normalised cross correlation of image patches of detected real-valued SAR intensity images. The successful estimation of the local image offsets depends on the presence of nearly identical features in the two SAR images at the scale of the employed patches. The location of the peak of the 2-D cross correlation function yields the image offset.

With coherence tracking, also known as the fringe visibility algorithm or coherence optimisation procedure, small data patches are selected throughout the SLCs. A series of small interferograms with changing offset is constructed and the coherence is estimated. The location of the coherence maximum determines the local offset. The magnitude of the coherence maximum relative to the average level is used as a quality factor to help reject unsuitable patches.

Offsets are then used as inputs to a least squares polynomial fit. The polynomial is a biquadratic function. Usually a simple polynomial model is sufficient for the offset function between SLCs. In the case of large scale topography and a large baseline this is not sufficient. A smart procedure when generating the polynomial is to use an approach that rejects offsets far from the initial fit.

The requirements of the misregistration error are satisfied only when complex interpolation filters are used. An ideal interpolator with a flat spectrum, i.e. an infinite sinc function, is not possible because filters only have a finite length. However, most of the SAR products are oversampled, the use of finite filters will not cause a loss of information. Resampling of the slave SLC image is typically performed using a complex sinc interpolator. Every band-limited signal can be reconstructed from discrete samples acquired at the Nyquist rate.

4.1.2 Baseline Estimation

Estimation of the baseline (see [Ren et al., 2003], [Sadhana et al., 1996]) is required for common band filtering, flattening of interferograms and phase unwrapping.

The interferometric baseline is defined as the difference of platform position vectors (antenna phase centres on the two passes) when a given scatterer is imaged. If the tracks are not parallel, in the case of repeat pass interferometry, the baseline changes along-track. The position on the track when the SAR images a point depends on the effective squint of the radar. Depending on the Doppler range dependence the effective platform positions will change as a function of range. Image

de-skew changes the SAR image geometry to appear in the zero-Doppler geometry independent of Doppler centroid used to process the data. The baseline is not changed by different processing algorithms. The baseline can be decomposed into components, in the reference co-ordinate system we use [Track, Cross-track, Normal] (TCN) co-ordinates. The parallel baseline is the component along the radar's line of sight, the perpendicular baseline is the component perpendicular to the line of sight. Transformations between the TCN and the parallel-perpendicular reference system are based on simple trigometric functions.

The measurement of the distance between two SAR antennas in space when they image the same object on the ground is difficult because it requires perfect knowledge of the satellite position and attitude as they travel along their orbits. In practice the baseline is estimated using a model of the baseline, the complexity of which can vary depending on the approach used and the precision one wants to obtain.

4.1.2.1 Baseline Determination from State Vectors

At first a point in the centre of the scene is selected and the reference system basis is constructed, e.g. with axis along track, across track and normal (TCN). The spacecraft location along the second track is moved until the point of closest approach to the position of the spacecraft on the reference track is found. The vector between the spacecrafts is the baseline estimate. This method works best when accurate state vectors are available.

4.1.2.2 Baseline Determination from Fringe Rate

The local fringe rate (rate at which the fringe cycles throughout) in the unflattened interferogram can be calculated. Over a small range of incidence angles, the fringe rate is constant so that this is easily detected when calulating a fast fourier transform of a region. Since the fast fourier transform gives the frequency of fringes the baseline can be solved for. An iterative flattening is possible by applying the baseline algorithm multiple times, each time removing a residual fringe rate. This method is most useful when the fringes due to the curved Earth are the dominant interferometric phase component. That is to say where topography is flat, atmospheric noise is small, water based noise is small and there are no ground displacements between image aquisitions.

4.1.2.3 Baseline Determination from Ground Control Point

This can only be used for the inversion of the unwrapped phase to height since elevation information and interferometric phase directly relate to the elevation information required. This method is the most accurate, but was not used here.

4.1.3 Common band filtering

If the perpendicular baseline of the interferometric system is non-zero, the frequency band of the signal received by the one radar is offset with respect to the band of the signal received by the other radar, i.e. the two SARs view the scene at slightly different look angles. The consequence is that the two signals do not fully correlate, i.e. the interference pattern between the images is corrupted. Total destruction of the interferometric fringes occurs when the spatial separation of the two SAR in space is such that the spectra do not overlap at a critical baseline.

The radar pulse samples a small bandwidth of the spatial reflectivity spectrum of the surface. The second interferometer antenna sees the scene from a slightly different look angle so it records a different part of the spectrum shifted by a certain frequency change.

When the slant range spectra of two images do not overlap completely, the non-common parts cause decorrelation and therefore must be filtered out prior to the generation of the interferogram. Spectral shift filtering removes the effects of baseline decorrelation for level surfaces. It consists of several operations and requires accurate baseline estimation from orbital parameters and slope estimation. The main drawback is a proportional loss of range resolution because of smaller bandwidth.

If the SAR antennas have different squint angles (where the SAR looks to the side at slightly different angles) at aquisition, the two images have a slight difference in the azimuth spectra. The shift between the two spectra creates a Doppler centroid not equal to zero frequency. To remove this effect, azimuth bandpass filtering is generally performed to retain the parts of the band common to the two images.

The complex interferogram is obtained from the cross-product of the co-registered SLC's and after common-band filtering. The interferogram consists of magnitude (correlation between images) and phase (InSAR phase). The lower the correlation, the noisier the phase. The InSAR phase is a combination of several contributions (curved Earth, topography, surface displacements, atmospheric delays, phase noise). The InSAR phase has a value between 0 and 2π, i.e. the phase is wrapped in this interval.

4.1.4 Interferogram Flattening

The interferogram generated from SLCs has an almost linear phase trend across the image as a function of the slant range and baseline due to the curved Earth. Removal of this phase term, leaves fringes only related to changes in elevation as well as noise, atmosphere and surface displacement. The operation is called flattening because in case of a flat surface this would be the only component of the interferometric phase, under the assumption that the other components are null.

Flattening is performed by computation of the fringe rate across the image in order to take into account the variations of slant range distance, incidence angle and perpendicular component of baseline. This operation assumes the surface of the Earth to be an ellipsoid without topographic features.

4.1.5 Coherence Estimation

Coherence is obtained from the cross-product of the two co-registered SLCs. When a DEM is available, it is possible to get a precise description of the slope correcting factor thus enhancing the accuracy of the coherence estimate. If the DEM is not available, it is possible to derive the correcting factor from the interferogram itself or use an approximation in which the phase is described by either a constant, linear, quadratic or higher order function over the estimation window.

The size of the estimation window is a crucial factor determining the coherence estimate. For increasing window size the estimation bias and the estimation uncertainty decrease while the spatial resolution of the coherence image decreases. To compromise between accurate estimation and high spatial resolution, the estimation algorithm can implement adaptive window size depending on an initial estimate of the coherence. In areas of low coherence, larger estimation windows are used.

Coherence is typically computed using a sliding window. For each pixel the coherence is obtained by the window sliding from pixel to pixel. To decrease the effect of resolution loss due to the windowing operation, weighting functions, e.g. linear or Gaussian, can be applied within the window. In this way pixels further away from the centre of the window have less weight on the estimate. The type of weights to be applied depends on the nature of the objects in the scene. If the scene includes distributed targets, weighting plays a minor role. On the contrary, if the scene is populated with small-size point targets - it is recommended to use small windows and strong weighting functions to preserve the coherence of each of the point targets.

4.1.6 Interferogram Filtering

Filtering an interferogram has the objective to reduce phase noise, thereby reducing the number of residues. A residue is a point in the interferogram when the sum of the phase differences between pixels around a closed path is not 0.0. Residues exist as pairs. Generally, thermal noise causes pairs of residues that are close together to be generated. The ultimate objective of filtering is to reduce the phase noise and therefore make the phase unwrapping simpler, more robust, and more efficient.

One popular way of filtering is to multi-look the complex interferogram, i.e. average complex samples. Multi-looking the interferogram reduces the standard deviation of the interferometric phase. The standard deviation of the estimated phase is in fact proportional to the number of pixels over which the average is computed. Other ways of filtering the image include using 2-D band-pass filter, accounting adaptively for the local phase gradients and using adaptive filtering with a filtering function based on the local fringe spectrum.

4.1.7 Phase Unwrapping

Since the interferometric phase is wrapped modulo 2π, an integer number of 2π has to be added to recover the absolute phase difference. This operation is called phase unwrapping. Unwrapping the phase means adding a correct multiple of 2π to the interferometric phase for each pixel in order to obtain sequential phase values across the entire image.

The phase unwrapping procedure assumes that the surface is relatively smooth and hence there should be an absence of jumps of the unwrapped phase. More precisely, phase unwrapping is based upon the assumption of smooth phase such that the phase differences are between adjacent samples. The algorithm must however take into account the fact that actual phase jumps do occur for several reasons.

Phase noise is caused by temporal decorrelation, baseline decorrelation, different Doppler centroids, shadows or low signal to noise ratio and phase undersampling due to steep slopes causing phase gradients to exceed π.

Phase discontinuitites from layover and vertical cliffs lead to phase jumps of multiples of 2π. There are many methods of phase unwrapping, two used by GAMMA are described here.

4.1.7.1 Branch-cut region growing algorithm

This detects inconsistencies in the phase data which cause errors in phase unwrapping. These data regions are isolated and only the phase data which give consistent

estimates are unwrapped. This algorithm has been refined to improve phase unwrapping in regions of high phase noise. In addition, areas of very low degree of coherence are masked to prevent phase unwrapping since the phase values are inaccurate and not useful for estimation of heights or displacements.

4.1.7.2 Minimum cost flow technique and triangular irregular networks

Triangular networks improve the unwrapping by generalising the network topology to be a triangulation network. Minimum cost flow is a global optimisation technique to the phase unwrapping problem. Gaps in the input data; for example locations of very low coherence and the higher density of the triangular network can be considered. Masking, adaptive thinning and patch processing are used to permit efficient and robust unwrapping even of very large interferograms. This algorithm has a small degree of user interaction. It is the method I use here.

4.1.8 Differential SAR Processing

This is the processing required to separate the contributory components of interferometric phase over the interval of the interferogram. These are summarised by the InSAR budget Equation (4.1).

$$\delta\Phi_{int} = \delta\Phi_{geom} + \delta\Phi_{topo} + \delta\Phi_{atm} + \delta\Phi_{noise} + \delta\Phi_{def}, \tag{4.1}$$

where $\delta\Phi$ is the change in phase; 'int' is the integrated value in the resulting inteferogram, 'geom' is that due to viewing geometry, 'atm' the atmospheric delay component, 'topo' the change in elevation, 'noise' due to random thermal pertubations and 'def' due to changes in the ground position. In our case we account for geometry and topography and assume that there is no ground motion. This leaves the differential interferograms represented by the atmospheric delay and noise.

4.1.9 2-Pass Differential Interferometry

For this, the reference interferogram (interferogram with phase corresponding to surface topography) is simulated based on the DEM. The DEM is first transformed from its original co-ordinate system to the reference SAR image co-ordinates. Then a geometric transformation is done based on the available information on the geometry of the DEM and the SAR image geometry used. The SAR image intensity is simulated based on the simulated local pixel resolution and incidence angle. Secondly the offsets between the simulated and real SAR image intensities are estimated

and used to accurately register the transformed DEM to the SAR image geometry. The topographic phase is found, based on the SAR reference geometry, interferometric baseline model and the transformed height map, the unwrapped interferometric phase corresponding exclusively to topography. The topographic phase may be either subtracted from the complex interferogram resulting in a complex differential interferogram or it may be subtracted from the unwrapped phase resulting in the unwrapped differential phase. Note that the complex interferogram does also include the ellipsoidal Earth phase trend, which has to be removed as well.

Using 2-pass differential interferometry the generation of a complex differential interferogram is very robust. The generation of the unwrapped differential phase depends on the capability to unwrap either before or after the reference phase subtraction. Especially in terrain with rugged topography the unwrapping of the differential phase, i.e. after the calculation of the phase difference, may be a much easier task than the unwrapping of the phase image which includes both phase due to topography and differential effects and is the approach I use.

4.1.10 Georeferencing

There are two types of georeferencing used here - forwards and backwards geocoding. In forwards geocoding Universal Transverse Mercator (UTM) coordinates are converted into a radar geometry. This is used with the DEM to create a simulated topographic phase field which can be subtracted from radar imagery. In backward geocoding radar geometry is converted into UTM coordinates. This is used when differential InSAR products are compared with WMM fields.

4.2 Results

4.2.1 InSAR Processing

X-band COSMO-SkyMed interferograms were obtained for two descending pass pairs (6th - 10th December 2014, Figure 4.2b and 10th-14th December 2014, Figure 4.2c) at 21:34 UTC and two ascending pass pairs (2nd - 3rd December 2014, Figure 4.2a and 18th - 19th December 2014, Figure 4.2d) at 9:58 UTC. Table 4.1 gives image details of the COSMO-SkyMed radar acquisitions over Montserrat in December 2014. Table 4.2 gives details of the interferograms produced from the images described in Table 4.1. The InSAR processing was undertaken by GAMMA software. using a 25 m pixel DEM of Montserrat and minimum cost flow unwrapping.

Table 4.1: COSMO-SkyMed radar acquisitions.

Date	Orbit	Mode	IA[2]	Time (UTC)	Image Size [1]	Pixel Size (m)[1]
2nd December	asc	HIMAGE	26.54	9:58	19622 x 21570	1.90 x 2.24
3rd December	asc	HIMAGE	26.54	9:58	19622 x 21570	1.90 x 2.24
6th December	des	HIMAGE	59.26	21:34	13874 x 19838	1.90 x 2.24
10th December	des	HIMAGE	59.26	21:34	13874 x 19838	1.90 x 2.24
14th December	des	HIMAGE	59.26	21:34	13874 x 19838	1.90 x 2.24
18th December	asc	HIMAGE	26.54	9:58	19622 x 21570	1.90 x 2.24
19th December	asc	HIMAGE	26.54	9:58	19622 x 21570	1.90 x 2.24

[1]Range first followed by azimuth (in pixel units).
[2]IA - incidence angle°.

Table 4.2: Inteferogram metrics.

Dates	Orbit	LD°[1][2]	IA°[2]	PB[2] (m)	AA[2] (m)	NL[2]
2nd - 3rd December	asc	79	26.65	241.88	20.0	4x4
6th - 10th December	des	281	59.24	173.85	93.7	4x4
10th - 14th December	des	281	59.24	199.61	81.6	4x4
18th - 19th December	asc	79	26.65	164.92	29.3	4x4

[1]Modulo 360°, 0°=north, 90°=east, 180°=south, 270°=west.
[2]LD - look direction, IA - incidence angle, PB - perpendicular baseline, AA - altitude of ambiguity, NL - number of looks.

4.2.2 InSAR intermediate products

Figure 4.1 illustrates some of the intermediate steps in the processing of the 2014 COSMO-SkyMed 18th-19th December interferogram. Figure 4.1a shows many fringes,

even after flattening due to an altitude of ambiguity of only 29.3 m. Figure 4.1b shows the effects of topographic phase removal, fringes are substantially less numerous ($\sim$ 2) and are of the opposite sense as the topographic fringes on the eastern side of the island. Figure 4.1c shows the coherence mask during this overpass. There are large amounts of incoherence over Centre Hills, in the centre of the island, and South Soufriere Hills, to the south-east of SHV, mainly due to vegetation. The island wide masks obtained from this procedure will be used in Chapter 6 to geocode WMM data. Figure 4.1d shows the unwrapped interferogram in UTM coordinates, the phase of which has been offset by -30 rad and a scale factor of 0.07 applied (before conversion to mm). Delay gradients are greatest over the west of the island.

4.2.3 Differential phase delay

From the 7 satellite passes in Table 4.1, 4 interferograms representing differential atmospheric phase delay and any noise have been produced (note that the 10th December image has been used twice). The interferograms have been masked using the final mask product from Chapter 6. The colour scale has been changed from cyan-magenta-yellow (GAMMA delay colours) to red-green-blue (WMM delay colours) for ease of interpretation. The very different viewing geometries of the ascending and descending interferograms produce very different patterns of incoherence, mainly over Centre Hills and South Soufriere Hills. More incoherence in descending passes is also noticeable in the Belham Valley which runs to the south-west of Centre Hills. There are similar features of opposite polarity in descending passes that arise from them both using 10th December 2014.

The 2nd-3rd December 2014 interferogram shows a strong delay gradient to the west of SHV, Figure 4.2a.

The 6th-10th December 2014 interferogram shown in Figure 4.2b has a band of low atmospheric delay gradient running down the west side of the island. High delay gradient fields are found in the extreme south-west and to the west of Centre Hills.

The 10th-14th December 2014 interferogram shown in Figure 4.2c is comprised of one delay gradient cycle running roughly north-west to south-east along the island where the highest delays run just to the west of the centre of the island. Superimposed on this is the topographic gradient around SHV.

The 18th-19th December 2014 interferogram, Figure 4.2d, shows a north to south band of low delay running up the east side of the island. There are generally higer delays on the west side of the island.

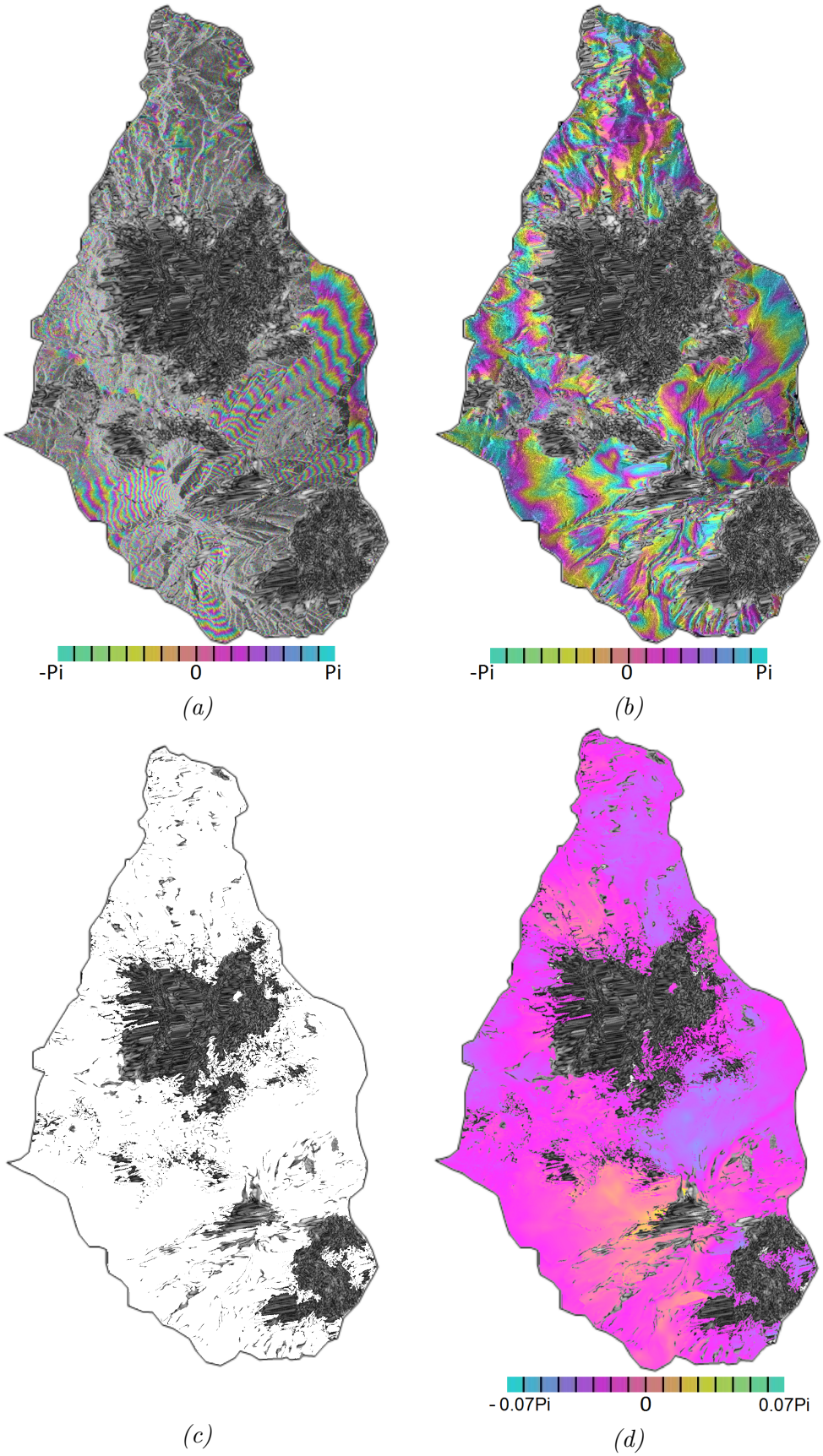

Figure 4.1: 18th December 2014 - 19th December 2014 interferogram processing. (a) flattened wrapped interferogram pre-DEM removal (rad), (b) DEM-removed wrapped interferogram (rad), (c) coherence mask greyscale, (d) unwrapped inteferogram in UTM coordinates, phase delay scale factor of 0.07 and phase offset of -30 rad.

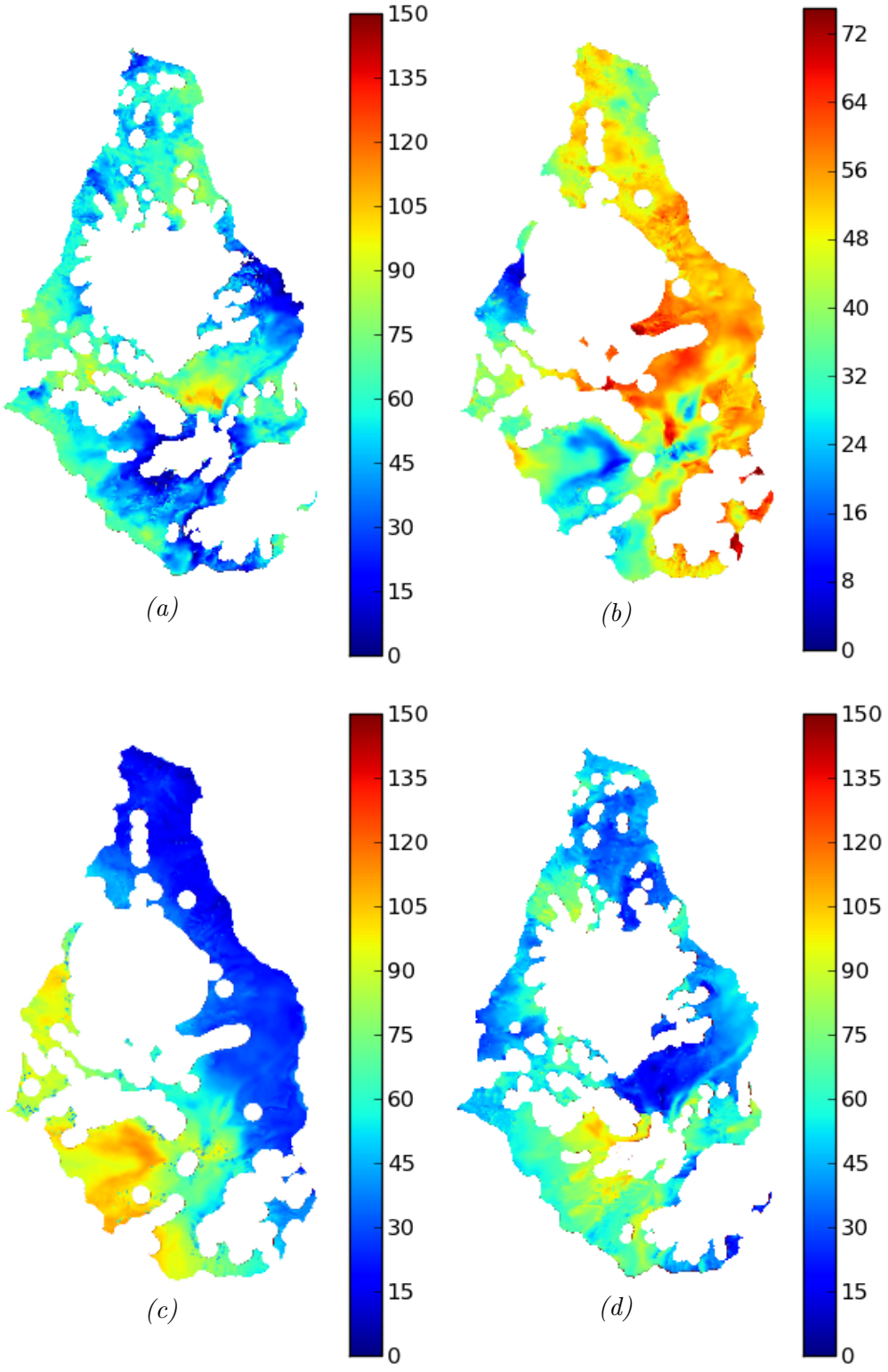

Figure 4.2: Unwrapped inteferograms (mm). (a) 2nd December 2014 - 3rd December 2014, (b) 6th December 2014 - 10th December 2014, (c) 10th December 2014 - 14th December 2014 (d) 18th December 2014 - 19th December 2014.

4.3 Summary of InSAR Processing

GAMMA InSAR software has been used to create differential interferograms for comparison with slantwise WMM data in subsequent chapters. As no deformation was recorded on Montserrat during the 2014 field campaign we can assume all interferometric fringes are due to atmospheric effects. COSMO-SkyMed images from two ascending and two descending passes have been processed and georeferenced for atmospheric correction. Descending passes use a COSMO-SkyMed inclination angle of 59.24° which is at the upper limit for COSMO-SkyMed inclination angle. This means that the descending passes are more likely to be affected by atmospheric delay fields than ascending passes at an inclination angle of 23.26°.

In chapter 6 the resolution of the COSMO-SkyMed images will be decreased in order to match with a WMM grid of 300 m x 300 m horizontal resolution.

Chapter 5

Atmospheric Refractivity and GPS

5.1 Introduction

There are three main contributers to refractivity changes in the lower atmosphere; zenith wet delay (ZWD), hydrostatic delay (HSD) and liquid water delay (LWD), previously shown in Equation (1.1) [Wadge et al., 2010]. In Equation (1.1) I used q_v as the cumulative water vapour in the WMM along a chosen line-of-sight and z_{cu} as the WMM cumulative cloud amount, determined taking into account variable vertical grid spacing in the WMM. Unlike many other properties of the atmosphere, the mixing ratio of water vapour is highly variable in time and space. In this study I use two main ways of calculating the change in refractivity caused by the lower atmosphere (and ignoring ionospheric effects): WMM and GPS. Values of total water vapour content can be found by integrating the 3D values of water vapour mixing ratio along lines-of-sight through the WMM. The WMM model also outputs the cloud mixing ratio, which can be used as a logic test (true/false) in each grid square for liquid water determination. In order to calculate the LWD, we assume clouds around Montserrat are cumulus formed by orographic lifting [Smith et al., 2009] or surface heating convection. This chapter is devoted to explaining the way in which GPS data are used to estimate atmospheric refractivity. It begins with an introduction to GPS calculations of the delay fields and ZWD, and then compares ZWD data from Montserrat with equivalent data from the WMM.

5.1.1 Global Positioning System

The Global Positioning System (GPS) is a constellation of 24 satellites orbiting the Earth and providing accurate location information. Since its inception in 1978 it has been used extensively for military, scientific and commercial purposes. In this thesis I use the GPS data collected by the Montserrat Volcano Observatory (MVO) network to give ZWD measurements.

The distance between GPS satellites and ground-based receivers can be calculated in one of two distinct ways. The first is by measuring the travel time of the GPS signal, from satellite to receiver, and multiplying this by the signal velocity to find the distance travelled. The second is by measuring the phase of the GPS signal received from the satellite and comparing it with the receiver signal to find the phase offset, which is proportional to distance.

The difference between the received signal from a GPS satellite and the receiver's internal clock gives the time or phase difference between the two signals and hence the distance (range) from one satellite to the receiver can be found. By using trilateration from many different satellites, finding the position of the receiver based on the distances from all the satellite transmitters, an accurate position of the receiver can be found. I now discuss the errors affecting the calculation of the receiver position: these are clock errors, ionospheric errors, tropospheric errors and geometry based errors. This is based on [Hofmann-Wellenhof et al., 1993].

5.1.1.1 GPS clock errors

We think of the GPS range as being a pseudorange because each clock, one in the satellite and one in the receiver, is biased due to its own internal error. The pseudorange, R is defined in Equation (5.1).

$$R = \rho + c(\delta t_r - \delta t_s + \delta t_p), \tag{5.1}$$

where ρ is the range, c is the speed of light in a vacuum, δt_r is the range relative to the receiver clock offset, δt_s is the range relative to the satellite clock offset and δ_{tp} is the offset due to other sources, mainly atmospheric in origin. The carrier phase (ϕ_r^s) is the difference between the phase of the signal generated by the GPS receiver at signal reception time and the phase of the satellite-generated carrier signal at transmission time (Equation (5.2)).

$$\phi_r^s = fc\rho_r^s + N_r^s + \frac{f}{c}A_r^s + f\vartheta t_r + f\vartheta t_s, \tag{5.2}$$

where f is the frequency, ρ_r^s is the range between satellite and receiver, N_r^s is the integer ambiguity, A_r^s is the atmospheric error, $f\vartheta t_r$ is the receiver clock offset from GPS time and $f\vartheta t_s$ is the satellite clock offset from GPS time. Single difference measurements still contain receiver clock errors but these errors can be removed by taking the difference between two single differences. To remove satellite and receiver clock errors from Equation (5.2) we construct Equation (5.3) with two receivers (a,b) and two satellites (i,j).

$$\phi^{ij}_{ab} = fc\rho^{ij}_{ab} + N^{ij}_{ab} + \frac{f}{c}A^{ij}_{ab} \tag{5.3}$$

5.1.1.2 Ionospheric delay errors

Dual-frequency GPS transmission (1.2 and 1.6 GHz) eliminates ionospheric refraction common for L-band satellites (Section 1.4). The phase relationship observed at the GPS receiving site assuming a constant frequency, f, is given by Equation (5.4).

$$\phi = f\ t - \frac{d}{c}\ , \tag{5.4}$$

where t is the received time of the GPS signal and d is the distance from the satellite to receiver. When a GPS range is expressed in units of the carrier frequency it is known as a carrier phase. The linear combination of L1 and L2 carrier phases, Φ_{L1} and Φ_{L2} gives a signal with the first order ionospheric component removed (Equation (5.5)).

$$\Phi_{L3} = \Phi_{L1} - \frac{f_{L2}}{f_{L1}}\Phi_{L2}\ , \tag{5.5}$$

where L3 is the resulting phase combination. After this correction the only atmospheric effect left is the delay due to tropospheric water.

5.1.1.3 Antenna phase centre variation errors

The phase centre of an antenna is the electrical point to which the GPS signal is referred and generally is not identical to the geometric centre. Antenna phase centre variations occur as the position of the phase centre varies independently of the position of the geometric centre by as much as 10 cm. This is accounted for in the GPS processing.

5.1.1.4 Earth body tide errors

Earth body tides result from changes in the Earth's mantle, creating changes in the gravitational potential. In low latitude areas the Earth's surface can move by up to 40 cm in 6 hours. This is accounted for in the GPS processing.

5.1.1.5 Multipath errors

Variable reflecting surfaces near to the receiver (e.g. tree growth) can cause non receiver-satellite signals contributing multipath errors with secondary effects from reflections off the satellite. Multipath errors cannot be removed by differencing. By appropriate use of the signal-to-noise ratio and selecting a suitable antenna, they can be identified, reduced and eliminated. The magnitudes of multipath errors are related to the wavelength and in most environments low angle observations are most affected. A cut-off angle of 10° - 20° above the horizon is therefore usually employed. In static applications without tree growth, multipath errors tend to average to zero over long periods of time, so they do not lead to systematic errors. This source of error is ignored for Montserrat. For small islands with large topographic features it is possible that the tropospheric delay component of GPS satellites with low inclination angles may be blocked by topography and the true delay may be offset from another location. We have no evidence of this effect at Montserrat.

5.1.2 Tropospheric delay using GPS software

Section 1.4 detailed the effects of the atmosphere on radar signals.The same effects are relevant to GPS signals.

The GPS signal paths from each satellite are combined to yield a geometric estimate of ZWD. There are several methods of ZWD estimation e.g. Kalman filter or least squares fitting. In the software used by MVO (GAMIT/GlobK), the ZWD is estimated using a piecewise-linear function over the span of satellite observations for each receiver using Equation (5.6).

$$ZTD(\Phi) = ZHD * DMap(\Phi) + ZWD * WMap(\Phi), \tag{5.6}$$

where ZTD is the zenith total delay, Φ is the satellite elevation angle, DMap is the mapping function for dry delay and WMap is the mapping function for wet delay.

The mapping functions are models for the elevation angle dependence of the respective delays and are approximately equal to the cosecant of the elevation angle, although deviations may arise due to the curvature of the earth and path of

the GPS signal through the atmosphere, which we choose to ignore [Saastamoinen, 1972]. The pressure and temperature at each GPS receiver is also required to calculate the refractivity. These values may come from observations or models. The Global Pressure and Temperature (GPT) model is used here. The GPT generates pressure and temperature values based on a spherical harmonic fit to 20 years of meteorological data and is used as an alternative for using the Standard Temperature and Pressure (STP) model [Boehm et al., 2006]. GPT reduces biases in height estimates better than STP. Relative humidity is set to 50% for each calculation. This is a cautious underestimation for Montserrat but large variations can be introduced to the relative humidity without the resulting ZWD becoming affected. The mapping function used for both wet and dry delay is the Global Mapping Function (GMF) which improves upon older mapping functions, which had a latitude and time of year dependence, by including a longitude dependence [Boehm et al., 2006].

In the GAMIT processing, piecewise-linear functions are calcuated with breakpoints every hour (25 per day) and every day starting a new function though this leads to discontinuities between the end of one day and the start of another. To compensate for this the data has been postprocessed using a cubic spline across $\pm$ 3 hours of each day end (00 UTC).

5.1.3 Determination of PWV from ZWD

It is possible to convert ZWD to PWV using a simple linear relationship: $PWV = ZWD/\kappa$, where κ ~6.5-7.0. We can find the conversion factor (κ) using Equation (5.7) [Saastamoinen, 1972].

$$\kappa = 10^6 \left[R_v \frac{k_3}{T_m} + k_2 \right], \tag{5.7}$$

where R_v is the specific gas constant for water vapour, T_m is the mean atmospheric temperature of the path through the atmosphere, and k_3 and k_2 are empirical constants related to the refractivity of moist air.

There is not enough information obtained by each GPS station to estimate T_m and calculate κ in this way and so GAMIT assumes $\kappa = 7.0$. Although this is on the high side it is still within reasonable bounds. Later I find WMM models to produce lower, more reasonable estimates however the sensitivity of this system to κ is not great over the range in question.

5.1.4 GPS and the Montserrat field campaigns

For the 2012, 2013 and 2014 field campaigns ZWD estimates from the dense 14-station Montserrat GPS network shown in Figure 1.4 were provided by Dr. Karen Pascal, deformation scientist, at the Montserrat Volcano Observatory (MVO).

GAMIT/GlobK software, developed and supplied by the Department of Earth Atmospheric and Planetary Sciences, Massachusetts Institute of Technology, was used to produce ZWD values at 30 s intervals for each of the GPS receivers as a point measurement. This software uses a least squares approximation (we cannot assume a Gaussian distribution of ZWD) to determine ZWD (Section 5.1.2).

Kriging is used to interpolate between receiver ZWD values to give a dense, regular spatial mapping across Montserrat. I use the following steps:

- Normalise the site ZWD values to sea-level using a linear fit ZWD lapse rate. Departures from linearity are assumed to be due to lateral variability of delay.
- Interpolate these 14 values of lateral delay to a 25 m grid, call this field A.
- Multiply the elevation values at each pixel of a 25 m posting DEM by the ZWD lapse rate to represent the vertical variability between GPS sites, call this field B.
- Add the fields A and B.

The GPS-ZWD, can be determined for the whole of Montserrat via this process. The GPS-dervived ZWD can be transformed into a value of precipitable water vapour (PWV) and compared with the WMM-ZWD using a κ value of 7.0 (Section 5.1.2).

Changing the GAMIT/GlobK values of relative humidity and temperature produced virtually no change in the GPS water vapour output. At first Kestrel relative humidity, temperature and pressure values were used (taken at Olveston GPS site, Figure 1.4) to calculate GPS derived ZWD values. However it was later found that this method produced unphysical results owing to corrupted Kestrel pressure data and so the GTP model was used to calculate all GPS ZWD values.

5.2 Results of GPS measurements

Discontinuities arise in the GPS data at day boundaries. This is caused by the way in which time is processed in the GAMIT software. The GPS data in the GAMIT software is processed using a six hour time window, three hours either side of the processed measurement. This time window runs on a 24-hour cycle. At day boundaries (24:00 UTC, 00:00 UTC) only the last three hours' worth of data are used, in the case of the preceding day and only the first three hours of GPS data are used in the case of the next day. For all cases a bi-cubic interpolation has been performed across the day boundaries to order to lessen the effects of these discontinuities. However in some cases, characterised by day with low water vapour amounts and followed by a day of high water vapour amounts these discontinuities persist. This is the case when mesoscale systems pass through the region and on these days the GPS data tells us less concerning the absolute magnitude of ZWD amounts and more about the general characteristics of the water vapour signal.

5.2.1 ZWD temporal variability from 2012

The range of ZWD values is between 161 mm and 357 mm, averaged over each 5 minute recording interval, for the whole 2012 recording period. The GPS-determined ZWD values normalised to sea level for the 2012 field campaign are shown in Figure 5.1.

Mesoscale and synoptic scale processes dominate the ZWD plots, with a range of almost 210 mm over two major excursions between 1st and 7th October. There is a qualitative correlation between the highest GPS ZWD concentrations (1st and 4th October) and the arrival of mesoscale cloud systems from the east seen in the MODIS imagery (Sections 3.4.2.3 and 5.3). The dry intrusion (also seen in MODIS imagery on the 3rd October 2012, not presented here) is recognised as a ZWD low of 154 mm. ZWD highs of 350 mm on the 2nd and 4th October 2012 are seen in the GPS signal. There is some evidence of diurnal variation of ZWD. It generally decreases before dawn, showing a strong inflection around dawn (30th September), sometimes as late as 11:00 (8th October), then rising throughout the late morning and early afternoon, flattening off after sunset (6th October). The amplitude of the diurnal cycle varies from about 35 to 70 mm.

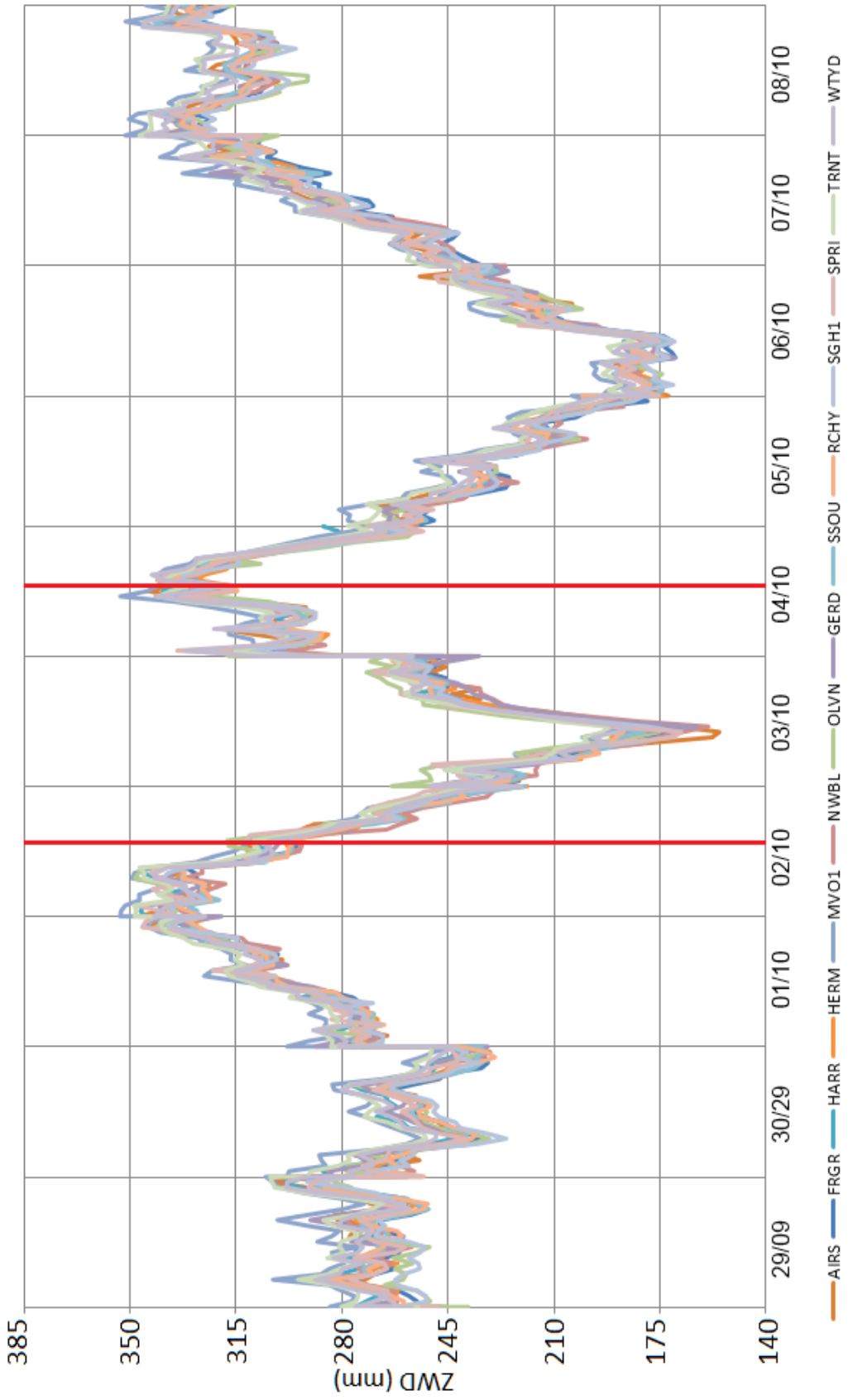

Figure 5.1: Elevation corrected (normalised to sea level) GPS ZWD for the 14 station Montserrat GPS network (Figure 1.4) between 29th September and 8th October 2012. Approximate times of spatial mappings shown by vertical red lines.

5.2.2 Spatial Mapping of ZWD from 2012

Figure 5.2 shows kriged ZWD data at 15:30 UTC on the 2nd October 2012 and 15:10 UTC on 4th October 2012 and using lapse rates of 0.080 $mm\ m^{-1}$ and 0.077 $mm\ m^{-1}$ respectively and the process described in Section 5.1.4. The 2nd corresponds to a mesoscale feature in the region causing moderate to high ZWD measurements shown in Figure 3.24 and the 4th corresponds to higher than average absolute GPS ZWD values of $\sim 315\ mm$ (Figure 5.1 and meteorological data, Table 3.6 and Figure 3.25) due to a high water vapour mesoscale feature in the region.

There is a strong terrain-modulated ZWD GPS signal evident from Figure 5.2 that run south to north with 'low' values of ZWD $\sim 230\ mm$ on the 2nd and ZWD $\sim 265\ mm$ on the 4th. Surrounding this 'zone' on both days the highest ZWD values are $\sim 275\ mm$ on the 2nd and $\sim 315\ mm$ on the 4th.

5.2.2.1 Comparison with WMM

These features are present but overestimated in the WMM ZWD simulations for the 2nd, low ZWD of $\sim 259\ mm$ and high ZWD of $\sim 364\ mm$, with the exception that to the west of the island there is also a low area of ZWD (3.24). These features are present but overestimated in a WMM simulation on the 4th shown in Figure 3.25 where lows of $\sim 315\ mm$ are recorded over the terrain features and highs of $\sim 399\ mm$ are recorded around them. This analysis uses the GAMIT GPS κ value of 7.0 (Section 5.1.2) but even using a lower κ value of 6.1 would result in the WMM overestimating the GPS ZWD values.

5.2.3 ZWD temporal variability from 2013

Figure 5.3 shows the "raw" ZWD values for the 2013 field campaign, not normalised for elevation as was shown in Figure 5.1. For the 2013 data the range of ZWD was found to be between 119 mm and 392 mm. Mesoscale features on the 4th and 5th August are supported by MODIS imagery (Section 3.4.2.3). A dry intrusion on the 4th August 2013 is captured by the WMM and shows up as a low of 168 mm in the GPS signal shown in Figure 5.3.

r

5.2.4 Spatial mapping of ZWD from 2013

Figure 5.4 shows example interpolated ZWD fields from the Montserrat GPS network at 15:10 UTC on 4th August 2013 and 14:20 on the 5th August 2013 and accounting

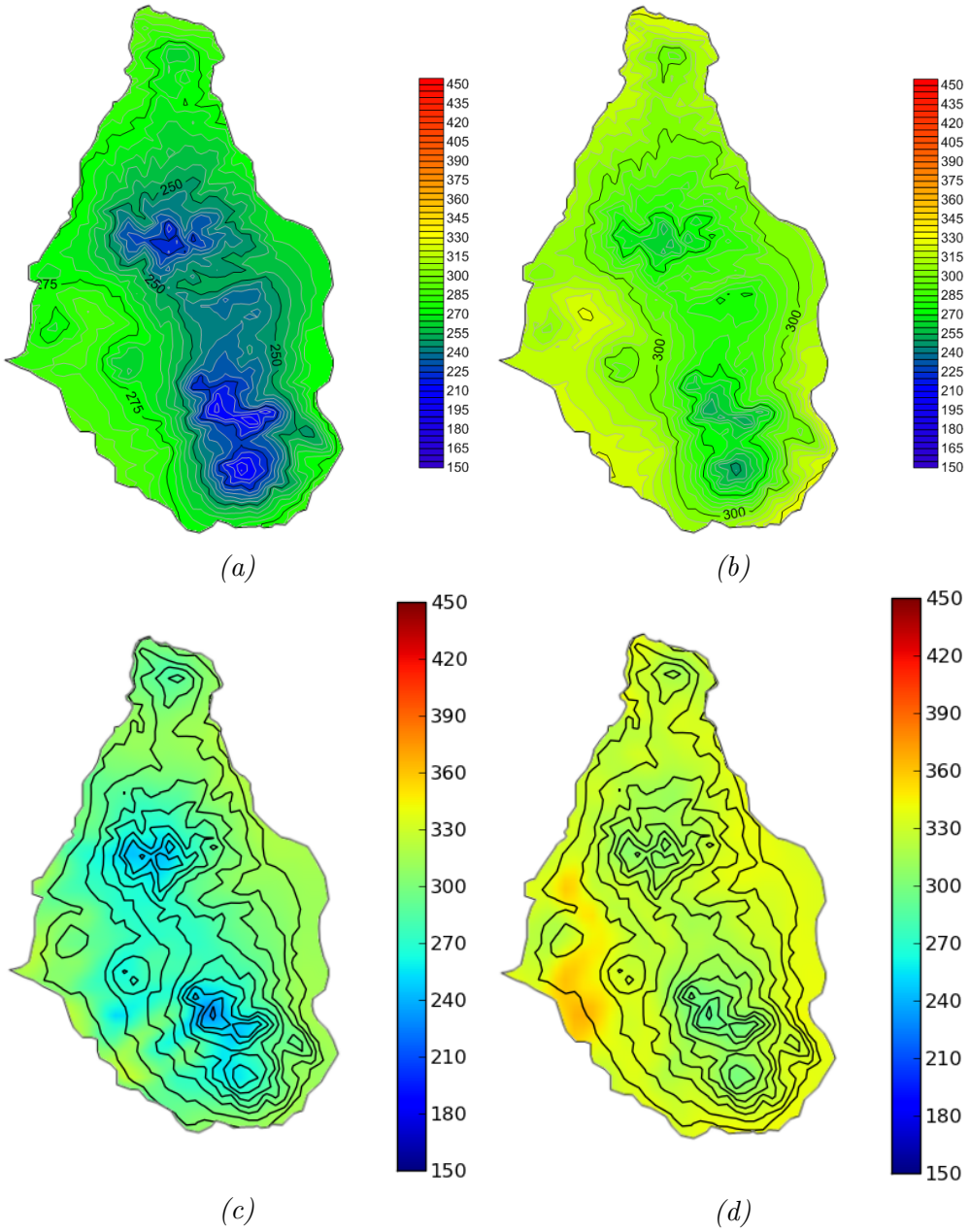

Figure 5.2: Interpolated ZWD fields (mm) determined by 14 station GPS network, Figure 1.4. (a) 2nd October 2012 15:30 UTC. (b) 4th October 2012 15:10 UTC. WMM water vapour cumulative column (mm) model output (c) at 15:30 UTC on 2nd October 2012, Montserrat terrain shown by black contour lines. (d) 15:10 UTC on 4th October 2012.

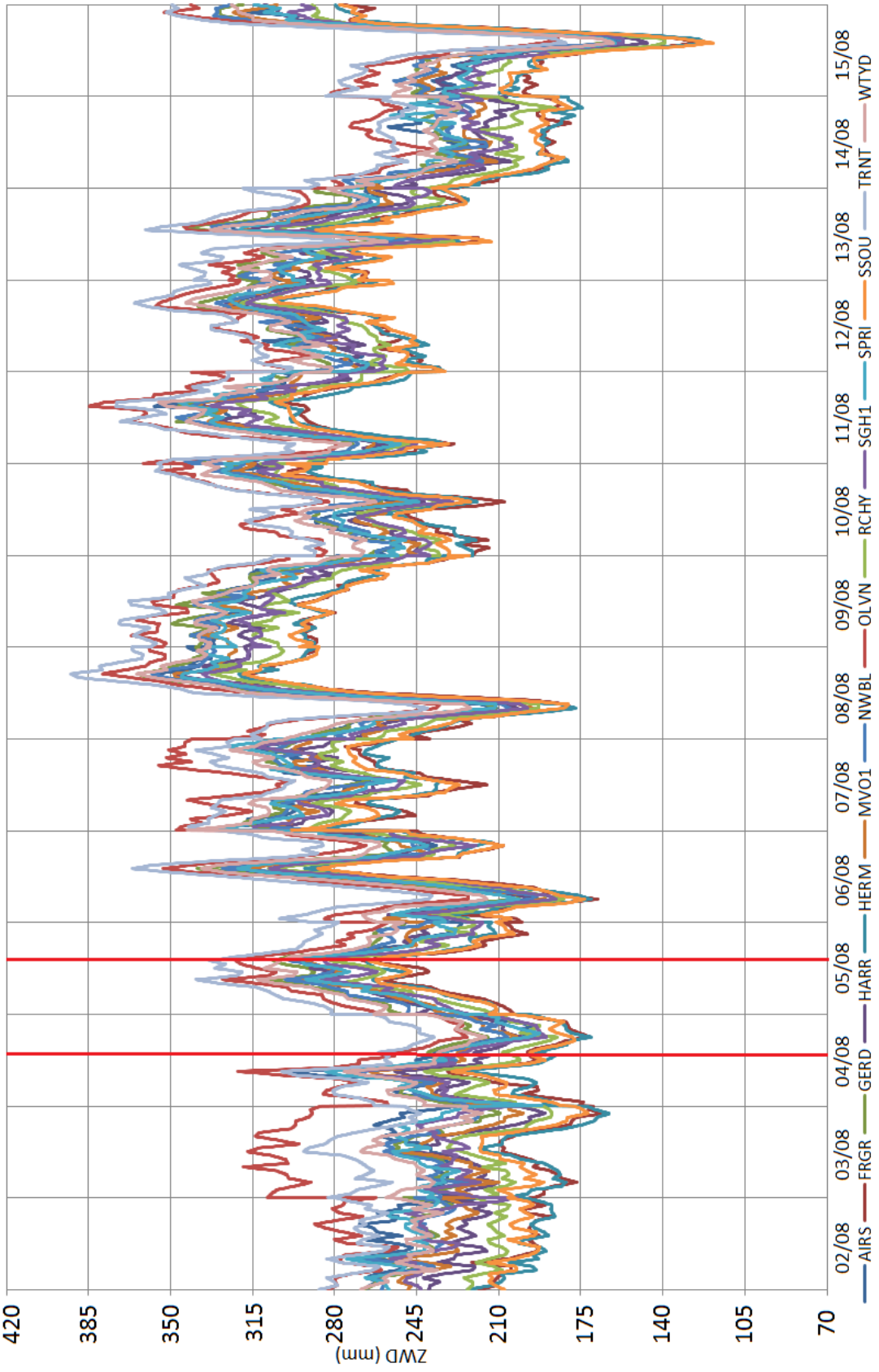

Figure 5.3: GPS ZWD for the 14 station Montserrat GPS network, Figure 1.4, between 2nd August and 15th August 2013 with no elevation correction. Approximate times of spatial mappings shown by vertical red lines.

for lapse rates of 0.080 $mm\ m^{-1}$ and 0.110 $mm\ m^{-1}$ respectively. The first date and time corresponds to lower than average absolute GPS ZWD values of $\sim$ 168 mm, Figure 5.3. Meteorological data, Table 3.7 and Figure 3.26) show that this is due to a dry inclusion in the region. The second date and time correspond to moderate to high average absolute GPS ZWD values upto $\sim$ 329 mm shown in Figure 5.3 and this corresponds well with Figure 3.27 in both description and magnitude.

On both dates there is a very strong degree of terrain modulation, - the main terrain features that run south to north along Montserrat are seen as ZWD lows of $\sim$ 140 mm on the 4th and the same features as $\sim$ 175 mm on the 5th. The east side of Montserrat has high ZWD values of $\sim$ 210 mm on the 4th and $\sim$ 275 mm on the 5th.

5.2.4.1 Comparison with WMM

These features are present but overestimated in a WMM simulation on the 4th shown in Figure 5.4c where ZWD lows of $\sim$ 175 mm are recorded over the terrain features and ZWD highs of $\sim$ 280 mm are recorded to the east of Montserrat. The same is true of the 5th as for the WMM simulation shown in Figure 5.4d ZWD lows of $\sim$ 294 mm are found over terrain in the centre of the island and ZWD highs of $\sim$ 378 mm are found to the west and east of the island. Note that on the 4th there are distinct mountain waves in the lee of the island shown in Figure 5.4c.

5.3 2012 and 2013 MODIS water vapour

The Terra-MODIS 1 km resolution column infrared-derived ZWD product (using a conversion factor of 7.0) can be used to compare against the GPS ZWD for spatial correlation. The GPS ZWD has a higher resolution especially with concern to topography and so should be considered more accurate over the land. Also MODIS is susceptible to cloud cover and contaminated by sub-pixel cumulus. However MODIS still provides good maximum ZWD values to compare with GPS. Figure 5.5 shows the equivalent MODIS ZWD for the dates and nearest times to the 2012 and 2013 case study dates. Due to the early and late times of the 2014 aquisitions there is no MODIS data available at a time close to that of COSMO-SkyMed overpass.

On the 2nd October 2012, MODIS shows $\sim$ 250 mm ZWD which is similar in value to GPS. On 4th October 2012, MODIS shows $\sim$ 315-350 mm ZWD, this is approximately the same or slightly higher than GPS. On 4th August 2013, MODIS shows $\sim$ 50 mm ZWD. On 5th August 2013, MODIS shows $\sim$ 315 mm ZWD, this is $\sim$ 40 mm higher than the GPS average value.

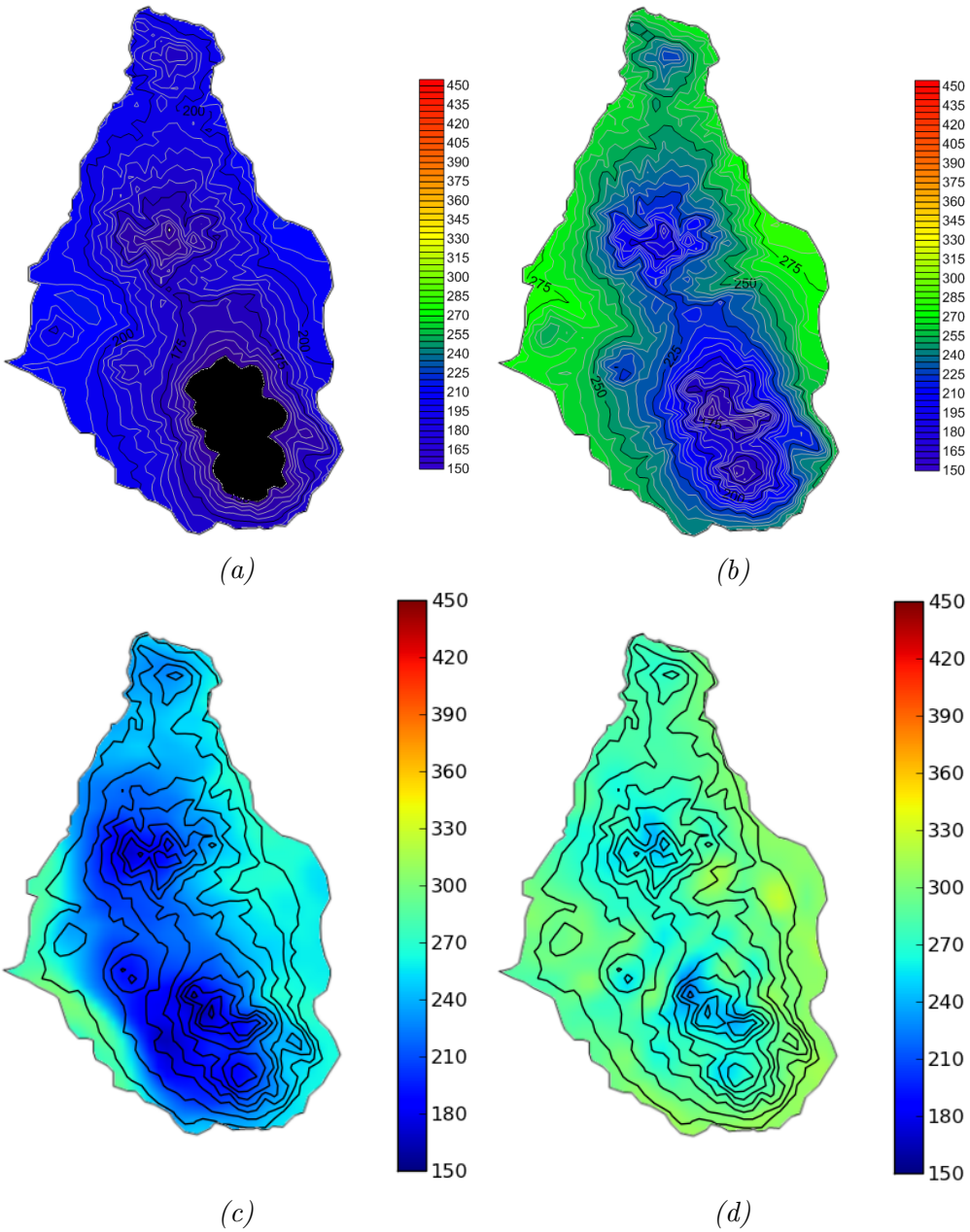

Figure 5.4: Interpolated ZWD fields (mm) determined by 14 station GPS network, Figure 1.4. (a) 4th August 2013 15:10 UTC, values below 150 mm are blacked out. (b) 5th August 2013 14:20 UTC. WMM water vapour cumulative column (mm) model output (c) at 15:10 UTC on 4th August 2013 black fill is less than 150 mm, Montserrat terrain shown by black contour lines. (d) 14:20 UTC on 5th August 2013.

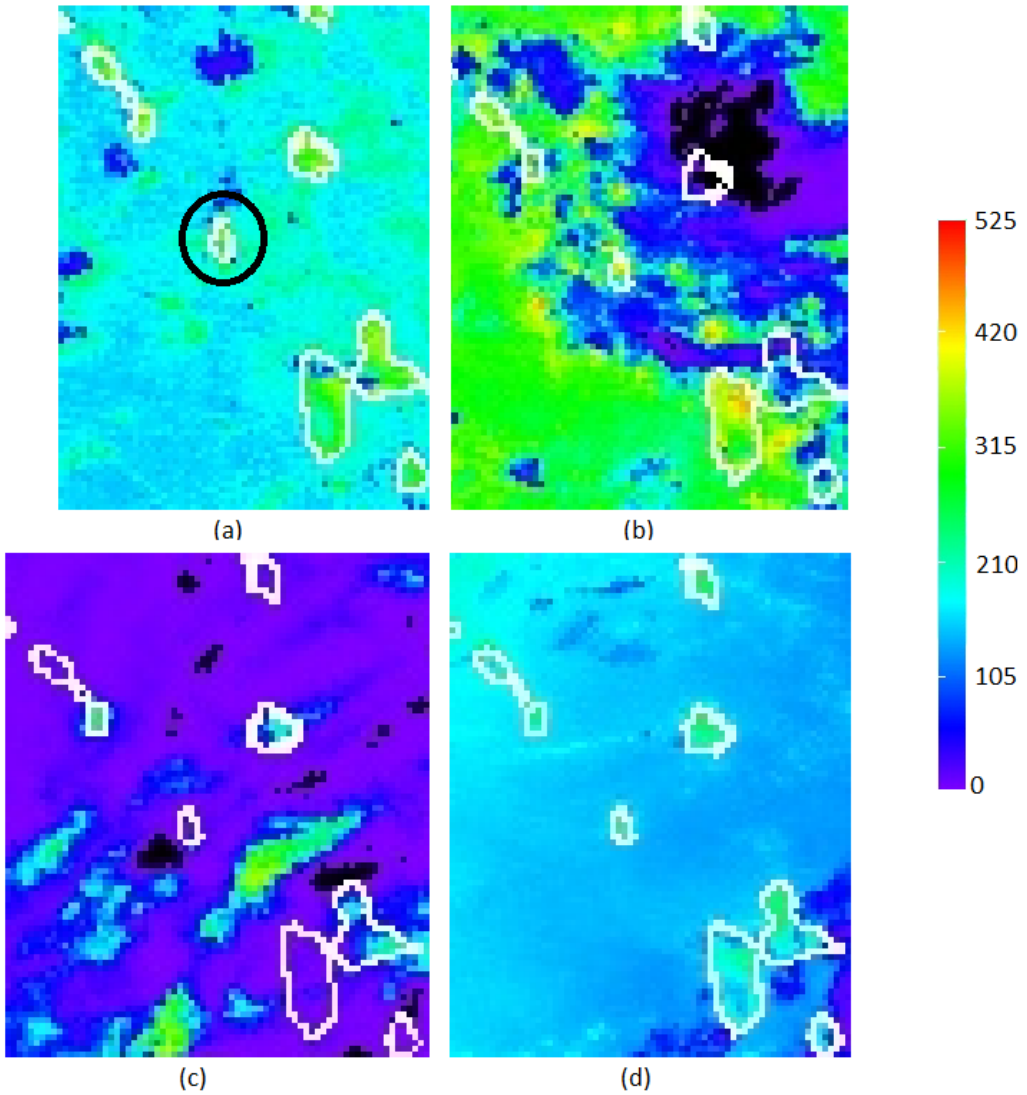

Figure 5.5: Terra-MODIS ZWD (mm). Island outlines in white. (a) 15:25 UTC 2nd October 2012, Montserrat circled in black. (b) 1510 UTC 4th October 2012, (c) 15:10 UTC 4th August 2013, (d) 14:15 UTC 5th August 2013.

5.4 2014 measurement campaign

COSMO-SkyMed radar images were collected during the 2014 field measurement campaign. COSMO-SkyMed overpasses are at specific times (ascending - 9:58 UTC, descending 21:34 UTC) on any given day and were not acquired on all days of the case study. Hence here we will examine the spatial ZWD data at the same time as selected COSMO overpasses - ascending on 2nd, 3rd, 18th and 19th December and descending on 6th, 10th and 14th December (Chapter 4). ZWD lapse rates are needed to normalise GPS data to sea level, calculated as the gradient to the linear fit of all GPS stations with elevation at any given time. These can be found in Table 5.1.

Using Table 3.8, Kestrel weather station data at Olveston GPS site and Guadeloupe rainfall radar data we can build up an idea of the weather conditions during each overpass. For the dates of the COSMO-SkyMed overpasses weather conditions are given by Table 5.1. Figure 5.6 shows mesoscale rainfall recorded near Montserrat on the 18th December 2014 at 10:00 UTC, side from this the rainfall radar didn't show any major precipitation during overpasses.

Climatologically, we expect low pressure and high relative humidity values accompanied by rain during November-December, Figure 3.20 - 3.23. The relative humidity was slightly higher during the overpasses than in the climatology.

The majority of overpass days were characterised by calm conditions, easterly waves with gravity rolls to the west. The exception is the 6th December when the wind direction reversed (to westerly) due to a mesoscale feature to the south.

Table 5.1: Ambient conditions at time of COSMO-SkyMed images.

Date	Pass[1]	Time (UTC)	LR[1] ($mm\ m^{-1}$)	G[2] (°)/ (ms^{-1})	TR[3] (°)/ (ms^{-1})	T ($°C$)[1]	RH (%)[1]	C (Oktas)
2nd December	asc	9:58	0.075	250/2	355/1	24	89	3
3rd December	asc	9:58	0.107	210/11	320/2	24	89	3
6th December	des	21:34	0.097	150/7	10/2	23	90	3
10th December	des	21:34	0.098	350/3	280/2	25	80	7
14th December	des	21:34	0.098	350/3	280/2	25.5	70	7
18th December	asc	9:58	0.095	250/2	180/2	23	83	1
19th December	asc	9:58	0.083	290/6	-	24	78	3

[1] RH - relative humidity, T- temperature, asc - ascending, des - descending, LR - lapse rate, C - cloud cover.
[2] Wind direction / strength at Geralds airport (G).
[3] Wind direction / strength at anemomenter places near TRNT (TR) GPS station, Figure 1.4.

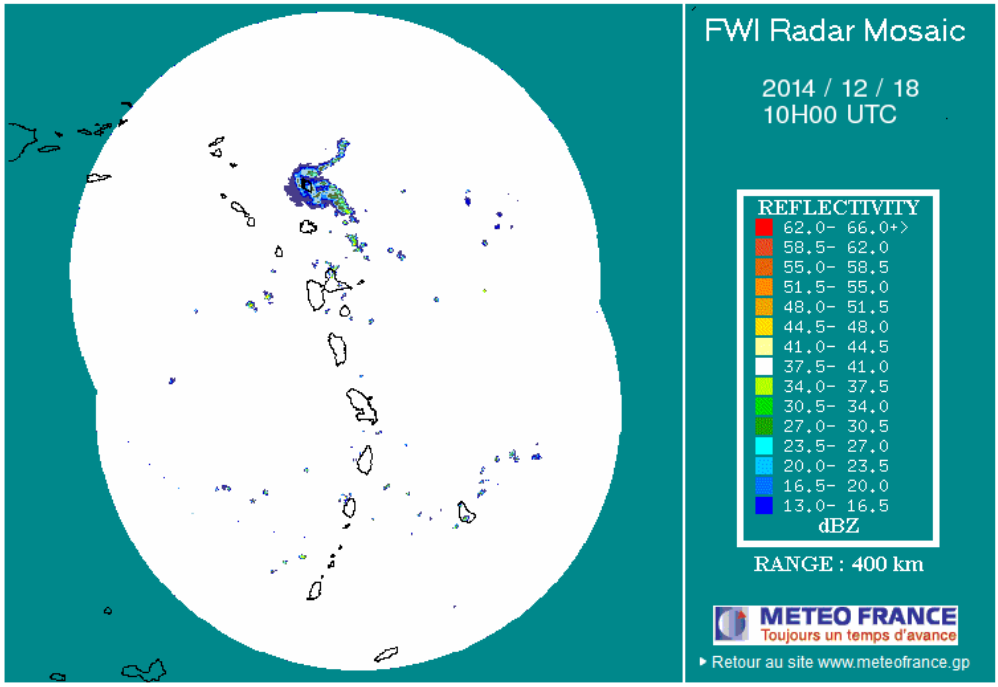

(a)

Figure 5.6: Full Waveform Inversion (FWI) radar mosaic from MeteoFrance Guadeloupe. Outline of islands shown in black and reflectivity colour coded. 10:00 UTC 18th December 2014.

5.4.1 GPS Spatial ZWD delay field

The same procedure as used in Section 5.1.4 was followed to generate the 2014 fields. Table 5.2 illustrates the vertical and horizontal components of these fields. Vertical components are the change in delay lapse rate between the two dates and horizontal components refer to the spatial range of ZWD values after normalisation to sea-level. The 6th-10th December 2014 has virtually no vertical contribution to the field. The 2nd-3rd December 2014 has the highest vertical component to the field.

Table 5.2: Horizontal and vertical GPS-ZWD fields for individual days and interferometric pairs.

Date	V[1] ($mm\ m^{-1}$)	H[1] (mm)	PV[1] ($mm\ m^{-1}$)	PH[1] (mm)
2nd December	0.075	100	0.032	17
3rd December	0.107	117		
6th December	0.097	120	0.001	9
10th December	0.098	111		
10th December	0.098	111	0.002	14
14th December	0.100	97		
18th December	0.095	120	0.013	13
19thDecember	0.083	107		

[1] V - vertical, H- horizontal, PV - pair vertical, PH - pair horizontal.

Spatial GPS-ZWD fields for the 2014 field campaign are compared with WMM-ZWD in Section 6.6.1.

5.5 Inaccuracies in GPS-derived values of ZWD

There are several reasons why GPS-derived ZWD fields might not be accurate. The use of climatological parameters in the ZWD calculation is one source. Also the spatial interpolation of the horizontal component of the ZWD is relatively crude. Two potential sources of inaccuracy are related to the geometry of GPS data aquisition. Firstly, a 10° cutoff angle for the GPS stations means that for those located on hilltops (e.g. St. Georges Hill), water vapour in neighbouring valleys is not measured, leading to a misrepresentation of the lowest, water-vapour rich part of the atmosphere. Ground-based radar interferometry in 2013 revealed typical patterns

of 20 mm of relative delay change above the Belham River Valley in a one hour period, Figure 5.7 [Wadge et al., 2016]. The change in WMM-ZWD from removing

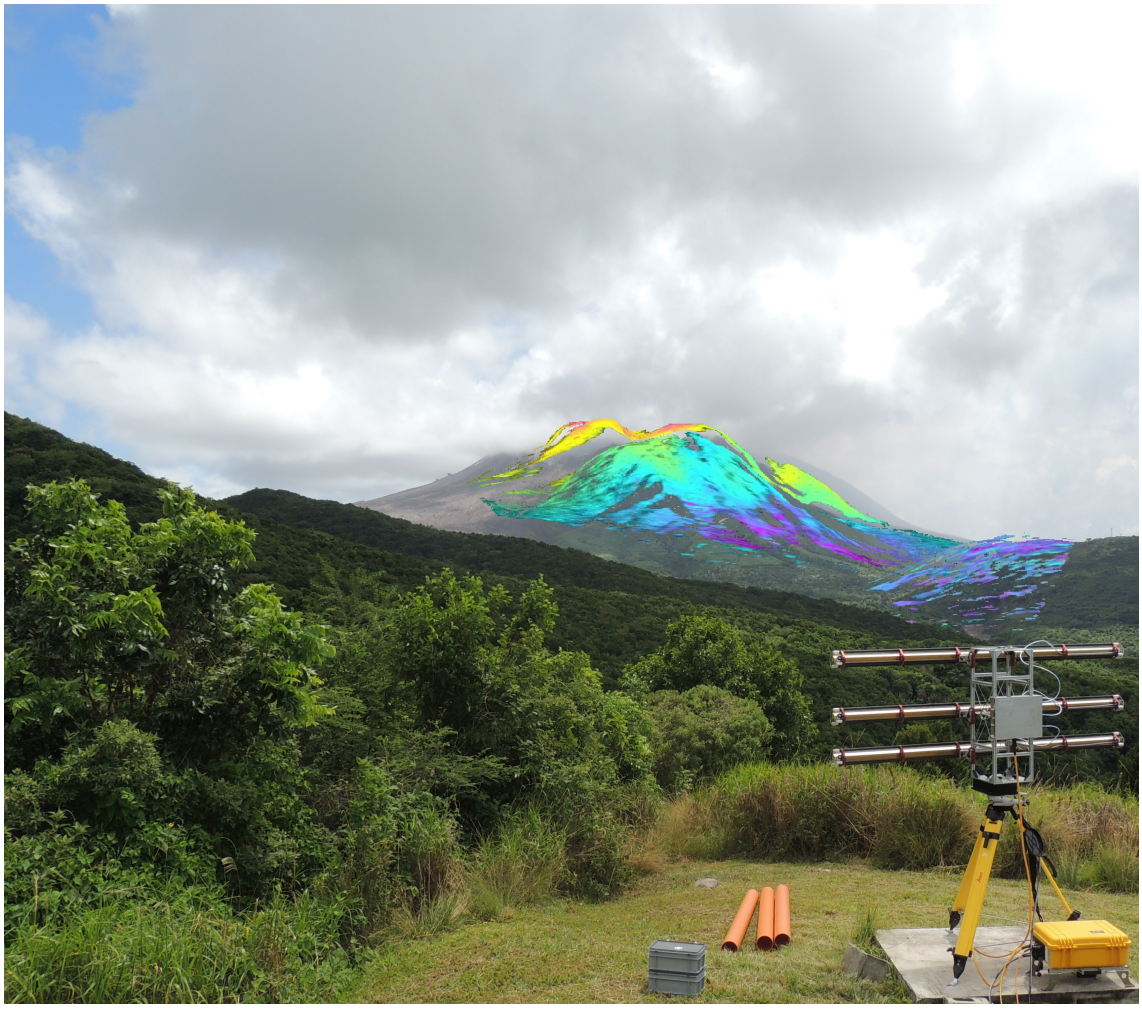

Figure 5.7: Low elevation phase delays measured by ground-based radar between MVO and SHV along the Belham River Valley. Purple to orange represents an increase in phase delay of 21 mm in one hour. Located at MVO on Figure 1.4.

the bottom 1000 m (terrain modulated) of simulation for the 10th December 2014 is shown in Figure 5.8 causing a loss of $\sim$ 160 - 180 mm ZWD. Secondly, each GPS station acquires data from multiple satellites at different positions in the sky around Montserrat. Mountains in the centre of the island tend to block the lines-of-sight from neighbouring, lower GPS sites and thus prevent acquisitions from satellites at low elevations in the east, for GPS stations in the west, and vice versa. For example, GPS stations on the eastern side of the island may not record low-elevation-angle satellites in the west and thus underrepresent the high water vapour fields caused by mountain linear wave formation on the leeside (west) of the island.

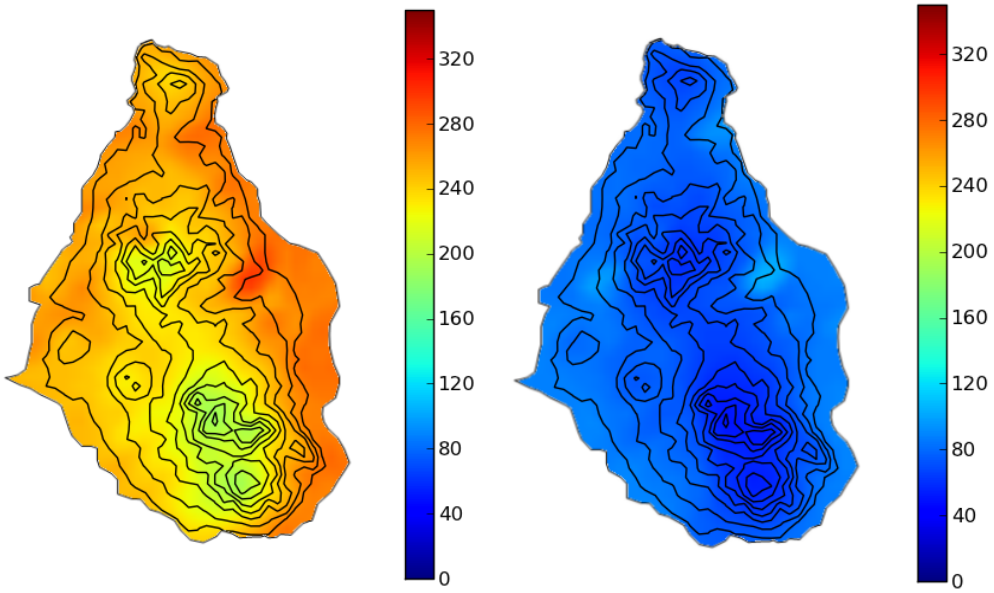

(a) *(b)*

Figure 5.8: Effect of removing vertical levels in WMM. Black lines are contour levels of 100 m. 10th December 2014 at 21:30 UTC. (a) WMM-ZWD (mm). (b) WMM-ZWD (mm) with bottom 1000 m of simulation removed.

5.6 Summary of GPS comparisons

This chapter has described the technique for calculating ZWD and water vapour from the MVO GPS network. Both 2012 and 2013 GPS and WMM data have been compared, citing cases of contrasting meteorological conditions, finding the WMM to be able to simulate key features in the GPS fields:

- GPS-ZWD temporal varibility - slight over an hour time scale of $\sim$ 10 mm across topographic features. This is explained in more detail in Section 6.6.2.
- GPS-ZWD spatial correlation with WMM-ZWD - well matched, mostly capturing onshore WMM features but WMM-ZWD overestimates GPS-ZWD by $\sim$ 30-60 mm.
- GPS-ZWD spatial correlation with MODIS - MODIS provides point values of ZWD $\sim$ 50 mm higher than the highest GPS-ZWD except for on one date where I suspect poor MODIS coverage.

The apparent overestimation of GPS-ZWD values relative to WMM-ZWD may have been caused by geometric or map effects. The GPS-ZWD fields have been compared with MODIS 1 km water vapour products, which usually confirms more water vapour in the area. However the GPS is at higher resolution than the MODIS so we expect a greater range of data.

GPS ZWD for the days of the 2014 InSAR case study from the previous chapter are shown here and these will be used with WMM measurements in the next chapter to explore the WMM as an InSAR atmospheric correction tool. Due to the slant-looking nature of InSAR it is important that water vapour features are placed by WMM in the correct location above Montserrat.

Chapter 6

InSAR Correction

In this chapter I use ray-tracing to calculate slantwise-, liquid water- and hydrostatic-delay fields and use them to correct COSMO-SkyMed data [Hobiger et al., 2008], [Hobiger et al., 2009]. I perform spatial comparison of the GPS and WMM delay fields for the 2014 field campaign.

6.1 Ray-tracing algorithm

Previously, I have looked at column (vertical) integrated variables. However, space-borne radars are side-looking at angles in this case of about 20° to 60° from the vertical. Therefore to simulate the radar path delay, the correct look and azimuth angles need to be used to trace the path through the WMM. For this the Bresenham ray-tracing algorithm has been utilised as it has been a well known solution to the same problem in computer graphics for many decades [Pitteway et al., 1980].

Given a point (y,z), the Bresenham algorithm chooses the z value corresponding to the grid square centre that is closest to the ideal z for the same y, so the z value can remain the same or decrease by 1 on successive y columns, Figure 6.1. In column y, z is given by rounding of Equation (6.1). The slope of the Bresenham ray-trace depends on the start and endpoint coordinates. New endpoint coordinates are repeatedly updated at each subsequent coordinate value to get the next y and z along the ray-trace.

$$z = \frac{(z_1 - z_0)}{(y_1 - y_0)\,(y - y_0)} + z_0 \tag{6.1}$$

Consider the 2-dimensional case shown in Figure 6.1 which shows that the Bresenham algorithm chooses the integer vertical co-ordinate corresponding to the pixel

centre that is closest to the fractional (actual) vertical co-ordinate for the same horizontal co-ordinate, so the vertical co-ordinate can remain the same or decrease by one with each horizontal increment. This technique is implemented until the ray moves from the satellite (represented in Figure 6.1 by grid reference [y,z]=[0,0]) to the Earth's surface (represented in Figure 6.1 by grid reference [5,11]). In this case the ray trace moves through [0,0], [0,1], [1,2], [1,3], [2,4], [2,5], [2,6], [3,7], [3,8], [4,9] and [4,10].

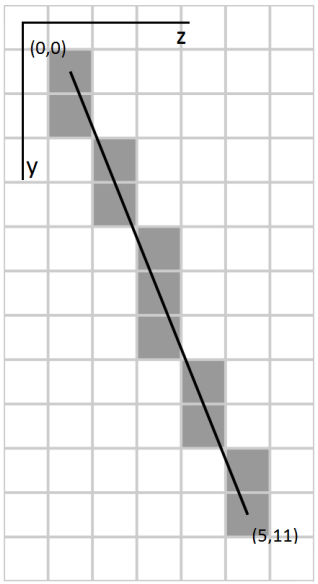

Figure 6.1: Illustration of the principle of Bresenham's line algorithm in 2D.

As applied to WMM, the 2-dimensional case can be expanded into its 3-dimensional counterpart, Figure 6.2. A polar orbiting satellite on a descending path has an azimuth angle of, say, 11° west of south and its path can be accounted for by extending the Breshenham algorithm to the horizontal as well as the vertical dimensions.

An across-track ray mapping is produced for each pixel increment of the WMM. However, consider the case of a 59.24° incidence angle in COSMO-SkyMed descending passes - encountering the most atmospheric delay. As it leaves the satellite the Stripmap HIMAGE H4-24 pulse has a median incidence angle of 51.56°, 51.15° in the near- and 51.98° in the far-range and an altitude of 617 km. By the time it reaches the curving Earth's surface about 1000 km away the 40 km wide swath subtends a median angle of 59.24° with a similar near to far range separation of about 0.8°. Montserrat is approximately a quarter of the width of the COSMO swath - so will only have a difference of incidence angle on land of about 0.2°. 0.2° compared with 59.24° is neglible. For this reason this offset in incidence angle between pixels is ignored.

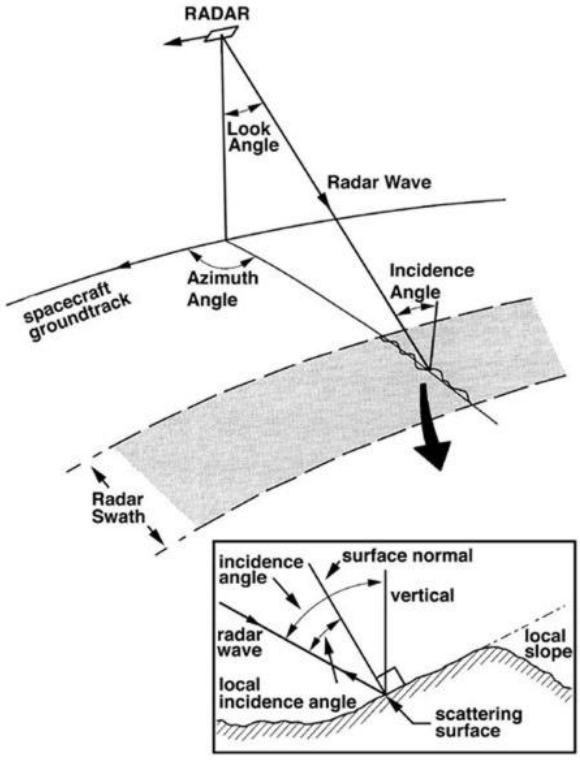

Figure 6.2: Knowledge of both look angle and azimuth angle (spacecraft groundtrack) is required to find the path through a 3D atmospheric volume from satellite to ground e.g. WMM model.

6.1.1 Adapting ray-tracing to the WMM grid

My adaptation of the Bresenham algorithm determines the cells of a 3D array that should be selected in order to form a close approximation to a straight line between two points. I start at the point $(189, 189, 189)$ - the array is a cube so that a movement of 1 in the x-direction is the same as a movement of 1 in the y- or z-direction. The new point I aim to get to (endpoint coordinate) is at $(189, 189 - (189 * tan(yangle)), 189 - (189 * tan(xangle)))$, where yangle is the incidence angle and xangle is the along-track azimuth angle.

In the case of angles greater than 45° this will give a negative coordinate. In principle the Bresenham algorithm can work with negative coordinates but these are not stored for further processing because physically they refer to coordinates outside the WMM domain.

Once the ray-trace has been made in ray-trace coordinates they are converted into WMM coordinates. This is needed because x- and y- dimensions in the WMM are not the same as in the z-dimension. If we consider 189 horizontal grid boxes of 300 m resolution in the WMM, the WMM domain only extends to 67 grid boxes vertically at 300 m resolution. Those 67 vertical grid boxes are split into 50 vertical WMM levels of different heights. Eta levels are normalised from 0 to 1 and for this method to work I multiply them by 67 to get a value between 0 and 67. To avoid counting WMM grid boxes twice I make an array of grid box coordinates that have already been used and allow only those to be used that have not been so before.

6.1.2 Box types in the WMM grid

Owing to the variable vertical grid level height in the WMM, there are three types of grid box which the ray-trace encounters, explained here.

Figure 6.3 shows the incident ray moving through ray-trace- (a) and WMM- (b) coordinates along the zenith and in the slantwise direction. I find the nearest vertical grid box (eta levels) in the WMM to the supplied coordinate from the ray-trace. Figure 6.3b shows for levels near the surface the ray trace may jump several WMM vertical levels because they are small compared to the ray-trace coordinate vertical levels. It was found to be too computationally expensive to make the ray-trace and WMM grids the same.

Figure 6.3b also shows that at the top of the WMM domain horizontally neighbouring grid boxes are accounted for if the ray-trace goes through them. This effect is only present in slantwise ray-traces.

There is a third type of grid box, one in which only one WMM box fits perfectly

into the ray-trace box, this is the simplest case to solve.

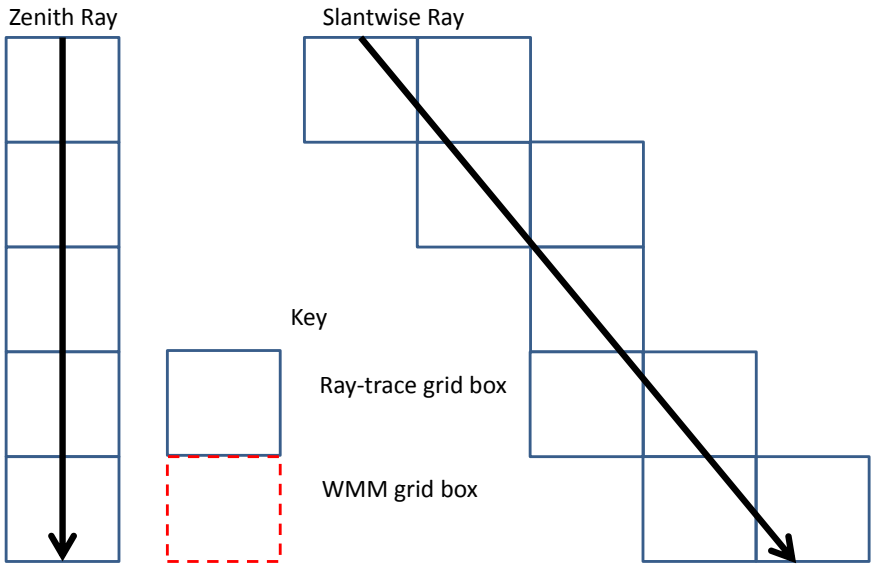

(a)

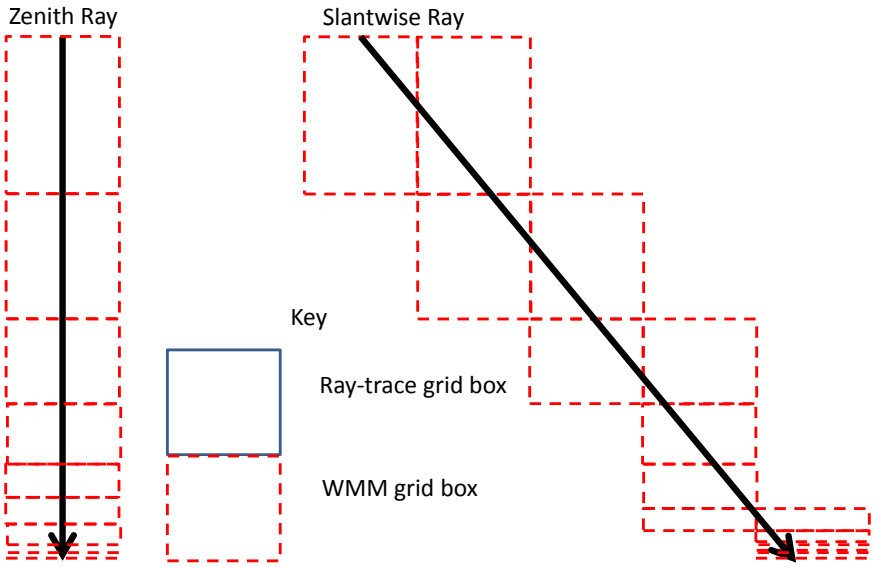

(b)

Figure 6.3: Comparison of grid boxes used. (a) ray tracing, (b) WMM .

It is necessary to find the WMM boxes through which the ray-trace goes but also calculate the increase or decrease in delay seen by each ray-trace in each WMM grid box. In Figure 6.3 the ray-trace may be in one grid box for a very short distance compared with another grid box of similar dimensions. With this in mind each type of WMM grid box is treated differently and described seperately.

6.1.2.1 Close to top of WMM

Close to the top the height of the WMM box is over 300 m and the ray passes through adjacent lateral WMM boxes with different values. The delay in such a box is given by Equation (6.2).

$$d = D\frac{z_b}{cos\,(\phi)}, \tag{6.2}$$

where d is the delay in the box, z_b is the box height, ϕ is the look-angle shown in Figure 6.2 and D is the averaged delay over n boxes; d_1+d_2+.....d_n/n.

6.1.2.2 Close to the surface of the WMM

Close to the ground the height of WMM grid boxes is less than 300 m and multiple boxes are stacked within one Bresenham grid box. The delay in such a box is given by Equation (6.3).

$$d = nD\frac{1}{cos\,(\phi)}. \tag{6.3}$$

6.1.2.3 n=1

This is the special case of both box types where there is one box and either Equation (6.2) or Equation (6.3) can be used.

6.1.2.4 Horizontal and vertical offsets

As WMM boxes get shorter vertically then the ray passes through one or more WMM box in each Bresenham box with fractions of the full path. As all WMM boxes are the same size horizontally, we can find horizontal offsets between subsequent boxes at different vertical levels by taking $z_b/cos(\phi)$ for the previous box on the trace.

6.1.3 Geometric problems

The first ray-trace is saved and used for all other subsequent ray-trace offsets by stepping through the x pixels. If we consider the ray-trace travelling through our [y,z] grid then towards the edges of the WMM domain it is conceivable that we will get ray-tracing coordinates like [0,188], [-1,187]. The second of these coordinates and all other subsequent values with one or more negative coordinate are discarded. We know that most water vapour lies towards the bottom of the troposphere and therefore towards the surface of the WMM (low z values). In Figure 6.4a we can see that ray (1) travels along the original ray-trace, ray (2) is the ray-trace with preferentially lower WMM (and ray-trace) levels sampled, offset horizontally giving ray (3). For descending passes this is the ray-trace we would use, coming from the right to the left. This illustration is in 2- but can be extended to 3-dimensions. In the final image, grid square (0,0) corresponds to the ray trace from point (189,189) to its endpoint.

6.2 Testing the ray-trace geometrically

I now test the ray-tracing using a fictitious box of test values in the field of view of the ray-trace. A ray-trace at a sample incidence angle of 56.16° goes through grid boxes as shown in Figure 6.4b. This shows the horizontal distance over 67 grid squares to be 100 as we would expect. Figure 6.4c shows the same ray-trace in the WMM. It is curved because each WMM grid box is a different height and in this image the grid boxes are all the same size. Evidence of the effect described in Section 6.1.2.1 is present in higher vertical levels and the process described in 6.1.2.2 in lower vertical levels.

In the case shown in Figure 6.5 a 50 x 50 x 50 grid is placed off the centre of a 189 x 189 x 189 domain. The grid cells contain delays of magnitude 1.0, elsewhere there is no delay (0.0).

The 50 x 50 x 50 cube occupies the left half of the domain and we just wish to test the change in magnitude by varying the angle of intersection of the slant ray and each grid cell.

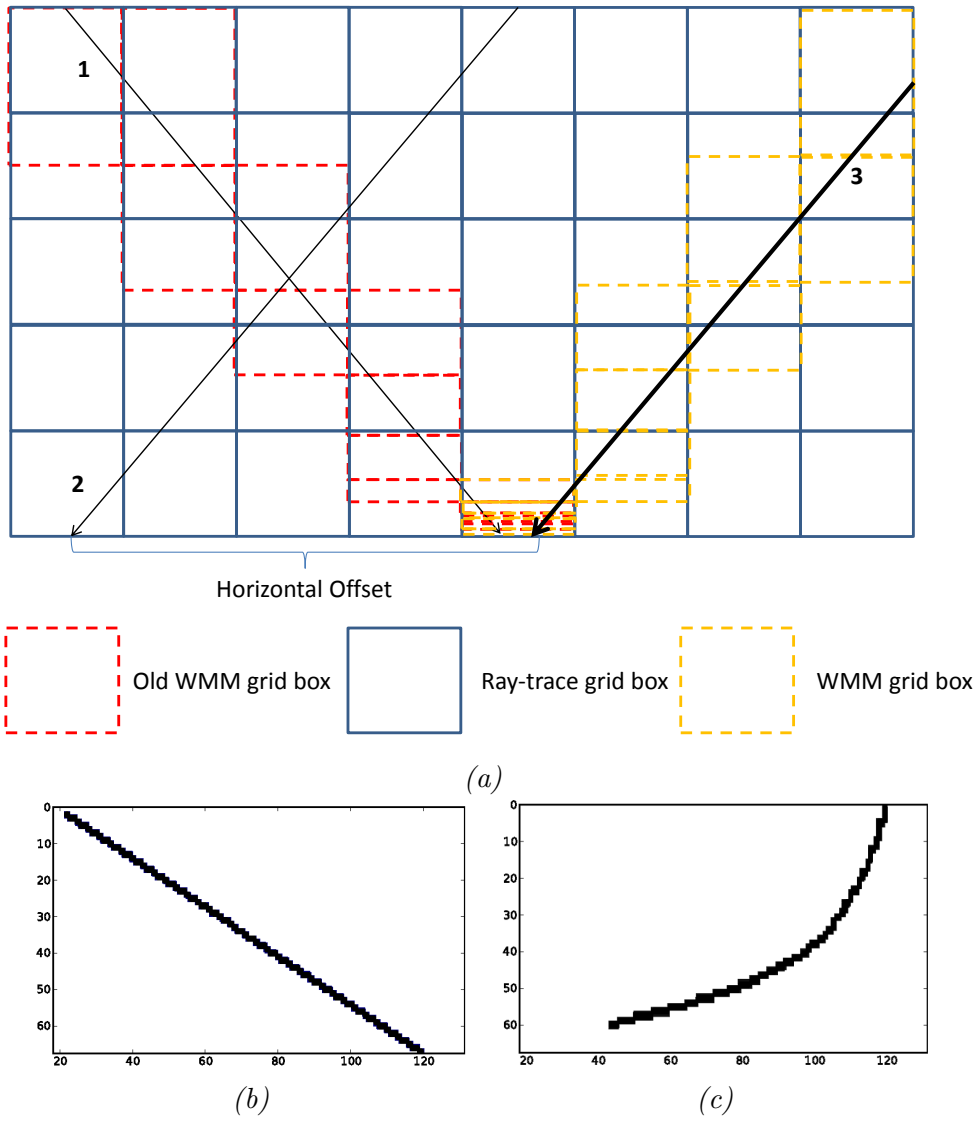

Figure 6.4: (a) Geometric problems. (1) Original ray-trace. (2) Reversal of height. (3) Horizontal offset correction. 2-D ray test - Vertically model levels from 0 to 68 and horizontally grid cells from 20 to 120 (grid voxels). (b) Original ray-trace. (c) WMM equivalent ray-trace.

Test traces at 0° from vertical, Figure 6.5a, and 45° from vertical give the correct magnitudes, Figure 6.5b. In Figure 6.5b the first 50 grid cells do not encounter the box, then we are effectively taking slices up one side of the box and along the top. Notice that the maximum magnitude this slantwise-ray goes up to is 50. This is because the algorithm assumes that the ray-trace occupies the same amount of each grid cell and each ray-trace is essentially summing all the cells along its line of sight. Figure 6.5c shows the equivalent results from a descending pass.

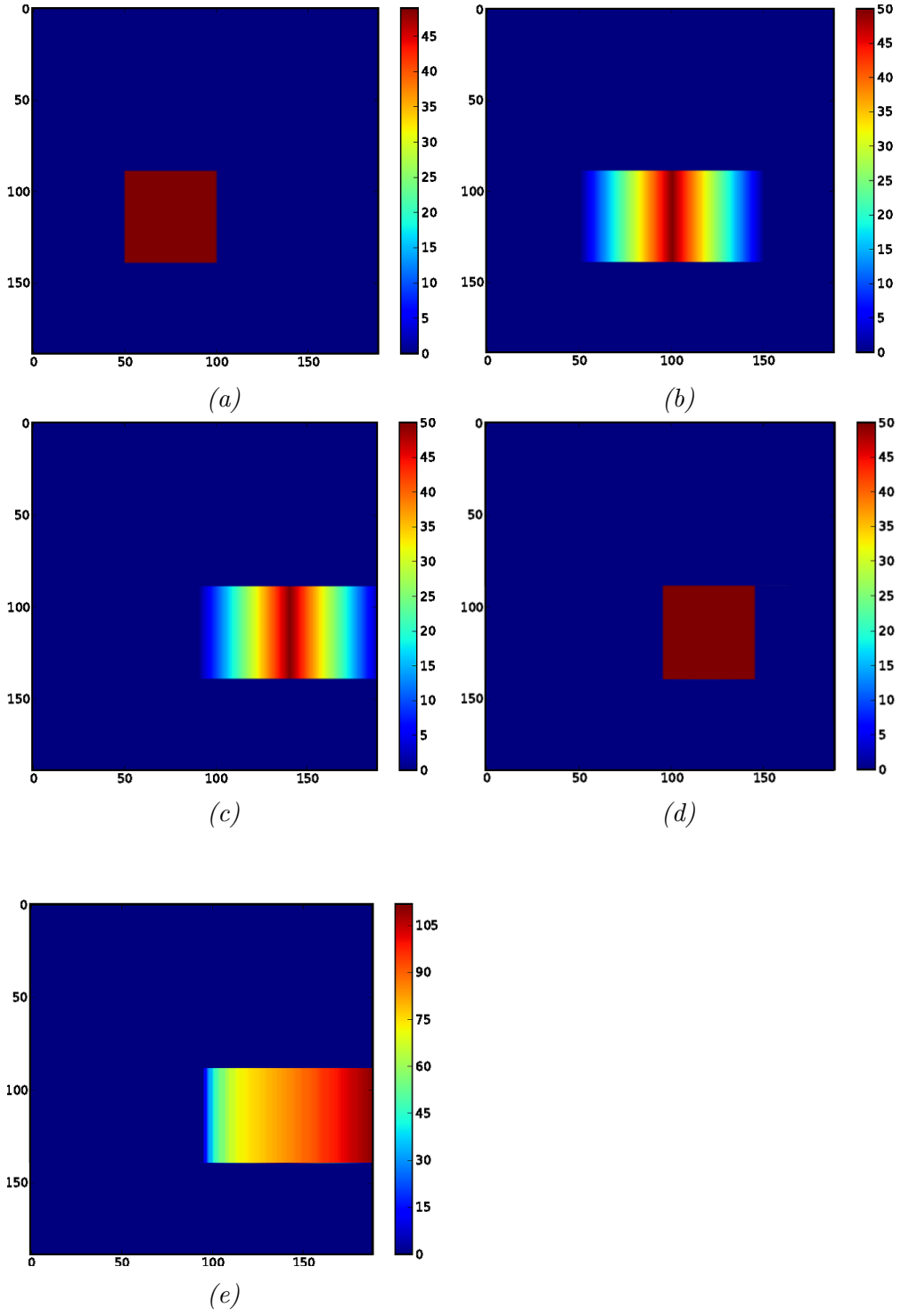

Figure 6.5: Box test. (a) 0° (vertical rays) (b) +45° - ascending (c) -45° - descending. Ray-trace including path-length changes. (d) 0° (vertical rays) (e) 59.24°.

6.2.1 Magnitude and lateral changes

In order to find the correct slant magnitudes we must know the path length the ray takes through each grid box, to this end the WMM grid boxes can be split into the three types described previously.

Figure 6.5d shows the magnitude for zenith ray traces through a box taking up half the domain and to a height of 50 grid boxes. Figure 6.5e shows the same for an example incidence angle of 59.24°. The maximum difference in magnitude is approximately double which is what we would expect.

There are other features present as a result of this algorithm. Levels higher up in the WMM have larger vertical level spacing and so the ray-trace samples their neighbouring grid boxes more frequently. Rays passing either side of the grid box with the higher delay in it, at higher WMM levels, will inadvertantly sample the box with the delay in it. Of course whilst this happens more frequently aloft it also happens nearer the surface on occassion. Also the apparent translation of each delay 'ridge' to the right is proportional to the vertical level. In the case of the WMM grid, because of the variable vertical grid box spacing we have to use (Figure 6.4c) to calculate, analytically, the projected horizontal distance. This is the source of the apparent increase or decrease in the projection distance of ray-traces. Hence when dealing with a WMM-like grid then these delay fields would be translated by amounts proportional to their vertical level.

The tests use a descending pass geometry, for ascending passes the COSMO-SkyMed incidence angle in WMM geometry is 26.65°, producing a ray trace from the west. These same checks have also been applied to the azimuth angle in 3D: for COSMO-SkyMed the ascending look direction is 79° and the descending look direction is 281° and the along track azimuth is 11°.

6.3 Sampling Referencing

The WMM mitigation is performed after sampling the WMM by a factor of 6 to increase its resolution to 50 m whilst decreasing COSMO-SkyMed data to 50 m resolution, then matching the mask image produced by COSMO with the terrain fields used by WMM.

6.4 Water vapour to delay conversion

The output from the WMM is water vapour and liquid water. We require the path delay given by these fields. In Equation (5.7) the average atmospheric temperature is needed to find κ. As this varies slowly over large distances they have been calculated in the zenith rather than along a slant ray-trace. This is a less computationally intensive calculation as grid box changes (Section 6.1.2) are not needed to be taken into account. Thus this conversion is the same as described in Section 5.1.3.

6.5 Results of Delay Constituents

6.5.1 Initial Conditions

Unless otherwise specified, the following results use the 77 km ECMWF truncation (77IC) for their initial conditions. Both the 19 km (19IC) truncation and 77IC agree on mesoscale atmospheric flow patterns although locally the winds across Montserrat were more variable, in the case of 77IC especially sometimes deviating slightly from recorded mesoscale and trade wind conditions.

6.5.2 Hydrostatic delay

The hydrostatic delay (HSD), due to non-water vapour molecules in the air is dependent on zenith temperature and pressure. It varies slowly in space and time. The absolute magnitude of the signal is large but the differential signal is very small. For example Figure 6.6 shows this difference for 18th-19th December 2014 at 10:00 UTC over Montserrat for 19IC and Figure 6.7 for 77IC, reaching maximum values of + 4-6 mm. The stripey signal in Figure 6.6 is caused by local pressure variations. Note that there is more structure seen, albeit small, in the difference field of the 19IC simulation.

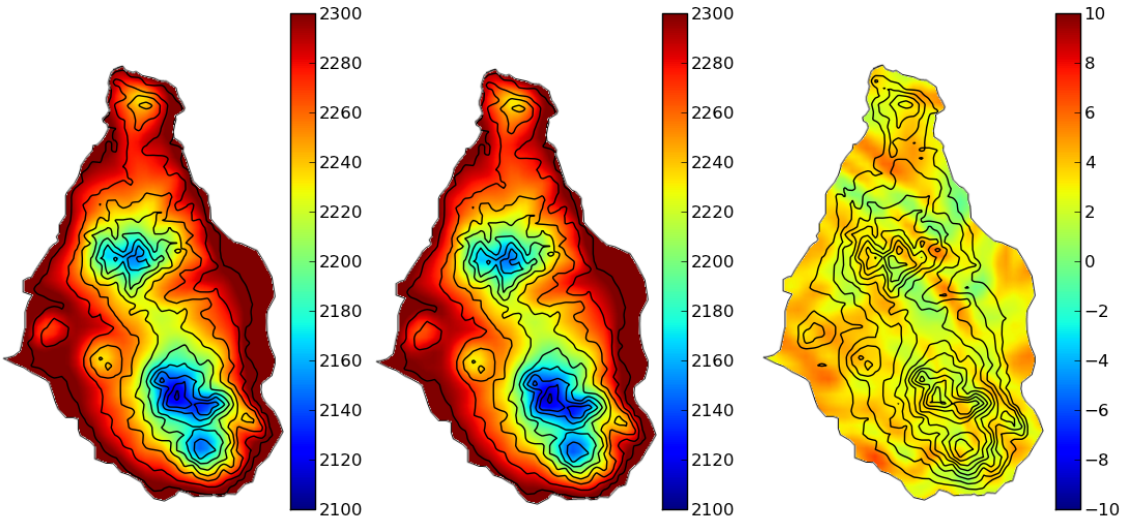

(a) *(b)* *(c)*

Figure 6.6: WMM-computed HSD (mm) at 10:00 UTC from 19IC. (a) HSD for 18th December (mm) 2014. (b) HSD for 19th December (mm) 2014. (c) Change in HSD (mm) 18th-19th December 2014.

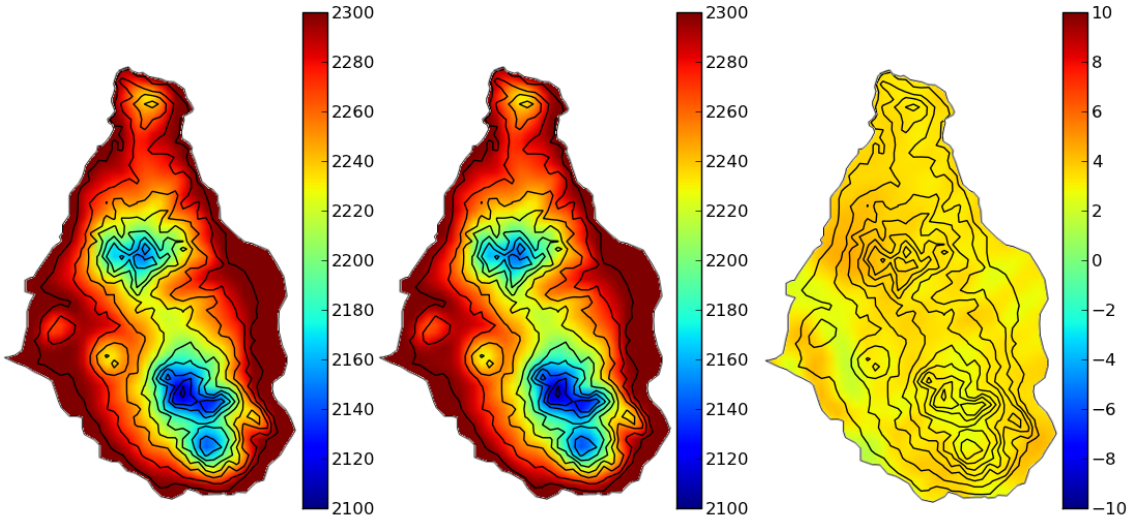

(a) *(b)* *(c)*

Figure 6.7: WMM-computed HSD (mm) at 10:00 UTC from 77IC. (a) HSD for 18th December (mm) 2014. (b) HSD for 19th December (mm) 2014. (c) Change in HSD (mm) 18th-19th December 2014.

6.5.3 Liquid water delay

The liquid water delay (LWD) is calculated from the WMM by summing through grid-boxes of different cloud fraction (0 or 1). Delay associated with different cloud types can be found in Table 1.1, it was assumed all cloud in the WMM was cumulus. For example, Figure 6.8 shows the delay and associated difference for 18th-19th December 2014 at 10:00 UTC for 19IC and Figure 6.9 for 77IC. Between these dates the difference is never more than 3.5 mm for 19IC and 1.5 mm for 77IC. Note that there was no radar detected rainfall over the island at the time of radar aquisition.

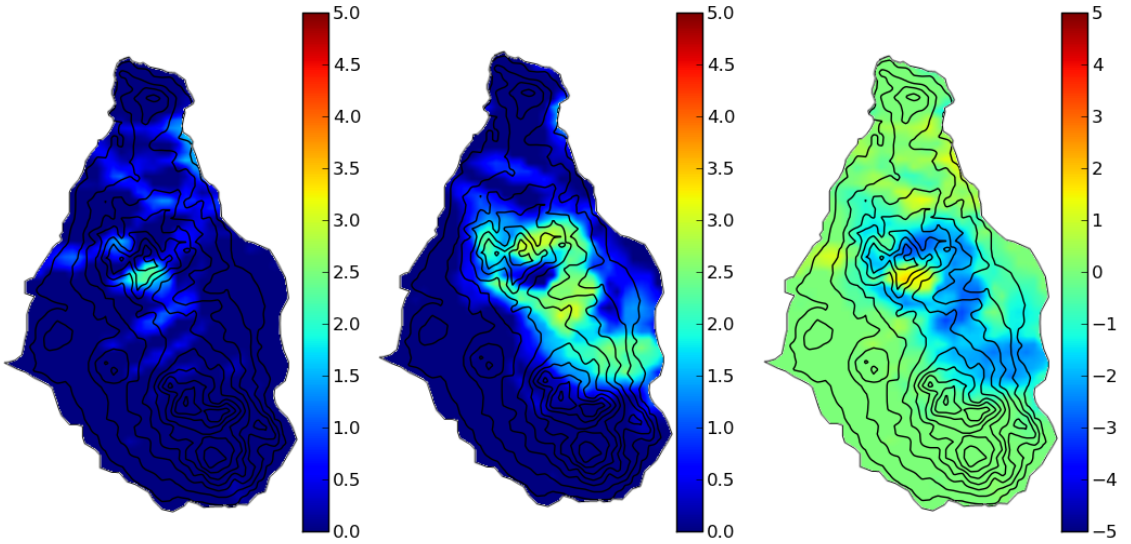

(a) *(b)* *(c)*

Figure 6.8: WMM-computed LWD (mm) at 10:00 UTC from 19IC. (a) LWD for 18th December (mm) 2014. (b) LWD for 19th December (mm) 2014. (c) Change in LWD (mm) 18th-19th December 2014.

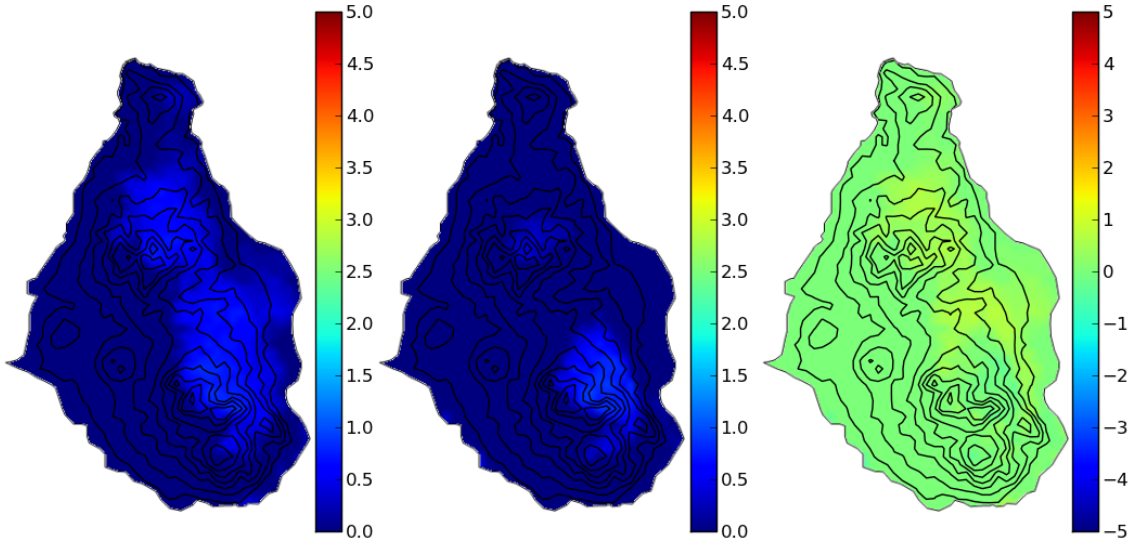

(a) *(b)* *(c)*

Figure 6.9: WMM-computed LWD (mm) at 10:00 UTC from 77IC. (a) LWD for 18th December (mm) 2014. (b) LWD for 19th December (mm) 2014. (c) Change in LWD (mm) 18th-19th December 2014.

6.6 ZWD from WMM

WMM-PWV values have been converted into ZWD on all the dates of the 2014 field study using conversion factors (κ) of $\sim$ 6.14 - 6.15 which were found from average temperature profiles.

6.6.1 Comparison of zenith difference delays for WMM and GPS in 2014

A comparison of these two zenith fields is made for the four interferogram intervals in December 2014 (Figures 6.10 - 6.13). Asides from the 77IC 10th-14th December 2014 the WMM-ZWD shows the same sense of delay difference as the GPS-ZWD. The WMM-ZWD shows less obvious stratified (terrain-modulated) structure but tend to show a gradient on the southwestern slopes of SHV. One possible cause of the differences seen is the temporal fit of the WMM simulation to the GPS data. For example if there are lateral tropospheric gradients. There is a clear east-west gradient present in the GPS-ZWD for the dates and times of descending passes. In comparison the GPS-ZWD for dates and times of ascending passes have much higher differentials in delay lapse rate than those of the ascending passes. So the GPS-ZWD for descending passes have much more 'topography' evident relative to the ascending passes.

6.6.1.1 2nd December 2014 -3rd December 2014

The differential delay from GPS-ZWD shown in Figure 6.10 is clearly modified by terrain in agreement with results from Chapter 4, highs of 35 mm are found over SHV ranging to lows of -2 mm along the west and north coasts. The WMM-ZWD 77IC field is broadly similar and has lows of -12 mm to the west and south-west and highs of 48 mm to the south-east. The WMM-ZWD 19IC field has highs to the south-west of 15 mm and lows to the east of -15 mm.

6.6.1.2 6th December 2014 - 10th December 2014

The GPS-ZWD field has a small negative gradient from -37.5 mm to -45 mm running east-west over Montserrat with little terrain modulation, Figure 6.11. The WMM-ZWD 77IC has a similar distribution of ZWD but with a much greater magnitude between 43 mm on the west and -60 mm on the east. The WMM-ZWD 19IC has an area of low delay of -35 mm in the north, elsewhere the pattern is generally similar to the GPS-ZWD but with slightly higher magnitudes between 15 mm in the west and -15 mm in the east.

6.6.1.3 10th December 2014 - 14th December 2014

The GPS-ZWD field has an northeast-southwest gradient from 35 mm in the north to 50 mm in the south with little terrain modulation, Figure 6.12. The WMM-ZWD 77IC field shows a reversal of this gradient from 60 mm in the north to -18 mm in

the south, though, like the GPS field it is dominated by positive values. The WMM-ZWD 19IC shows a general north-south gradient like the GPS-ZWD, -15 mm in the north to 30 mm in the south (asides from a high point of 40 mm in the north-west). Note that on 14th December 2014 (slave) there was lower wind strengths recorded in the WMM with 77IC and 19IC (although in the latter case the wind direction changed to blow more from the south) than on the 10th December 2014 (master). It is reasonable to assume that high delay in the east and low delay is the west for 77IC is partly controlled by by the higher wind strengths from the 10th December 2014. It is also reasonable to assume that the changes of direction of the wind, locally, away from the normal trade winds, resulted in the 19IC gradient becoming weaker than the 77IC gradient.

6.6.1.4 18th December 2014 - 19th December 2014

The GPS-ZWD field shows evidence of terrain structures, lows of 23 mm at SHV to highs of 42 mm to the east, Figure 6.13. WMM-ZWD 77IC has highs of 16 mm over most of Montserrat and lows of -12 mm to the south and south-west. WMM-ZWD 19IC shows similar evidence of terrain to that of GPS-ZWD but with different magnitudes, lows of -60 mm at SHV to highs of 0 mm to the east.

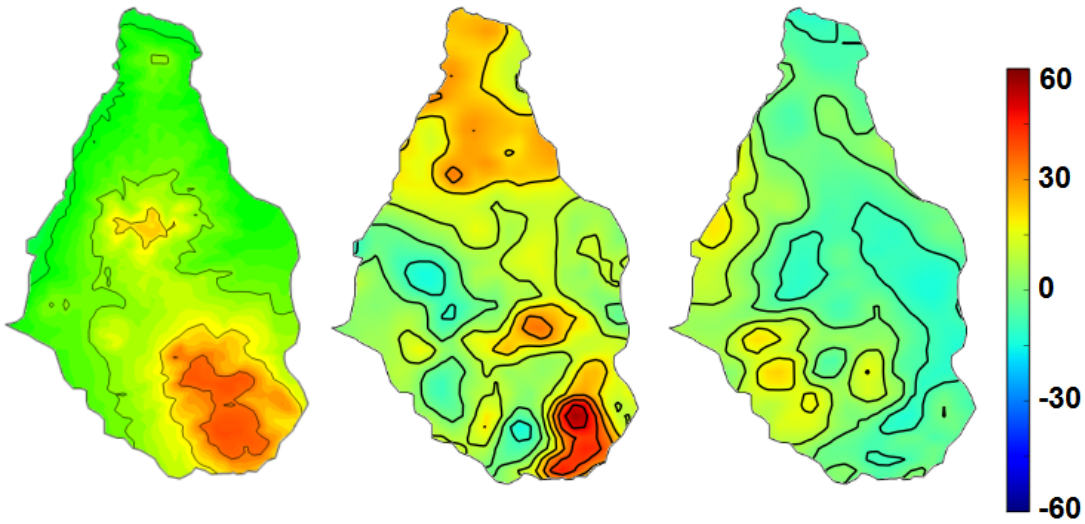

(a) *(b)* *(c)*

Figure 6.10: Change in ZWD (2nd December 2014 - 3rd December 2014 at 10:00 UTC) mm, contour intervals every 12 mm unless stated. (a) GPS - contours every 5 mm. (b) WMM from 77IC. (c) WMM from 19IC.

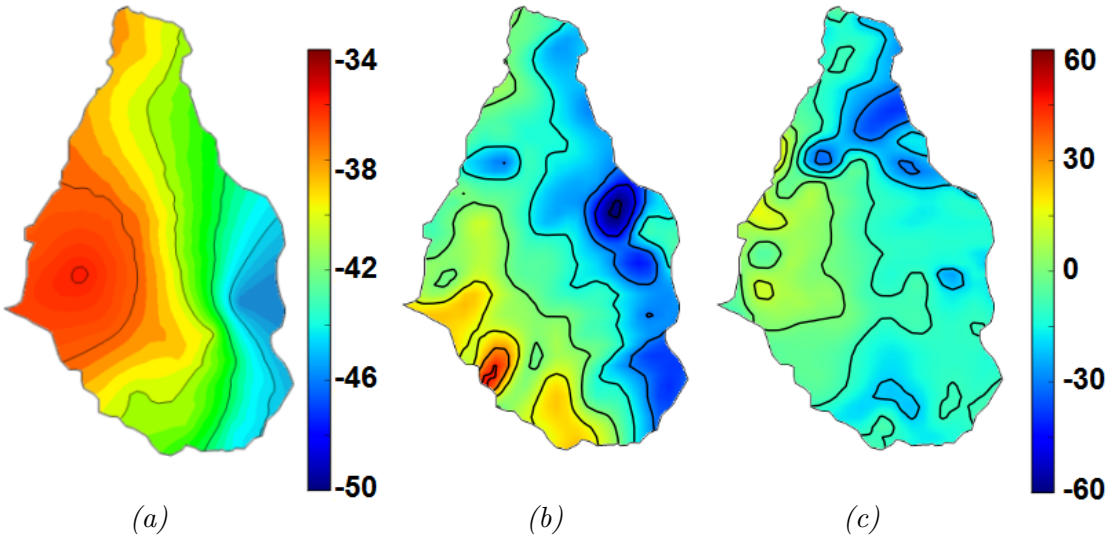

Figure 6.11: Change in ZWD (6th December 2014 - 10th December 2014 at 21:30 UTC) mm, contour intervals every 12 mm unless stated. (a) GPS - contours every 5 mm. (b) WMM from 77IC. (c) WMM from 19IC.

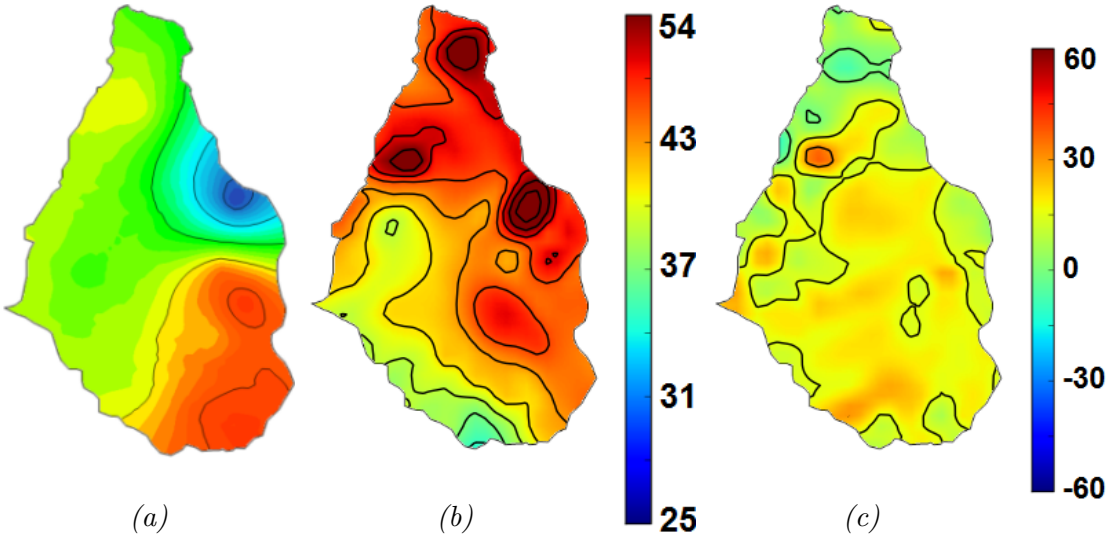

Figure 6.12: Change in ZWD (10th December 2014 - 14th December 2014 at 21:30 UTC) mm, contour intervals every 12 mm unless stated. (a) GPS - contours every 5 mm. (b) WMM from 77IC. (c) WMM from 19IC.

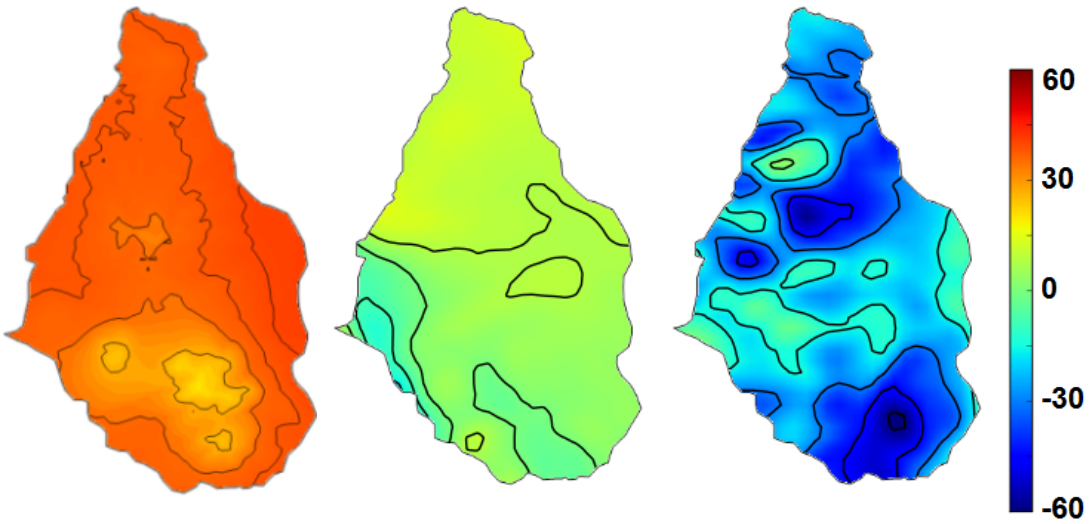

(a) *(b)* *(c)*

Figure 6.13: Change in ZWD (18th December 2014 - 19th December 2014 at 10:00 UTC) mm, contour intervals every 12 mm unless stated. (a) GPS - contours every 5 mm. (b) WMM from 77IC. (c) WMM from 19IC.

6.6.2 Temporal fit of GPS- and WMM-ZWD

Both the GPS and WMM data sets permit a time series of results to be calculated. Here we show how variable the resultant ZWD delay fields are over six, ten-minute intervals.

Figure 6.14 shows the temporal variability in WMM-ZWD for 10th December 2014 between 21:10 UTC and 22:00 UTC (77IC). This brackets a COSMO-SkyMed overpass at 21:34 UTC. The topographic component of the signal is evident around the terrain. A mesoscale feature advects to the north-west throughout the hour. On Montserrat the varibility ranges from 320 mm (21:10 UTC) on the east of the island to 175 mm (21:30 UTC) over SHV.

Figures 6.15 (19IC) and 6.16 (77IC) shows the temporal variability in WMM-ZWD around Montserrat for 10th December 2014 between 21:10 UTC and 22:00 UTC. There is a large topographic component to the WMM signal. 19IC and 77IC show slight variations at each time but a similar general pattern. Using the 21:30 UTC output as a measure for 21:34 UTC output rather than 21:40 UTC output would not greatly effect the results because there is little difference in the WRF model output over the island during this time (for both 19IC and 77IC) .

Figure 6.17 shows the temporal variability in GPS-ZWD for 10th December betweem 21:10 UTC and 22:00 UTC. The topographic component is strongest at 22:00 UTC and weakest at 21:10 UTC. The across-island change is small but noticeable across the hour. The variability changes from 240 mm (21:40, 21:50 and 22:00 UTC) on the east of the island to 110 mm (21:10 UTC) over SHV. In comparison with Figure 6.16 the GPS-ZWD usually has lower overall values in the same locations as the WMM and similar maximum values in the same locations as the WMM. The 21:30 UTC GPS-ZWD map fits well to the 21:10 UTC WMM-ZWD map which captures the lower ZWD over the hills to the west of SHV. However the 21:10 UTC WMM-ZWD also displays high values to the south of SHV and along the north-west coast which are not present in the GPS-ZWD at 21:30 UTC. 21:30 UTC WMM-ZWD captures the general contours of GPS-ZWD at 21:30 UTC and does not has the high ZWD in the correct locations. Therefore this time is the best qualitative fit between the two datasets.

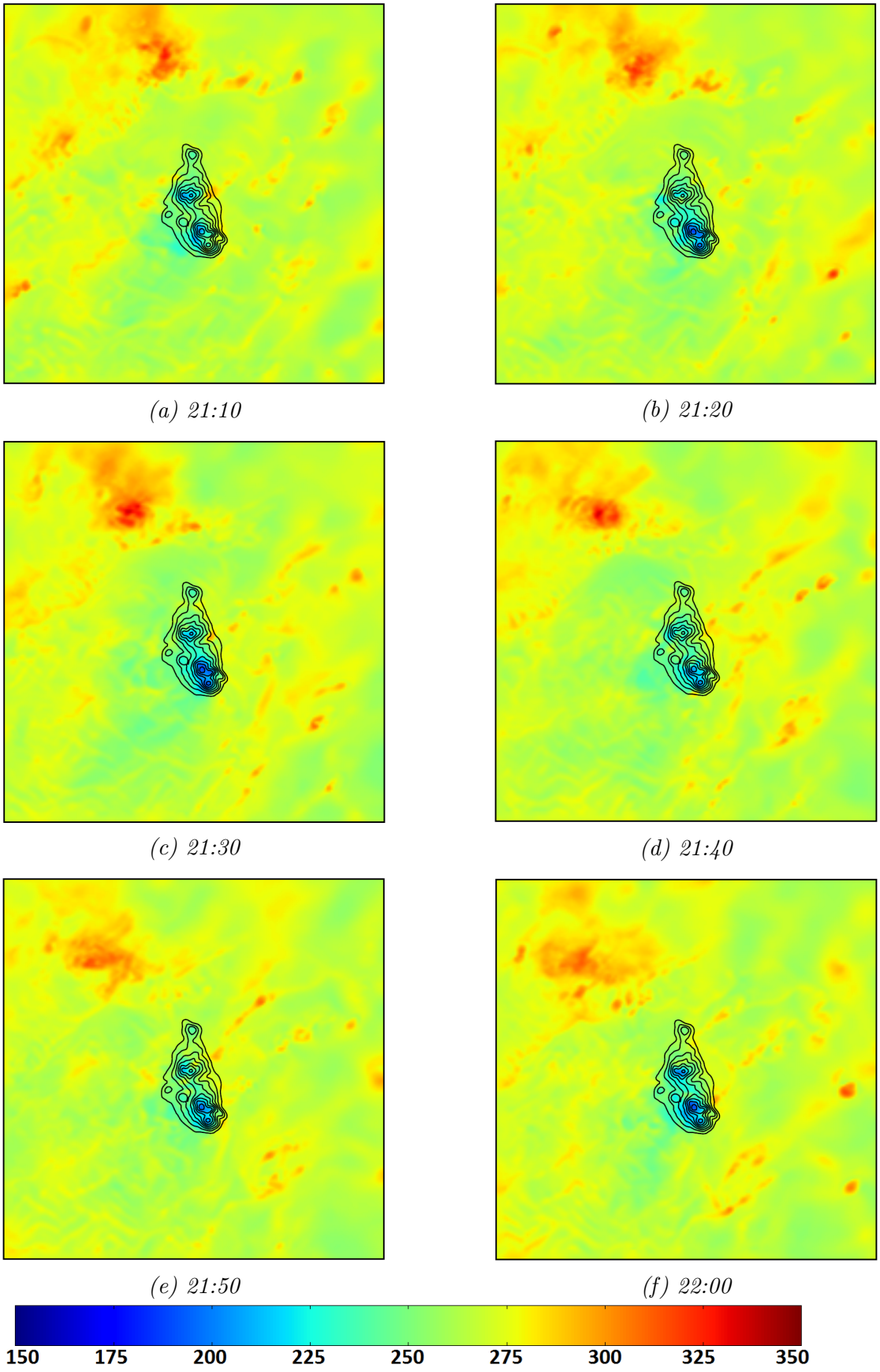

(a) 21:10 *(b) 21:20*

(c) 21:30 *(d) 21:40*

(e) 21:50 *(f) 22:00*

Figure 6.14: WMM-ZWD (mm) for 77IC: 10th December 2014, 21:10 UTC - 22:00 UTC. Black contour lines every 100 m indicate terrain features.

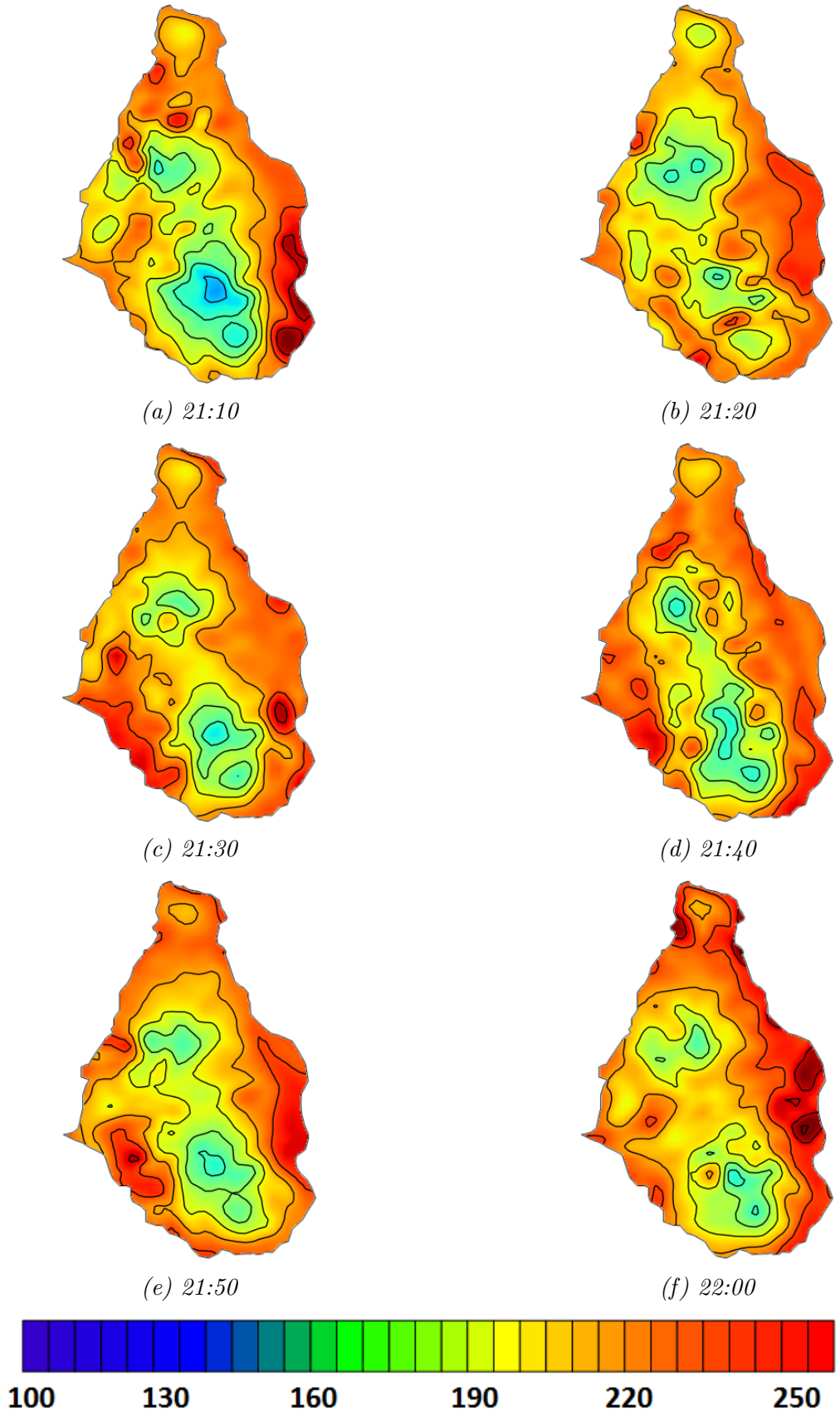

(a) 21:10 *(b) 21:20*

(c) 21:30 *(d) 21:40*

(e) 21:50 *(f) 22:00*

Figure 6.15: Detailed delay fields of WMM-ZWD (mm) 19IC: 10th December 2014, 21:10 UTC - 22:00 UTC over Montserrat, contour intervals every 12.5 mm.

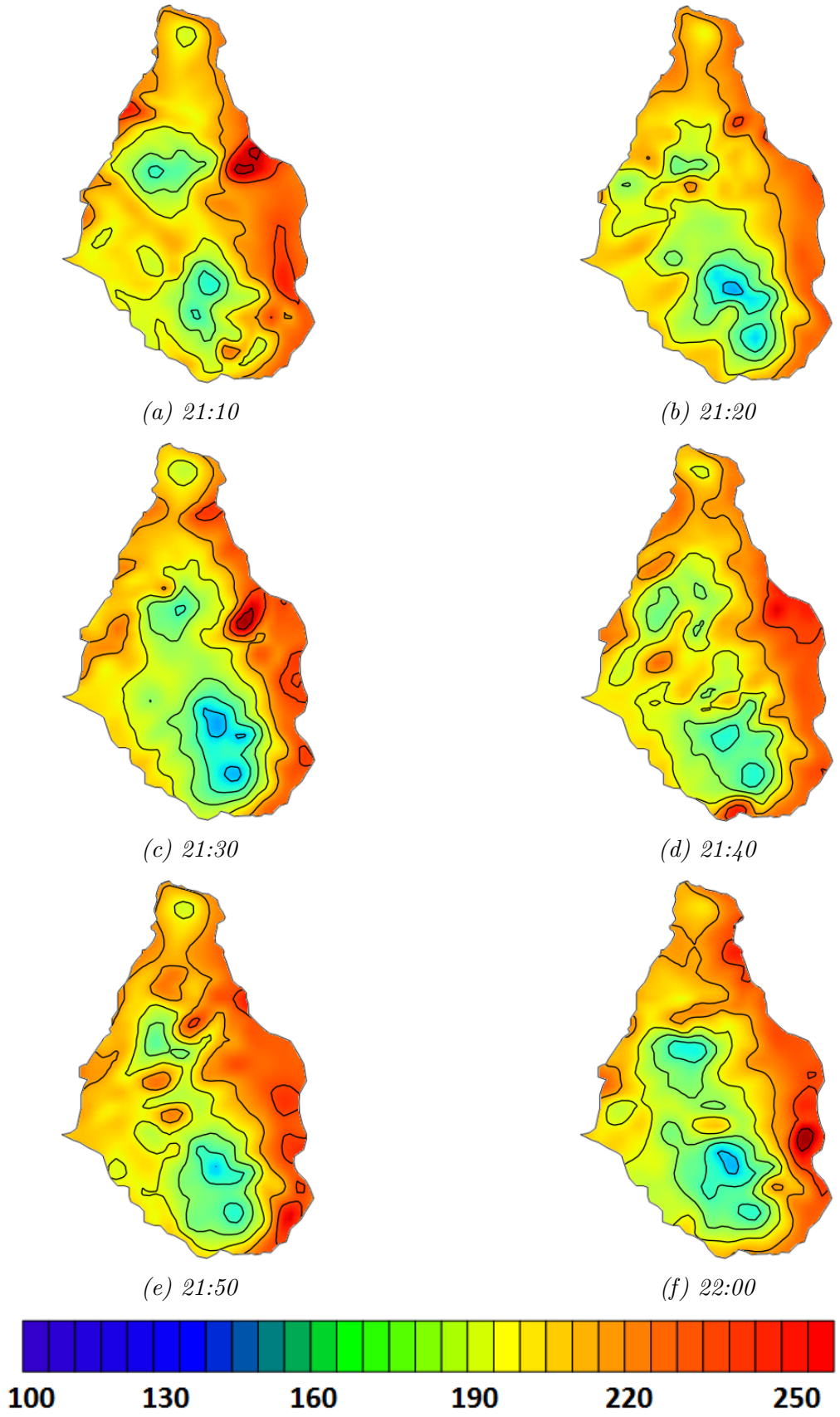

(a) 21:10 *(b) 21:20*

(c) 21:30 *(d) 21:40*

(e) 21:50 *(f) 22:00*

Figure 6.16: Detailed delay fields of WMM-ZWD (mm) shown in Figure 6.14 7TIC: 10th December 2014, 21:10 UTC - 22:00 UTC over Montserrat, contour intervals every 12.5 mm.

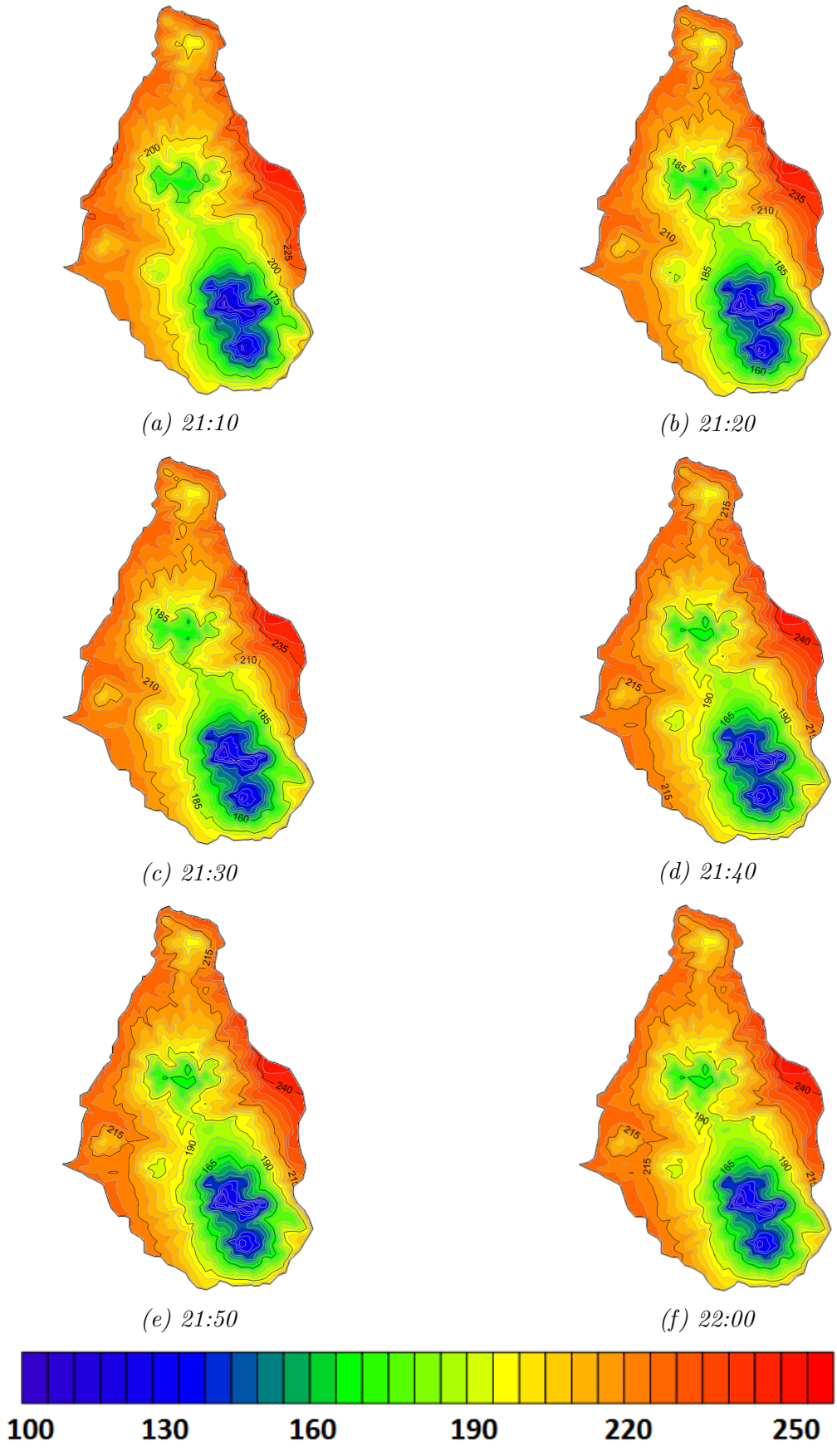

(a) 21:10 *(b) 21:20*

(c) 21:30 *(d) 21:40*

(e) 21:50 *(f) 22:00*

Figure 6.17: GPS-ZWD: 10th December 2014, 21:10 UTC - 22:00 UTC.

6.7 SWD from WMM

We now move from the vertical delay fields to the slantwise delay fields that were experienced by the COSMO-SkyMed radar. Table 6.1 shows the relative contribution of SWD, LWD and HSD for all the 2014 December overpasses in this study and for both the 19IC and 77IC to the WMM. The contribution of LWD and HSD is less than SWD in all cases. The contribution from HSD is low - it is of slightly larger magnitude for 19IC. However the contribution from LWD increases for the field initialised with the 77IC truncated initial conditions and the SWD falls in all cases. All subsequent fields are of WMM-SWD + HSD + LWD (two way delay). An examination of the delay fields found that in general there is little difference in the location of delay, rather the magnitude increases when HSD and LWD are included.

Table 6.1: Percentage contribution of SWD, LWD and HSD to delay field.

I.C. resolution	Dates	SWD %	LWD %	HSD %
19 km	2nd-3rd December 2014	81.89	11.31	6.79
19 km	6th-10th December 2014	86.49	9.54	3.96
19 km	10th-14th December 2014	88.04	7.09	4.87
19 km	18th-19th December 2014	84.75	9.85	5.40
77 km	2nd-3rd December 2014	79.27	14.26	6.47
77 km	6th-10th December 2014	75.21	20.90	3.89
77 km	10th-14th December 2014	75.20	20.98	3.82
77 km	18th-19th December 2014	72.29	23.97	3.75

Comparisons between the delay contributions show that HSD is usually not changed significantly using 77IC rather than 19IC. Instead the LWD is about 10 % higher in the case of 77IC than 19IC. This indicates that 77IC has more precipitation compared with 19IC model runs. The magnitude of the HSD in all cases is less than that found by [Jolivet et al., 2014] who noted that HSD accounted for 15 % of the varience. Indeed following similar logic this thesis recommends that accurate LWD estimates play a larger role than that of the HSD.

6.7.1 Effect of incidence angle on interferogram correction

Slantwise wet delay values are generally greater than zenith wet delay values because the slanted line of sight goes through more atmosphere. Descending pairs have an incidence angle of 59.24° whilst ascending pairs have an incidence angle of 26.65°. Water vapour features at higher altitudes contribute to integrated slant

delays projected on the ground further from their zenith position than features at lower altitudes [Kinoshita et al., 2013]. The distance that the water vapour appears to be displaced is a function of incidence angle and elevation of the water vapour field. Water vapour at high altitude above sea level or at high incidence angle will be displaced more than water water at low altitude or low incidence angle.

6.7.2 WMM-SWD and COSMO-SkyMed comparison

Figure 6.18 (19IC) and 6.19 (77IC) shows the four WMM-SWD images, with values modulated over ± 100 mm so that they can be compared. The ascending passes have a less extreme range of values than the descending passes most likely due to a lower incidence angle through the WMM and shorter path length. The 19IC simulation has a more moderate range of values than the 77IC simulation. In general there is a northeast-southwest gradient WMM-SWD on days of descending passes (this is also found in the GPS-ZWD). This is a result of the dynamics of the trade winds over the island. The strength of the flow will determine the magnitude of the water vapour field and then the polarity of the difference of any two fields depends on the order of the pairing.

6.7.2.1 2nd December 2014 -3rd December 2014

Figure 6.18a (19IC) shows a general east-west gradient. Gradients in the south-west of the island are low. The general locations and magnitudes of these gradients are captured by the COSMO-SkyMed interferogram in Figure 4.2. Figure 6.19a (77IC) shows a more terrain modified delay signal with highs of 100 mm and lows to the north of -20 mm.

6.7.2.2 6th December 2014 - 10th December 2014

Figure 6.18b (19IC) shows a general east-west gradient from -20 mm to -60 mm. Figure 6.19b (77IC) displays a terrain-modulated pattern. The strong negative values over the centre of the island are replaced by positive values in the south east. These values and locations also match up well with COSMO-SkyMed interferogram except that a terrain modulated gradient is not as evident in the satellite data. On 6th December the normal trade wind flow was reversed. This would tend to amplify the gradient (which is given by the subtraction of two fields with different polarities). This is especially the case for the 77IC simulation but can also be observed to a lesser extent in the 19IC.

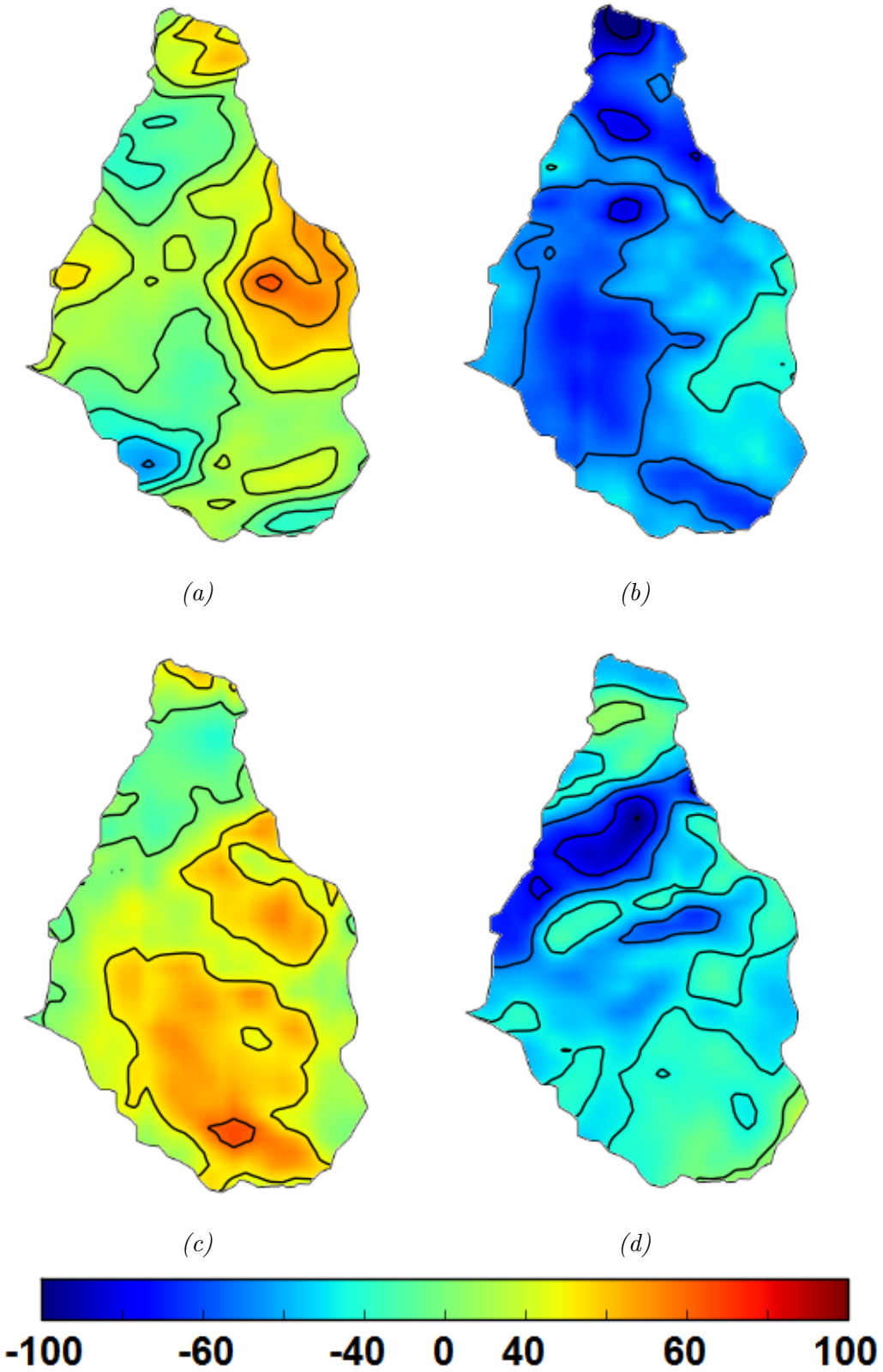

Figure 6.18: WMM-SWD+HSD+LWD difference fields (mm) for 19IC, contour intervals every 20 mm. (a) 2nd December 2014 - 3rd December 2014 at 10:00 UTC, (b) 6th December 2014 - 10th December 2014 at 21:30 UTC, (c) 10th December 2014 - 14th December 2014 at 21:30 UTC (d) 18th December 2014 - 19th December 2014 at 10:00 UTC.

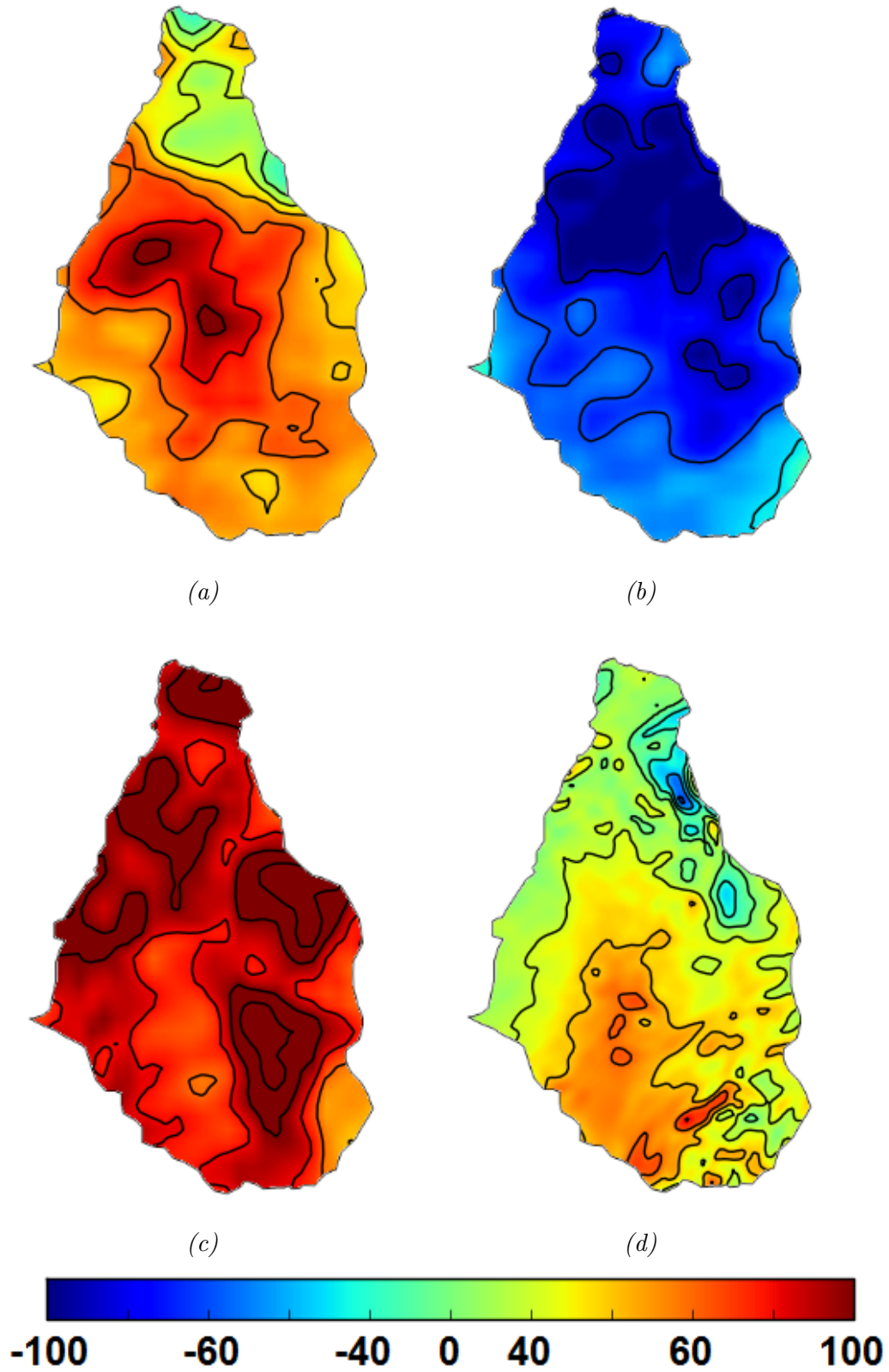

Figure 6.19: WMM-SWD+HSD+LWD difference fields (mm) for 77IC, contour intervals every 20 mm. (a) 2nd December 2014 - 3rd December 2014 at 10:00 UTC, (b) 6th December 2014 - 10th December 2014 at 21:30 UTC, (c) 10th December 2014 - 14th December 2014 at 21:30 UTC (d) 18th December 2014 - 19th December 2014 at 10:00 UTC.

6.7.2.3 10th December 2014 - 14th December 2014

Figure 6.18c (19IC) shows a light terrain modified signal. Figure 6.19c (77IC) shows high positive values over most of the island and the south-west sector displays the least changes. The COSMO-SkyMed data agrees with these values especially in the north of the island.

6.7.2.4 18th December 2014 - 19th December 2014

Figure 6.18c (19IC) has a mostly small terrain modified delay signal. Figure 6.19d (77IC) has a heavily terrain modified signal and a north-south gradient with lows in the north-east and highs in the south-west.

6.7.3 WMM mitigation

6.7.3.1 Interpolation and sampling

Using GAMMA software it was possible to multilook the COSMO-SkyMed satellite data (spatial reduction by averaging in range and/or azimuth directions). I investigate here the benefit of up-and down-scaling the delay field of COSMO-SkyMed and WMM, using interpolation and sampling to produce WMM and COSMO-SkyMed images of the same resolution. The author acknowledges that multilooking could of been used here but it was easier to use sampling methods in the same process as the WMM subsampling, then calculating the residual between them.

Until now all WMM images have had a nearest neighbour interpolation applied to them in order to smooth out the 300 m blockiness and aid visual comparisons. Over-sampling the WMM data using a linear interpolation (by a factor of 6) to 50 m resolution is used so that the two products can be georeferenced together. The resulting image is almost identical to a nearest neighbour interpolated WMM field at 300 m resolution.

6.7.3.2 COSMO-SkyMed atmospheric delay mitigation using WMM

Note that the delay mask has been thresholded so does not appear as part of the calculations. The area to the south-east of TRNTS, Figure 1.4, has been used to match the COSMO-SkyMed to the WMM image. This area is low lying so will not be disturbed by any topographic atmospheric delay features. There is no vegetation in this area - it is exposed to the trade winds which are incident on the site from the west mainly. This means that the chances of local convective features being present is less. On this small island, this is the best site to use.

In the following I use standard deviation and the percentage of pixel delay as the two metrics of the mitigation equation:

$$Residual = COSMO - WMM \tag{6.4}$$

The standard deviation is lowest in the COSMO-SkyMed data on the 6th-10th December 2014 pass and highest on the 10th-14th December 2014 pass. The standard deviation of WMM data is always approximately ~ 20 mm with the exception of 77IC 18th-19th December 2014. On both ascending passes the standard deviation of the COSMO-SkyMed is also approximately ~ 20 mm. The largest standard deviation of the residual corresponds to high standard deviation of the COSMO-SkyMed whereas the lowest standard deviation of the residual corresponds to the lowest standard deviation of the WMM. The 19IC generally has a lower residual standard deviation than the 77IC but this situation is reversed on the 18th-19th December 2014.

The percentage of pixel delay (PPD) is defined here as the pixel-wise offset in the difference field from zero expressed as a percentage, where 100% would mean a difference field at zero (perfect match) and 0% would mean all pixels in the difference image would exceed the threshold of the residual image. Note that the 19IC outperforms the 77IC for 2nd-3rd December 2014 and 6th-10th December 2014. On the other passes the 77IC outperforms the 19IC but their PPD's are almost equal and so the 19IC is at least as good or better than the 77IC. Local changes in the wind field by mesoscale features in the region could account for the differences between 19IC and 77IC and their resulting PPD values.

For 2nd-3rd December 2014 (19IC), shown in Figure 6.20, the WMM fails to capture the magnitude of the delay extending north-south along the west of the island and to the north of SHV, resulting in a poor PPD (Table 6.2). Figure 6.21 shows the 77IC simulation in which the WMM underestimates the delay along the west and on the north sides but performs well around SHV. This results in a poor PPD below 60% (Table 6.3).F

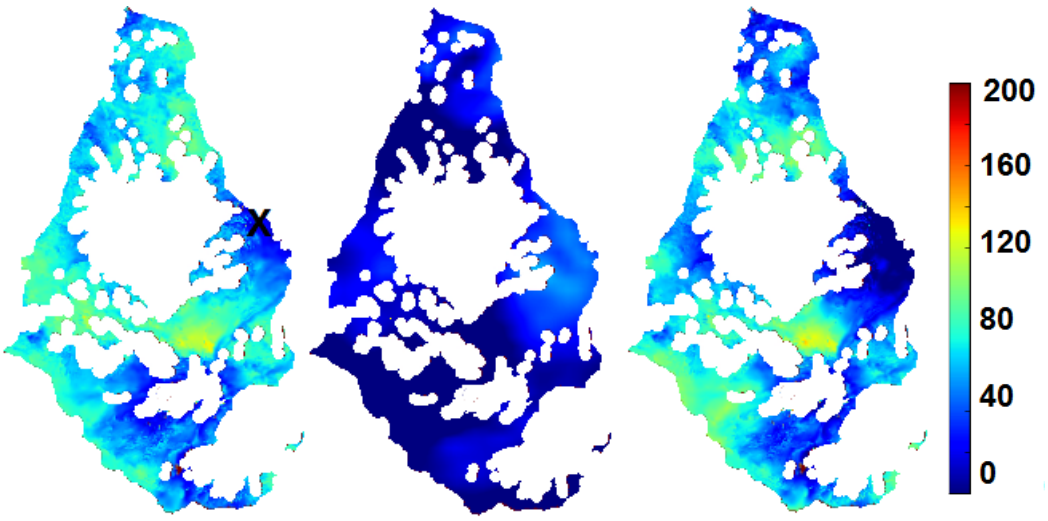

Figure 6.20: Delay mitigation with 19IC at 10:00 UTC. (a) COSMO-SkyMed 2nd-3rd December (mm) 2014. 'X' indicates the calibration point. (b) WMM 2nd-3rd December (mm) 2014. (c) Difference between WMM - COSMO-SkyMed 2nd-3rd December (mm) 2014.

Table 6.2: Standard deviation and PPD on coherent parts of image 2nd-3rd December 2014 10:00 UTC 19IC.

COSMO-SkyMed	WMM	Residual	PPD (%)
19.58	19.01	22.78	64.51

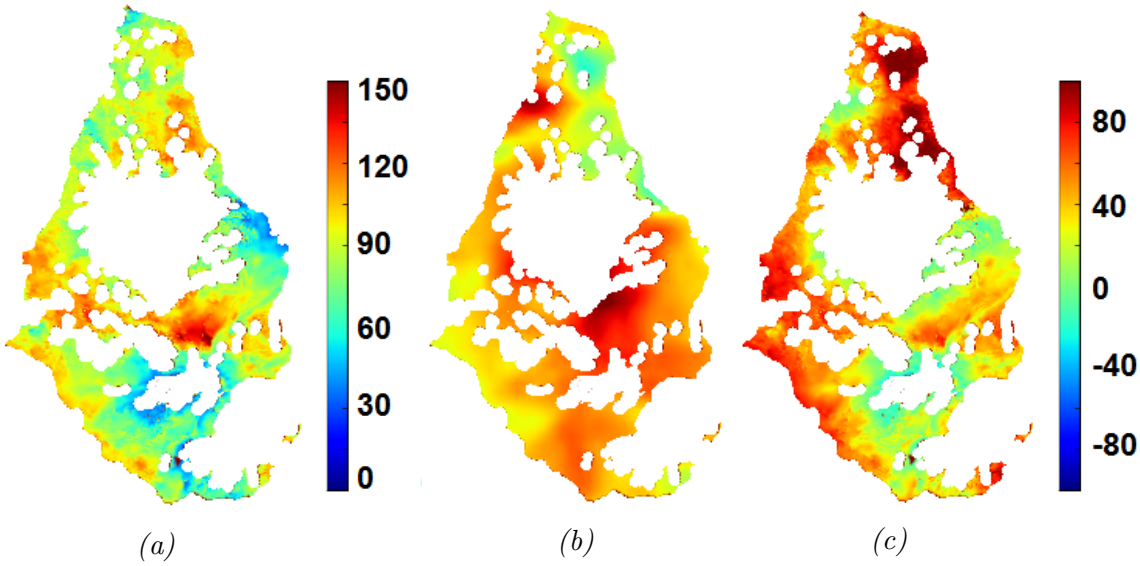

Figure 6.21: Delay mitigation with 77 km truncated initial conditions. (a) COSMO-SkyMed 2nd-3rd December (mm) 2014. (b) WMM 2nd-3rd December (mm) 2014. (c) Difference between WMM - COSMO-SkyMed 2nd-3rd December 2014.

Table 6.3: Standard deviation and PPD on coherent parts of image 2nd-3rd December 2014 (77IC).

COSMO-SkyMed	WMM	Residual	PPD (%)
19.58	18.97	26.39	57.93

For 6th-10th December 2014 (19IC), shown in Figure 6.22, the WMM only fails to produce appropriate delay values in the north of the island, resulting in an excellent PPD above 80% (Table 6.4). Figure 6.23 shows the 77IC simulation in which the WMM under-represents delay on the south of the island but in other places does well resulting in a reasonable pixel correlation (Table 6.5).

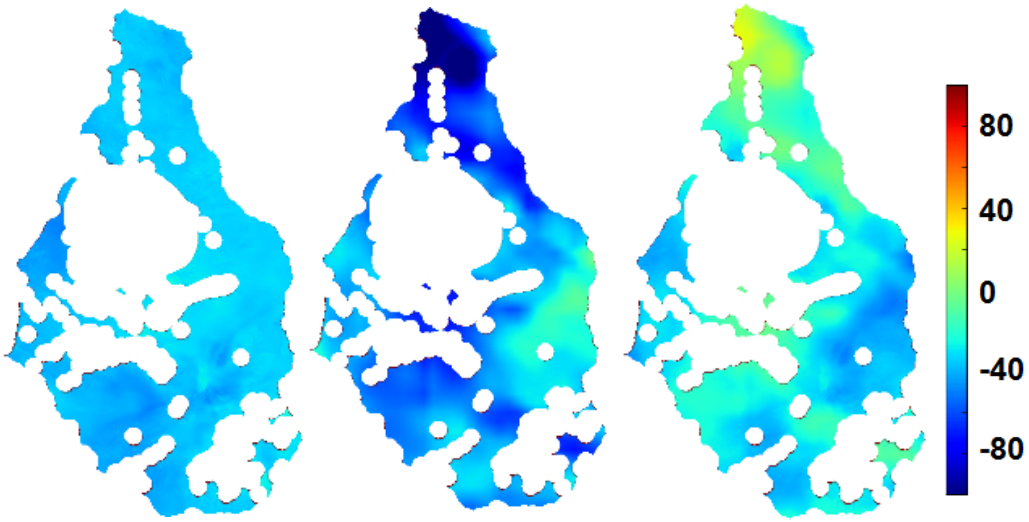

Figure 6.22: Delay mitigation with 19IC at 21:30 UTC. (a) COSMO-SkyMed 6th-10th December (mm) 2014. (b) WMM 6th-10th December (mm) 2014. (c) Difference between WMM - COSMO-SkyMed 6th-10th December (mm) 2014.

Table 6.4: Standard deviation on coherent parts of image 6th-10th December 2014 (19IC).

COSMO-SkyMed	WMM	Residual	PPD (%)
12.29	20.41	24.03	80.95

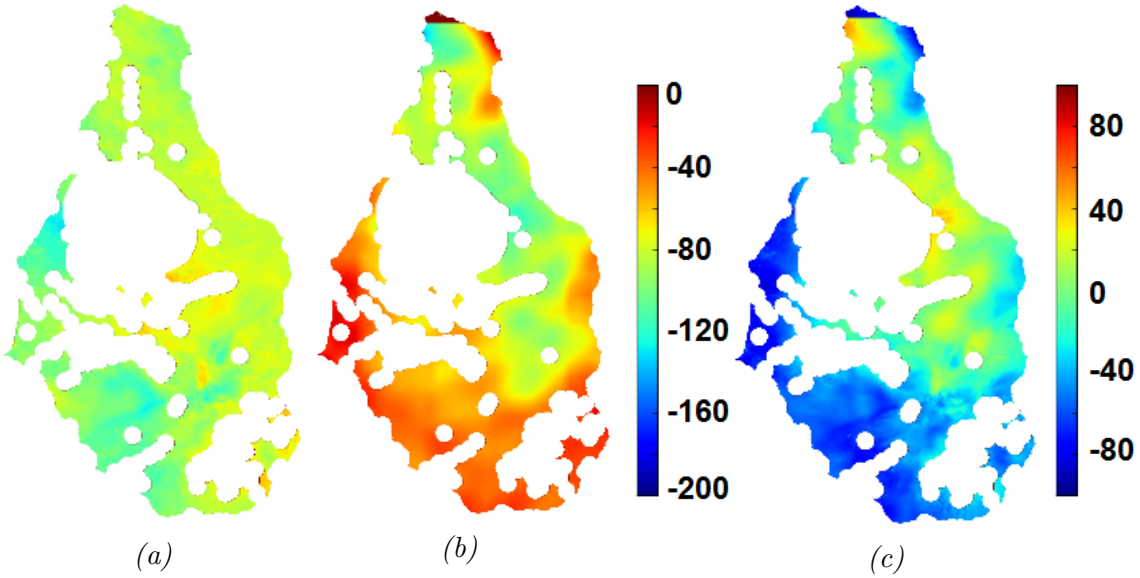

Figure 6.23: Delay mitigation with 77IC at 21:30 UTC. (a) WMM 6th-10th December (mm) 2014. (b) COSMO-SkyMed 6th-10th December (mm) 2014. (c) Difference between WMM - COSMO-SkyMed 6th-10th December (mm) 2014.

Table 6.5: Standard deviation on coherent parts of image 6th-10th December 2014 (77IC).

COSMO-SkyMed	WMM	Residual	PPD (%)
12.29	23.73	30.31	68.16

For 10th-14th December 2014 (19IC), shown in Figure 6.24, the WMM fails to correctly simulate the large delay field present on the west of the island in the COSMO-SkyMed data but captures the magnitude of delay over the rest of the island resulting in a reasonable PPD (Table 6.6). Similarly in Figure 6.25 the 77IC simulation underestimates features in the west but correctly simulates structures in the east resulting in a reasonable PPD (Table 6.7). Note that the sense of the gradient is correct in this case.

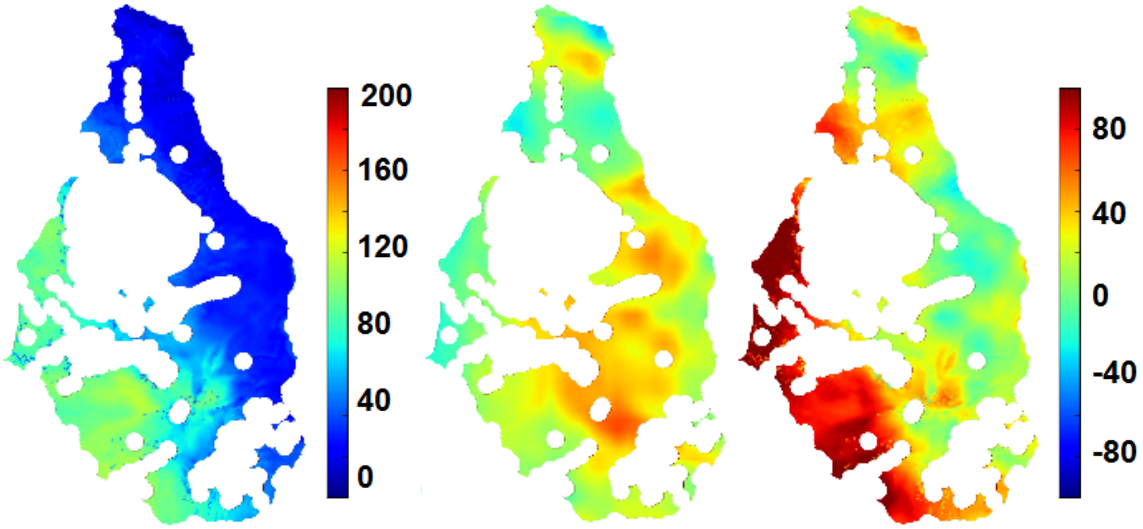

(a) *(b)* *(c)*

Figure 6.24: Delay mitigation with 19IC at 21:30 UTC. (a) COSMO-SkyMed 10th-14th December (mm) 2014. (b) WMM10th-14th December (mm) 2014. (c) Difference between WMM - COSMO-SkyMed 10th-14th December (mm) 2014.

Table 6.6: Standard deviation on coherent parts of image 10th-14th December 2014 (19IC).

COSMO-SkyMed	WMM	Residual	PPD (%)
30.05	18.64	32.61	65.42

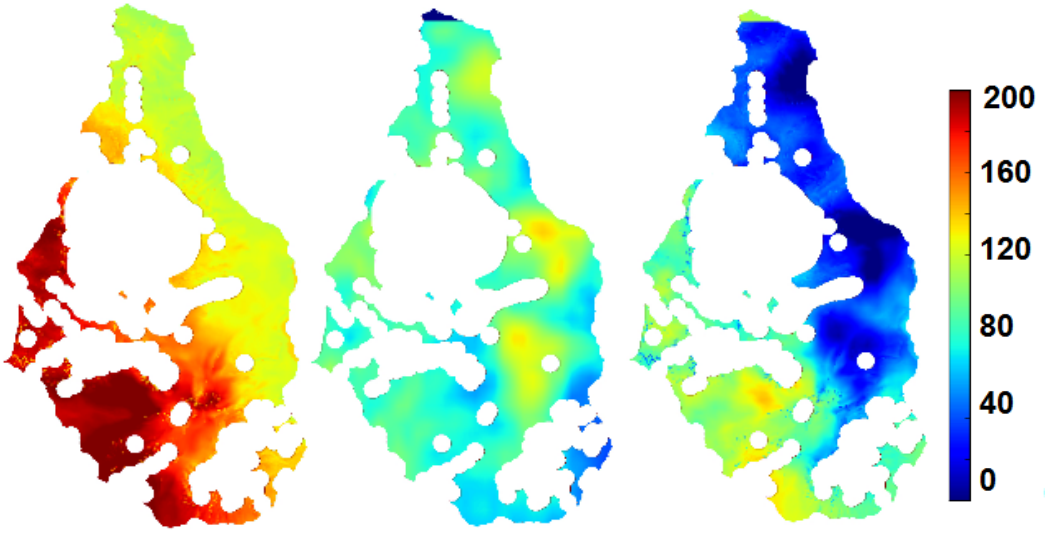

(a) *(b)* *(c)*

Figure 6.25: Delay mitigation with 7IC at 21:30 UTC. (a) COSMO-SkyMed 10th-14th December (mm) 2014. (b) WMM 10th-14th December (mm) 2014. (c) Difference between WMM - COSMO-SkyMed 10th-14th December (mm) 2014.

Table 6.7: Standard deviation on coherent parts of image 10th-14th December 2014 (77IC).

COSMO-SkyMed	WMM	Residual	PPD (%)
30.05	19.01	38.48	68.08

For 18th-19th December 2014 (19IC), shown in Figure 6.26, the WMM underestimates the magnitude of the COSMO-SkyMed delay but captures its general structure resulting in a good pixel correlation (Table 6.8). Figure 6.27 the 77IC simulation simulates the region to the south and west of SHV well but does not capture delay gradients along the west and east coasts of Montserrat. However this gives a good pixel correlation (Table 6.9).

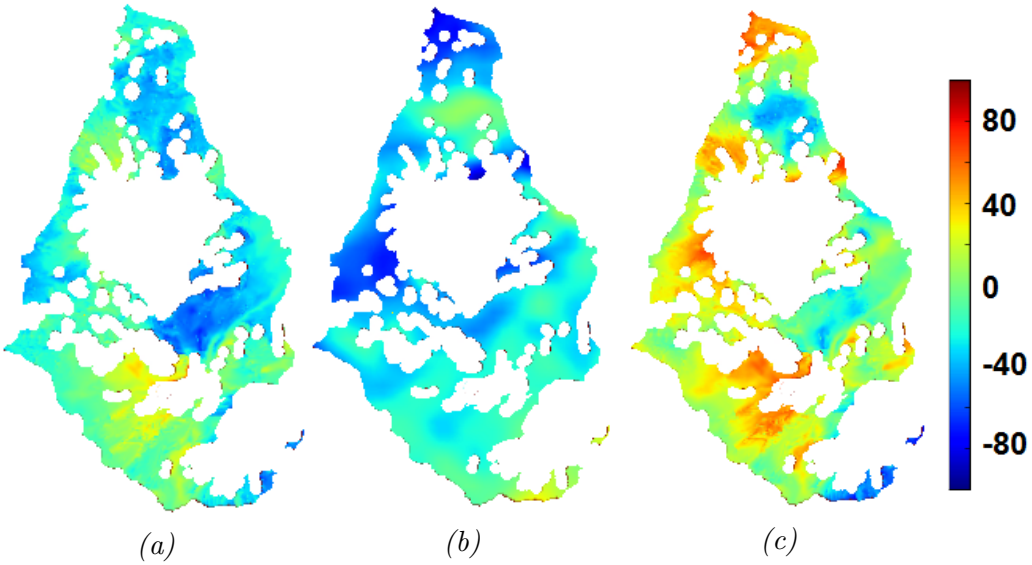

Figure 6.26: Delay mitigation with 19IC at 10:00 UTC. (a) COSMO-SkyMed 18th-19th December (mm) 2014. (b) WMM 18th-19th December (mm) 2014. (c) Difference between WMM - COSMO-SkyMed 18th-19th December (mm) 2014.

Table 6.8: Standard deviation on coherent parts of image 18th-19th December 2014 (19IC).

COSMO-SkyMed	WMM	Residual	PPD (%)
20.14	18.10	26.06	76.82

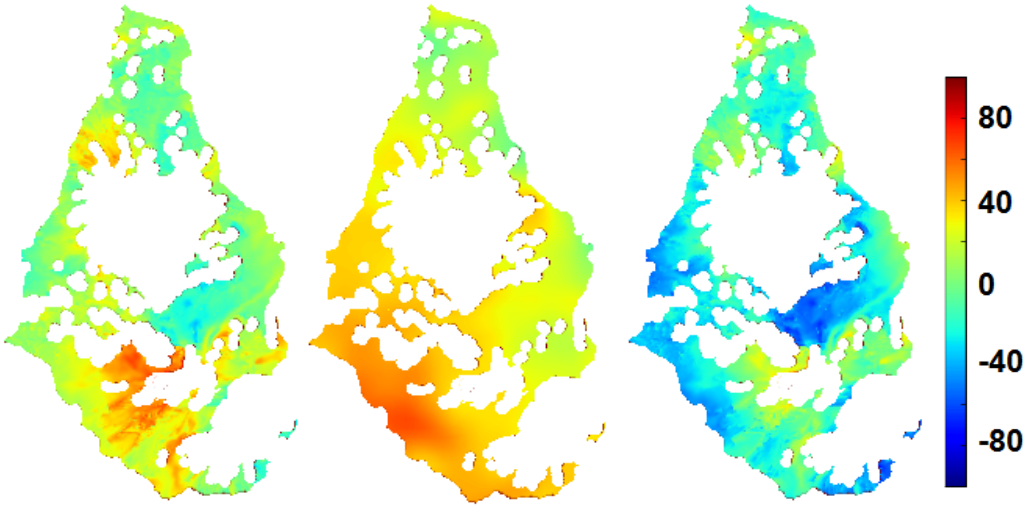

(a) (b) (c)

Figure 6.27: Delay mitigation with 7TIC at 10:00 UTC. (a) COSMO-SkyMed 18th-19th December (mm) 2014. (b) WMM 18th-19th December (mm) 2014. (c) Difference between WMM - COSMO-SkyMed 18th-19th December (mm) 2014.

Table 6.9: Standard deviation on coherent parts of image 18th-19th December 2014 (7TIC).

COSMO-SkyMed	WMM	Residual	PPD (%)
20.14	14.20	19.90	77.48

6.8 Summary of WMM InSAR Atmospheric Correction

- The effects of LWD and HSD have been explored and included in the final WMM-SWD calculations.The magnitude of the LWD effect is higher than might be expected. This could be caused by the way in which LWD is calculated - it is proportional to the WMM cloud depth (km) and uses Table 1.1 to calculate the phase delay. It is noted by [Hanssen, 2001] that droplet size does not play a part in the calculation of phase delay of different clouds because these measurements are proportional to the liquid water content of each cloud type. This study assumes all clouds are cumulus which have a small horizontal scale but large cloud depth and water vapour content which leads to the larger than expected LWD contribution. If other cloud types were to be included in the study we would expect the LWD contribution of delay to decrease.

  comparison between WMM-ZWD and GPS-ZWD found an overestimation of both range and magnitude of WMM zenith fields but the correct location of

local differential delay features. Reasons for some of these differences have been explored in Chapter 5.

- Time series fields of both GPS and WMM delays found that a 10 min WMM interval was sufficient to generate small variations in delay fields for COSMO-SkyMed passes.

- A comparison between COSMO-SkyMed and WMM-SWD found general locations and magnitudes of delay changes were captured by WMM. An atmospheric correction has been performed using WMM-SWD products and difference maps found varying levels of skill in the forecast of delay (Table 6.10).

Table 6.10: Standard deviation and PPD on coherent parts of difference images from Section 6.7.3.

Pass[1]	IC[2]	COSMO-SkyMed	WMM	Residual	PPD (%)
1	19	19.58	19.01	22.78	64.51
1	77	19.58	18.97	26.39	57.93
2	19	12.29	20.41	24.03	80.95
2	77	12.29	23.73	30.31	68.16
3	19	30.05	18.64	32.61	65.42
3	77	30.05	19.01	38.48	68.08
4	19	20.14	18.10	26.06	76.82
4	77	20.14	14.20	19.90	77.48

[1] 1: 2nd - 3rd December 2014, 2: 6th - 10th December 2014, 3: 10th - 14th December 2014, 4: 18th - 19th December 2014

[2] 19: 19IC, 77: 77IC

The accuracy of the residual measured by PPD correlates well with the spatial scales I am trying to simulate. In the case of difference images with less meteorological features their standard deviation is lower compared to others. In cases where local meteorological conditions matter most we see that the 19 km WMM to outperform the 77 km WMM. Likewise in the case of mesoscale events we see that both the 19 km and 77 km WMM have reduced accuracy and that there is less difference between the accuracy of their outputs. It is also worth noting that different levels of accuracy are needed for different applications.

- The 19IC performed approximately as well as or better than the 77IC. This could be caused by the treatment of local winds in WMM (Table 7.1). On 3rd

December 2014 there were stronger trade winds than on 2nd December 2014. Crucially the wind direction changed in the 77IC to blow from the south to the north on 3rd December 2014 which may have been responsible for the drop in PPD from 64% (19IC) to 57% (77IC). Note that on the 3rd December winds had an east-west direction (Table 3.8). For the 6th-10th December 2014 there was a large difference in PPD between the models - 81% for 19IC and 68% for 77IC. On 6th December the wind changed to blow from the west which was correctly represented by the 19IC. However in the 77IC the wind direction changed to the north-west and this could be responsible for the difference in accuracy.

Chapter 7

Conclusions

7.1 Summary of findings

- The WMM simulated water vapour fields over a tropical island, Montserrat. This used 16 km ECMWF initial conditions truncated onto 19 km and 77 km grids. High resolution static geographic data combined with a parameterisation sensitivity testing was used to construct a 300 m resolution model for Montserrat. Idealised hydrostatic flow generated by WMM around obstacles of the same scale as Montserrat agrees qualitatively with results from literature. Precipitation output from WMM has been analysed at a regional length-scale and compared with TRMM data which was of particular use for sensitivity testing cumulus schemes. It has been shown how non-idealised, non-hydrostatic models can be used to find water vapour fields at the time of satellite overpasses. The output of these fields have been compared qualitatively with MODIS, radiosonde, weather diary and GOES-East data to build up an idea of how WMM performs at a local lengthscale during field trips to Montserrat in 2012 and 2013. WMM data produced realistic gravity waves and mesoscale features in 2012 and 2013. Kestrel weather station data have been recorded from the 2013 field trip to show typical temperature and relative humidity values. The 2012 and 2013 field trips took place in conditions normal for the wet season from a climatological perspective - a climatology of Montserrat was obtained and analysed for this study.

- ZWD values were measured from the MVO GPS network. Both 2012 and 2013 GPS and WMM data have been compared, citing cases of contrasting meteorlogical conditions, finding the WMM to be able to simulate key features in the GPS fields. The apparent overestimation of GPS-ZWD values relative to WMM-ZWD may have been caused by geometric and topographic effects.

The GPS-ZWD fields have been compared with MODIS 1 km water vapour products, which usually confirmed high levels of water vapour in the area. However the GPS is at higher resolution than the MODIS so we expect a greater range of data. GPS ZWD for the days of the 2014 InSAR case study have been used with WMM measurements to explore the WMM as an InSAR atmospheric mitigation tool. Due to the slant-looking nature of InSAR it is important that water vapour features are placed by WMM in the correct location above Montserrat.

- GAMMA InSAR software has been used to create differential interferograms for comparison with WMM-SWD data. As no deformation was recorded on Montserrat during the 2014 field campaign we can assume all interferometric fringes are due to atmospheric effects. COSMO-SkyMed images from two ascending and two descending passes have been processed and georeferenced for atmospheric correction. Descending passes use a COSMO-SkyMed inclination angle of 59.24°, meaning that the descending passes are more likely to be affected by atmospheric delay fields than ascending passes at an inclination angle of 23.26°. The resolution of the COSMO-SkyMed images is decreased and WMM increased in order to match each other with 50 m horizontal resolution.

- The effects of LWD and HSD have been explored and included in the final WMM-SWD calculations.

- A comparison between WMM-ZWD and GPS-ZWD found an overestimation of both range and magnitude of WMM zenith fields but the correct location of local differential delay features. A temporal fit to both GPS and WMM found that a 10 min WMM output was sufficient to measure small variation in delay fields for COSMO-SkyMed passes. A comparison between COSMO-SkyMed and WMM-SWD found general locations and magnitudes of delay changes were captured by WMM. An atmospheric correction to the COSMO-SkyMed interferograms was performed using WMM-SWD products. For the four pairs of interferograms (in each case 19IC followed by 77IC): 2nd-3rd December 2014, 6th-10th December 2014, 10th-14th December 2014, 18th-19th December 2014, the WMM delay fields and the residual field after subtraction shows the following standard deviations and PPD values: 22.78, 64.51%, 26.39, 57.93%, 24.03, 80.95%, 30.31, 68.16%, 32.61, 65.42%, 38.48, 68.08%, 26.06, 76.82%, 19.90, 77.48%.

- On ascending passes the variance in COSMO-SkyMed and WMM are approx-

imately the same with the exception of the 77IC 18th-19th December 2014. This could be caused by the treatment of local winds in WMM (Table 7.1). As found by idealised models in Chapter 3, strong winds create a tendency for water vapour to go over hills and weaker winds for water vapour to pool in their leeside. Hence wind sensitivity is an important consideration for InSAR mitigation using the WMM.

7.2 Future Work

7.2.1 Sentinel-1 InSAR

This C-band radar satellite constellation will be the InSAR workhorse for the next twenty years. There are UK-led international research programmes that could benefit from this type of high resolution atmospheric correction at volcanoes (e.g. Centre for the Observation and Modelling of Earthquakes, Volcanoes and Tectonics [*COMET*, 2015]).

7.2.2 Wind-speed for DOAS measurements

Differential Optical Absorption Spectroscopy (DOAS) is a form of ground-based remote spectroscopy used to measure concentration of trace gases. In the case of SHV, MVO measure sulphur dioxide (SO_2) daily loadings around the volcano. SO_2 is easy to detect as it absorbs strongly in the ultra-violet wavelengths and has low background concentrations in the atmosphere. The DOAS array at SHV estimates the flux of SO_2 using processing that takes into account the advection of the volcanic plume. The SO_2 flux values are highly dependent on accurate wind data and the error due to this parameter is estimated [Edmonds et al., 2003] to account for 30% of the measurement error. It is a standard practise, by the MVO, to use the wind speed and direction of from the anemometers at Geralds airport (near GPS site GERD) on the north side of Montserrat in place of the wind speed at the top of SHV for DOAS calculations, Figure 1.4.

The wind speeds used for DOAS calculations during the dates of the 2014 field campaign are shown in Figure 7.1. Note that these measurements were taken every 3 hours and averaged for the DOAS measurement. Wind speeds always remain under 17 $m\ s^{-1}$ and oscillate between about 11-13 $m\ s^{-1}$ on days 333-338 and 343-348 to close to no wind on day 341 and 349. Wind direction is usually approximately westerly (0°) with major deviations between days 337 and 344.

During the 2014 field campaign a meteorological mast was placed near TRNT GPS station shown in Figure 1.4 close to sea level to measure the wind speed and direction on the east side of Montserrat near SHV. Wind speeds from this mast are shown in Figure 7.2. Note that these measurements were taken every 5 minutes. The wind speed stays under 8 $m\ s^{-1}$ and there is no discernible pattern in the wind direction.

WMM measurements for wind speed at the time of COSMO-SkyMed overpass are found in Table 7.1 for both 19IC and 77IC. The direction of the winds broadly follow existing records except for the 3rd December 2014 77IC where wind was blown south-north when all other evidence suggests that it was actually blown east-west.

The two surface wind measurements (by instrumentation) are very different, GERD is at an elevation of about 160 m asl on the islands watershed which may explain the higher average speeds and it is conceivable that the true local wind speed value at SHV would depart from these measurements also. The WMM could be used to provide wind estimates for DOAS at the top of SHV. Initial tests found a difference of up to 4.7 ms^{-1} (19IC, 3.7 ms^{-1} - 77IC) between horizontal wind speed measurements at the top of SHV and GERD just within the WMM (Table 7.1). For this to be operationally practicable, a simplified version of WMM would need to be running continuously preferrably at MVO.

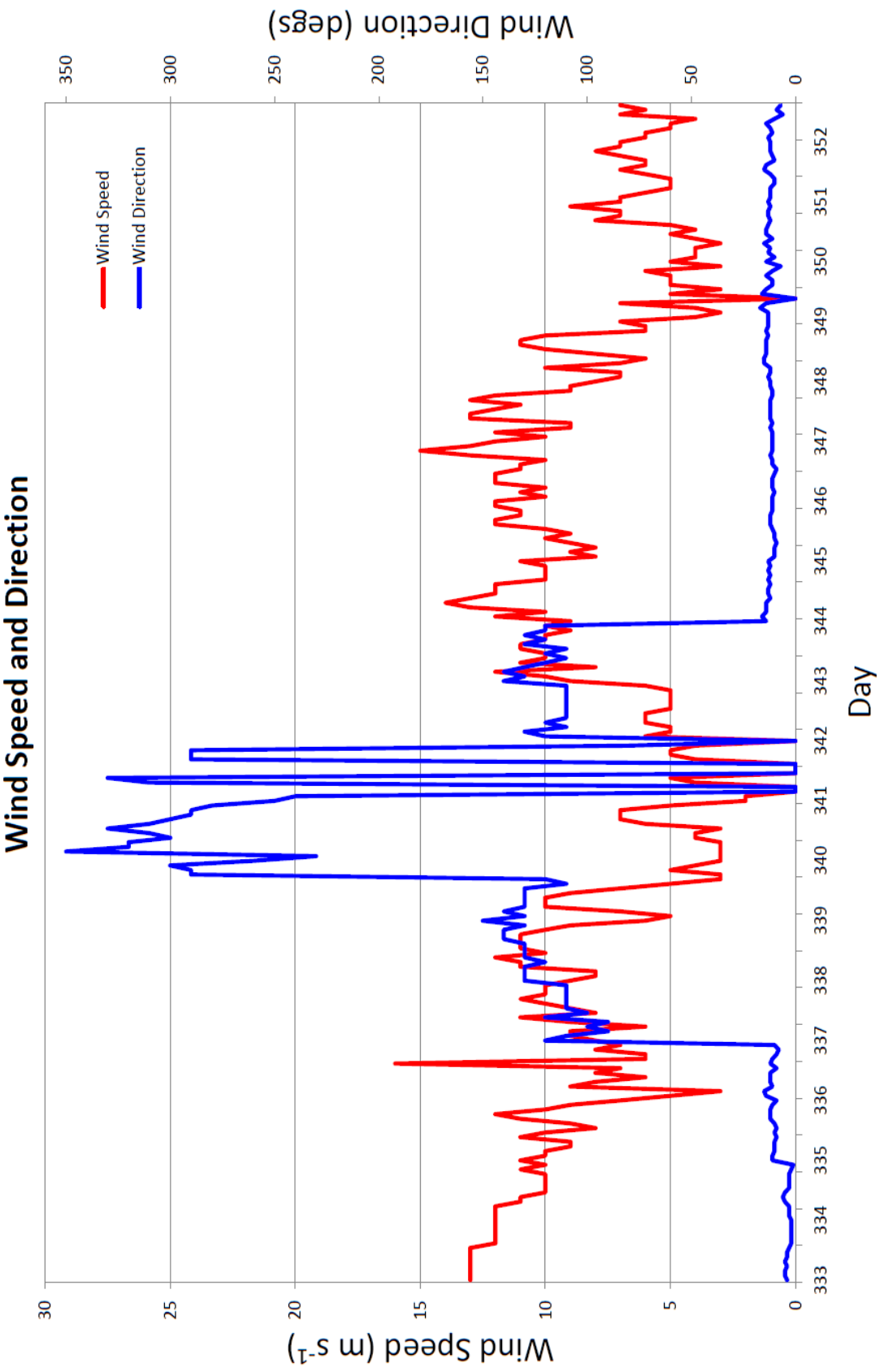

Figure 7.1: Wind speed ($m\ s^{-1}$) and direction (0^{o} is west) recorded at GERD for MVO DOAS measurements (29th November 2014, day 333 - 18th December 2014, day 352).

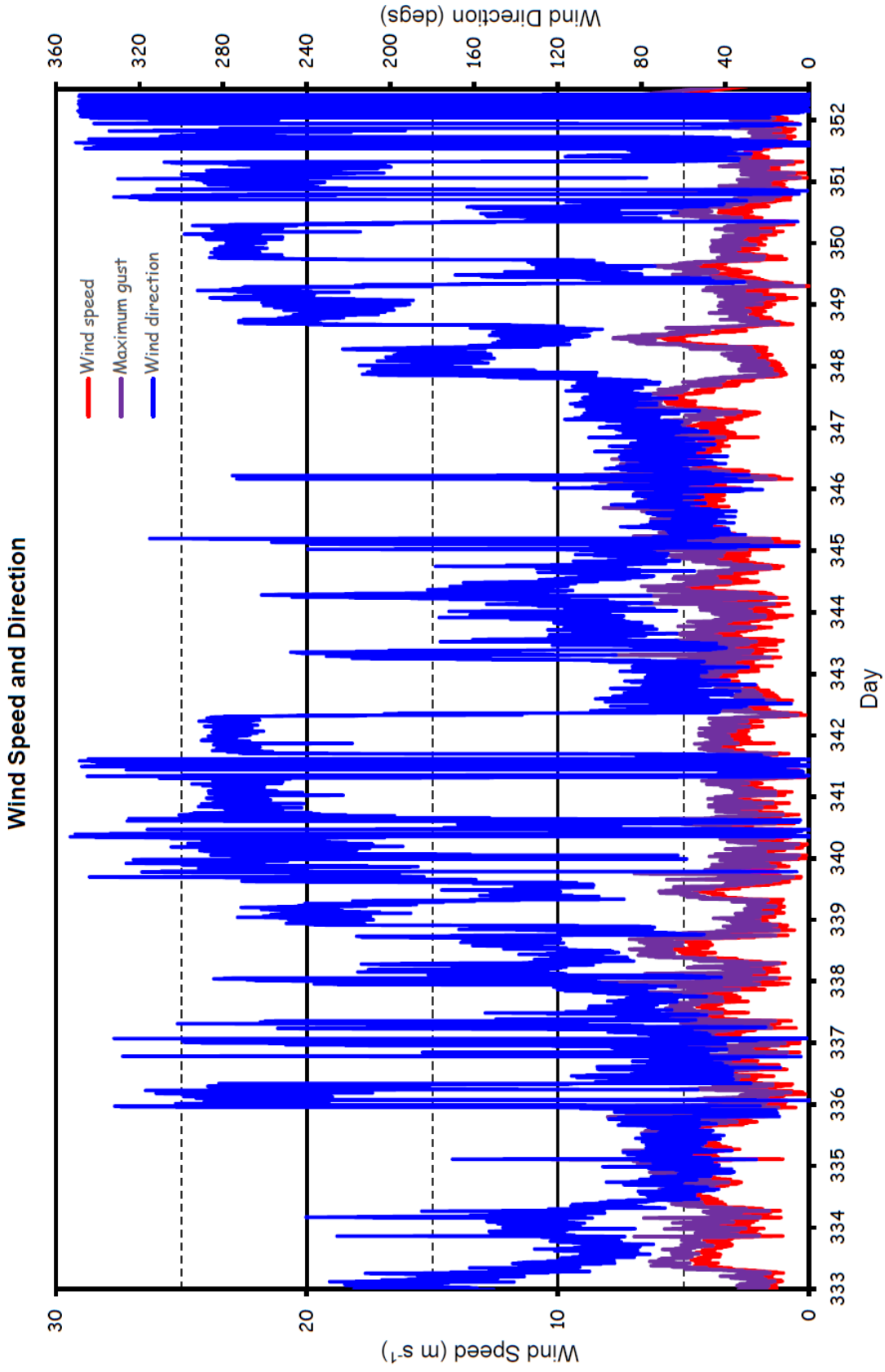

Figure 7.2: Wind speed ($m\ s^{-1}$) and direction (0^{o} in north) recorded at TRNT (29th November 2014, day 333 - 18th December 2014, day 352).

Table 7.1: WMM (19IC and 77IC) wind velocity during 2014 field study and general wind conditions for times of COSMO-SkyMed overpass.

Pass[1]	19TU[2]	19SU[2]	19GU[2]	19TV[2]	19SV[2]	19GV[2]	General wind conditions
1	-3.2	-2.5	-2.2	0.2	1.0	0.2	Direction from east to west, downstream of terrain flow reversed
2	-5.6	-8.0	-7.6	0.2	-2.5	1.0	Strong winds moving from east to west
3	3.4	5.1	4.8	-1.2	-0.8	-3.0	Winds moving from west to east
4	-6.0	-2.5	-6.2	-0.7	-2.4	-0.8	Direction from east to west
5	-5.3	1.3	0.2	2.3	7.5	0.0	Direction from south to north, possibly hydraulic jump near GERD
6	-4.0	-9.0	-5.7	-4.6	-3.1	-4.6	Direction from north-east to south-west
7	-5.1	-11.8	-7.1	-3.3	-6.6	-3.3	Direction from east to west
Pass	77TU	77SU	77GU	77TV	77SV	77GV	General wind conditions
1	-1.0	-2.9	-3.4	0.7	2.3	0.4	Direction from east to west
2	4.4	2.5	3.0	4.6	6.6	3.0	Direction from south to north
3	-2.9	6.5	2.8	-1.7	-1.1	0.5	Direction from north-west to south-east
4	-6.0	-5.0	-5.6	-1.8	-2.1	-0.7	Direction from east to west
5	0.2	1.5	0.6	4.5	7.3	3.7	Direction from south to north
6	-5.9	-6.6	-6.2	-4.4	-8.2	-3.8	Direction from north-east to south-west
7	-5.5	-9.4	-6.8	-4.0	-4.1	-3.2	Direction from east to west

[1] 1: 2nd December 2014, 2: 3rd December 2014, 3: 6th December 2014 4: 10th December 2014, 5: 14th December 2014, 6: 18th December 2014, 7: 19th December 2014

[2] U: east-west wind (positive is moving west), V: south-north wind (positive is moving north), T: TRNTS GPS station, S: SHV, G: Geralds airport, 19: 19IC, 77: 77IC

7.2.2.1 A model volcanic plume

To accurately simulate the atmosphere above a volcanic system a simulated volcanic plume may be necessary. There are no good quantitative measurements of the water vapour loading from such plumes, but it is expected to be at least an order of magnitude less than that of any background water vapour within a few kilometres of the vent.

Sulphur dioxide is readily measured in volcanic plumes using field spectrometry. Sulphur can be used as a proxy for water vapour by assuming a constant partition ratio from the parent magma and so the approximate amount of water vapour released from the volcano can be calculated in a post-processing step.

Sulphur degassing from SHV can be modelled using WRF-Chem, which contains a kinetic pre-processor (KPP) that takes tabulated chemical data and reactions for each chemical mechanism within the WMM. Daily SO_2 volcanic emission data from MVO could be used to initialise the KPP. The KPP is fully coupled to the WMM and provides an easy way to update the system with new data. However sulphur has a moderate lifetime compared to other chemical species. Water vapour can exist on any scale from the microscale to the synoptic and also interacts with sulphur released from SHV. So it should be noted that this proxy association is at its most valid closest to the volcanic vents on SHV, decreasingly valid with increasing time and space scales. Measurements have shown that 500 tonnes per day (t/d) SO_2 (the long-term flux from the volcano) is equivalent to about $8,000 - 25,000$ t/d of H_2O emitted from the magma [Hammouya et al., 2006], [Edmonds et al., 2010].

To find a delay effect in the InSAR data caused by the volcanic plume in that way it is important to look at days in which the wind is blowing from different directions, so that the volcanic plume is present and absent in the fields of measurement. The climatological data tells us that this is a rare event on Montserrat, Figure 3.20, however on the 6th December 2014 the wind blew from the west. As this was a day of a descending COSMO-SkyMed pass, the pair with the 6th December 2014 (an east wind day) would permit such a simulation.

7.2.3 Additional WMM developments

I will now describe a series of additional developments that could be applied in the WMM in order to increase its accuracy and applicability.

7.2.3.1 ECMWF initial conditions

Note that at the start of this project, model-level ECMWF initial conditions were not fully supported by the WRF preprocessing system. This project devised a new method to integrate model-level initial conditions to the preprocessor which has now been adopted by the WRF community and is available from the University of Reading WRF group homepage [*Initial conditions integration*, 2015]. This was a significant achievement. It was not possible to use 16 km ECMWF operational analysis initial conditions, using this method, with version of WRF-preprocessor used in this project. As a result the $\sim$ 16 km operational analysis has been truncated onto a Gaussian grid of coarser resolution than 16 km before preprocessing by the WRF model. Truncation to 19 km and 77 km was found to be numerically stable and has been used for the main results contained within this thesis but additional computation improvements could be made to finding the cost-benefits of using truncated initial conditions at coarser resolutions. A discussion of truncation to coarser resolutions is presented in Section 3.2.2.2.

7.2.3.2 Introducing ensemble methods to WMM

A single run of WMM is subject to noise dervived from data and imperfect representation of atmospheric processes. We would like to have an estimate of the range of that noisy output. Generating ensembles of simulations is a way of acquiring such an estimate. I therefore investigated the possibility of using ensemble methods, by perturbing non-hydrostatic initial conditions, to obtain a better estimate of local atmospheric conditions across Montserrat. There are two approaches to ensemble modelling that would be appropriate here.

Firstly, by changing the start time of each forecast run. However as WMM intakes new initial conditions every 6 hours, this is not an effective method at generating an ensemble of forecasts. The ECMWF can provide initial conditions from an ensemble of 50 members at a horizontal resolution of 27 km [Molteni et al., 1996].

Secondly, by using varying initial conditions using the 50 members of the ECMWF ensemble model (or using a random number generator to pick less members from the ensemble model). This is available at a maximum resolution of 30 km but includes a coupled-ocean unlike the ECMWF analysis model, ultimately leading to an improved but coarser resolution model. WMM domain nesting conditions can remain the same even with the decrease in inital condition resolution because the outermost WMM domain is still within the recommended requirements (2-5 times aspect ratio).

7.2.3.3 Data assimilation

WRFDA is a system akin to WRF-Chem (an 'addon' specifically tailored to be included in WRF) but for data assimilation so that WRF models can be perturbed towards observations. This could increase the accuracy of the model for example a system perturbed by the MVO GPS network estimates of ZWD could be converted into PWV. This would no doubt be difficult but also immensely valuable.

7.2.3.4 Planetary boundary layer

Sensitivty testing opted for a PBL scheme on all domains before the adoption of increased vertical levels. With increased vertical levels in the lower troposphere the assumptions surrounding PBL schemes may break down, especially when horizontal scales become much bigger than vertical scales. Tests were made to remove the PBL on different domains and it was concluded that the WMM still produced realistic fields in spite of this. It was also confirmed by the National Center for Atmospheric Research (NCAR) that of time of writing, the PBL scheme employed in this project is recommended for the use of WRF at high resolution. In the future an alternative to this may be the introduction of a sub-grid PBL model.

References

Bekaert, D., Walters, R. J., Wright, T. J., Hooper, A. and Parker, D. [2015], 'Statistical comparison of InSAR tropospheric correction techniques', *Remote Sens. Environ.* pp. 40–47. 33

Beljaars, A. C. M. [1994], 'The parameterization of surface fluxes in large-scale models under free convection', *Quart. J. Roy. Meteor. Soc.* **121**, 255–270. 34

Berardino, R., Fornaro, G., Lanari, R. and Sansosti, E. [2002], 'new algorithm for surface deformation monitoring based on small baseline differential interferograms', *IEEE Trans. Geosci. Remote Sens.* **40**(11), 2375–2383. 9

Bevis, M., Businger and Steven [1992], 'GPS meteorology: Remote sensing of atmospheric water vapor using the Global Positioning System', *J. Geophys. Res.* **97**(92), 787–801. 7

Boehm, J., Heinkelmann, R. and H., S. [2006], 'Short note: a global model of pressure and temperature for geodetic applications', *Journal of Geodesy* **81**(10), 679–683. 95

Cece, R., Bernard, D. Christophe, A. and Dorville, J. [2014], 'Numerical Simulations of Island-Induced Circulations and Windward Katabatic Flow over the Guadeloupe Archipelago', *Mon. Weather Rev.* **141**(2), 850–867. 26, 61

Cheng, S., Perissin, D., Lin, H. and Chen, F. [2012], 'Atmospheric delay analysis from GPS meteorology and InSAR APS', *J. Atmos. Sol.-Terr. Phy.* **86**, 71–82. 7

COMET [2015]. [Online; accessed 24 Sept. 2015].
URL: *http://comet.nerc.ac.uk/* 149

Comparison of weather models [2014]. [Online; accessed 11 Aug. 2014].
URL: *http://apps.ecmwf.int/wmolcdnv/* 28

Davis, J. L., Herring, T. A., Shapiro, I. I., Rogers, A. E. E. and Elgered, G. [1985], 'Geodesy by radio interferometry: Effects of atmopsheric modeling errors on estimates of baseline length', *Radio Sci.* **20**, 1593–1607. 6

Ding, X., Li, Z., Zhu, J., Feng, G. and Long, J. [2008], 'Atmospheric Effects on InSAR Measurements and Their Mitigation', *Sensors* **8**(9), 5426–5448. 1

Doin, M. P., Lasserre, C., Peltzer, G., Cavalié, O. and Doubre, C. [2009], 'Corrections of stratified tropospheric delays in SAR interferometry: Validation with global atmospheric models', *J. Appl. Geophys.* **69**, 35–50. 10

Edmonds, M., Aiuppa, A., Humphreys, M., Moretti, R., Giudice, G., Martin, R. S., Herd, R. A. and T., C. [2010], 'Excess volatiles supplied by mingling of mafic magma at an andesite arc volcano', *Geochem. Geophys. Geosyst.* **11**(4), 1525–2027. 154

Edmonds, M., Oppenheimer, C., Pyle, D. M., Herd, R. A. and Thompson, G. [2003], 'SO2 emissions from Soufrire Hills Volcano and their relationship to conduit permeability, hydrothermal interaction and degassing regime', *J. Volcanol. Geotherm. Res.* **124**, 23–43. 149

Ferretti, A., Prati, C. and Rocca, F. [2001], 'Permanent scatterers in SAR interferometry', *IEEE Trans. Geosci. Remote Sens.* **39**(1), 8–20. 9

Foster, J., Brooks, B., Cherubini, T., Shacat, C., Businger, S. and Werner, C. [2006], 'Mitigating atmospheric noise for InSAR using a high resolution weather model', *Geophys. Res. Lett.* **33**(16). 10

GAMMA Software [2015]. [Online; accessed 3 Aug. 2015].
URL: *http://www.gamma-rs.ch/courses/past-courses.html* 78

Gilliland, E. and Rowe, C. [2007], 'A Comparison of Cumulus Parameterization Schemes in the WRF Model', *Proceedings, Conference of Hydrology* . 41

Gong, W., Meyer, F. J., Lee, C. W., Lu, Z. and Freymueller, J. [2015], 'Measurement and interpretation of subtle deformation signals at Unimak Island from 2003 to 2010 using weather model-assisted time series InSAR', *J. Geophys. Res. Solid Earth* **120**, 1174–1194. 6, 9

Gonzalez, A., Exposito, F. J., Perez, J. C., Diaz, J. P. and Taima, D. [2013], 'Verification of precipitable water vapour in high-resolution WRF simulations over a mountainous arcipelago', *Q. J. R. Meteorol. Soc.* **139**, 2119–2133. 6

Good, B., Gadian, A., Lock, S. and Ross, A. [2014], 'Performance of the cut-cell method of representing orography in idealized simulations', *Atmosph. Sci. Lett.* **15**, 4449. 33

Gray, A. L., Mattar, K. E. and Sofko, G. [2000], 'Influence of ionospheric electron density fluctuations on satellite radar interferometry', *Geophys. Res. Lett.* **27**(10), 1451–1454. 5

Hammouya, G., Allard, P., Jean-Baptiste, P., Parello, F., Semet, M. P. and Young, S. R. [2006], 'Pre- and syn-eruptive geochemistry of volcanic gases from Soufriere Hills of Montserrat, West Indies', *Geophys. Res. Lett.* **36**(19), 3685–3688. 154

Hammouya, T. [1994], 'Implications of the Hydrostatic Assumption on Atmospheric Gravity Waves', *J. Atmos. Sci.* **51**, 1915–1929. 55

Hanssen, R. F. [2001], *Radar Interferometry: Data Interpretation and Error Analysis*. x, xix, 5, 6, 21, 144

Heleno, S. I. N., Frischknecht, C., D'Oreye, N., Lima, J. N. P., Faria, B., Wall, R. and Kervyn, F. [2010], 'Seasonal tropospheric influence on SAR interferograms near the ITCZ - The case of Fogo Volcano and Mount Cameroon', *Journal of African Earth Sciences* **58**, 833–856. 2

Hetland, E. A., Musé, P., Simons, M., Lin, Y. N., Agram, P. S. and DiCaprio, C. J. [2012], 'Multiscale InSAR Time Series (MInTS) analysis of surface deformation', *J. Geophys. Res.* **117**. 6

Hobiger, T., Ichikawa, R. and Kondo, T. [2008], 'Fast and accurate ray-tracing algorithms for real-time space eodetic applications using numerical weather models', *J. Geophys. Res.* **113**. 111

Hobiger, T., Ichikawa, R., Koyama, Y. and Kondo, T. [2009], 'Computation of troposphere slant delays on a GPU', *IEEE Trans. Geosci. Remote Sens.* **47**, 3313–3318. 111

Hofmann-Wellenhof, B., Lichtenegger, H. and J., C. [1993], 'Global Positioning System. Theory and Practice', *J. Springer* . 92

Hu, X. M., John, W., Gammon, N. and Fuqing, Z. [2010], 'Evaluation of three planetary boundary layer schemes in the WRF model', *J. Climate Appl. Meteor.* **49**(9), 1831–1844. 45

Hunt, J. R. and Snyder, W. H. [1980], 'Experiments on stably and neutrally stratified flow over a model three dimensional hill', *J. Fluid Mech.* **96**, 671–704. 57

Initial conditions integration [2015]. [Online; accessed 31 Aug. 2015].
URL: *https://www.met.reading.ac.uk/wrf/* 155

Jolivet, R., Angram, P. S., Lin, N. Y. and Simons, M. [2014], 'Improving InSAR geodesy using global atmospheric models', *J. Geophys. Res.* . 6, 133

Jolivet, R., Grandin, R., Lasserre, C., Doin, M. P. and Peltzer, G. [2011], 'Systematic InSAR tropospheric phase delay corrections from global meteorological reanalysis data', *Geophys. Res. Lett.* **38**. 1

Katsougiannopoulos, S. [2006], 'Tropospheric Refraction Estimation Using Various Models, Radiosonde Measurements and Permanent GPS Data', *GNSS Processing and Applications* . 6

Kinoshita, Y., Shimada, M. and Furuya, M. [2013], 'InSAR observation and numerical modeling of the water vapor signal during a heavy rain: A case study of the 2008 Seino event, central Japan', *Geophys. Res. Lett.* **40**, 4740–4744. 10, 134

Laprise, R. [1992], 'The Euler Equations of Motion with Hydrostatic Pressure as an Independent Variable', *Mon. Weather Rev.* **120**(1), 1183–1196. 14, 25

Li, Z., Muller, J., Cross, P. and Fielding, E. J. [2005], 'Interferometric synthetic aperture radar (InSAR) atmospheric correction: GPS, Moderate Resolution Imaging Spectroradiometer (MODIS), and InSAR integration', *J. Geophys. Res.* **110**. 9

Liu, S. Z. [2012], 'Satellite radar interferometry: estimation of atmospheric delay', *Ph.D. Thesis, Delft University of Technology.* . 10

Massonnet, D., Briole, P. and Arnaud, A. [1995], 'Deflation of Mount Etna monitored by spaceborne radar interferometry', *Nature* **6532**(375), 567–570. 22

Matthews, A., Barclay, J., Carn, S., Thompson, G., Alexander, J., Herd, R. and C., W. [2002], 'Rainfall-Induced Volcanic Activity on Montserrat', *Geophys. Res. Lett.* **29**(13). 37, 45

Mendillo, M. [2006], 'Storms in the ionosphere: Patterns and processes for total electron content', *Rev. Geophys* **44**(4). 5

Meteo-france Rainfall Radar [2015]. [Online; accessed 2 Aug. 2015].
URL: *http://www.meteofrance.gp/previsions-meteo-antilles-guyane/animation/radar/antilles* 48

Miranda, P. M. A. and James, I. N. [1992], 'Non-Linear Three-Dimensional Effects On Gravity-Wave Drag: Splitting Flow and Breaking Waves', *Quart. J. Roy. Meteor. Soc.* **118**(508), 1057–1081. xi, 26, 51, 52, 53, 57, 74

Molteni, F., Buizza, R., Palmer, T. and Petroliagis, T. [1996], 'The ECMWF Ensemble Prediction System: Methodology and validation', *Q. J. R. Meteorol. Soc.* **112**, 73–119. 155

Onn, F. and Zebker, H. A. [2006], 'Correction for interferometric synthetic aperture radar atmospheric phase artifacts using time series of zenith wet delay observations from a GPS network', *J. Geophys. Res. Solid Earth* . 7

Otkin, J., Olson, E., Huang, H., Lui, C. and Wanzon, S. [2006], 'WRF model simulations used in support of infrared hyperspectral forward model and product algorithm development', *Proceedings, WRF Users Workshop* . 46

Pagowski, M. [2014], 'Some comments on PBL parameterizations in WRF', *Proceedings, The Joint WRF/MM5 Users Workshop, Boulder, CO* **1**(9). 45

Pinel, V., Poland, M. P. and Hooper, A. [2014], 'Volcanology: Lessons learned from Synthetic Aperture Radar imagery', *J. Volcanol. Geotherm. Res.* **289**, 81–113. 3

Pitteway, M., L., D. and Watkinson, J. [1980], 'Bresenham's algorithm with grey scale', *Communications of the ACM 23* (11), 625–626. 111

Porter, J., Miller, M., Pietras, C. and Motell, C. [2001], 'Ship-based sun photometer measurements using microtops sun photometers', *J. Atmos. Oceanic Technol.* **18**, 765–774. 7

Reagan, J., Thome, K., Herman, B. and Gall, R. [1987], 'Water vapor measurements in the 0.94 micron absorption band: calibration , measurements and data applications', *Proceedings, International Geoscience and Remote Sensing Symposium* . 46

Ren, K., Prinet, V., Shi, X. and Wang, F. [2003], 'Comparison of Satellite Baseline Estimation Methods for Interferometry Applications', *IEEE Trans. Geosci. Remote Sens.* p. 38213823. 79

Rosen, P. A., Hensley, S., Zebker, H. A., Webb, F. H. and Fielding, E. J. [1996], 'Surface deformation and coherence measurements of Kilauea Volcano, Hawaii, from SIR C radar interferometry', *J. Geophys. Res.* **E10**(101), 23,109–23,126. 22

Saastamoinen, J. [1972], 'Contribution to the theory of atmospheric refraction', *Bulletin of Geodesy* (11), 279–298. 95

Sadhana, J., Goyal, R. and Verma, A. [1996], 'Mathematical formulation for estimation of baseline in synthetic aperture radar interferometry', *Springer India* **21**(4), 511522. 79

Sandwell, D. T. and Price, E. J. [1998], 'Phase gradient approach to stacking interferograms', *J. Geophys. Res.* **103**(30), 183–204. 9

Shin, H. H. and Hong, S. [2011], 'Intercomparison of planetary boundary-layer parametrizations in the wrf model for a single day from cases-99', *Bound.-Layer Meteor* **139**(2). 45

Skamarock, W. C., Klemp, J. B. and Dudhia, J. [2001], 'Prototypes for the WRF (Weather Research and Forecasting) model', *Amer. Meteorol. Soc.* . 37

Skamarock, W. C., Klemp, J. B., Dudhia, J., Gill, D., Barker, D., Duda, K. G., Huang, X., Wang, W. and Powers, J. G. [2008], 'A description of the Advanced Research WRF Version 3', *NCAR Technical Note NCAR/TN-468+STR* . ix, x, 10, 12, 14, 15, 20, 25, 33, 36

Smith, R. B., Schafer, P., Kirshbaum, D. and Regina, E. [2009], 'Orographic enhancement of precipitation inside hurricane dean', *Journal of Hydrometeorology* **10**(3), 820–831. 2, 91

Smolarkiewicz, P. K., Rasmussen, R. M. and Clark, T. L. [1988], 'On the dynamics of hawaiian cloud bands: Island forcing', *J. Atmos. Sci* **45**, 1872–1905. 1

Smolarkiewicz, P. K. and Rotunno, R. [1989], 'Low Froude number flow past three-dimensional obstacles. Part I: Baroclinically generated lee vortices', *J. Atmos. Sci.* **46**, 1154–1164. 57

Tewari, M., Chen, F., Wang, W., Dudhia, J., Lemone, M., Mitchell, K., Ek, M., Gayno, G., Wegiel, J. and Cuenca, R. [2004], 'Implementation and verification of the unified noah land-surface model in the wrf model', *20th Conference on Weather Analysis and Forecasting/16th Conference on Numerical Weather Prediction, Seattle, WA, American Meteorological Society* . 34

Wadge, G., Costa, A., Pascal, K., Werner, C. and Webb, T. [2016], 'The variability of refractivity in the atmospheric boundary layer of a tropical island volcano measured by ground-based interferometric radar', *Submitted to Bound.-Layer Meteor.* . 108

Wadge, G., Mattioli, G. S. and Herd, R. A. [2006], 'Ground deformation at Soufriere Hills Volcano, Montserrat during 1998-2000 measured by radar interferometry and GPS', *Journal Of Volcanology And Geothermal Research* **152**(1-2), 157–173. 1

Wadge, G., Webley, P. W., James, I. N., Bingley, R., Dodson, A., Waugh, S., Veneboer, T., Puglisi, G., Mattia, M., Baker, D., Edwards, S. C., Edwards, S. J., Clarke and J., P. [2002], 'Atmospheric models, GPS and InSAR measurements of the tropospheric water vapour field over Mount Etna', *Geophys. Res. Lett.* **29**(19). 10

Wadge, G., Zhu, M., Holley, R. J., James, L. N., Clark, P. A., Wang, C. and Woodange, M. J. [2010], 'Correction of atmospheric delay effects in radar interferometry using a nested mesoscale atmospheric model', *J. Appl. Geophys.* **72**(2), 141–149. 91

Wang, W. and Seaman, N. [1997], 'A comparison study of convective parameterization schemes in a mesoscale mode', *Mon. Wea. Rev.* **2**(125), 252–278. 38

Wang, W., Wei, W., Bruyre, C., Duda, M., Dudhia, J., Gill, D., Lin, H., Michaelakes, J., Rizvi, S. and Zhang, X. [2014], 'WRF-ARW Version 3 Modeling System Users Guide', *Mesoscale and Microscale Meteorology Division, National Center for Atmospheric Research* . 28, 34

Webley, P. W., Bingley, R. M., Dodson, A. H., Wadge, G., Waugh, S. J. and James, I. N. [2002], 'Atmospheric water vapour correction to InSAR surface motion measurements on mountains: results from a dense GPS network on Mount Etna', *Physics and Chemistry of the Earth, Parts A/B/C* **27**(45), 363–370. 7

Weiss, S. J., Pyle, M. E., Janjic, Z., Bright, D. R., Kain, J. S. and DiMego, G. J. [2008], 'The operational High Resolution Window WRF model runs at NCEP: Advantages of multiple model runs for severe convective weather forecasting', *Preprints, 24th Conf. on Severe Local Storms* . 37

Wicker, L. J. and Skamarock, W. C. [2002], 'Time splitting methods for elastic models using forward time schemes', *Mon. Wea. Rev.* (130), 2088–2097. 16

Wyoming Radiosonde Database [2015]. [Online; accessed 2 Aug. 2015].
URL: *http://weather.uwyo.edu/upperair/sounding.html* 48

Zebker, H. A. and Goldstein, R. M. [1986], 'Topographic mapping from interferometric synthetic aperture radar observations', *J. Geophys. Res.* **B5**(91), 4993–4999. 22

Zhang, D. and Wang, X. [2003], 'Dependence of hurricane intensity and structures on vertical resolution and time-step size', *Advances in Atmospheric Sci.* **20**, 711–725. 34

Zhenhong, L., Fielding, E. J., Cross, P. and Muller, J. [2006], 'Interferometric synthetic aperture radar atmospheric correction: GPS topography-dependent turbulence model', *J. Geophys. Res. Solid Earth* **111**. 7